

A NEW FORMULATION FOR THE ANALYSIS OF
BONDED ELASTIC LAYERS

A THESIS SUBMITTED TO
THE GRADUATE SCHOOL OF NATURAL AND APPLIED SCIENCES
OF
MIDDLE EAST TECHNICAL UNIVERSITY

BY

SEVAL PINARBAŞI

IN PARTIAL FULFILLMENT OF THE REQUIREMENTS
FOR
THE DEGREE OF DOCTOR OF PHILOSOPHY
IN
CIVIL ENGINEERING

APRIL 2007

Approval of the Graduate School of Natural and Applied Sciences

Prof. Dr. Canan Özgen
Director

I certify that this thesis satisfies all the requirements as a thesis for the degree of Doctor of Philosophy.

Prof. Dr. Güney Özcebe
Head of Department

This is to certify that we have read this thesis and that in our opinion it is fully adequate, in scope and quality, as a thesis for the degree of Doctor of Philosophy.

Assoc. Prof. Dr. Uğurhan Akyüz
Supervisor

Examining Committee Members

Prof. Dr. Polat Gülkan (METU,CE)_____

Assoc. Prof. Dr. Uğurhan Akyüz (METU,CE)_____

Prof. Dr. Yalçın Mengi (METU,ES)_____

Assoc. Prof. Dr. Ahmet Yakut (METU,CE)_____

Assist. Prof. Dr. A. Hakan Argeşo (Baskent Univ., ME)_____

I hereby declare that all information in this document has been obtained and presented in accordance with academic rules and ethical conduct. I also declare that, as required by these rules and conduct, I have fully cited and referenced all material and results that are not original to this work.

Name, Last Name: Seval Pınarbaşı

Signature :

ABSTRACT

A NEW FORMULATION FOR THE ANALYSIS OF BONDED ELASTIC LAYERS

Pınarbaşı, Seval

Ph. D., Department of Civil Engineering

Supervisor: Assoc. Prof. Dr. Uğurhan Akyüz

April 2007, 248 pages

Elastic layers bonded to reinforcing sheets are widely used in many engineering applications, e.g., as elastic foundations to machinery, as seismic isolators to structures, etc. Because of its practical importance, the behavior of bonded elastic layers under some basic deformation modes (e.g., compression, bending and shear modes) has attracted the attention of many researchers. However, the analytical works available in literature involve, with the object of obtaining design formulas, many simplifying assumptions. In this dissertation, a new formulation is developed for the analysis of bonded elastic layers, which removes most of the assumptions used in the earlier formulations. Since the displacement boundary conditions are included in the formulation itself, there is no need to start the formulation with some assumptions on stress and/or displacement distributions

or with some limitations on geometrical and/or material properties. For this reason, the solutions derived from this formulation are valid not only for “thin” layers of strictly/nearly incompressible materials but also for “thick” layers and/or compressible materials.

The advanced solutions obtained within the framework of the new formulation are used to study the behavior of bonded elastic layers under basic deformation modes. The effects of three key parameters, shape factor, Poisson’s ratio and reinforcement flexibility, on effective layer moduli, displacement/stress distributions, and location/magnitude of maximum stresses are investigated. It is shown that the stress assumptions of the “pressure” method are inconsistent with the results obtained for thick layers and/or compressible materials and/or flexible reinforcements, and that the assumption “plane sections remain plane” is not valid, in general.

Keywords: Bonded Elastic Layers, Elastomeric Bearing, Seismic Isolation, Shape Factor, Poisson’s Ratio

ÖZ

ÜST VE ALT YÜZEYLERİNDEN YAPIŞTIRILMIŞ ELASTİK TABAKALARIN ANALİZİ İÇİN YENİ BİR FORMÜLASYON

Pınarbaşı, Seval

Doktora, İnşaat Mühendisliği Bölümü

Tez Yöneticisi: Doç. Dr. Uğurhan Akyüz

Nisan 2007, 248 sayfa

Üst ve alt yüzeylerinden güçlendirici plakalara yapıştırılmış elastik tabakalar, elastik makina temelleri ve sismik yapı izolatörleri gibi pek çok mühendislik uygulamasında yaygın olarak kullanılmaktadır. Pratik önemi nedeni ile, güçlendirilmiş elastik tabakaların bazı temel deformasyon modları (basınç, eğilme ve kayma modları gibi) altındaki davranışları bir çok araştırmacının dikkatini çekmiştir. Ancak, literatürde konu ile ilgili mevcut analitik çalışmalar, tasarım formülleri elde edilmesi amacı ile, bir çok basitleştirici kabul içermektedir. Bu tezde, güçlendirilmiş elastik tabakaların bazı temel deformasyon modlarındaki davranışlarının analizi için yeni bir formülasyon geliştirilmiştir. Bu formülasyon, daha önceki çalışmalarda kullanılan kabüllerin pek çoğunu elimine etmektedir.

Deplasman sınır kořulları formülasyonun içinde yer aldığı için analize, tabakadaki gerilme ve/veya deplasman dağılımları üzerine bazı varsayımlar yapılarak ya da tabakanın geometrik ve/veya malzeme özelliklerine bazı sınırlandırmalar getirilerek başlanması gerekmemektedir. Bu nedenle, bu formülasyondan elde edilen çözümler sadece sıkıştırılmaz ya da sıkıştırılmazıya yakın malzemelerden üretilen “ince” tabakalar için değil sıkıştırılabilir malzemelerden üretilen “kalın” tabakalar için de geçerlidir.

Yeni formülasyon çerçevesinde elde edilen ileri çözümler, güçlendirilmiş elastik tabakaların temel deformasyon modlarındaki davranışlarının incelenmesinde kullanılmıştır. Analizlerde, üç anahtar parametrenin, tabakanın şekil faktörü, malzemenin Poisson oranı ve güçlendirici plakaların rijitliklerinin, etkili tabaka modülleri, tabakadaki deplasman ve gerilme dağılımları ile tabakada oluşan maksimum gerilmelerin yer ve büyüklüğü üzerindeki etkileri incelenmiştir. Kalın tabaka ve/veya sıkıştırılabilir tabaka ve/veya esnek donatı durumları için elde edilen sonuçların yaygın olarak kullanılan basınç metodundaki gerilme varsayımları ile tutarsız olduğu kanıtlanmış; “düzlem kesitler düzlem kalır” varsayımının genel olarak geçerli olmadığı gösterilmiştir.

Anahtar Kelimeler: Güçlendirilmiş Elastik Tabakalar, Elastomerik Yastık, Sismik İzolasyon, Şekil Faktörü, Poisson Oranı

To my mother, ÜLKER, with all my love...

ACKNOWLEDGEMENTS

I would like to express my deepest gratitude to *all* –not only to those whose names are listed below which are, in fact, extremely lucky to come to my little brain– who gave me their support, encouragement and, most importantly, their love which made it possible for me to accomplish this dissertation. Thank you all for being in my life and please stay there forever...

Specially, my sincere appreciation and gratitude go to my supervisor, Dr. Uğurhan Akyüz, who gave me the freedom to pursue my own research interests.

It is really hard to find the proper words to be able to express my appreciation to Dr. Yalçın MENGİ, whose contribution to the entire work is invaluable. However, I can easily say one thing: This dissertation could not have been completed without his guidance...

I would also like to thank to the other members of my dissertation committee: Dr. Polat Gülkan and Dr. Ahmet Yakut, for their valuable suggestions and encouragements during my research.

This study is partially funded by the State Planning Organization (DPT) Grant No: BAP-08-11-DPT2002K120510, which is also gratefully acknowledged.

I also thank Mr. Burhan Avcı and the staff of the Structural Mechanics Laboratory for their help during the realization of the tests, which constituted one stage of my Ph.D. studies.

I would like to extend my gratitude to Prof. James M. Kelly for giving me the opportunity to work with him at the Earthquake Engineering Research Center of the University of California at Berkeley. It was a great privilege for me to study under the supervision of my “idol”.

Special thanks go to Yalın Arıcı and Barbaros Sarıca for helping to start my Berkeley adventure, and to my home mate Çağla Meral for sharing not only her home but also her life and love. I would also like to express my gratitude to Nergiz Dinçer, Dimitrios Konstantinidis, İsmail Ergen, Tufan Karalar, Afşin Sarıtaş, Feyzi Tecellioğlu and Türel Gür for their valuable friendship and support before/during/after my Berkeley days. My sincere appreciation also goes to Dr. Yousef Bozorgnia, Mr. Charles D. James and Ms. Nancy Nelson for their help, support and valuable friendship during my Berkeley experience.

My colleagues Burcu Erdoğan, Dilek Okuyucu, Beyhan Bayhan, Bora Acun, Serhat Bayılı, Emre Akın, Özgür Avşar, Abdullah Dilsiz, Barış Erdil, Ramazan Özçelik, and Hakan Erdoğan are also acknowledged for their friendship.

Never to be forgotten are my dearest friends; Ali Cihan Pay, Fatih Kürşat Fırat, Gökhan Özdemir, İbrahim Erdem, Metin Yılmaz, Onur Pekcan, Reyhan (Eğri) Şahin, Seçkin Çaban, Sezgin Küçükçoban and Sinan Akarsu, whose friendship, moral support and love are invaluable for me.

My heartfelt gratitude goes to three special persons in my life: Fatma (Durna) Akar, Volkan Aydoğan and Şevket Özden. Without their endless support, encouragement and love, this dissertation would not have been completed.

Finally, I would like to express my deepest gratitude to my parents, Ülker Pınarbaşı and Mehmet Pınarbaşı, my brother Ali Seyhun Pınarbaşı, and also to my aunt Ülkü Durna for their unconditional love, support and encouragement they have provided me throughout my whole life.

TABLE OF CONTENTS

ABSTRACT	iv
ÖZ	vi
ACKNOWLEDGEMENTS	ix
TABLE OF CONTENTS	xi
LIST OF TABLES	xv
LIST OF FIGURES.....	xvi
CHAPTER	
1. INTRODUCTION.....	1
1.1 BONDED ELASTIC LAYERS	1
1.2 AIM OF THE DISSERTATION	5
1.3 SCOPE AND ORGANIZATION OF THE DISSERTATION.....	7
2. THEORY ON BONDED ELASTIC LAYERS	9
2.1 ELASTIC LAYERS BONDED TO RIGID SURFACES	9
2.1.1 Compressive Behavior.....	13
2.1.2 Bending Behavior	26
2.1.3 Apparent Shear Behavior.....	29
2.2 ELASTIC LAYERS BONDED TO FLEXIBLE REINFORCEMENTS .	31
2.2.1 Compressive Behavior.....	33
2.2.2 Bending Behavior	39
2.2.3 Warping Behavior.....	41
3. THE NEW FORMULATION FOR THE ANALYSIS OF BONDED ELASTIC LAYERS	47

3.1	REVIEW OF THE APPROXIMATE THEORY USED IN THE DISSERTATION	49
3.2	APPLICATION OF THE APPROXIMATE THEORY TO ELASTIC LAYERS BONDED TO RIGID SURFACES	54
3.2.1	Derivation of Reduced Governing Equations	56
3.2.1.1	Uniform Compression	56
3.2.1.2	Pure Bending	58
3.2.1.3	Apparent Shear	60
3.2.2	Reduced Governing Equations in Cylindrical Coordinates	61
3.2.2.1	Uniform Compression	64
3.2.2.2	Pure Bending	65
3.2.2.3	Apparent Shear	67
3.2.3	Determination of Displacement/Stress Distributions	68
3.2.4	Compression, Bending and Apparent Shear Moduli	69
3.3	APPLICATION OF THE APPROXIMATE THEORY TO ELASTIC LAYERS BONDED TO FLEXIBLE REINFORCEMENTS	71
3.3.1	Derivation of Reduced Governing Equations	73
3.3.1.1	Uniform Compression	73
3.3.1.2	Pure Bending	77
3.3.1.3	Pure Warping	79
3.3.2	Determination of Displacement/Stress Distributions and Effective Moduli of the Layer	80
4.	ANALYSIS OF BONDED ELASTIC LAYERS USING THE NEW FORMULATION	82
4.1	ANALYTICAL SOLUTIONS FOR ELASTIC LAYERS BONDED TO RIGID SURFACES	83
4.1.1	Bonded Elastic Strips	83
4.1.1.1	Uniform Compression	83
4.1.1.1.1	Solution for Zeroth Order Theory	83
4.1.1.1.2	Solution for First Order Theory	84
4.1.1.2	Pure Bending	86

4.1.1.3	Apparent Shear	88
4.1.2	Bonded Elastic Discs	90
4.1.2.1	Uniform Compression	90
4.1.2.1.1	Solid Circular Sections	91
4.1.2.1.2	Hollow Circular Sections	94
4.2	ANALYTICAL SOLUTIONS FOR ELASTIC LAYERS BONDED TO FLEXIBLE REINFORCEMENTS.....	96
4.2.1	Bonded Elastic Strips.....	96
4.2.1.1	Uniform Compression	96
4.2.1.1.1	Solution for Zeroth Order Theory	96
4.2.1.1.2	Solution for First Order Theory.....	100
4.2.1.2	Pure Bending	103
4.2.1.3	Pure Warping.....	107
5.	ASSESSMENT OF THE FORMULATION.....	113
5.1	PROBLEM 1: A C-SHAPED LAYER UNDER COMPRESSION	114
5.1.1	BEM Model	114
5.1.2	Compression Modulus	116
5.1.3	Displacement Distributions	116
5.1.4	Stress Distributions	119
5.1.5	Effect of Mesh Size	124
5.2	PROBLEM 2: AN HC-SHAPED LAYER UNDER COMPRESSION .	126
5.2.1	BEM Model	126
5.2.2	Compression Modulus	127
5.2.3	Stress Distributions	128
5.3	PROBLEM 3: AN IS-SHAPED LAYER UNDER COMPRESSION ...	131
5.3.1	BEM Model	131
5.3.2	Compression Modulus	132
5.3.3	Displacement Distributions	133
5.4	PROBLEM 4: AN IS-SHAPED LAYER UNDER BENDING	133
5.4.1	BEM Model	133
5.4.2	Bending Modulus.....	135

5.4.3	Displacement and Stress Distributions	135
5.5	PROBLEM 5: AN IS-SHAPED LAYER UNDER APPARENT SHEAR.....	137
5.5.1	BEM Model	137
5.5.2	Apparent Shear Modulus	137
5.5.3	Displacement and Stress Distributions	138
6.	EFFECT OF POISSON’S RATIO AND SHAPE FACTOR ON BEHAVIOR OF BONDED ELASTIC LAYERS.....	140
6.1	COMPRESSIVE BEHAVIOR	140
6.2	BENDING BEHAVIOR.....	156
6.3	APPARENT SHEAR BEHAVIOR	168
7.	EFFECT OF THE PRESENCE OF A CENTRAL HOLE ON COMPRESSIVE BEHAVIOR OF BONDED DISCS.....	173
7.1	COMPRESSION MODULUS.....	174
7.2	STRESS DISTRIBUTIONS	183
7.3	MAXIMUM SHEAR STRESS AND SHEAR STRAIN	191
8.	EFFECT OF REINFORCEMENT FLEXIBILITY ON BEHAVIOR OF BONDED ELASTIC LAYERS	198
8.1	COMPRESSIVE BEHAVIOR	199
8.2	BENDING BEHAVIOR.....	210
8.3	WARPING BEHAVIOR	220
9.	CONCLUSIONS	234
	REFERENCES.....	241
	CURRICULUM VITAE	247

LIST OF TABLES

Table 2.1 Definition of the notation for bonded layers of different shapes (Figure for the rectangular shape is taken from [22]).....	12
Table 3.1 c_{nj} coefficients (ϕ_n 's are Legendre polynomials)	55
Table 3.2 Coefficients a_k^i and constants $\gamma_j, \gamma^\ddagger$ for the 0 th , 1 st and 2 nd order theories (ϕ_n 's are Legendre polynomials).....	56
Table 5.1 Definition of BEM models with different mesh sizes and their predictions for compression modulus ($S=2, \nu=0.45$)	124
Table 5.2 BEM and FOT predictions for compression modulus of the HC- shaped layer ($S_0=2, \nu=0.499$) with different hole sizes.....	127
Table 5.3 BEM and FOT predictions for compression modulus of the IS-shaped layer of $S=5$ with different compressibility characteristics	132
Table 7.1 Limiting β values, denoted as β_{Ceq} and β_{Iseq} , computed for 1% error in the prediction of compression modulus.....	183

LIST OF FIGURES

Figure 1.1 A typical steel-reinforced elastomeric bearing used in seismic isolation technique (taken from [8])	3
Figure 1.2 Definition of shape factor for a cylindrical steel-reinforced elastomeric bearing (taken from [9]).....	3
Figure 2.1 An elastic layer bonded to rigid surfaces under its three basic deformation modes	10
Figure 2.2 Compression modulus of bonded rubber blocks (taken from [2]).....	15
Figure 2.3 Deformed and undeformed configurations for an IS-shaped bonded elastic layer under uniform compression (taken from [20]).....	17
Figure 2.4 Deformation of an elastic layer bonded to flexible reinforcements under the effects of the compression force P , bending moment M and warping moment Q (taken from [46])	32
Figure 2.5 Forces on a reinforcing sheet bonded to IS-shaped rubber layers at its top and bottom faces (taken from [47]).....	34
Figure 2.6 Forces on an infinitesimal area of a reinforcing sheet bonded to RC-shaped rubber layers (taken from [47])	37
Figure 3.1 Cartesian coordinate system defined for a layer.....	49
Figure 3.2 Undeformed and deformed configurations for an elastic layer bonded to rigid plates under its three basic deformation modes	54
Figure 3.3 Cylindrical coordinate system defined for axisymmetric case (taken from [30])	61
Figure 3.4 Undeformed and deformed configurations for an elastic layer bonded to flexible reinforcements under compression and bending (taken from [46])..	72

Figure 3.5 Forces on an infinitesimal area of a reinforcing sheet bonded to rubber layers at its top and bottom faces (taken from [47])	76
Figure 4.1 Undeformed and deformed configurations of a bonded disc (i) without and (ii) with a central hole under uniform compression	90
Figure 5.1 Discretization of the bonded elastic disc in r-z plane for axisymmetric BEM solution (Boundary conditions (BC's) are also specified).....	115
Figure 5.2 Definition of the sections in the bonded elastic disc over which the displacement and stress distributions are plotted	116
Figure 5.3 Variation of normalized radial displacement through the layer thickness at various sections.....	117
Figure 5.4 Variation of normalized radial displacement through the radius at $z=0, t/4$	117
Figure 5.5 Variation of normalized axial displacement through the layer thickness at various sections.....	118
Figure 5.6 Variation of normalized axial displacement through the radius at $z=t/4$	118
Figure 5.7 Variation of normalized radial stress through the layer thickness.....	120
Figure 5.8 Variation of normalized axial stress through the layer thickness	120
Figure 5.9 Variation of normalized radial, circumferential and axial stresses ($\tau_{ii}/\mu\epsilon_c$ for $i=r,\theta,z$) through the layer thickness at $r=R/2$	121
Figure 5.10 Variation of normalized shear stress through the layer thickness	121
Figure 5.11 Variation of normalized axial stress through the radius	122
Figure 5.12 Variation of normalized radial, circumferential and axial stresses ($\tau_{ii}/\mu\epsilon_c$ for $i=r,\theta,z$) through radius at $z=t/4$	122
Figure 5.13 Variation of normalized shear stress through the radius	123
Figure 5.14 Effect of mesh size on BEM predictions for stress distributions.....	125
Figure 5.15 Discretization of the HC-shaped bonded elastic layer for BEM analysis	126

Figure 5.16 Variation of shear stress through the layer thickness in the HC-shaped layer ($S_0=2$, $\nu=0.499$) with different radius ratios predicted by FOT (continuous lines) and BEM (discrete points)	128
Figure 5.17 Normal stress distributions through the layer thickness in the HC-shaped layer ($S_0=2$, $\nu=0.499$) with different radius ratios predicted by FOT (continuous lines) and BEM (discrete points)	129
Figure 5.18 Stress distributions over the bonded faces in the HC-shaped layer ($S_0=2$, $\nu=0.499$) with different radius ratios predicted by FOT (continuous lines) and BEM (discrete points)	130
Figure 5.19 Discretization of the IS-shaped bonded elastic layer for the compression problem (Boundary conditions (BC's) are also specified).....	131
Figure 5.20 Assessment of the validity of two basic assumptions through the comparison of FOT (continuous lines) and BEM (discrete points) predictions	134
Figure 5.21 Discretization of the IS-shaped bonded elastic layer for the bending problem (Boundary conditions (BC's) are also specified).....	135
Figure 5.22 Displacement distributions through the layer thickness under pure bending	136
Figure 5.23 Stress distributions through the layer thickness under pure bending .	136
Figure 5.24 Stress distributions at the bonded faces under pure bending.....	137
Figure 5.25 Discretization of the IS-shaped bonded elastic layer for apparent shear problem (Boundary conditions (BC's) are also specified).....	138
Figure 5.26 Displacement distributions under apparent shear	138
Figure 5.27 Stress distributions at the bonded faces under apparent shear.....	139
Figure 6.1 Effect of shape factor and Poisson's ratio on compression modulus ...	141
Figure 6.2 Effect of Poisson's ratio on displacement distributions in lateral direction under uniform compression.....	142
Figure 6.3 Effect of Poisson's ratio on displacement distributions through the layer thickness under uniform compression	143
Figure 6.4 Effect of shape factor and Poisson's ratio on maximum bulging under uniform compression	144

Figure 6.5 Effect of shape factor and Poisson's ratio on axial displacement of the layer at the quarter thickness under uniform compression	145
Figure 6.6 Effect of Poisson's ratio on stress distributions in lateral direction in bonded IS-shaped layers with $S=1$ (left hand side) and $S=30$ (right hand side)	146
Figure 6.7 Effect of shape factor on stress distributions in lateral direction in bonded IS-shaped layers for $\nu=0.45$ (left hand side), $\nu=0.499$ (right hand side)	147
Figure 6.8 Effect of Poisson's ratio on stress distributions in axial direction in bonded IS-shaped layers with $S=1$ (left hand side) and $S=30$ (right hand side)	150
Figure 6.9 Effect of shape factor on stress distributions in axial direction in bonded IS-shaped layers for $\nu=0.45$ (left hand side), $\nu=0.499$ (right hand side)	151
Figure 6.10 Comparison of the predictions of FOT (continuous lines) and PM (discrete points) for lateral normal stress distribution in the axial direction....	152
Figure 6.11 Effect of shape factor and Poisson's ratio on maximum normalized stresses under uniform compression.....	155
Figure 6.12 Predictions of zeroth and first order theories for bending modulus ...	156
Figure 6.13 Effect of Poisson's ratio and shape factor on E_c/E_b ratio	157
Figure 6.14 Effects of shape factor and Poisson's ratio on displacement distributions under pure bending	158
Figure 6.15 Effect of Poisson's ratio on stress distributions in lateral direction in bonded IS-shaped layers with $S=2.5$ (left hand side) and $S=30$ (right hand side)	160
Figure 6.16 Effect of Poisson's ratio on stress distributions in axial direction in bonded IS-shaped layers with $S=2.5$ (left hand side) and $S=30$ (right hand side)	162
Figure 6.17 Effect of shape factor on stress distributions in axial direction in bonded IS-shaped layers for $\nu=0.45$ (left hand side), $\nu=0.499$ (right hand side)	163

Figure 6.18 Effect of shape factor and Poisson’s ratio on magnitude and location of maximum lateral normal stress under pure bending	164
Figure 6.19 Maximum pressure in a bonded elastic layer under pure bending	166
Figure 6.20 Assessment of the predictions of the pressure method (PM) for the “critical” pressure in an IS-shaped layer under pure bending	167
Figure 6.21 Effect of shape factor and Poisson’s ratio on maximum shear stress under pure bending	168
Figure 6.22 Effect of shape factor and Poisson’s ratio on apparent shear modulus	169
Figure 6.23 Comparison of the prediction of FOT for apparent shear modulus of an IS-shaped layer with the predictions of the other expressions in literature .	170
Figure 6.24 Displacement distributions in axial direction under apparent shear ...	171
Figure 6.25 Axial and shear stress distribution in lateral direction under apparent shear.....	172
Figure 7.1 Effect of radius ratio on $E_{c,HC}$, normalized with respect to (a) μ and (b) $E_{c,C}$, for two different initial shape factors $S_o=2,30$	175
Figure 7.2 Effect of Poisson’s ratio and initial shape factor on $E_{c,HC}$, normalized with respect to $E_{c,C}$, for two different initial shape factors.....	178
Figure 7.3 E_c predictions computed from (solid) C, exact HC, “equivalent” C and “equivalent” IS expressions for $S_o=2$ (left hand side) and $S_o=30$ (right hand side).....	180
Figure 7.4 Assessment of the success of the “equivalent” C (left hand side) and “equivalent” IS (right hand side) expressions in predicting $E_{c,HC}$	182
Figure 7.5 Effect of radius ratio on axial stress distribution in radial direction in bonded annular layers with $S_o=2$ (left hand side) and $S_o=30$ (right hand side)	184
Figure 7.6 Comparison of the predictions of the exact HC expression and the “equivalent” IS expression for axial stress distribution in radial direction in an HC-shaped layer with $\beta=0.5$ for two different initial shape factors	187
Figure 7.7 Effect of initial shape factor on shear stress distribution in radial direction in a bonded annular layer of slightly compressible material ($\nu=0.499$).....	189

Figure 7.8 Effect of radius ratio on radial stress distribution in axial direction in bonded annular layers with $S_0=2$ (left hand side) and $S_0=30$ (right hand side)	190
Figure 7.9 Effect of shape factor and Poisson's ratio on maximum shear stress in C-shaped bonded elastic layers	191
Figure 7.10 Variation of shear stress at the inner (left hand side) and outer (right hand side) faces of a bonded annular layer with initial shape factor.....	193
Figure 7.11 Magnification of maximum shear strain due to the existence of a hole in the center of a bonded circular disc as a function of radius ratio	195
Figure 7.12 Assessment of the success of the simple expression proposed by Constantinou et al. [16] for the maximum shear strain ratio (discrete points in filled triangular shapes)	197
Figure 8.1 Effect of reinforcement flexibility on normalized compression modulus of bonded IS-shaped layers.....	199
Figure 8.2 Effects of shape factor and Poisson's ratio on normalized compression modulus of an IS-shaped layer bonded to flexible reinforcements	201
Figure 8.3 Effect of reinforcement flexibility on stress distributions in lateral direction under uniform compression for $S=1$	202
Figure 8.4 Effect of reinforcement flexibility on normal stress distributions in lateral direction under uniform compression for $S=30$	204
Figure 8.5 Effect of reinforcement flexibility on shear stress distribution in lateral direction under uniform compression for $S=30$	205
Figure 8.6 Effect of reinforcement flexibility on normal stress distributions in axial direction under uniform compression for $S=1$	205
Figure 8.7 Effect of reinforcement flexibility on normal stress distributions in axial direction under uniform compression for $S=30$	206
Figure 8.8 Effect of reinforcement flexibility on maximum stresses in a bonded IS-shaped layer under uniform compression.....	208
Figure 8.9 Effect of shape factor on maximum stresses in an IS-shaped layer bonded to extensible reinforcements under uniform compression.....	209

Figure 8.10 Predictions of zeroth and first order theories for bending modulus of IS-shaped layers bonded to flexible reinforcements	211
Figure 8.11 Effect of reinforcement flexibility on E_c/E_b ratio	212
Figure 8.12 Effect of reinforcement flexibility on normalized bending modulus .	213
Figure 8.13 Effect of reinforcement flexibility on stress distributions in lateral direction under pure bending for S=2.5.....	214
Figure 8.14 Effect of reinforcement flexibility on normal stress distributions in lateral direction under pure bending for S=30.....	216
Figure 8.15 Effect of reinforcement flexibility on shear stress distribution under pure bending in lateral direction for S=30.....	217
Figure 8.16 Effect of reinforcement flexibility on lateral normal stress distribution in axial direction under pure bending for S=2.5 (on the left hand side) and S=30 (on the right hand side).....	217
Figure 8.17 Effect of reinforcement flexibility on maximum shear stress in an IS-shaped layer bonded to extensible reinforcements under pure bending.....	219
Figure 8.18 Predictions of zeroth and first order theories for warping constant “F”	220
Figure 8.19 Effect of reinforcement flexibility on warping constant “F”	222
Figure 8.20 Predictions of zeroth and first order theories for warping modulus ...	222
Figure 8.21 Effect of reinforcement flexibility on normalized warping modulus .	223
Figure 8.22 Effect of reinforcement flexibility on E_c/E_w ratio.....	225
Figure 8.23 Effect of reinforcement flexibility on stress distributions in lateral direction under pure warping for S=2.5	226
Figure 8.24 Effect of reinforcement flexibility on lateral normal stress distribution in lateral direction under pure warping for S=30.....	227
Figure 8.25 Effect of reinforcement flexibility on shear stress distribution under pure bending in lateral direction for S=30.....	228
Figure 8.26 Convergence of FOT solution to PM solution for stress distributions in an HSF layer (S=30, $k_f/\mu t=30000$) of incompressible materials.....	229

Figure 8.27 Convergence of FOT solution to the “short beam” solution for axial stress distribution in an LSF (S=2.5) and HSF (S=30) layer of compressible ($\nu=0.3$) materials bonded to flexible reinforcements ($k_f/\mu t=30000$).....	230
Figure 8.28 Effect of reinforcement flexibility on stress distributions in axial direction under pure warping for S=2.5	232
Figure 8.29 Effect of reinforcement flexibility on stress distributions in axial direction under pure warping for S=30	233

CHAPTER 1

INTRODUCTION

1.1 BONDED ELASTIC LAYERS

Elastic layers bonded to reinforcing sheets have long been used as suspension and support systems, compression and shear mountings, and as sealing components [1]. Earlier studies on “bonded elastic layers” [2,3] have shown that the reinforcing plates bonded to top and bottom faces of an elastic layer may cause considerable changes on the layer behavior. These studies have also shown that the effects of the bonded surfaces on the layer behavior highly depend on the geometric and material properties of the layer, and become much more pronounced as material compressibility decreases, i.e., as Poisson’s ratio approaches 0.5, since, as stated by Lindley [4], “for materials such as rubber which have a low shear modulus but a relatively high bulk modulus, any restrictions on their freedom to change shape can have a very marked effect on their stiffness in compression”.

It is now very well known that not only the compression but also the bending stiffness of a bonded rubber layer may be several orders of magnitude greater than that of the corresponding unbonded layer. It is to be noted that despite their significant effects on the compressive or bending behavior, the bonded surfaces do *not* influence the shear behavior of the layer considerably. This is an important property considering that the resistance of a soft elastic layer to compression and bending can be increased without compromising from its flexibility in shear.

Composed of several elastomer layers sandwiched between and bonded to steel plates, “elastomeric bearings” have been developed using this favorable mechanical property of bonded elastic layers. In the earlier applications, elastomeric bearings were primarily used as expansion bearings for highway bridges to accommodate thermal expansion and slow differential movements, helicopter rotor bearings, wharf fenders, elastic foundations to machinery and motors and as sealing components. Recently, their applications have been extended to seismic isolation, which is a new earthquake resistant design concept in which flexible and energy dissipating elements are inserted at the base of the structure to reduce the transmission of seismic force from the soil to the structure. The main philosophy behind this technique is to shift the fundamental period of the structure sufficiently away from both its fixed-base period and the predominant period of most earthquakes so that the behavior of the entire structure can be governed by its first mode where the deformations are concentrated at the isolation level, while the superstructure moves almost rigidly.

Combination of soft elastomer layers, which provide flexibility in horizontal direction to shift the period of the isolated structure away from its fixed-base period, with comparatively rigid steel plates, which provide resistance to support the heavy weight of the superstructure and to resist possible rotations, in a single unit makes multi-layered steel-laminated elastomeric bearings (Figure 1.1) favorable to use as effective seismic isolators [5-7].

Under the applied loads, the behavior of a steel-laminated elastomeric bearing is controlled primarily by the elastomer thickness. Independent from the interior steel-elastomer composition, the *total* elastomer thickness is the main parameter determining the shear stiffness of the bearing. On the other hand, the thickness of the *individual* “bonded elastomer layers” governs the behavior of the bearing under compression and bending. In fact, as shown by many analytical and experimental studies, it is the aspect ratio of a typical interior bonded elastomer layer (Figure 1.2), named as **shape factor (S)**, which mainly controls the compressive and bending behavior of a multi-layered elastomeric bearing.

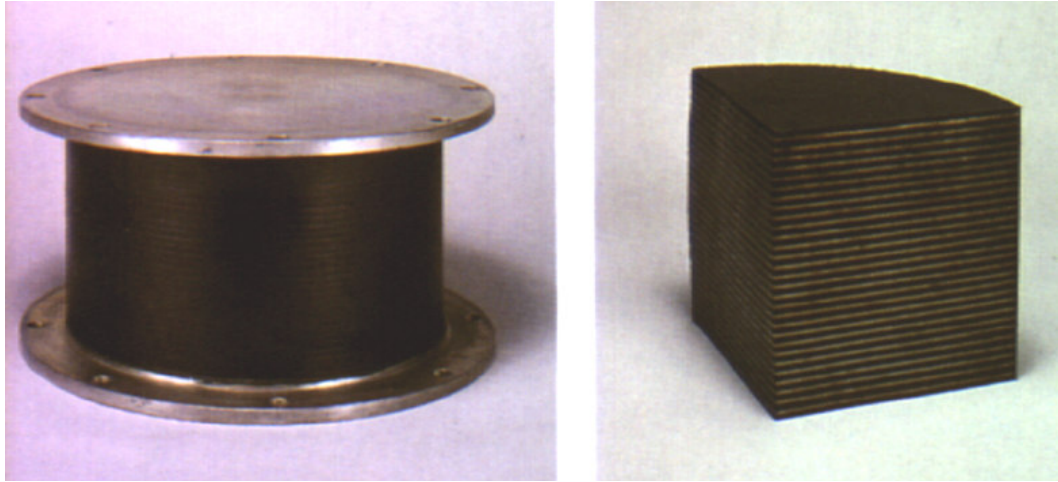


Figure 1.1 A typical steel-reinforced elastomeric bearing used in seismic isolation technique (taken from [8])

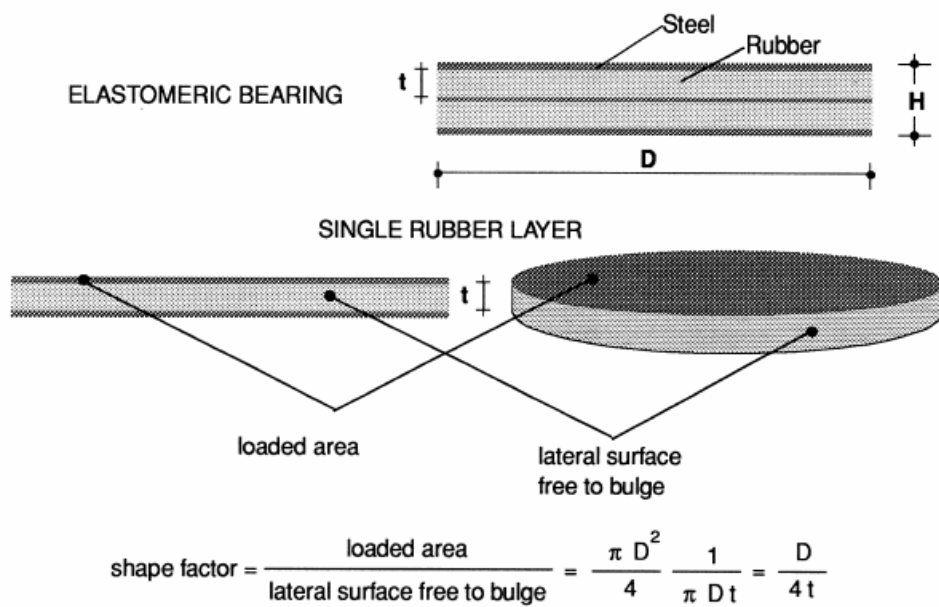


Figure 1.2 Definition of shape factor for a cylindrical steel-reinforced elastomeric bearing (taken from [9])

Shape factor of a bonded elastic layer is defined as the ratio of “*one* loaded area” to the “*entire* force free area”, i.e., the area of the perimeter free to bulge, as illustrated in Figure 1.2 [9]. Accordingly, “thin” layers which have high shape factors, called **HSF** (high shape factor) layers, have considerably high compressive and bending stiffnesses while “thick” layers which have low shape factors, called **LSF** (low shape factor) layers, have low stiffnesses. As it can easily be inferred, an HSF bearing is mainly designed to provide isolation only in the horizontal direction while an LSF bearing can provide three dimensional (3D) isolation.

While most of the elastomeric bearings used in seismic isolation technique are reinforced with steel plates, in a recent study, Kelly [10] proposed to replace steel reinforcement with fiber reinforcement to produce cost-effective light-weight isolators to be used in developing countries. Since with recent technology, the fiber materials with elastic stiffness comparable to that of steel can be produced, it is possible to produce a fiber-reinforced bearing which matches the behavior of the steel-reinforced bearing [11]. Even though the idea of using fiber reinforcement in seismic isolation bearings is very new, the viability of the concept has already been shown through several experimental studies [12-15].

Although the use of bonded elastic layers for reducing the devastating effects of severe earthquakes on structures is relatively new, its use in engineering applications is not new, as already mentioned. In fact, the studies on bonded rubber layers, or more generally on bonded elastic layers, go back as early as the beginning of the twentieth century. Even though the behavior of most elastomers can be highly nonlinear and they may undergo considerable finite deformations, in most of these analytical treatments, linear behavior is assumed and the derivations are performed for small strains because the use of finite strain analysis with nonlinear constitutive models usually leads to highly nonlinear and complex equations [7]. Further, with the purpose of obtaining simple design formulas, some simplifying assumptions are used in these studies, such as parabolic bulging assumption for the lateral boundary of the layer, the assumption that horizontal plane sections remain plane during deformation, rigidity assumption for the reinforcing sheets, “pressure” assumption for the state of stress, incompressibility assumption for the layer material, etc. [16].

It can also be recognized that most of the earlier studies on bonded elastic layers have focused on the derivation of closed form expressions only for the stiffnesses, particularly the compressive stiffness, of the layers. On the other hand, as emphasized by Gent et al. [17], the knowledge of the detailed displacement and stress distributions, and the location and magnitude of the critical local stresses developing in the layer is also essential for a rational design. For instance, an important parameter that can control the design of a bonded elastic layer is the bulging of the layers. Control of bulging is essential because increased bulging implies increased shear strain [18]. Similarly, the interfacial stresses, i.e., the stresses developing at the bonded faces, become one of the main parameters for the design of the reinforcements. Reinforcing sheets can fail due to excessive shear or normal stresses. Likewise, the knowledge of stress distribution at reinforcement-rubber bond is essential for the bond design. In some cases, even the failure of the elastomer itself may be taken as a design criterion, which can be evaluated only if the detailed stress distributions are known [17].

Thus, in order to study the behavior of a bonded elastic layer thoroughly, it is necessary to investigate not only the stiffness of the layer but also the displacement and stress distributions developing in the layer in detail. However, as already discussed, most of the earlier studies on bonded elastic layers have been based on assumed displacement fields with assumed stress distributions, which usually lead to approximate and/or “average” solutions, hindering a comprehensive study on displacement and stress distributions over the entire layer and on the effects of the geometrical and material properties on the layer behavior.

1.2 AIM OF THE DISSERTATION

The main object of this dissertation is

- (i) to develop a new formulation for linear analysis of bonded elastic layers by removing most of the in-priori assumptions used in the earlier formulations, and

- (ii) to study comprehensively, by using the advanced solutions obtained from this new formulation, the behavior of bonded elastic layers under their fundamental deformation modes.

The new analytical formulation presented in this dissertation is developed by employing an approximate theory proposed by Mengi [19], which is based on a modified version of the Galerkin Method. The use of the theory by Mengi [19] in the formulation brings in the following distinct advantages over the other formulations in literature:

- Since the displacement boundary conditions are included in the formulation itself, any possible inconsistency between the assumed displacement field and the boundary conditions at the bonded surfaces are eliminated. Thus, there is no need to start the formulation with some assumptions on stress and/or displacement distributions, or some limitations on the geometrical and material properties.
- Since the effect of compressibility is naturally included in the formulation, the solutions are valid not only for incompressible or nearly incompressible materials but also for highly compressible materials.
- Because of the appearance of face variables in the approximate theory, there is no need to make additional assumptions when the flexibility of the reinforcement is included in the formulation.
- The order of the theory is arbitrary; this facilitates improving the prediction of the theory and obtaining solutions much closer to the exact by increasing its order.

Consequently, within the framework of this new formulation, it is possible to derive the solutions in a form which can be used for the comprehensive study of stress and displacement distributions at any section in a bonded elastic layer.

While studying the behavior of bonded elastic layers in their basic deformation states, the main emphases are given to the investigation of the effects of three key parameters

- shape factor of the layer
- Poisson's ratio of the layer material
- flexibility of the reinforcing sheets

on

- effective moduli of the layer
- displacement and stress distributions over any section in the layer
- location and magnitude of maximum stresses developing in the layer.

The effects of the existence of a central hole on compressive behavior of bonded elastic discs are also examined in the dissertation.

1.3 SCOPE AND ORGANIZATION OF THE DISSERTATION

The dissertation starts with a review chapter where the theory and the earlier studies on bonded elastic layers are discussed (CHAPTER 2). Then, in CHAPTER 3, the new formulation proposed in this dissertation for the analysis of bonded elastic layers is presented. Since in the dissertation, the main emphasis is given to the elastic layers bonded to rigid reinforcements, first, the rigidly-bonded case is discussed in this chapter for three fundamental deformation modes: (i) uniform compression, (ii) pure bending and (iii) apparent shear. For each deformation mode, keeping the order of the theory arbitrary, the relevant equations are presented in general forms, in view of displacement boundary conditions at the top and bottom faces of the layer. To have a formulation applicable to all possible shapes (circular as well as infinite-strip, square and rectangular shapes), the reduced governing equations, originally derived in rectangular Cartesian coordinates, are also extended to cylindrical coordinates. The constants which appear in the approximate theory are determined and tabulated by choosing the distribution functions employed in the theory as Legendre polynomials. Regardless of the layer shape or order of the theory, determination of displacement/stress distributions and relevant effective modulus for each deformation mode is also formulated and presented. Then, in the same chapter (CHAPTER 3), the formulation is extended to the case where the elastic layer is bonded to extensible reinforcements. This case is discussed for three

simple deformation modes: (i) uniform compression, (ii) pure bending and (iii) pure warping. Similar to the rigid-reinforcement case, for each deformation mode, reduced governing equations are derived by keeping the shape of the layer and order of the theory arbitrary. However, in this case, the relevant equations are presented only in rectangular Cartesian coordinates.

CHAPTER 4 contains the application of the general formulation for various shapes of bonded elastic layers. In this chapter, closed form solutions for displacement/stress distributions and effective layer moduli are obtained, through the solution of governing equations presented in CHAPTER 3, for the cases involving an elastic layer of

- infinite-strip shape, bonded to rigid reinforcements
- solid and hollow circular shape, bonded to rigid reinforcements
- infinite-strip shape, bonded to extensible reinforcements.

CHAPTER 5 is devoted to the assessment of the new formulation proposed in the dissertation, which involves comparing the analytical solutions derived using first order theory for elastic layers of infinite-strip, circular and hollow-circular shapes, bonded to rigid reinforcements with the numerical solutions. For this purpose, some simple ‘numerical’ problems are designed and analyzed using a widely used numerical technique: boundary element method (BEM).

The solutions obtained in CHAPTER 4 are used

- in CHAPTER 6, to investigate the effects of shape factor and Poisson’s ratio on the behavior of infinite-strip elastic layers bonded to rigid surfaces
- in CHAPTER 7, to study the effect of the presence of a central hole on the compressive behavior of elastic discs bonded to rigid reinforcements
- in CHAPTER 8, to investigate the effect of reinforcement flexibility on the behavior of bonded infinite-strip elastic layers.

Finally, in view of the findings of the dissertation, some conclusions are stated in CHAPTER 9.

CHAPTER 2

THEORY ON BONDED ELASTIC LAYERS

2.1 ELASTIC LAYERS BONDED TO RIGID SURFACES

As stated by Gent and Meinecke [20], there are three basic deformation modes for an elastic layer bonded to rigid surfaces (Figure 2.1a): (i) uniform compression/extension (Figure 2.1b), (ii) pure bending (Figure 2.1c) and (iii) apparent shear (Figure 2.1d). Comprehensive analysis of a bonded elastic layer under each fundamental deformation mode is essential for understanding the effects of the bonded surfaces.

As already mentioned, in the last century, many researchers have studied the behavior of bonded elastic layers, specifically bonded rubber layers. Most of these studies have been conducted to determine the compression stiffness of the rigidly-bonded rubber layers. According to Kelly [7], “the first analysis of the compression stiffness was done using an energy approach by Rocard” in 1937 “and further developments were made” by Gent and Lindley [2] and Gent and Meinecke [20]”. These earliest studies put forward three basic assumptions for small deformation and linear analysis of bonded elastic layers:

- (i) horizontal plane sections remain plane after deformation,
- (ii) initially vertical lateral surfaces take a parabolic shape in the deformed configuration (parabolic bulging assumption),
- (iii) state of stress at any point in the material is dominated by the hydrostatic pressure (“pressure” assumption).

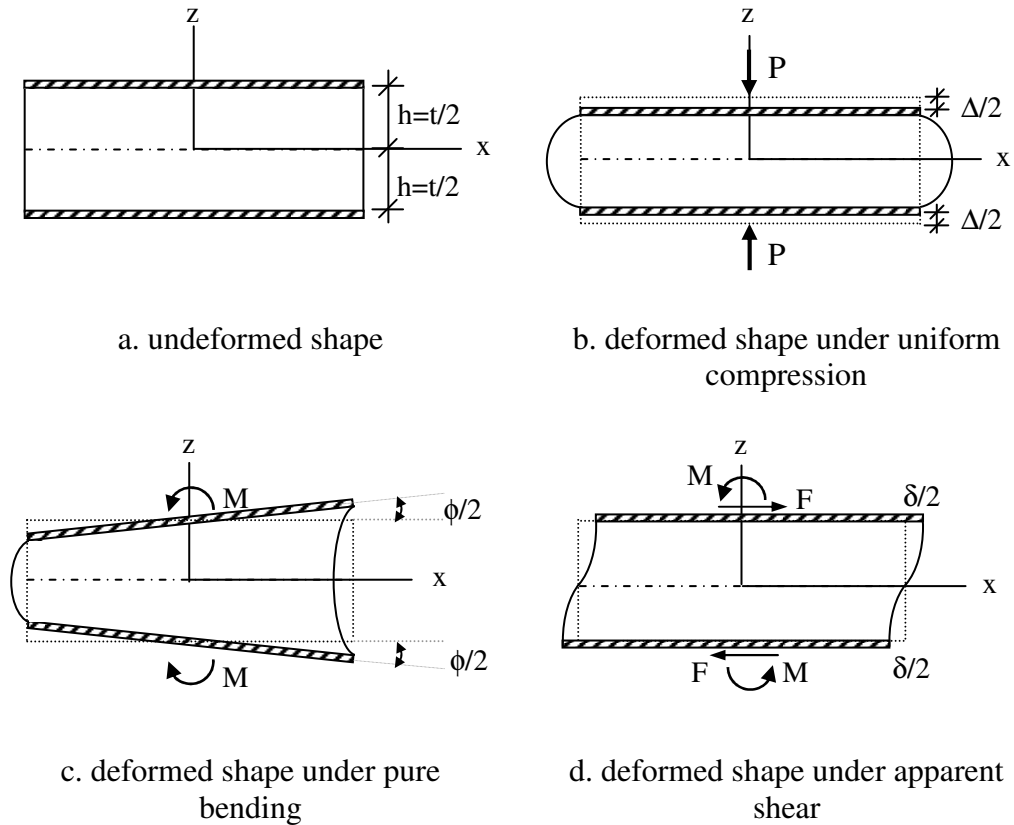


Figure 2.1 An elastic layer bonded to rigid surfaces under its three basic deformation modes

These three assumptions can be accepted as the fundamental assumptions of the linear theory developed for the analysis of bonded elastic layers since most of the earlier studies on this subject have been conducted based on these three assumptions. As it will be discussed later in detail, even if different formulations are used, these fundamental assumptions always lead to the same differential equation in terms of the “pressure” term, which is commonly called as the “pressure equation”. Most of the case, the solution of this differential equation was sufficient for the analysis since the effective stiffness of the layer can easily be derived once the pressure distribution is obtained. Thus, it seems to be reasonable to name all the formulations developed based on these three fundamental assumptions as the “pressure method”. Since most of the studies in literature have been based on this method of analysis, in the following sections, first, the pressure method is reviewed.

In this review, only the formulations of Gent and Lindley [2] and Kelly [7] are discussed with some detail. For the other formulations, the related references should be referred. After defining these two methodologies, the closed form expressions derived using different formulations are presented without giving details on their derivations. Other studies including those that used energy methods, variational methods and finite or boundary element methods are also mentioned shortly.

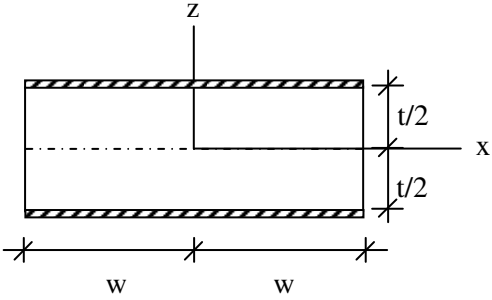
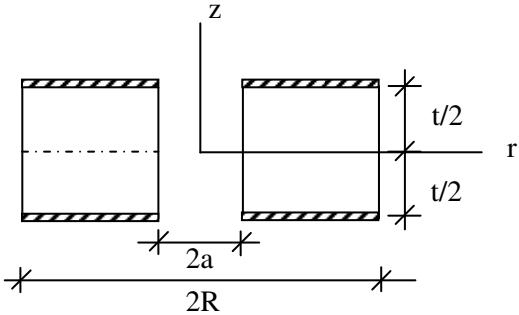
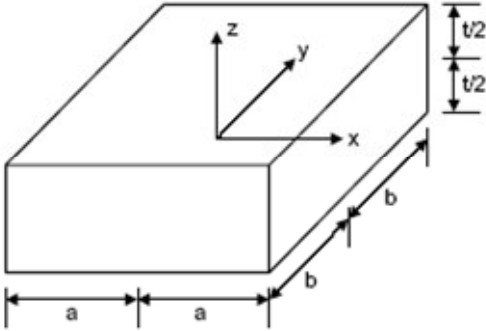
Considering that several different notations have been defined and used in the previous studies for the geometrical properties of the elastic layer and/or for the coordinate system to which the derived equations are referred, it seems to be reasonable and practical to define the notation that is used throughout this chapter at this point. Table 2.1 summarizes the geometrical properties of the commonly used cross sectional shapes for bonded elastic layers, namely, infinite strip (IS), hollow circular (HC) and rectangular (RC) shapes. It should be noted that circular (C) section is a special case of HC section in which $a=0$. Similarly, square (SQ) section is a special case of RC section in which $b=a$.

In linear elasticity, the state of an isotropic material in its undeformed configuration can be described by two basic elastic constants [21]: bulk modulus K , which is used to define the resistance of the material to hydrostatic pressure, and shear modulus μ , which is used to define the resistance of the material to simple shearing forces. The other elastic constants; namely, Young's modulus E , Poisson's ratio ν , and Lamé constant λ can easily be derived from these constants using the simple relations given below:

$$E = \frac{9K\mu}{3K + \mu}, \quad \nu = \frac{1}{2} \frac{3K - 2\mu}{3K + \mu} \quad \text{and} \quad \lambda = \frac{3K - 2\mu}{3} \quad (2.1)$$

The selection of the two basic elastic constants to be used in the equations is usually related to the formulation. The presentation of the fundamental equations or the resulting expressions may be much easier when the suitable "pair" of material constants is used. Since the conversions between these elastic constants can easily be made using Eqs. (2.1), in the following sections, the form of the equations is not changed and the researchers' preference for the two elastic constants is accepted.

Table 2.1 Definition of the notation for bonded layers of different shapes
 (Figure for the rectangular shape is taken from [22])

Shape	Geometrical Properties	Shape Factor
Infinite Strip (IS) width $2w$		$\frac{w}{t}$
Hollow Circular (HC) outer radius R , inner radius a		$\frac{R - a}{2t}$
Rectangular (RC) sides $2a, 2b$		$\frac{ab}{t(a + b)}$

2.1.1 Compressive Behavior

The vertical stiffness (K_v) of a bearing composed of several bonded rubber layers (without any horizontal displacement) is given by the following well-known expression [6]:

$$K_v = \frac{E_c A}{t_r} \quad (2.2)$$

where A is the cross sectional area of the reinforcing plates, t_r is the total rubber thickness and E_c is named as the “effective compression modulus” of the bearing. Effective (or sometimes called apparent) compression modulus of a multilayered steel laminated elastomeric bearing can be determined from the effective compression modulus of its typical interior rubber layer bonded to steel plates, which is simply the ratio of the nominal compressive stress (σ_c) to the nominal compressive strain (ε_c) as follows:

$$E_c = \frac{\sigma_c}{\varepsilon_c} \quad (2.3)$$

in which

$$\sigma_c = \frac{P}{A} \quad \text{and} \quad \varepsilon_c = \frac{\Delta}{t} \quad (2.4)$$

where P is the applied compressive load, Δ is the corresponding vertical displacement and t is the thickness of the typical interior rubber layer, as shown in Figure 2.1a,b.

As discussed in detail by Lindley [4], there are three limiting cases for the compression of an elastic layer.

- i. Compression without any restraint: if a layer is free from any lateral restraint ($S \rightarrow 0$), it will be in “homogeneous compression” state under a uniaxial load. Compression modulus in this case, denoted as $(E_c)_0$, can be written in terms of elastic modulus E and Poisson’s ratio ν as [23,24]:

$$(E_c)_0 = \begin{cases} E & \text{for symmetrical cross sections} \\ \frac{E}{1-\nu^2} & \text{for plane strain case} \end{cases} \quad (2.5)$$

- ii. Compression with complete lateral restraint: This case corresponds to the compression of an infinite strip layer whose bulging at the lateral faces is completely restrained ($S \rightarrow \infty$). Compression modulus in this case, denoted as $(E_c)_\infty$, can be expressed in terms of E and ν as:

$$(E_c)_\infty = \frac{(1-\nu)}{(1-\nu-2\nu^2)} E \quad (2.6)$$

- iii. Bulk compression: Under equal hydrostatic pressure in all three directions, the behavior of the layer is governed by the bulk modulus K , which is related to $(E_c)_\infty$ with

$$K = \frac{(1+\nu)}{3(1-\nu)} (E_c)_\infty \quad (2.7)$$

From Eq. (2.7), it is clear that $(E_c)_\infty \geq K$ for all materials (equality holds only for incompressible materials). Thus, it can be concluded that the compression modulus of a bonded elastic layer (E_c) is always greater than $(E_c)_0$, which requires perfect slip, but smaller than $(E_c)_\infty$, which requires infinite lateral restraint. While LSF layers are closer to the lower bound $(E_c)_0$, as shape factor increases, E_c approaches to the upper bound $(E_c)_\infty$. This range is very sensitive to the Poisson's ratio of the material and can increase considerably as $\nu \rightarrow 0.5$. Thus, as stated in [4], "for materials such as rubber which have a low shear modulus but a relatively high bulk modulus, any restrictions on their freedom to change shape can have a very marked effect on their stiffness in compression".

This effect of bonding the on compressive behavior of rubber layers was investigated by Gent and Lindley [2] through an experimental study in which the behavior of various bonded rubber blocks with different geometries was examined under uniform compression. The tested blocks had one of the following four shapes: C, HC with R/a ratios of 8, 4 or 2, SQ or RC with a/b ratio of 3. The discrete points, in the shapes of circles, squares and rectangles, plotted in the graphs presented in Figure 2.2a-b show the experimental data obtained by the researchers for the compression modulus of the tested blocks [2].

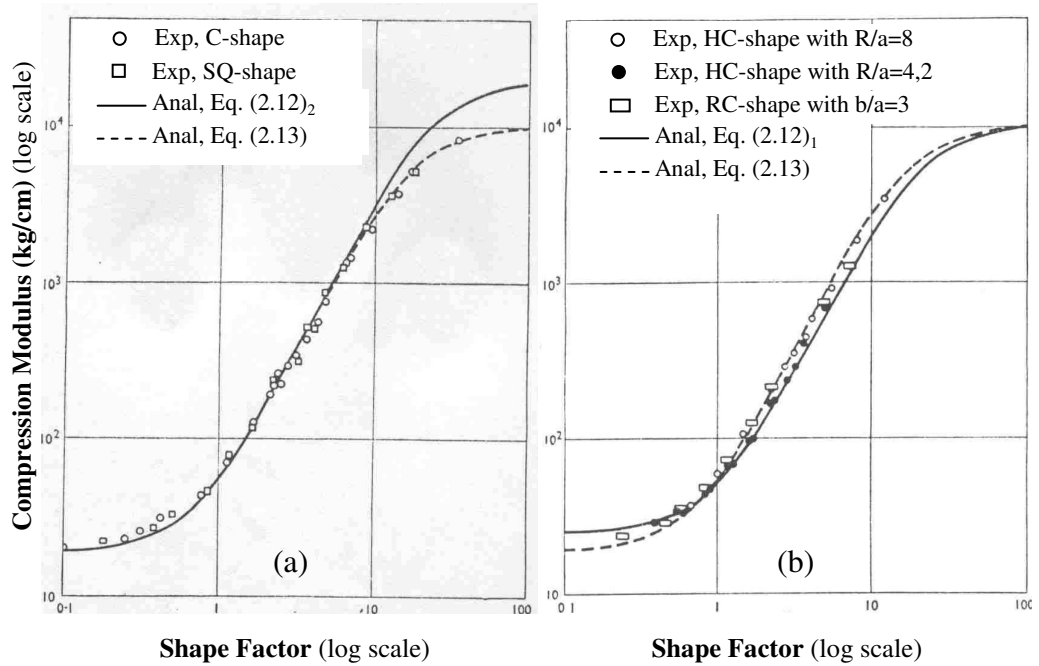


Figure 2.2 Compression modulus of bonded rubber blocks (taken from [2])

It should be noted the points plotted in the shapes of squares and circles in Figure 2.2a correspond to the experimental data, respectively, for SQ and C-shaped rubber blocks. Similarly, the points plotted in the shapes of rectangles and circles in Figure 2.2b correspond to the data obtained from the tests of RC and HC-shaped blocks. The test results for the HC-shaped blocks with different R/a ratios are differentiated by plotting the data for the blocks with a R/a ratio of 8 in the shape of “empty” circles and those with R/a ratios of 4 or 2 in the shape of “filled” circles. The graphs in Figure 2.2 clearly illustrate the strong effect of the shape factor of a bonded elastic layer on its compression modulus: the compression modulus of an HSF layer can be about 500 times greater than that of an LSF layer.

It is to be noted that the continuous and dashed curves tried to fit to the test data in Figure 2.2a,b were drawn, by the researchers, using the approximate relations they derived for the compression modulus of IS and C-shaped bonded elastic layers. In their theoretical study, Gent and Lindley [2] considered that, under

uniform compression, the total displacement of a bonded rubber layer is composed of the superposition of two simple displacements; (1) pure homogeneous compression of the corresponding unbonded layer and (2) the additional displacement required to keep the points on the bonded surfaces in their original positions. Under homogenous compression, the deformation of the layer is uniform. Thus, for incompressible case, the compressive stress developing in *IS* and *C*-shaped bonded layers under the 1st stage deformations, ($\sigma_{z1i,IS}$ and $\sigma_{z1i,C}$) are

$$\sigma_{z1i,IS}^{GL} = -\frac{4E}{3}\epsilon_c \quad \text{and} \quad \sigma_{z1i,C}^{GL} = -E\epsilon_c \quad (2.8)$$

Note that as in Eq. (2.8), a superscript consisting of the initial letters of the researchers' surnames (e.g., GL in this case) will be added to any formula/equation that will be given in this review for reader's convenience.

The formulation of the second stage deformations requires some simplifying assumptions on the displacement and stress distributions in the layer. Using the fundamental assumptions of the pressure method and assuming strict incompressibility ($\nu=0.5$), Gent and Lindley [2] derived the following well-known pressure equation,

$$\nabla^2 p = -\frac{12\mu}{t^2}\epsilon_c \quad (2.9)$$

where

$$\nabla^2 p(x, y) = \frac{\partial^2 p}{\partial x^2} + \frac{\partial^2 p}{\partial y^2} \quad \text{or} \quad \nabla^2 p(r) = \frac{d^2 p}{dr^2} + \frac{1}{r} \frac{dp}{dr} \quad (2.10)$$

in Cartesian coordinates or cylindrical coordinates, respectively. It is to be noted that their formulation was rather complicated. They derived the incompressibility equation from the geometry of an IS-shaped layer by equating the volumes contained between the central vertical plane and a plane at a distance x from the center in the deformed and undeformed states as shown in Figure 2.3. Similarly, they derived the equilibrium equation in the horizontal direction by computing the excess hydrostatic pressure (dp_x) that is required to maintain the parabolic bulging of an interior section of width dx (Figure 2.3).

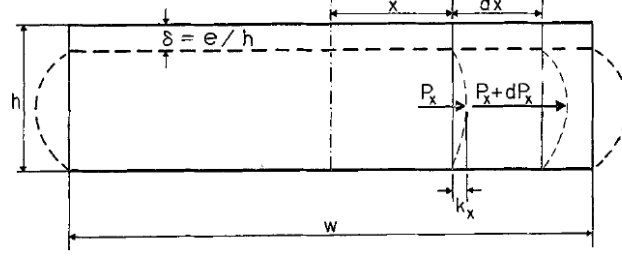


Figure 2.3 Deformed and undeformed configurations for an IS-shaped bonded elastic layer under uniform compression (taken from [20])

Using the “pressure free boundary conditions” at the lateral surfaces, Gent and Lindley [2] solved Eq. (2.9) and obtained the following expressions for the pressure distribution in *IS* and *C*-shaped bonded layers ($\sigma_{z2i,IS}$ and $\sigma_{z2i,C}$):

$$\sigma_{z2i,IS}^{GL} = -p_{ci,IS}^{GL} = -2E\epsilon_c S^2 \left(1 - \frac{x^2}{w^2}\right), \quad \sigma_{z2i,C}^{GL} = -p_{ci,C}^{GL} = -4E\epsilon_c S^2 \left(1 - \frac{r^2}{R^2}\right) \quad (2.11)$$

It should be noted that before deriving the expressions for the compression modulus, it is necessary to superpose the first and second stage solutions; i.e., add Eqs. (2.8) and Eqs. (2.11).

Thus, the Gent and Lindley’s formulation leads to the following well-known expressions for the compression modulus of *IS* and *C*-shaped incompressible bonded layers ($E_{ci,IS}$ and $E_{ci,C}$):

$$E_{ci,IS}^{GL} = \frac{4}{3}E(1+S^2) \quad \text{and} \quad E_{ci,C}^{GL} = E(1+2S^2) \quad (2.12)$$

It is worth mentioning that, realizing the significant effect of the material compressibility in HSF rubber layers, Gent and Lindley [2] also proposed an “ad-hoc” modification -independent of the shape of the layer- to account for the bulk compressibility of rubber on compression modulus.

$$\frac{1}{E_{cc}^{GL}} = \frac{1}{E_{ci}^{GL}} + \frac{1}{K} \quad (2.13)$$

where E_{cc} is the compression modulus including material compressibility and E_{ci} is the compression modulus obtained assuming strict incompressibility. To evaluate

the validity of their analytical formulation, the researchers compared the predictions of their analytical solutions with the experimental results (Figure 2.2). It is to be noted that the continuous curve in Figure 2.2a is plotted using the second of Eqs. (2.12). Similarly, the continuous curve in Figure 2.2b is plotted using the first of Eqs. (2.12). Since these “incompressible” curves deviate from the experimental data considerably especially when S is large, the researchers also plot the “compressible” curves, in dashed lines, using Eq. (2.13). By comparing their analytical predictions with the test data, Gent and Lindley [2] suggested that the E_c expression derived for C-shaped layers (the second of Eqs. (2.12)) can be used for layers with compact sections; i.e., nearly square or circular cross section with a small hole, while the use of the E_c expression derived for IS-shaped layers (the first of Eqs. (2.12)) is more convenient for layers with very dissimilar side lengths or large holes.

Recognizing the similarity of the pressure equation to the equation of torsion problem for torsional stress function, Gent and Meinecke [20] solved the pressure equation for different shapes by adopting the problem to its corresponding torsion problem. The following expression for “incompressible” compression modulus for RC-shaped layers ($E_{ci,RC}$) is worth mentioning in this review:

$$E_{ci,RC}^{GM} = E \left[\left(\frac{4}{3} - \frac{2}{3} \frac{ab+t^2}{a^2+b^2+2t^2} \right) + \frac{4}{3} \frac{a^2}{t^2} \left(1 - \frac{192}{\pi^5} \frac{a}{b} \sum_{n=1,3,5} \frac{1}{n^5} \tanh\left(\frac{n\pi b}{2a}\right) \right) \right] \quad (2.14)$$

which leads to the following simple expression for the special SQ case ($E_{ci,SQ}$):

$$E_{ci,SQ}^{GM} \cong E \left(1 + 0.562 \frac{a^2}{t^2} \right) \quad (2.15)$$

It is to be noted that the expression in the first parenthesis in Eq. (2.14), which represents the contribution of the first stage solution, is an empirical relation suggested in [20] in such a way that it satisfies the two basic requirements: it yields 1.0 for symmetrical shapes and 4/3 for plane strain case.

For the prediction of the pressure method for the compression modulus of incompressible HC-shaped layers, it is necessary to refer to the more recent studies. The expression derived by Gent [24] for the compression modulus of incompressible HC-shaped bonded layers ($E_{ci,HC}$) can be expressed as

$$E_{ci,HC}^G = E \left\{ 1 + \frac{1}{2t^2} \left[(R^2 + a^2) - \frac{(R^2 - a^2)}{\ln(R/a)} \right] \right\} \quad (2.16)$$

Although the incompressibility assumption is generally accepted as a realistic assumption for LSF rubber layers, the contribution of bulk compression of rubber to the total compression of the layer has to be considered for HSF rubber layers [25]. Lindley [26] may be accepted as the first researcher attempting to derive closed form expressions for the “compressible” compression modulus of bonded elastic layers. In his analytical treatment, which was based on an energy approach, in addition to the three fundamental assumptions of the pressure method, he assumed that the distribution of bulk strain over any horizontal section is parabolic. He obtained closed-form expressions for the compressible compression modulus of IS and C-shaped layers.

Compared to the above-mentioned formulations of the pressure method, Kelly’s formulation [7] can be said to be much simpler and more methodological. He started his formulation by simplifying the displacement field of the rubber layer based on the displacement assumptions of the pressure method. Thus, for a bonded elastic layer with an arbitrary shape, Kelly [7] wrote the displacements in the x , y and z directions, denoted as u , v and w respectively, in the form of:

$$\begin{aligned} u(x, y, z) &= u_o(x, y) \left(1 - \frac{4z^2}{t^2} \right) \\ v(x, y, z) &= v_o(x, y) \left(1 - \frac{4z^2}{t^2} \right) \\ w(x, y, z) &= w(z) \end{aligned} \quad (2.17)$$

where u_0 and v_0 are the maximum bulging of the layer in x and y directions, respectively. From Eq. (2.17), it is easy to see that the displacement function in z direction represents directly the first kinematics assumption, i.e., the assumption that the horizontal planes remain horizontal, while the first two functions written for the horizontal components are based on the second kinematics assumption, i.e., the parabolic bulging.

In the case of strict incompressibility, the incompressibility equation, i.e., $\varepsilon_{xx} + \varepsilon_{yy} + \varepsilon_{zz} = 0$ when written in terms of the normal strain components ($\varepsilon_{xx}, \varepsilon_{yy}, \varepsilon_{zz}$), can be written, in terms of the displacement functions, as:

$$(u_{0,x} + v_{0,y}) \left(1 - \frac{4z^2}{t^2} \right) + w_{,z} = 0 \quad (2.18)$$

where the commas imply partial differentiation with respect to the indicated coordinate. If the effect of compressibility is wanted to be included, the equation of incompressibility must be replaced with $\varepsilon_{xx} + \varepsilon_{yy} + \varepsilon_{zz} = -p/K$, where K is the bulk modulus of the material, which leads to

$$(u_{0,x} + v_{0,y}) \left(1 - \frac{4z^2}{t^2} \right) + w_{,z} = -\frac{p}{K} \quad (2.19)$$

Assuming infinitesimal strains and linearly elastic material behavior, integrating Eq. (2.18) or Eq. (2.19) through the layer thickness, writing equilibrium equations in x and y directions and using the stress assumption of the pressure method (i.e., that $\sigma_{xx} = \sigma_{yy} = \sigma_{zz} = -p$ where $\sigma_{xx}, \sigma_{yy}, \sigma_{zz}$ are normal stress components), the following equations are obtained for the pressure term $p(x,y)$

$$\nabla^2 p = -\frac{12\mu}{t^2} \varepsilon_c \quad (2.20)$$

for the incompressible case and

$$\nabla^2 p = -\frac{12\mu}{t^2} \varepsilon_c + \frac{12\mu}{Kt^2} p \quad (2.21)$$

for the compressible case. It is to be noted that in equilibrium equations, shear stress τ_{xy} was assumed to be negligible when compared to the normal stresses, i.e., to the pressure, and to the other shear stresses τ_{xz} and τ_{yz} .

Thus, Kelly's formulation leads to the same pressure equation resulted from Gent and Lindley's formulation (Eq. (2.9)) for the incompressible case. As already mentioned, this is due to the fact that both formulations were based on the same fundamental assumptions. When Eq. (2.21) is compared with Eq. (2.20), it can be seen that including the material compressibility in the formulation results in an

addition of one compressibility term to the original (incompressible) pressure equation. Indeed, as shown later by Gent [24], exactly the same equation can be obtained when Gent and Lindley's approach was directly applied to the compressible materials.

Since Kelly's formulation leads to the same expressions for the incompressible case, only the compressible solutions are mentioned here. By applying Kelly's formulation, Chalhoub and Kelly [27,28] derived the following closed form expressions for the pressure distribution and "compressible" compression modulus of *IS* and *C*-shaped layers under uniform compression:

$$p_{cc,IS}^{CK} = K\epsilon_c \left[1 - \frac{\cosh(\lambda x)}{\cosh(\lambda w)} \right] \quad \text{and} \quad p_{cc,C}^{CK} = K\epsilon_c \left[1 - \frac{I_0(\lambda r)}{I_0(\lambda R)} \right] \quad (2.22)$$

and

$$E_{cc,IS}^{CK} = K \left[1 - \frac{\tanh(\lambda w)}{\lambda w} \right] \quad \text{and} \quad E_{cc,C}^{CK} = K \left[1 - \frac{2I_1(\lambda R)}{(\lambda R)I_0(\lambda R)} \right] \quad (2.23)$$

where

$$\lambda^2 = \frac{12\mu}{Kt^2} \quad (2.24)$$

Realizing that the presence of even a very small hole in the center of a steel laminated elastomeric bearing can decrease the compression modulus of the bearing enormously, Constantinou et al. [16] analyzed this compression problem for bonded annular layers using the pressure method and obtained the following expression for the compressible compression modulus of *HC*-shaped bonded rubber layers:

$$E_{cc,HC}^{CKK} = K \left\{ \begin{aligned} &1 - \frac{2[K_0(\beta_i) - K_0(\beta_o)]}{d(S_o^2 - S_i^2)} [S_o I_1(\beta_o)] \left(\frac{K}{48\mu}\right)^{1/2} \\ &+ \frac{2[I_0(\beta_o) - I_0(\beta_i)]}{d(S_o^2 - S_i^2)} [S_o K_1(\beta_o) - S_i K_1(\beta_i)] \left(\frac{K}{48\mu}\right)^{1/2} \end{aligned} \right\} \quad (2.25)$$

where

$$S_o = \frac{R}{2t}, \quad S_i = \frac{a}{2t} \quad \beta_o = S_o \left(\frac{48\mu}{K}\right)^{1/2}, \quad \beta_i = S_i \left(\frac{48\mu}{K}\right)^{1/2} \quad (2.26)$$

$$d = I_0(\beta_o)K_0(\beta_i) - I_0(\beta_i)K_0(\beta_o),$$

In Eqs. (2.23) to (2.26), I_0 , I_1 and K_1 are modified Bessel functions of the first kind of zero order, first kind of first order and second kind of first order, respectively. Constantinou et al. [16] pointed out that the existence of a central hole does not only reduce the compression modulus of the bearing but also increase the shear strain developing in the elastomer due to compression substantially. Emphasizing the fact that maximum shear strain is considered as “the most consistent measure of potential fatigue failure and potential delamination of the bearing”, they proposed some simple design formulae for the calculation of the maximum shear strain due to the compression. They also simplified the E_c expression predicted by the pressure method and proposed to calculate the E_c of an HC-shaped bonded elastic layer from the expression derived for a C-shaped layer by using the shape factor of the annular layer.

The predictions of the pressure method for the compression modulus of the layers with the remaining two shapes, SQ and RC shapes, can be found in Refs. [3,29]. Koh and Kelly [3] presented the following expression for the compressible compression modulus of SQ-shaped bonded rubber layers in their appendix:

$$E_{cc,SQ}^{KK} = \frac{48E}{1+\nu} S^2 \sum_{n=1}^{\infty} \frac{1}{\alpha_n^2 \beta_n^2} \left(1 - \frac{\tanh(\beta_n)}{\beta_n} \right) \quad (2.27)$$

where

$$\beta_n^2 = \left[\alpha_n^2 + 72 \frac{1-2\nu}{1+\nu} S^2 \right] \quad \text{and} \quad \alpha_n = \left(n - \frac{1}{2} \right) \pi \quad (2.28)$$

For the compressible compression modulus of RC-shaped bonded elastic layers, Yeoh et al. [29] derived the following expression:

$$E_{cc,RC}^{YPB} = \left\{ \frac{96\mu}{abt^2} \sum_{n=1,3,5}^{\infty} \left[\frac{ab}{n^2 \pi^2 \lambda_n^2} - \frac{b}{n^2 \pi^2 \lambda_n^3} \tanh(\lambda_n a) \right] \right\} \quad (2.29)$$

where

$$\lambda_n^2 = \left(\frac{n^2 \pi^2}{4b^2} + \frac{12\mu}{Kt^2} \right) \quad (2.30)$$

It can easily be recognized that Eqs. (2.23), (2.25), (2.27) and (2.29) include only the second stage solutions. It is known that as the shape factor of a layer

increases, the constant term in E_c coming from the first stage solution becomes negligibly small compared to the shape-factor-dependent terms coming from the second stage. Thus, it is a common practice to ignore the first stage solutions in the design of bonded elastic layers with high shape factors. However, it should not be forgotten that it may be essential to include the first stage solutions corresponding to homogenous compression of the layer especially if the shape factor of the layer is low and/or the compressibility of the material is high.

As already stated, the pressure method assumes “fluid-like stress state”. Without using this assumption, Koh and Kelly [3] derived expressions for the compression modulus of SQ-shaped layers using two direct solutions. In their first solution, they retained the displacement assumptions of the pressure method and derived solutions in single series form using variable transform method. In their second solution, they further eliminated the assumption on the bulging shape; instead of assuming a parabolic bulge shape, they described the bulging shape in terms of Fourier series. They concluded that the basic assumptions used in the pressure method are valid for rubber bearings commonly used in seismic isolation.

In a similar way, using the same displacement field proposed by Kelly [7] but removing the pressure assumption, Tsai and Lee [30] derived closed form expressions for the compressible compression modulus of IS, C and SQ-shaped bonded elastic layers. The expressions they obtained for IS and C-shaped layers are

$$E_{cc,IS}^{TL} = 2\mu + \lambda \left[1 - \left(\frac{\lambda}{\lambda + 2\mu} \right) \frac{\tanh(\alpha w)}{\alpha w} \right] \quad (2.31)$$

$$E_{cc,C}^{TL} = 2\mu + \lambda \left[1 - \left(\frac{\lambda}{\lambda + 2\mu} \right) \frac{1}{\frac{(\alpha R)I_0(\alpha R)}{2I_1(\alpha R)} - \mu} \right] \quad (2.32)$$

where

$$\alpha^2 = \frac{12\mu}{(\lambda + 2\mu)t^2} \quad (2.33)$$

In their formulation, Tsai and Lee [30] used a direct solution formulated in terms of the “mean pressure”. Comparing their solutions with the pressure solution, they

concluded that the pressure assumption is valid only for HSF layers and nearly or strictly incompressible materials.

The study of Koh and Lim [25] may be accepted as the first study attempting to derive an analytical solution for the compressible compression modulus of bonded RC-shaped layers without using the pressure assumption. Their method of treatment is very similar to the first direct solution in [3]. Later, Tsai [22] extended the method of treatment proposed by Tsai and Lee [30] to RC-shaped layers and derived a closed form solution for their compression modulus in single series form, which they showed to converge faster than the double series given in [25].

The studies of Horton et al. [31,32] differ from the many others in that they eliminated the parabolic bulging assumption while keeping the assumption that plane sections remain plane. In their formulation, they first assumed strict incompressibility and, then, used the ad-hoc modification proposed by Gent and Lindley [2] to account for the bulk compression of rubber. With a similar analytical approach they had used for the derivation of radial and tilting stiffness of cylindrical rubber bush mountings, they derived closed form expressions for the compression modulus of IS, C and HC-shaped bonded rubber blocks. The authors concluded that the shape of the bulging could not be approximated by a parabolic shape for extremely low shape factors (e.g., $S=0.2$). Their results were in good agreement with the experimental results obtained by Mott and Rolland [33], who investigated the compressive behavior of very slender rubber cylinders (with $0.1 < S < 0.3$).

The study of Moghe and Neff [34] is also worth mentioning in that they obtained exact solutions to the compression problem of bonded elastic cylinders by using the small deformation and linear elasticity theory. Involving infinite series of Bessel and trigonometric functions, their solutions are, however, too complex and is not convenient for design calculations.

In literature, there are also studies investigating the compressive behavior of bonded elastic layers using variational or energy approaches. As an example, Papoulia and Kelly [35] formulated the compression problem of bonded elastic layers using the principle of minimum potential energy. They first derived the Euler-Lagrange equations for a bonded elastic layer of arbitrary shape and, then,

solved the equations for the IS-shape. They realized that to have a consistent result, they had to release the assumption that horizontal plane sections remain plane. In another study, Ling [36] investigated the compressive behavior of HC-shaped layers. His analysis was based on the so called Perturbation-Ritz method and stated to be valid only for HSF layers and slightly compressible materials.

The studies conducted to investigate the compressive behavior of bonded elastic layers are surely not limited to the analytical studies. Several researchers [9,37,38] studied the behavior of bonded elastic layers using numerical methods, such as, dynamic relaxation, boundary element or finite element methods. Main advantage of using these methods is that they do not usually include assumptions on neither displacement nor stress distributions. However, it is generally difficult and unpractical to study the behavior of bonded layers for various geometrical and material properties by using numerical methods. Moreover, these solutions are also approximate and mostly very sensitive to modeling.

Several experimental studies were also conducted to examine the compressive behavior of rubber layers bonded to rigid plates. Since in a compression test, the most easily obtained characteristic of the layer is its compression modulus, most of these studies (see, e.g., Ref. [2]) concentrated on the determination of the compression modulus of the test specimens. The study of Hall [1] can be accepted as the first study attempting to measure the stress distributions in a bonded rubber layer subjected to uniform compression. He found that the shape of the pressure distribution over the bonded surfaces of a cylindrical bonded rubber layer is approximately parabolic under very small compressions, as predicted by the pressure method. While Hall [1] investigated only the C-shaped layers and their normal stress distribution under compression, Gent et al. [17] studied both the shear and normal stress distributions over the bonded faces of different sized C and SQ-shaped bonded rubber blocks under both compression and shear loads. They also tried to measure the stress singularities at the edges, which, they concluded, “must be confined to extremely small regions in the neighborhood of the edges”.

2.1.2 Bending Behavior

Another important mechanical property of an elastomeric bearing is its bending (also called tilting) stiffness. Bending stiffness of an elastomeric bearing can be denoted as $(EI)_{eff}$, with an analogy to the elastic beam theory, or simply K_b . Bending stiffness is usually one of the key parameters in the design of a rubber bearing since it is the fundamental parameter determining its buckling behavior [7]. Similar to the compression modulus, the bending modulus of an elastomeric bearing, E_b , can be determined from the bending modulus of a typical interior bonded rubber layer.

For a bonded elastic layer which is purely bended by bending moments so that the bonded faces rotate with respect to each other about y axis with a relative angle of rotation ϕ (Figure 2.1c), the effective bending modulus can be determined from the ratio of bending stiffness to the moment of inertia I of the layer about the axis of rotation. Similar to an elastic beam, if the bending stiffness of the layer is defined as the ratio of the applied moment M to the resultant curvature κ ; the effective bending modulus E_b can be obtained from

$$E_b = \frac{K_b}{I} \quad \text{and} \quad K_b = \frac{M}{\kappa} \quad \text{with} \quad \kappa = \frac{\phi}{t} \quad (2.34)$$

As in the compression case, the bending behavior of an elastic layer can change considerably if its lateral movement is restricted at its top and bottom faces. For this reason, most of the earlier studies on bonded elastic layers have also included analytical formulations to derive their bending modulus. In these studies, the bending problem for a bonded elastic layer is generally handled using the same analytical approach with the same assumptions imposed in the corresponding compression problem.

Using the method of treatment proposed by Gent and Lindley [2], Gent and Meinecke [20] derived and tabulated the bending stiffness factors to be used in the calculation of the bending modulus of bonded elastic layers for various shapes. Thus, the predictions of the pressure method for the “incompressible” bending stiffness of *IS* and *C*-shaped bonded layers ($E_{bi,IS}$ and $E_{bi,C}$) can be expressed as

$$E_{bi,IS}^{GM} = \frac{4}{3}E \left(1 + \frac{1}{5}S^2\right) \quad \text{and} \quad E_{bi,C}^{GM} = E \left(1 + \frac{2}{3}S^2\right) \quad (2.35)$$

It is to be noted that, for incompressible case and under pure bending, the pressure equation becomes,

$$\nabla^2 p = -\frac{12\mu}{t^2} \kappa x \quad (2.36)$$

whose solution leads to the following expressions for the pressure distribution in IS and C-shaped bonded elastic layers of incompressible materials under pure bending:

$$p_{bi,IS} = \frac{2}{3}E\kappa S^2 \left(1 - \frac{x^2}{w^2}\right)x \quad \text{and} \quad p_{bi,C} = 2E\kappa S^2 \left(1 - \frac{r^2}{R^2}\right)r \cos \theta \quad (2.37)$$

For RC-shaped bonded elastic layers bended about an axis parallel to the $2b$ side, the solution of the pressure equation leads to the following expression for E_b :

$$E_{bi,RC}^{GM} = E \left[\left(\frac{4}{3} - \frac{2}{3} \frac{\frac{ab}{2} + t^2}{\frac{a^2}{4} + b^2 + 2t^2} \right) + \frac{24}{\pi^4} \frac{a^2}{t^2} \left\{ \sum_{n=1}^{\infty} \frac{1}{n^4} \left[1 - \left(\frac{n\pi b}{a} \right)^{-1} \tanh \left(\frac{n\pi b}{a} \right) \right] \right\} \right] \quad (2.38)$$

which simplifies, for the special square case, to

$$E_{bi,SQ}^{GM} \cong E \left[1 + 0.1856 \frac{a^2}{t^2} \right] \quad (2.39)$$

Gent and Meinecke [20] also investigated the “internal rupture” phenomenon observed in a bonded elastic layer subjected to tension/bending when the critical local hydrostatic pressure is reached. They defined the internal rupture of the layer as the failure of the layer where “any small cavity will increase indefinitely in size”. This occurs when the magnitude of hydrostatic tension exceeds a critical value, typically, the value $3/4E$ where E is the Young’s modulus of the rubber. Using the pressure method, Gent and Meinecke [20] obtained the following values for the location (x_1^*) and magnitude (ϕ^*) of the critical rotation at which an IS-shaped bonded rubber layer fails due to internal rupture under pure bending:

$$x_1^* = \frac{w}{\sqrt{3}} \quad \text{and} \quad \phi^* = \frac{27\sqrt{3}}{16S^3} \quad (2.40)$$

As in the compression case, the formulation of Gent and Meinecke [20] was based on the assumption of incompressibility. However, just like the compressive behavior, the material compressibility is a crucial parameter affecting the bending behavior of HSF layers and therefore has to be included in the formulations. Including the material compressibility and using the same approach he used for the compression case, Lindley [39] derived a closed form expression for the compressible bending modulus of IS-shaped bonded layers.

Similarly, Kelly [7] formulated this bending problem by applying the same methodology he used for the compression problem. By modifying the displacement field as

$$\begin{aligned} u(x, y, z) &= u_o(x, y)\left(1 - \frac{4z^2}{t^2}\right) - \frac{\kappa}{2}z^2 \\ v(x, y, z) &= v_o(x, y)\left(1 - \frac{4z^2}{t^2}\right) \\ w(x, y, z) &= -\kappa xz \end{aligned} \quad (2.41)$$

he derived the pressure equation for the compressible, bending case as:

$$\nabla^2 p = -\frac{12\mu}{t^2}\kappa x + \frac{12\mu}{t^2}\frac{p}{K} \quad (2.42)$$

Solving this pressure equation for two different shapes, Chalhoub and Kelly [27, 28] derived the following expressions for the “compressible” bending modulus of IS and C-shaped bonded elastic layers:

$$E_{bc,IS}^{CK} = K \left[1 - \frac{3}{(\lambda w)^2} \left[\frac{\lambda w}{\tanh(\lambda w)} - 1 \right] \right] \quad (2.43)$$

$$E_{bc,C}^{CK} = K \left[1 - \frac{4I_2(\lambda R)}{(\lambda R)I_1(\lambda R)} \right] \quad (2.44)$$

where λ is defined as in Eq. (2.24).

Eliminating the stress assumption of the pressure method, Tsai and Lee [40] obtained the following closed form expressions for the compressible bending modulus of *IS* and *C*-shaped bonded layers:

$$E_{bc,IS}^{TL} = 2\mu + \lambda \left[1 - \frac{\lambda}{\lambda + 2\mu} \frac{3}{(\alpha w)^2} \left(\frac{\alpha w}{\tanh(\alpha w)} - 1 \right) \right] \quad (2.45)$$

$$E_{bc,C}^{TL} = 2\mu + \lambda \left[1 - \left(\frac{2\lambda}{\mu} \right) \frac{\alpha R I_0(\alpha R) - 2I_1(\alpha R)}{2(1+12S^2)I_1(\alpha R) - \alpha R I_0(\alpha R)} \right] \quad (2.46)$$

where α is defined in Eq. (2.33). They also obtained a solution for the bending modulus of *SQ*-shaped layers in series form whose coefficients are required to be solved numerically. Recently, Tsai [41] formulated a new procedure to treat the bending problem of bonded circular layers by directly establishing the relations in terms of the “average” horizontal displacements. He pointed out that the expression derived by Tsai and Lee [40] for the bending modulus yields results very close to the results of this approach although in this earlier formulation one additional constraint had to be made.

Recently, Horton et al. [42] studied the linear and incompressible behavior of *C*-shaped rubber blocks under combined shear and bending. After obtaining general expressions, they examined three special loading cases: (a) pure bending, (b) cantilever loading and (c) apparent shear. For pure bending case, they derived closed form expressions for the bending modulus and stress distributions. It is to be noted that although they eliminated the bulging assumption in their formulation, they kept the incompressibility assumption and the assumption that plane sections remain plane.

2.1.3 Apparent Shear Behavior

In their common use, bonded rubber layers may also undergo shearing deformations in such a manner that one of the bonded surfaces of the layer displaces in its own plane with respect to the other bonded face, which frequently remains fixed in its place (Figure 2.1d). As stated in [43], this deformation state is *not*

“simple shear” since a state of simple shear requires suitable additional forces at the lateral surface of the layer. Absence of these additional forces leads to the addition of the bending deformations to the simple shear deformations in the resulting deformation state. In literature, this state of deformation is commonly named as “apparent shear”.

It is widely accepted that the effect of bonded surfaces to the shear behavior of the layer is negligible. This is a very realistic assumption for HSF layers. However, as also stated in [20], bending displacements may become an important component of the total displacement when the layer thickness is relatively large.

Although many analytical studies have been conducted on the compressive and bending behavior of bonded elastic layers, there is rather limited work in literature on their apparent shear behavior. Rivlin and Saunders [43] studied experimentally the apparent shear behavior of cylindrical mountings with different geometries. They also suggested an approximate expression for the apparent shear modulus of bonded elastic layers using an approximate theory developed with the aid of the similarity of the problem to the problem of a cantilever beam loaded at its free end. Ignoring the end effects, they formulated the resulting tip deflection from the superposition of the displacements due to simple shear and bending. They, then, defined the apparent shear modulus by regarding that the combined deflection is resulted from only simple shear. Thus, they obtained the following relationship for the “incompressible” apparent (μ_{ai}) shear modulus in terms of the true shear modulus (μ) for incompressible materials.

$$\mu_{ai}^{RS} = \mu \left(\frac{1}{1 + \frac{\mu A t^2}{12EI}} \right) \quad (2.47)$$

Despite the slight overestimation of the analytical results to the experimental results, the authors declared a good agreement on the whole considering the approximate nature of the analytical treatment they used.

Later, Gent and Meinecke [20] recognized that Rivlin and Saunders [43] ignored the effect of bonded surfaces to the bending modulus and they proposed to

use the “modified” bending modulus in Rivlin’s formula. Then, the revised formula for the incompressible apparent shear modulus can be expressed as

$$\mu_{ai}^{GM} = \mu \left(\frac{1}{1 + \frac{\mu A t^2}{12 E_b I}} \right) \quad (2.48)$$

The expression obtained by Horton et al. [42] for the incompressible apparent shear modulus seems to have the same form with the expression proposed in [20]. The basic difference in these expressions arises from the fact that while the E_b expression used by Gent and Meinecke [20] was derived based on the parabolic bulging assumption, the expression used by Horton et al. [42] does not include it.

2.2 ELASTIC LAYERS BONDED TO FLEXIBLE REINFORCEMENTS

Kelly [44] can be accepted as the first researcher who studied the effect of the reinforcement flexibility on the behavior of rubber bearings. He developed an approximate theory for the buckling analysis of rubber bearings that includes the effect of the reinforcement flexibility. Different from the existing theories, he considered both the shear and warping of the cross section in his formulation. Since he assumed “inextensible” reinforcements, he did not study the effect of the reinforcement extensibility on the effective stiffnesses of the bearing.

Recently, Tsai and Kelly [45,46] extended Kelly’s theory [44] in a way that the effect of the reinforcement extensibility on the effective stiffnesses of the bearing was also included in the analysis. In their formulation, they derived closed form expressions for the effective compression, bending and warping stiffnesses of an IS-shaped fiber-reinforced elastomeric bearing. For this purpose, they analyzed linear behavior of a single rubber layer bonded to extensible reinforcements, with no flexural rigidity, under the combined effects of the compressive load P , bending moment M and warping moment Q (Figure 2.4). It is to be noted that in this study, Tsai and Kelly [46] assumed strictly incompressible ($\nu=0.5$) behavior for the rubber layer.

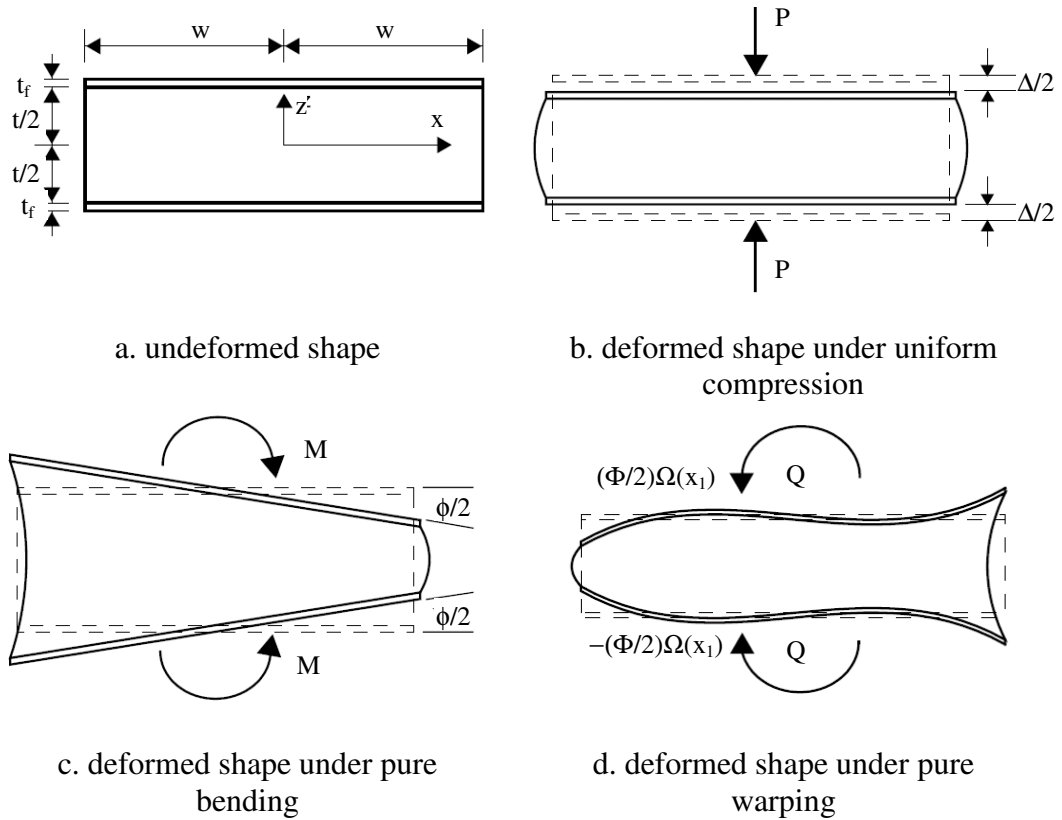


Figure 2.4 Deformation of an elastic layer bonded to flexible reinforcements under the effects of the compression force P , bending moment M and warping moment Q (taken from [46])

At this point, it is also important to note that as emphasized in [45], “the terminology of warping used here is *not* associated with torsion; it just specifies the distortion of the cross-section created by moment and shear”.

While the study of Tsai and Kelly [46] can be accepted as the first study where the derivation for the warping stiffness of a rubber layer bonded to flexible reinforcements appears, it is indeed Kelly [10] who first analyzed the compressive and bending behavior of a rubber layer bonded to flexible reinforcements. In [10], Kelly clearly explained how the effect of the reinforcement flexibility can be incorporated into the formulation he developed for the analysis of rigidly-bonded elastic layers and derived closed-form expressions for the incompressible compression and bending modulus of a fiber-reinforced IS-shaped rubber layer.

Kelly's approach was later applied to RC and C-shaped rubber layers by Tsai and Kelly [47]. However, their solutions were still based on the incompressibility assumption. Incorporation of the material compressibility to the formulation was again shown by Kelly [13], who derived the "compressible" compression modulus for IS-shaped rubber layers bonded to flexible reinforcements.

In the following sections, first, the Kelly's approach [10] to incorporate the reinforcement flexibility into the pressure method is discussed. Then, the closed form expressions derived for the compression and bending modulus of the layers using this formulation are presented. Different from Kelly's approach, the study of Tsai [48] is also discussed shortly. Finally, the studies conducted to determine the warping behavior of bonded elastic layers are reviewed shortly.

2.2.1 Compressive Behavior

In [10], Kelly explains how the reinforcement flexibility can be incorporated to the pressure method. Since the analysis for elastic layers bonded to flexible reinforcements is somewhat more complicated than that for layers bonded to rigid reinforcements, he developed his formulation for IS-shaped layers. Similar to the rigidly-bonded case, Kelly [10] started his formulation by simplifying the displacement field for the rubber layer using the basic displacement assumptions of the pressure method. Since he assumed that the reinforcements to which the elastic layer is bonded are flexible in extension with no flexural rigidity, he incorporated the effect of the reinforcement flexibility to the formulation by considering an additional displacement term in the horizontal direction (u_1). Assumed to be constant through the layer thickness, this term is "intended to accommodate the stretching of reinforcement" [10]. Thus, the simplified form of the displacement field for an IS-shaped elastic layer bonded to flexible reinforcements under uniform compression (Figure 2.4b) can be written as:

$$u(x, z) = u_o(x) \left(1 - \frac{4z^2}{t^2} \right) + u_1(x), \quad w(x, z) = w(z) \quad (2.49)$$

where u_1 is the extension of the reinforcement in the x direction.

Incompressibility condition, when written in terms of the displacement components and after integrated through the layer thickness, becomes

$$u_{0,x} + \frac{3}{2}u_{1,x} = \frac{3}{2} \frac{\Delta}{t} \quad (2.50)$$

The pressure assumption, when used in the equation of stress equilibrium for the rubber layer in the horizontal direction, leads to the following equation in terms of the pressure term and the displacement of the elastomer:

$$p_{,x} = -\frac{8\mu}{t^2}u_0 \quad (2.51)$$

Another equation comes from the equilibrium equation written for the flexible reinforcements (Figure 2.5). Considering that the equivalent thickness of the reinforcing sheet, denoted as t_f , is much smaller than the thickness of the layer t , the sheet can be idealized to be in the plane state of stress. Thus, the normal force per unit length in the reinforcement in the x direction N_{xx} , can be expressed in terms of the shear stresses at the top and bottom rubber layers denoted, respectively $\tau_{xz}(z=-t/2)$ and $\tau_{xz}(z=t/2)$, as (Figure 2.5)

$$N_{xx,x} = \tau_{xz}|_{z=t/2} - \tau_{xz}|_{z=-t/2} \quad (2.52)$$

which can be written in terms of the rubber displacement as

$$N_{xx,x}(x) = -\frac{8\mu}{t}u_0 \quad (2.53)$$

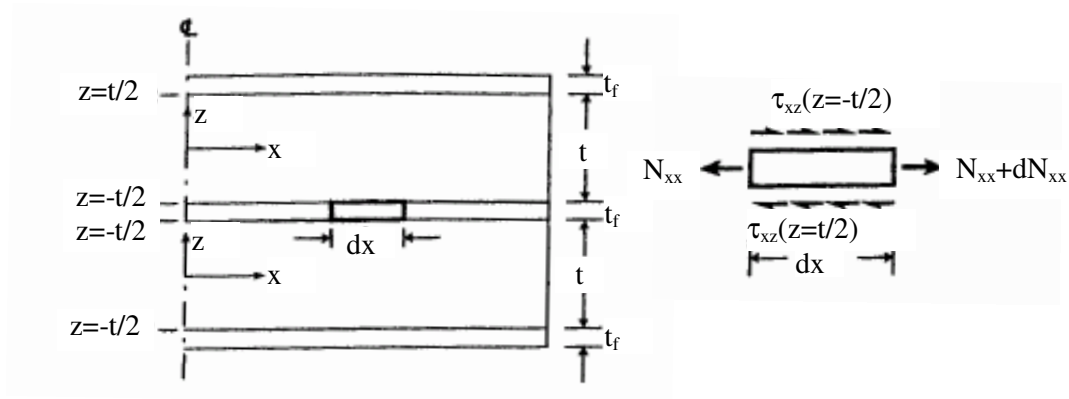


Figure 2.5 Forces on a reinforcing sheet bonded to IS-shaped rubber layers at its top and bottom faces (taken from [47])

The stretching force N_{xx} in the reinforcement can be related to the extensional strain $u_{1,x}$, in view of the linearly elastic stress strain relation, as follows:

$$u_{1,x} = \frac{(N_{xx} - \nu_f N_{yy})}{E_f t_f} \quad (2.54)$$

where E_f and ν_f are, respectively, elastic modulus and Poisson's ratio of the reinforcement and N_{yy} is the internal normal force per unit length in the reinforcement in y direction. Since for the plane strain case, $N_{yy} = \nu_f N_{xx}$, Eq. (2.54) reduces to

$$u_{1,x} = \frac{N_{xx}}{k_f} \quad (2.55)$$

where "in plane stiffness of the reinforcement", denoted as k_f , is

$$k_f = \frac{E_f t_f}{1 - \nu_f^2} \quad (2.56)$$

Eq. (2.55), when inserted into Eq. (2.53), results in

$$u_{1,xx} = -\frac{8\mu}{k_f t} u_0 \quad (2.57)$$

Thus, the complete set of equations for the three unknown functions of the problem, u_0 , u_1 and p , is

$$u_{0,x} + \frac{3}{2} u_{1,x} = \frac{3\Delta}{2t}, \quad p_{,x} = -\frac{8\mu}{t^2} u_0 \quad \text{and} \quad u_{1,xx} = -\frac{8\mu}{k_f t} u_0 \quad (2.58)$$

The necessary boundary or symmetry conditions for the solution of the above set of equations are

$$u_0(0) = 0, \quad u_1(0) = 0, \quad p(\pm w) = 0 \quad \text{and} \quad N_{xx}(\pm w) = k_f u_{1,x}(\pm w) = 0 \quad (2.59)$$

While Kelly [10] solved these equations by solving the displacement components first, it is possible to obtain the pressure distribution directly from the pressure equation. It is not difficult to show that for an IS-shaped rubber layer bonded to flexible reinforcement, the pressure equation becomes

$$\nabla^2 p = -\frac{12\mu}{t^2} \varepsilon_c + \frac{12\mu}{k_f t} p \quad (2.60)$$

The solution of the pressure equation, in view of the condition $p(\pm w) = 0$, yields

$$p_{cif,IS} = \frac{k_f}{t} \left[1 - \frac{\cosh(\alpha x)}{\cosh(\alpha w)} \right] \varepsilon_c \quad (2.61)$$

where

$$\alpha^2 = \frac{12\mu}{k_f t} \quad (2.62)$$

from which the *incompressible* compression modulus for *IS*-shaped layers bonded to *flexible* reinforcements $E_{cif,IS}$ is determined as

$$E_{cif,IS}^K = \frac{k_f}{t} \left[1 - \frac{\tanh(\alpha w)}{\alpha w} \right] \quad (2.63)$$

At this point, it is worth studying Eq. (2.60) thoroughly. Comparison of Eq. (2.60) with Eqs. (2.20) shows that inclusion of the reinforcement flexibility adds an additional pressure term to the pressure equation. What may be more interesting to realize is that the reinforcement flexibility influences the layer behavior in the same way the material compressibility affects. This can be seen from the comparison of Eq. (2.60) with Eqs. (2.21). Thus, the stiffness expressions derived for the compressible layers bonded to rigid reinforcements can easily be adapted to the incompressible layers bonded to flexible reinforcements. This can be done, for example, by replacing K with k_f/t . As an example, it can be shown that if this replacement is done in the first of Eq. (2.23), exactly the same equation as Eq. (2.63) is obtained. However, it should be noted that this conclusion is valid only for the *IS*-shaped layers. For the other shapes, it may not always be possible to write the pressure equation in its regular form due to the complex form of the differential equations. In such cases, the pressure distribution cannot be obtained without solving the unknown displacement functions.

Kelly's approach was later applied to *C* and *RC*-shaped layers by Tsai and Kelly [47], who derived the following expression for the *incompressible* compression modulus of circular discs bonded to *flexible* reinforcements ($E_{cif,C}$):

$$E_{cif,C}^{TK} = \frac{k_f}{t} \frac{(1 + \nu_f)}{2} \left[\frac{(\alpha R)I_0(\alpha R) - 2I_1(\alpha R)}{(\alpha R)I_0(\alpha R) - (1 - \nu_f)I_1(\alpha R)} \right] \quad (2.64)$$

Due to its lengthy form, the expression derived for the rectangular case is not presented here (one may refer to Ref. [47]). However, considering that the rectangular case is the more general 3D case, some discussion is made on the derivation of the reinforcement equilibrium equations in terms of the reinforcement displacements when the layer has a finite length. From Eq. (2.49), it can be inferred that the most general forms of the displacement functions are

$$\begin{aligned}
 u(x, z) &= u_o(x) \left(1 - \frac{4z^2}{t^2} \right) + u_1(x) \\
 v(x, z) &= v_o(x) \left(1 - \frac{4z^2}{t^2} \right) + v_1(x) \\
 w(x, z) &= w(z)
 \end{aligned}
 \tag{2.65}$$

where v_1 is the extension of the reinforcement in the y direction.

Figure 2.6 illustrates the internal forces acting on an infinitesimal area of the reinforcing sheet in an RC-shaped bonded elastic layer. Then, the most general form of the equilibrium equations for the sheet in the two horizontal directions can be written as

$$\begin{aligned}
 N_{xx,x} + N_{xy,y} &= \tau_{xz} \Big|_{z=t/2} - \tau_{xz} \Big|_{z=-t/2} \\
 N_{yy,y} + N_{xy,x} &= \tau_{yz} \Big|_{z=t/2} - \tau_{yz} \Big|_{z=-t/2}
 \end{aligned}
 \tag{2.66}$$

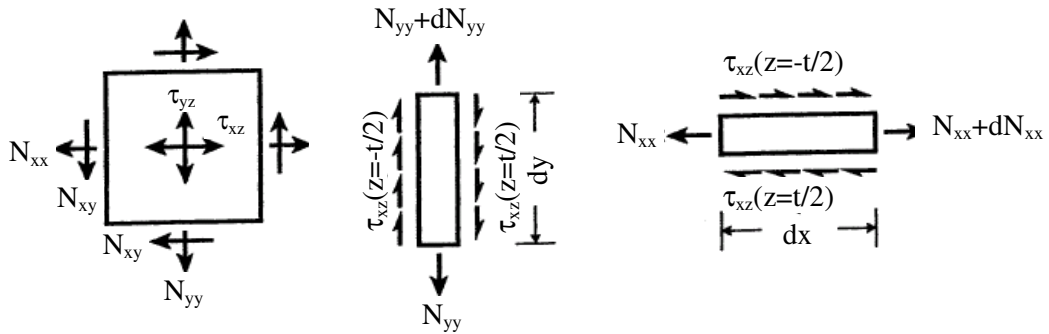


Figure 2.6 Forces on an infinitesimal area of a reinforcing sheet bonded to RC-shaped rubber layers (taken from [47])

To be able to write the equilibrium equations in terms of the displacements of the reinforcement, it is necessary to relate the internal forces to the displacements. Using the linearly elastic stress strain relations, the internal forces can be expressed in terms of the displacement components as follows:

$$\begin{aligned} N_{xx} &= k_f (u_{1,x} + \nu_f v_{1,y}), & N_{yy} &= k_f (v_{1,y} + \nu_f u_{1,x}) \\ N_{xy} &= k_f \left(\frac{1-\nu_f}{2} \right) (u_{1,y} + v_{1,x}) \end{aligned} \quad (2.67)$$

where the in-plane stiffness of the reinforcement k_f is as defined in Eq. (2.56). Then, the most general form of the equilibrium equations in terms of the reinforcement displacements and interfacial shear stresses becomes

$$\begin{aligned} u_{1,xx} + \nu_f v_{1,yx} + \frac{1-\nu_f}{2} (u_{1,yy} + v_{1,xy}) &= \frac{1}{k_f} (\tau_{xz}|_{z=t/2} - \tau_{xz}|_{z=-t/2}) \\ v_{1,yy} + \nu_f u_{1,xy} + \frac{1-\nu_f}{2} (u_{1,yx} + v_{1,xx}) &= \frac{1}{k_f} (\tau_{yz}|_{z=t/2} - \tau_{yz}|_{z=-t/2}) \end{aligned} \quad (2.68)$$

Kelly [13] also investigated the effect of the material compressibility on the compressive behavior of IS-shaped rubber layers bonded to flexible reinforcements. He showed that the material compressibility can be incorporated into the formulation just as done in the rigidly-bonded case, i.e., by replacing the incompressibility condition $\varepsilon_{xx} + \varepsilon_{yy} + \varepsilon_{zz} = 0$ with $\varepsilon_{xx} + \varepsilon_{yy} + \varepsilon_{zz} = -p/K$. Then, the complete set of the equations for the three unknown functions becomes

$$u_{0,x} + \frac{3}{2} u_{1,x} = \frac{3}{2} \frac{\Delta}{t} - \frac{3}{2} \frac{p}{K}, \quad p_{,x} = -\frac{8\mu}{t^2} u_0, \quad u_{1,xx} = -\frac{8\mu}{k_f t} u_0 \quad (2.69)$$

It is again easy to reduce these equations into a single pressure equation, which can be expressed as

$$\nabla^2 p = -\frac{12\mu}{t^2} \varepsilon_c + \left(\frac{12\mu}{k_f t} + \frac{12\mu}{Kt^2} \right) p \quad (2.70)$$

from which the compressible compression modulus for fiber-reinforced IS-shaped layer $E_{ccf,IS}$ is determined as

$$E_{cf,IS}^K = \frac{k_f}{t} \frac{\lambda^2}{\beta^2} \left[1 - \frac{\tanh(\beta w)}{\beta w} \right] \quad (2.71)$$

where

$$\beta^2 = \lambda^2 + \alpha^2 \quad \text{with} \quad \lambda^2 = \frac{12\mu}{Kt^2} \quad \text{and} \quad \alpha^2 = \frac{12\mu}{k_f t} \quad (2.72)$$

By applying the approach Tsai and Lee [30] used for the analysis of rigidly-bonded elastic layers, Tsai [48] derived analytical expressions for the compressible compression modulus of IS-shaped layers bonded to flexible reinforcements. In his study, he investigated the effect of the boundary conditions at the ends of a fiber reinforced bearing on its compression modulus. The following expression he derived for the compressible compression modulus of IS-shaped elastic layers bonded to flexible reinforcement under uniform compression is worth mentioning in this review:

$$E_{cf,IS}^T = 2\mu + \frac{2\mu\lambda}{\lambda + 2\mu} + \frac{\lambda^2}{\lambda + 2\mu} \left(\frac{\alpha_0^2}{\beta_0^2} \right) \left[1 - \frac{\tanh(\beta_0 w)}{\beta_0 w} \right] \quad (2.73)$$

where

$$\beta_0^2 = \alpha_0^2 + \alpha_1^2 \quad \text{with} \quad \alpha_0^2 = \frac{12\mu}{(\lambda + 2\mu)t^2} \quad \text{and} \quad \alpha_1^2 = \frac{12\mu}{k_f t} \quad (2.74)$$

2.2.2 Bending Behavior

Adaptation of Kelly's formulation [10] to the bending case is very similar. Under the effect of bending moments M , (Figure 2.4a,c), the displacement field for the elastic layer-idealized to IS-shape- can be simplified as:

$$u(x, z) = u_o(x) \left(1 - \frac{4z^2}{t^2} \right) + u_1(x) + \frac{\kappa}{2} z^2, \quad w(x, z) = -\kappa x z \quad (2.75)$$

from which the complete set of the equations for the three unknown functions of the problem, u_0 , u_1 and p , can be obtained as

$$u_{0,x} + \frac{3}{2} u_{1,x} = \frac{3}{2} \frac{\phi}{t} x, \quad p_{,x} = -\frac{8\mu}{t^2} u_0, \quad u_{1,xx} = -\frac{8\mu}{k_f t} u_0 \quad (2.76)$$

The necessary boundary or symmetry conditions for the solution of the above equations are

$$u_0(0) = 0, \quad u_1(0) = 0, \quad p(\pm w) = 0 \quad \text{and} \quad N_{xx}(\pm w) = k_f u_{1,x}(\pm w) = 0 \quad (2.77)$$

Thus, the pressure equation for the bending case has the following form:

$$\nabla^2 p = -\frac{12\mu}{t^2} x\kappa + \frac{12\mu}{k_f t} p \quad (2.78)$$

The solution of the pressure equation, in view of the condition $p(\pm w) = 0$, leads to

$$p(x) = \frac{k_f}{t} \left[\frac{x}{w} - \frac{\sinh(\alpha x)}{\sinh(\alpha w)} \right] \kappa w \quad \text{where} \quad \alpha^2 = \frac{12\mu}{k_f t} \quad (2.79)$$

from which the incompressible bending modulus for IS-shaped layers bonded to flexible reinforcements $E_{bif,IS}$ is determined as

$$E_{bif,IS}^K = \frac{k_f}{t} \left[1 - \frac{3}{(\alpha w)^2} \left[\frac{\alpha w}{\tanh(\alpha w)} - 1 \right] \right] \quad (2.80)$$

Kelly's approach [10] was later applied to C and RC-shaped layers by Tsai and Kelly [47], who derived the following expression for the incompressible bending modulus of circular discs bonded to flexible reinforcements:

$$E_{bif,C}^{TK} = \frac{k_f (1 + \nu_f)}{t} \frac{1}{2} \left[\frac{(\alpha R) I_1(\alpha R) - 4 I_2(\alpha R)}{(\alpha R) I_1(\alpha R) - 2(1 - \nu_f) I_2(\alpha R)} \right] \quad (2.81)$$

It is to be noted that the compressive behavior of a reinforcing sheet can be very different from its tensile behavior. Then, the above-mentioned formulation, which is developed ignoring this behavior difference in the reinforcing sheet, will not be valid under pure bending. However, it is well known that such bonded elastic layers are usually subjected to compression in addition to bending. For instance, in their use, multilayered fiber-reinforced elastomeric bearings should support the heavy weight of the superstructure. Considering that the tension created in the reinforcement due to the compressive load typically exceeds the compression created by the bending moment in such elements, this assumption seems to be valid for practical use [47]. However, its limitation should always be kept in mind when the solutions derived based on this assumption are used.

2.2.3 Warping Behavior

As already mentioned, Kelly [44] can be accepted as the first researcher who studied the warping behavior of bonded elastic layers. In his study, he first developed a beam theory for buckling analysis of short beams including the shear deformation and warping of the cross section. Considering the cross sectional warping as an independent kinematic quantity, he defined the displacement field as

$$u(x, z) = \delta(z) \quad \text{and} \quad w(x, z) = \Delta(z) - \phi(z)x + \Phi(z)\Omega(x) \quad (2.82)$$

where δ and Δ are the displacements of “the middle surface” in x and z directions respectively; ϕ is the “average angle of rotation of the section”, Φ is the “measure of the warping of the section” and Ω , also called “warping function”, is the function describing the warping pattern of the section.

Assuming elastic behavior and using linear stress-strain relations, the axial stress in a uniform short beam can be written in terms of the displacement components as

$$\sigma_{zz} = E\Delta' - E\phi'x + E\Phi'\Omega \quad (2.83)$$

where the prime indicates derivation with respect to z .

Kelly [44] defined three axial stress resultants for this problem:

$$P = \int_A \sigma_{zz} dA, \quad M = -\int_A \sigma_{zz} x dA \quad \text{and} \quad Q = \int_A \sigma_{zz} \Omega dA \quad (2.84)$$

As it can be understood from Eqs. (2.84), to incorporate the effect of the section warping into the classical beam theory, it is necessary to define a new stress resultant Q , called the resultant “warping moment”, besides the known stress resultants P (resultant axial load) and M (resultant bending moment). Then, it is not difficult to show that these stress resultants are related to their kinematic variables by

$$P = EA\Delta', \quad M = EI\phi' \quad \text{and} \quad Q = EJ\Phi' \quad (2.85)$$

where the warping related cross sectional property J , which can be thought as a kind of sectional inertia, named “warping inertia”, is defined as

$$J = \int_A \Omega^2 dA \quad (2.86)$$

Thus, the axial stress in a uniform short beam can be written in terms of the stress resultants as

$$\sigma_{zz} = \frac{P}{A} - \frac{M}{I}x + \frac{Q}{J}\Omega \quad (2.87)$$

Eq. (2.87) indicates that, as in the classical beam theory, the variation of the axial stress over the cross section of a short beam is uniform under uniform compression and linear under pure bending. Eq. (2.87) also indicates that the axial stress distribution due to warping moment Q has the shape of the warping function Ω .

As stated by Tsai and Kelly [45], who verified the theory by Kelly [44] using the principle of virtual work, “it is convenient to select the warping function Ω such that the axial force and bending moment are independent of Ω ”. Thus, in view of Eq. (2.87), one has the following two conditions for the warping function Ω :

$$\int_A \Omega dA = 0 \quad \text{and} \quad \int_A \Omega x dA = 0 \quad (2.88)$$

In other words, it is necessary to select $\Omega(x)$ in such a way that it is orthogonal to both 1 and x . From the first of Eqs. (2.88), it is seen that Ω has to be an odd function of x . As stated in [45], “there are many forms that the warping function could take” but “the simplest function” is “a cubic polynomial” in the form of

$$\Omega(x) = \left(\frac{x}{w}\right)^3 + f\left(\frac{x}{w}\right) \quad (2.89)$$

where f is a constant that should be determined from the second of Eqs. (2.88). It can be shown that $f = -3/5$ for a uniform short beam.

It is known that the axial stress distribution in a bonded elastic layer can considerably be different than that in Eq. (2.87). In fact, for a rubber layer bonded to inextensible reinforcements with no flexural rigidity, one can write the following equation, using the pressure method and assuming strict incompressibility, for the axial stress:

$$\nabla^2 \sigma_{zz} = -\frac{12\mu}{t^2} \epsilon_{zz} \quad (2.90)$$

which, in view of Eq. (2.82), equals to

$$\nabla^2 \sigma_{zz} = -\frac{12\mu}{t^2} (\Delta' - \phi'x + \Phi'\Omega) \quad (2.91)$$

Kelly [44] showed that if a cubic function as in Eq. (2.89) is selected as the warping function, the value of f that “permits the uncoupling of the constitutive equation for bending moment M and warping resultant Q ” has to be $-3/7$.

When Eq. (2.90), with a cubic function for $\Omega(x)$, is solved with the condition that $\sigma_{zz}(\pm w)=0$, the axial stress distribution in a bonded elastic layer is determined as

$$\sigma_{zz} = \left\{ \begin{array}{l} -\frac{6\mu}{t^2} w^2 \left(\frac{x^2}{w^2} - 1 \right) \Delta' + \frac{2\mu}{t^2} w^3 \left(\frac{x^3}{w^3} - \frac{x}{w} \right) \phi' \\ -\frac{12\mu}{20t^2} w^2 \left(\frac{x^5}{w^5} - \frac{10}{7} \frac{x^3}{w^3} + \frac{3}{7} \frac{x}{w} \right) \Phi' \end{array} \right\} \quad (2.92)$$

Then, the relations between the stress resultants and their kinematic quantities can be written as

$$P = E_c A \Delta' \quad , \quad M = E_b I \phi' \quad \text{and} \quad Q = E_w J \Phi' \quad (2.93)$$

where

$$E_c = 4\mu S^2 \quad , \quad E_b = \frac{4}{5} \mu S^2 \quad \text{and} \quad E_w = \frac{2}{15} \mu S^2 \quad (2.94)$$

In Eqs. (2.93) and (2.94), the “effective warping modulus” E_w can be determined from the ratio of the warping stiffness K_w , which can be defined as the ratio of the resultant warping moment Q to the resultant change in Φ , to the warping inertia J . In other words, for the effective warping modulus E_w , one has

$$E_w = \frac{K_w}{J} \quad \text{where} \quad K_w = \frac{Q}{\Phi'} \quad (2.95)$$

Thus, as shown by Kelly [44], the buckling theory developed for uniform short beams can also be applied to elastomeric bearings consisting of several bonded rubber layers provided that the effects of the individual bonded rubber layers are accounted for by using the effective stiffnesses of the bearing.

As it can be understood from Eqs. (2.94), Kelly [44] included the effects of neither the reinforcement extensibility nor the material compressibility in his

formulation. The effect of the reinforcement flexibility is later incorporated into this buckling theory by Tsai and Kelly [46].

In fact, the warping behavior of an elastic layer bonded to flexible reinforcements can be studied similar to its bending behavior. It can be inferred from [46], the displacement field (Figure 2.4d) for an IS-shaped layer bonded to flexible reinforcements under a warping moment Q can be simplified, based on the kinematic assumptions of the pressure method, as

$$u(x, z) = u_0(x, y)\left(1 - \frac{4z^2}{t^2}\right) + u_1(x) \quad \text{and} \quad w(x, z) = \Omega\Phi \frac{z}{t} \quad (2.96)$$

From Eq. (2.96), it is clear that similar to the compression and bending cases, the displacement of the layer in the horizontal direction is first written based on the parabolic bulging assumption, then the flexibility of the reinforcement is taken into consideration by adding the term u_1 , which is assumed to be constant through the thickness. The effect of the cross section warping is considered with the term $\Phi\Omega$ in the vertical displacement. It is worth noting that Tsai and Kelly [46] defined this term as “a kinematic displacement function that produces no rotation of the section but measures the deviation from plane of the deformed cross section”.

Following the same procedure defined for the “incompressible” compression problem, one can obtain the following set of equations for the warping problem:

$$u_{0,x} + \frac{3}{2}u_{1,x} = -\frac{3}{2} \frac{\Phi}{t} \Omega, \quad p_{,x} = -\frac{8\mu}{t^2} u_0 + \frac{\mu}{t} \Phi \Omega_{,x}, \quad u_{1,xx} = -\frac{8\mu}{k_f t} u_0 + \frac{\mu}{k_f t} \Phi \Omega_{,x} \quad (2.97)$$

which can be reduced to

$$\nabla^2 p = \frac{12\mu}{t^2} \left[\left(\Omega + \frac{1}{12} t^2 \Omega_{,xx} \right) \frac{\Phi}{t} \right] + \frac{12\mu}{k_f t} p \quad (2.98)$$

Realizing that “term on the right-hand side of” Eq. (2.98), “ $t^2 \Omega_{,xx} / 12$, which is equal to $x/(2wS^2)$, is negligible because the pressure approach is applicable to isolators with shape factors greater than about five” and selecting the simplest cubic function (Eq. (2.89)) as their warping function, Tsai and Kelly [46] derived the following expression for the pressure distribution under pure warping:

$$p(x) = -\frac{k_f}{t} \left\{ \left(\frac{x}{w} \right)^3 + \left[f + \frac{6}{(\alpha w)^2} \right] \frac{x}{w} - \left[1 + f + \frac{6}{(\alpha w)^2} \right] \frac{\sinh(\alpha x)}{\sinh(\alpha w)} \right\} \frac{\Phi}{t} \quad (2.99)$$

where α is as defined in Eq. (2.62). They also derived a closed-form expression for the incompressible warping stiffness of an IS-shaped elastic layer bonded to flexible reinforcements, which can be expressed as

$$K_{wif,IS} = \mu \frac{w^3}{t^2} \left[\frac{16}{5} \frac{1}{(\alpha w)^2} \left(-\frac{3}{7} - f \right) \right] \quad (2.100)$$

It is to be noted that, in their formulation, Tsai and Kelly [46] also considered the effect of the flexural deformation of the reinforcements. The additional term coming from this effect is not included in the expression presented in Eq. (2.100).

As far as the constant f in the warping function is concerned, the formulation proposed by Tsai and Kelly [46] should be examined thoroughly. It can be realized that the authors selected the warping function Ω such that the virtual work done by the normal stress in the elastomeric layer can be written in an uncoupled form as far as the applied deformations are concerned. In what follows, this formulation is reviewed shortly.

Under the combined effects of the compressive load P , bending moment M and warping moment Q (Figure 2.4), the axial stress σ_{zz} in an IS-shaped elastic layer bonded to flexible reinforcements can be written as $\sigma_{zz} = \sigma_{zz,P} + \sigma_{zz,M} + \sigma_{zz,Q}$, where $\sigma_{zz,P}$, $\sigma_{zz,M}$ and $\sigma_{zz,Q}$ denote the axial stresses representing the effects of individual loadings P , M and Q , respectively. Similarly, if the axial displacement of the layer is assumed to vary linearly in the vertical direction, axial strain ϵ_{zz} under the combined effects of these loadings can be written as $\epsilon_{zz} = -\frac{\Delta}{t} - \frac{\phi}{t}x + \frac{\Phi}{t}\Omega$. To achieve the following decoupled form for the virtual work done by the axial stress in the layer,

$$\int_{-t/2}^{t/2} \int_A \sigma_{zz} \delta \epsilon_{zz} dA dz = \int_{-w}^w \left(-\sigma_{zz,P} \delta \Delta - \sigma_{zz,M} x \delta \phi + \sigma_{zz,Q} \Omega \delta \Phi \right) dx \quad (2.101)$$

the following conditions must be satisfied:

$$\begin{aligned}
\int_{-w}^w \sigma_{zz,M} dx = 0, & \quad \int_{-w}^w \sigma_{zz,P} x dx = 0 \\
\int_{-w}^w \sigma_{zz,Q} dx = 0, & \quad \int_{-w}^w \sigma_{zz,P} \Omega dx = 0 \\
\int_{-w}^w \sigma_{zz,Q} x dx = 0, & \quad \int_{-w}^w \sigma_{zz,M} \Omega dx = 0
\end{aligned} \tag{2.102}$$

It is clear that the first two conditions given in Eqs. (2.102) are satisfied trivially if the cross section is symmetric about the x and y axes. It can also be seen that the third and fourth conditions are satisfied easily if the warping function is selected to be an odd function of x . Thus, there remain two conditions to be satisfied by the selected warping shape, the fifth and sixth conditions in Eqs. (2.102).

Tsai and Kelly [46] showed that if the cubic function given in Eq. (2.89) is selected as the warping function, it is possible to compute the constant f from these two conditions, both of which, they showed, yield the same result. The expression derived in [46] for the constant f has the following form for an IS -shaped bonded elastic layer of incompressible materials:

$$f_{i,IS} = - \left[1 + \frac{6}{(\alpha w)^2} + \frac{\frac{2}{15}(\alpha w)^2}{\frac{\alpha w}{\tanh(\alpha w)} - 1 - \frac{1}{3}(\alpha w)^2} \right] \tag{2.103}$$

It should be kept in mind that Tsai and Kelly [46] used the pressure method while determining the axial stress distribution in the layer. Moreover, as mentioned previously, they simplified the pressure equation by removing one term from the right hand side of the pressure equation. On the other hand, if a more complicated analysis is used to determine the stress distributions, it can be really tedious to determine the correct form of the warping function. At this point, it is worth reemphasizing that Tsai and Kelly [45, 46] used such an uncoupling in their virtual work expression in order to simplify their stability analysis. Thus, this condition should not be considered as a requirement on the warping shape.

CHAPTER 3

THE NEW FORMULATION FOR THE ANALYSIS OF BONDED ELASTIC LAYERS

The main objective of this dissertation, as already mentioned, is to study the behavior of bonded elastic layers under basic deformation modes using a new analytical formulation which removes most of the in-priori assumptions used in the earlier formulations. In this chapter, this new formulation is presented.

As discussed in the previous chapter, most of the earlier studies on bonded elastic layers have been based on assumed displacement fields with assumed stress distributions, which usually lead to approximate and/or “average” solutions. These assumptions have somehow hindered the comprehensive study of the stress and/or displacement distributions over the entire layer. As indicated by Papoulia and Kelly [35], variational approaches, such as, the principle of minimum potential energy can also be used in the analysis of bonded layers. These approaches can satisfactorily eliminate the stress assumptions commonly used in the formulations. However, even these approaches necessitate the selection of the form of the displacement functions in advance to satisfy the displacement boundary conditions. Thus, their success also depends on how well the behavior is “guessed” at the beginning.

The approximate theory that is used in this dissertation, the theory developed by Mengi [19], overcomes this difficulty; inclusion of the displacement boundary conditions in the formulation itself eliminates any possible inconsistency between the assumed displacement field and the boundary conditions at the bonded surfaces. Thus, there is no need to start the formulation with some assumptions on

stress/displacement distributions or with some limitations on geometrical and material properties. Since the effect of compressibility is naturally included in the formulation, the solutions are valid not only for incompressible or nearly incompressible materials but also for highly compressible materials. Furthermore, since the theory has “orders”, it is possible to improve its prediction and obtain solutions much closer to the exact by only increasing the order of the theory. Consequently, by using this new formulation, it is possible to derive the solutions in a form which can be used for the comprehensive study of stress/displacement distributions at any section in a bonded elastic layer. Furthermore, it is also possible to investigate the effects of geometric and material properties on the layer behavior thoroughly.

In the following sections, first the approximate theory proposed by Mengi [19] is reviewed. Then, using this theory, the linear (small) deformation analysis of bonded elastic layers under some basic static deformation modes is presented. Since in this dissertation, the main emphasis is given to the elastic layers bonded to rigid reinforcements, the rigidly-bonded case is discussed first. For each deformation mode, the order of the theory is left arbitrary and the relevant equations are presented in general forms, in view of the displacement boundary conditions at the top and bottom faces of the layer. To have a formulation applicable to all possible shapes (circular as well as infinite-strip, square and rectangular shapes), the reduced governing equations which are derived in rectangular Cartesian coordinates are also extended to cylindrical coordinates. The constants which appear in the approximate theory are determined and tabulated by choosing the distribution functions employed in the theory as Legendre polynomials. Regardless of the layer shape or order of the theory, determination of the displacement/stress distributions and the relevant effective modulus for each deformation mode are also formulated and presented. After the formulation of the rigidly-bonded case, the case where the elastic layer is bonded to flexible reinforcements is also considered. For this case, the reduced governing equations are derived only in rectangular Cartesian coordinates.

3.1 REVIEW OF THE APPROXIMATE THEORY USED IN THE DISSERTATION

The new formulation proposed in this dissertation for the analysis of bonded elastic layers is developed by using the approximate theory proposed by Mengi [19]. Formulated originally to analyze the dynamic behavior of thermoelastic plates by using a modified version of the Galerkin Method, this approximate theory assumes that the material is isotropic and linearly elastic and that the layer has a uniform thickness of $2h$. The layer is referred to a Cartesian coordinate system (x_1, x_2, x_3), where the x_1, x_3 plane coincides the mid-plane of the layer (Figure 3.1).

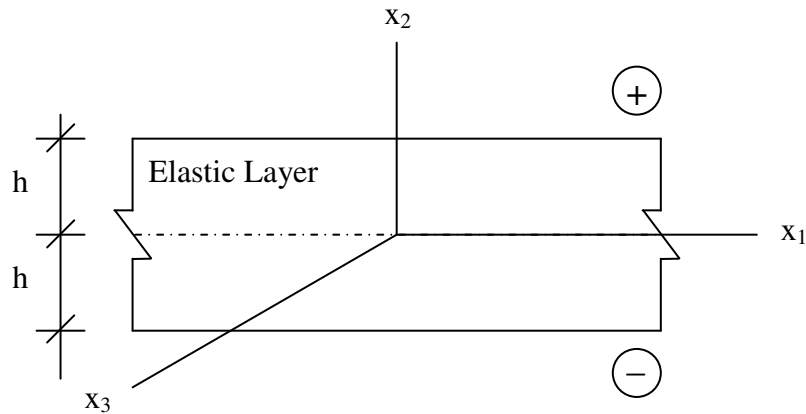


Figure 3.1 Cartesian coordinate system defined for a layer

The approximate theory contains two types of field variables: “generalized” variables representing the weighted averages of displacements and stresses over the thickness of the layer and “face” variables representing the displacements and tractions on the lateral faces of the layer. The inclusion of the face variables as the field variables in the theory eliminates any inconsistency which may exist between the displacement distributions assumed over the thickness of the layer and the boundary conditions on its flat faces. The theory due to Mengi [19] differs in this respect from others available in literature.

In the development of the theory, a set of “distribution functions” $\{\phi_n(\bar{x}_2), n = 0, 1, 2, \dots, \bar{x}_2 = x_2/h\}$ is chosen. The elements ϕ_n ($n = 0 - (m + 2)$) are retained in the set for m^{th} order theory. Keeping the last two elements ϕ_{m+1} and ϕ_{m+2} in the set is essential for establishing the constitutive equations for the face variables.

The theory is composed of two sets of equations. The first set of equations is derived by taking the weighted averages of the elasticity equations with the use of ϕ_n ($n = 0 - m$) as the weighting functions. The second set of equations representing the “constitutive equations for the face variables” is obtained through the expansion of the displacements in terms of the distribution functions ϕ_n ($n = 0 - (m + 2)$) and using them in the exact constitutive equations of the tractions on the flat faces of the layer. With this procedure, the governing equations of the approximate theory are obtained in terms of some constants whose values may be computed once the distribution functions are selected.

In what follows, a summary for the derivation of the equations of the approximate theory is given for the static case (for more details, see Ref. [19]).

Written in indicial notation, the fundamental equations of linear elasticity, equilibrium (in the absence of body forces) and constitutive equations are

$$\partial_j \tau_{ji} = 0 \quad (i, j = 1-3) \quad (3.1)$$

$$\tau_{ij} = \mu(\partial_i u_j + \partial_j u_i) + \delta_{ij} \lambda \partial_k u_k \quad (i, j = 1-3) \quad (3.2)$$

where λ and μ are Lamé’s constants; u_i are the displacement components; τ_{ij} are the stress components; and δ_{ij} is the Kronecker delta. In writing Eqs. (3.1) and (3.2), the summation convention is used, where any repeated index indicates summation over its range. Moreover, ∂_i implies partial differentiation with respect to x_i .

The weighted averages of fundamental equations are established by applying

the operator $L^n = \frac{1}{2h} \int_{-h}^{+h} (\cdot) \phi_n dx_2$ with $n=0-m$ to Eqs. (3.1) and (3.2), which gives

$$\partial_1 \tau_{1i}^n + \partial_3 \tau_{3i}^n + (R_i^n - \bar{\tau}_{2i}^n) = 0 \quad (n=0-m) \quad (3.3)$$

where

$$R_i^n = \frac{\hat{R}_i^n \phi_n(1)}{2h} \quad \text{where} \quad \hat{R}_i^n = \begin{cases} R_i^- = \tau_{2i}^+ - \tau_{2i}^- & \text{for even } n \\ R_i^+ = \tau_{2i}^+ + \tau_{2i}^- & \text{for odd } n \end{cases} \quad (3.4)$$

$$\text{with } \tau_{2i}^\pm = \tau_{2i} \Big|_{x_2=\pm h}$$

$$\bar{\tau}_{2i}^n = \bar{L}^n \tau_{2i} \quad \text{with} \quad \bar{L}^n = \frac{1}{2h} \int_{-h}^h (\cdot) \frac{d\phi_n}{dx_2} dx_2 \quad (3.5)$$

and

$$\begin{aligned} \tau_{11}^n &= (2\mu + \lambda) \partial_1 u_1^n + \lambda \partial_3 u_3^n + \lambda (S_2^n - \bar{u}_2^n) \\ \tau_{22}^n &= \lambda (\partial_1 u_1^n + \partial_3 u_3^n) + (2\mu + \lambda) (S_2^n - \bar{u}_2^n) \\ \tau_{33}^n &= (2\mu + \lambda) \partial_3 u_3^n + \lambda \partial_1 u_1^n + \lambda (S_2^n - \bar{u}_2^n) \\ \tau_{12}^n &= \mu \partial_1 u_2^n + \mu (S_1^n - \bar{u}_1^n) \\ \tau_{13}^n &= \mu \partial_1 u_3^n + \mu \partial_3 u_1^n \\ \tau_{23}^n &= \mu \partial_3 u_2^n + \mu (S_3^n - \bar{u}_3^n) \quad (n=0-m) \end{aligned} \quad (3.6)$$

where

$$S_i^n = \frac{\hat{S}_i^n \phi_n(1)}{2h} \quad \text{where} \quad \hat{S}_i^n = \begin{cases} S_i^- = u_i^+ - u_i^- & \text{for even } n \\ S_i^+ = u_i^+ + u_i^- & \text{for odd } n \end{cases} \quad \text{with} \quad u_i^\pm = u_i \Big|_{x_2=\pm h} \quad (3.7)$$

$$\bar{u}_i^n = \bar{L}^n u_i$$

In the derivation of Eqs. (3.3) to (3.7), it is assumed that ϕ_n is even function of \bar{x}_2 for even n and odd function of \bar{x}_2 for odd n . Also, it may be assumed without loss

of generality that $\phi_n' = \frac{d\phi_n}{d\bar{x}_2}$ is related to ϕ_j by $\phi_n' = \sum_{j=0}^m c_{nj} \phi_j$, implying that $\bar{\tau}_{2i}^n$ and

\bar{u}_i^n are related to τ_{2i}^n and u_i^n by

$$(\bar{\tau}_{2i}^n, \bar{u}_i^n) = \frac{1}{h} \sum_{j=0}^m c_{nj} (\tau_{2i}^j, u_i^j) \quad (3.8)$$

where the constants c_{nj} may be computed whenever the distribution functions are selected.

For the derivation of the constitutive equations for the face variables R_i^\pm , the displacements u_i are expanded in terms of ϕ_k ($k=0,1,2,\dots,m+2$) as

$$u_i = \sum_{k=0}^{m+2} a_k^i \phi_k \quad (3.9)$$

where a_k^i are some coefficients which are functions of x_1 and x_3 . It is to be noted that Eq. (3.9) is not an assumption on the shape of the displacements u_i over the thickness of the layer; it is the representation of u_i in terms of the complete shape (base) functions ϕ_k , in fact, this representation would be exact for $m \rightarrow \infty$. When L^n ($n=0-m$) operator is applied to this expression, one obtains

$$u_i^n = \sum_{k=0}^{m+2} d_{nk} a_k^i \quad \text{where} \quad d_{nk} = L^n \phi_k = \frac{1}{2h} \int_{-h}^h \phi_n \phi_k dx_2 \quad (3.10)$$

Assumed properties of ϕ_k lead to the following uncoupled system of equations for the determination of the coefficients a_k^i :

$$\begin{aligned} u_i^n &= \sum_{k=0,2}^{p+2} d_{nk} a_k^i \quad \text{and} \quad \frac{S_i^+}{2} = \sum_{k=0,2}^{p+2} a_k^i \phi_k(1) \quad (n=0,2,\dots,p) \quad \text{for even } k \\ u_i^n &= \sum_{k=1,3}^{p'+2} d_{nk} a_k^i \quad \text{and} \quad \frac{S_i^-}{2} = \sum_{k=1,3}^{p'+2} a_k^i \phi_k(1) \quad (n=1,3,\dots,p') \quad \text{for odd } k \end{aligned} \quad (3.11)$$

where $p=m$ and $p'=m-1$ for even m and $p=m-1$ and $p'=m$ for odd m . From the solutions of the above equations, the coefficients a_k^i are determined in terms of u_i^n and S_i^\pm as

$$\begin{aligned} a_k^i &= \sum_{j=0,2}^p f_{kj} u_i^j + f_{k,p+2} S_i^+ \quad \text{for } k=0,2,\dots,p+2 \\ a_k^i &= \sum_{j=1,3}^{p'} f_{kj} u_i^j + f_{k,p'+2} S_i^- \quad \text{for } k=1,3,\dots,p'+2 \end{aligned} \quad (3.12)$$

where the coefficients f_{kj} ($k,j=0-(m+2)$) may be computed whenever ϕ_n are chosen.

Finally, to obtain the constitutive equations for the face variables, one should use Eq. (3.9) in $R_i^\pm = \tau_{2i}^+ \pm \tau_{2i}^-$ with $\tau_{2i} = \mu(\partial_2 u_i + \partial_i u_2) + \lambda \delta_{i2} \partial_k u_k$, which gives

$$\begin{aligned}
R_1^+ &= \mu(\partial_1 S_2^+) + \frac{2\mu}{h} \left(\sum_{k=1,3}^{p'} \gamma_k u_1^k + \gamma^- S_1^- \right) \\
R_1^- &= \mu(\partial_1 S_2^-) + \frac{2\mu}{h} \left(\sum_{k=0,2}^p \gamma_k u_1^k + \gamma^+ S_1^+ \right) \\
R_2^+ &= \lambda(\partial_1 S_1^+ + \partial_3 S_3^+) + \frac{2(2\mu + \lambda)}{h} \left(\sum_{k=1,3}^{p'} \gamma_k u_2^k + \gamma^- S_2^- \right) \\
R_2^- &= \lambda(\partial_1 S_1^- + \partial_3 S_3^-) + \frac{2(2\mu + \lambda)}{h} \left(\sum_{k=0,2}^p \gamma_k u_2^k + \gamma^+ S_2^+ \right) \\
R_3^+ &= \mu(\partial_3 S_2^+) + \frac{2\mu}{h} \left(\sum_{k=1,3}^{p'} \gamma_k u_3^k + \gamma^- S_3^- \right) \\
R_3^- &= \mu(\partial_3 S_2^-) + \frac{2\mu}{h} \left(\sum_{k=0,2}^p \gamma_k u_3^k + \gamma^+ S_3^+ \right)
\end{aligned} \tag{3.13}$$

where

$$\begin{aligned}
\gamma_j &= \sum_{k=1,3}^{p'+2} f_{kj} \phi'_k(1) \quad \text{for } j=1,3,\dots, p' \\
\gamma_j &= \sum_{k=0,2}^{p+2} f_{kj} \phi'_k(1) \quad \text{for } j=0,2,\dots, p \\
\gamma^- &= \sum_{k=1,3}^{p'+2} f_{k,p'+2} \phi'_k(1), \quad \gamma^+ = \sum_{k=0,2}^{p+2} f_{k,p+2} \phi'_k(1)
\end{aligned} \tag{3.14}$$

In the approximate theory, the weighted forms of the equilibrium equations [3(m+1) equations] and constitutive equations [6(m+1) equations] provide [9(m+1)] equations. In addition, six equations come from the boundary conditions at the top and bottom faces of the layer. These boundary conditions specify one of the traction or displacement components, or their combination, in each direction on each face of the layer. On the other hand, the constitutive equations for the face variables provide six more equations. Thus, the number of available equations in the approximate theory is [9(m+1)+12], which is sufficient to compute the unknowns $(\tau_{ij}^n, u_i^n, S_i^\pm, R_i^\pm)$, whose number is also [9(m+1)+12].

3.2 APPLICATION OF THE APPROXIMATE THEORY TO ELASTIC LAYERS BONDED TO RIGID SURFACES

Figure 3.2a shows the undeformed configuration of an elastic layer of uniform thickness t bonded to rigid plates at its top and bottom faces. The deformed configurations of the layer under its three fundamental deformation modes are shown in Figure 3.2b-d.

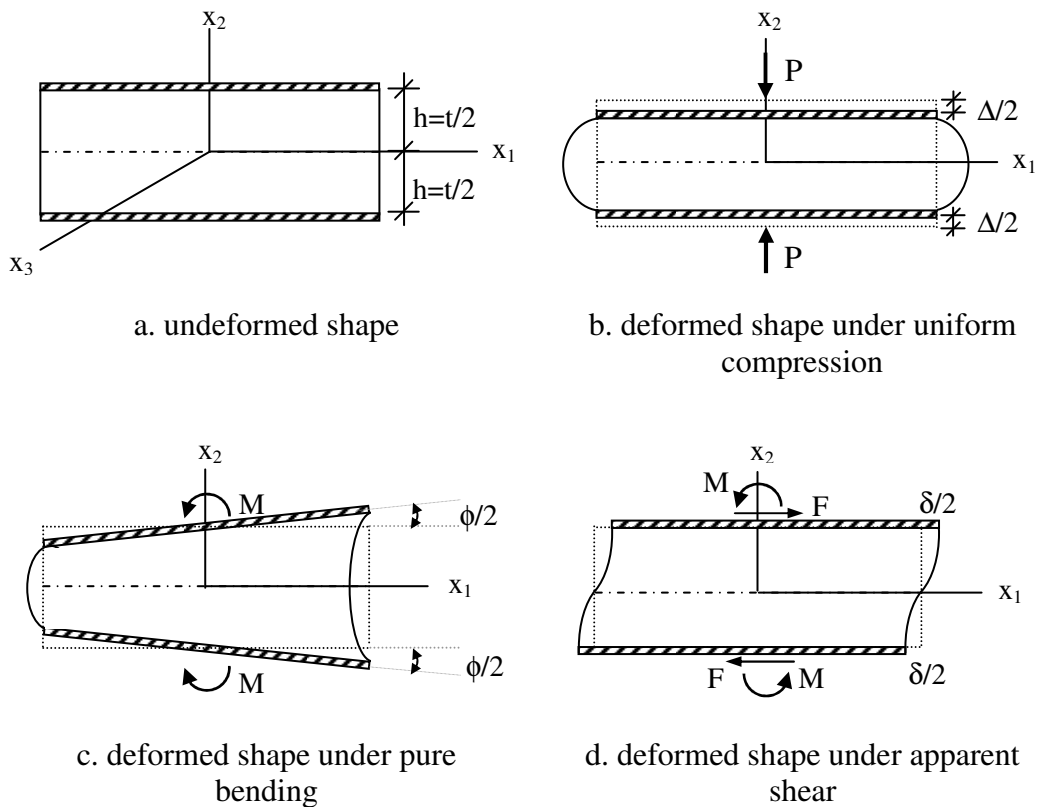


Figure 3.2 Undeformed and deformed configurations for an elastic layer bonded to rigid plates under its three basic deformation modes

In the first deformation mode (Figure 3.2b), the layer is compressed uniformly by a uniaxial compressive force P such that the bonded faces approach uniformly towards each other with a relative vertical displacement Δ . In the second

deformation mode (Figure 3.2c), the layer is purely bended by the bending moments M so that the bonded faces rotate with respect to each other about x_3 axis with a relative angle of rotation ϕ . Finally, in the third mode (Figure 3.2d), the bonded layer is subjected to the combined effects of the shearing force F and the bending moments $M=tF/2$ so that the bonded faces move with respect to each other in horizontal direction with a relative horizontal displacement δ .

The object in this section is to formulate each problem within the framework of the approximate theory presented in Section 3.1. In the formulation, the layer is referred to the same rectangular frame employed in the approximate theory. In the derivations and results presented in subsequent sections, the distribution functions in the approximate theory are chosen as Legendre polynomials of the first kind. The coefficients c_{nj} , a_k^i , γ_j and γ^\pm of the theory for these distribution functions are listed in Table 3.1 and Table 3.2.

It is worth noting that any distribution functions ϕ_n may be chosen in the approximate theory as long as they form a complete set implying that the prediction of the approximate theory approaches the actual response as the number of the terms retained in the set $\{\phi_n\}$ increases. Legendre polynomials, $P_n(x_2)$, selected as the distribution functions in the present study, are orthogonal implying that the completeness of the set $\{\phi_n\}$ is satisfied automatically; besides, the orthogonality of P_n facilitates the computations of constants appearing in the theory.

Table 3.1 c_{nj} coefficients (ϕ_n 's are Legendre polynomials)

$n \backslash j$	0	1	2	3	4
0	0	0	0	0	0
1	1	0	0	0	0
2	0	3	0	0	0
3	1	0	5	0	0
4	0	3	0	7	0

Table 3.2 Coefficients a_k^i and constants γ_j, γ^\pm for the 0th, 1st and 2nd order theories (ϕ_n 's are Legendre polynomials)

m	$a_k^i (k=0-(m+2))$	$\gamma_j (j=0-m)$	γ^+	γ^-
0	$\begin{bmatrix} u_i^0 \\ S_i^- / 2 \\ S_i^+ / 2 - u_i^0 \end{bmatrix}$	$\{-3\}$	3/2	1/2
1	$\begin{bmatrix} u_i^0 \\ 3u_i^1 \\ S_i^+ / 2 - u_i^0 \\ S_i^- / 2 - 3u_i^1 \end{bmatrix}$	$\begin{Bmatrix} -3 \\ -15 \end{Bmatrix}$	3/2	3
2	$\begin{bmatrix} u_i^0 \\ 3u_i^1 \\ 5u_i^2 \\ S_i^- / 2 - 3u_i^1 \\ S_i^+ / 2 - 5u_i^2 - u_i^0 \end{bmatrix}$	$\begin{Bmatrix} -10 \\ -15 \\ -35 \end{Bmatrix}$	5	3

3.2.1 Derivation of Reduced Governing Equations

3.2.1.1 Uniform Compression

From the deformed configuration of a uniformly compressed bonded elastic layer shown in Figure 3.2b, it is clear that the vertical displacement u_2 is antisymmetric whereas the horizontal displacements u_1 and u_3 are symmetric about the mid-plane of the layer. Since the distribution functions are even functions of \bar{x}_2 for even n and odd functions of \bar{x}_2 for odd n , one has

$$\begin{aligned} u_1^n = u_3^n = 0 \quad \text{and} \quad \bar{u}_2^n = 0 \quad \text{for odd } n \\ \bar{u}_1^n = \bar{u}_3^n = 0 \quad \text{and} \quad u_2^n = 0 \quad \text{for even } n \end{aligned} \tag{3.15}$$

Furthermore, since the elastic layer is bonded at its top and bottom faces, the material points at the bonded faces can only displace uniformly in the axial direction; this implies that

$$u_1^\pm = u_3^\pm = 0 \quad \text{and} \quad u_2^\pm = u_2|_{x_2=\pm h} = \mp \frac{\Delta}{2} \quad (3.16)$$

which leads to

$$S_1^\pm = S_3^\pm = S_2^+ = 0 \quad \text{and} \quad S_2^- = -\Delta \quad (3.17)$$

from which it is obvious that

$$S_1^n = S_3^n = 0 \quad \text{for all } n, \quad S_2^n = \begin{cases} -\Delta/t & \text{for even } n \\ 0 & \text{for odd } n \end{cases} \quad (3.18)$$

$$(\partial_1 S_i^n, \partial_3 S_i^n) = 0 \quad \text{for } i=1-3 \quad \text{for all } n$$

Then, the constitutive equations for the face variables and the weighted form of the constitutive equations have the following uncoupled forms:

- constitutive equations for the face variables:

$$R_i^n = \frac{4\mu}{t^2} \left(\sum_{k=0,2}^p \gamma_k u_i^k \right) \quad (i=1,3) \quad \text{for even } n, \quad (3.19)$$

$$R_2^n = \frac{4\alpha}{t^2} \left(\sum_{k=1,3}^{p'} \gamma_k u_2^k - \Delta \gamma^- \right) \quad \text{for odd } n$$

- weighted constitutive equations:

$$\left. \begin{aligned} \tau_{11}^n &= \alpha \partial_1 u_1^n + \lambda \partial_3 u_3^n - \frac{\lambda \Delta}{t} - \lambda \bar{u}_2^n \\ \tau_{22}^n &= \lambda \partial_1 u_1^n + \lambda \partial_3 u_3^n - \frac{\alpha \Delta}{t} - \alpha \bar{u}_2^n \\ \tau_{33}^n &= \lambda \partial_1 u_1^n + \alpha \partial_3 u_3^n - \frac{\lambda \Delta}{t} - \lambda \bar{u}_2^n \\ \tau_{13}^n &= \mu \partial_1 u_3^n + \mu \partial_3 u_1^n \end{aligned} \right\} \quad \text{for even } n \quad (3.20)$$

$$\left. \begin{aligned} \tau_{12}^n &= \mu \partial_1 u_2^n - \mu \bar{u}_1^n \\ \tau_{23}^n &= \mu \partial_3 u_2^n - \mu \bar{u}_3^n \end{aligned} \right\} \quad \text{for odd } n$$

where $\alpha = 2\mu + \lambda$, and other R_i^n and τ_{ij}^n being zero.

Substitution of Eqs. (3.19) and (3.20) into Eq. (3.3) gives the following governing equations for the weighted displacements u_i^n :

$$\left. \begin{aligned} \alpha \partial_{11} u_1^n + \mu \partial_{33} u_1^n + (\lambda + \mu) \partial_{13} u_3^n - \lambda \partial_1 \bar{u}_2^n + \frac{4\mu}{t^2} \left(\sum_{k=0,2}^p \gamma_k u_1^k \right) &= \bar{\tau}_{21}^n \\ \alpha \partial_{33} u_3^n + \mu \partial_{11} u_3^n + (\lambda + \mu) \partial_{13} u_1^n - \lambda \partial_3 \bar{u}_2^n + \frac{4\mu}{t^2} \left(\sum_{k=0,2}^p \gamma_k u_3^k \right) &= \bar{\tau}_{23}^n \end{aligned} \right\} \text{for even } n \quad (3.21)$$

$$\mu \partial_{11} u_2^n + \mu \partial_{33} u_2^n - \mu \partial_1 \bar{u}_1^n - \mu \partial_3 \bar{u}_3^n + \frac{4\alpha}{t^2} \left(\sum_{k=1,3}^p \gamma_k u_2^k \right) - \frac{4\alpha}{t^2} \Delta \gamma^- = \bar{\tau}_{22}^n \quad \text{for odd } n$$

where \bar{u}_i^n and $\bar{\tau}_{2i}^n$ are related to u_i^n and τ_{2i}^n by, in view of Eq. (3.8),

$$(\bar{u}_i^n, \bar{\tau}_{2i}^n) = \frac{2}{t} \sum_{j=0}^m c_{nj} (u_i^j, \tau_{2i}^j) \quad (3.22)$$

in which τ_{2i}^j can be expressed in terms of u_i^n by Eqs. (3.20). Eqs. (3.21) with Eqs. (3.20) and (3.22) comprise the reduced governing equations for the problem of uniform compression of bonded elastic layers.

3.2.1.2 Pure Bending

Similar to the uniform compression case, under pure bending, the vertical displacement u_2 is antisymmetric while the horizontal displacements u_1 and u_3 are symmetric about the mid-plane of the layer (Figure 3.2c). Therefore, Eqs. (3.15) are valid also for the bending problem, for which the displacement boundary conditions at the bonded faces of the layer are

$$u_1^\pm = u_3^\pm = 0 \quad \text{and} \quad u_2^\pm = u_2 \Big|_{x_2=\pm h} = \pm \frac{\phi}{2} x_1 \quad (3.23)$$

which leads to

$$S_1^\pm = S_3^\pm = S_2^+ = 0 \quad \text{and} \quad S_2^- = \phi x_1 \quad (3.24)$$

$$S_1^n = S_3^n = 0 \quad \text{for all } n, \quad S_2^n = \begin{cases} \phi x_1 / t & \text{for even } n \\ 0 & \text{for odd } n \end{cases} \quad (3.25)$$

Substituting Eqs. (3.15), (3.24) and (3.25) into the governing equations of the theory and following the same procedure described in Section 3.2.1.1, one can obtain the reduced form of the governing equations for the bending problem as

- weighted constitutive equations:

$$\left. \begin{aligned}
 \tau_{11}^n &= \alpha \partial_1 u_1^n + \lambda \partial_3 u_3^n + \frac{\lambda \phi}{t} x_1 - \lambda \bar{u}_2^n \\
 \tau_{22}^n &= \lambda \partial_1 u_1^n + \lambda \partial_3 u_3^n + \frac{\alpha \phi}{t} x_1 - \alpha \bar{u}_2^n \\
 \tau_{33}^n &= \lambda \partial_1 u_1^n + \alpha \partial_3 u_3^n + \frac{\lambda \phi}{t} x_1 - \lambda \bar{u}_2^n \\
 \tau_{13}^n &= \mu \partial_1 u_3^n + \mu \partial_3 u_1^n
 \end{aligned} \right\} \text{for even } n \quad (3.26)$$

$$\left. \begin{aligned}
 \tau_{12}^n &= \mu \partial_1 u_2^n - \mu \bar{u}_1^n \\
 \tau_{23}^n &= \mu \partial_3 u_2^n - \mu \bar{u}_3^n
 \end{aligned} \right\} \text{for odd } n$$

- weighted equilibrium equations:

$$\left. \begin{aligned}
 \left[\begin{aligned}
 &\alpha \partial_{11} u_1^n + \mu \partial_{33} u_1^n + (\lambda + \mu) \partial_{13} u_3^n - \lambda \partial_1 \bar{u}_2^n \\
 &+ \frac{4\mu}{t^2} \left(\sum_{k=0,2}^p \gamma_k u_1^k \right) + (\lambda + \mu) \frac{\phi}{t}
 \end{aligned} \right] &= \bar{\tau}_{21}^n \\
 \left[\begin{aligned}
 &\alpha \partial_{33} u_3^n + \mu \partial_{11} u_3^n + (\lambda + \mu) \partial_{13} u_1^n - \lambda \partial_3 \bar{u}_2^n \\
 &+ \frac{4\mu}{t^2} \left(\sum_{k=0,2}^p \gamma_k u_3^k \right)
 \end{aligned} \right] &= \bar{\tau}_{23}^n
 \end{aligned} \right\} \text{for even } n \quad (3.27)$$

$$\left[\begin{aligned}
 &\mu \partial_{11} u_2^n + \mu \partial_{33} u_2^n - \mu \partial_1 \bar{u}_1^n - \mu \partial_3 \bar{u}_3^n \\
 &+ \frac{4\alpha}{t^2} \left(\sum_{k=1,3}^{p'} \gamma_k u_2^k \right) + \frac{4\alpha}{t^2} \gamma^- \phi x_1
 \end{aligned} \right] = \bar{\tau}_{22}^n \quad \text{for odd } n$$

In Eqs. (3.27), \bar{u}_i^n and $\bar{\tau}_{2i}^n$ are related to u_i^n and τ_{2i}^n by Eq. (3.22), where τ_{2i}^j can be expressed in terms of u_i^n by Eqs. (3.26).

3.2.1.3 Apparent Shear

Apparent shear of the layer shown in Figure 3.2a results in the deformed shape shown in Figure 3.2d, from which it is obvious that the boundary conditions at the bonded faces are

$$u_1^\pm = u_1|_{x_2=\pm h} = \pm \frac{\delta}{2} \quad \text{and} \quad u_2^\pm = u_3^\pm = 0 \quad (3.28)$$

Then,

$$S_1^+ = S_2^\pm = S_3^\pm = 0 \quad \text{and} \quad S_1^- = \delta$$

$$S_2^n = S_3^n = 0 \quad \text{for all } n, \quad S_1^n = \begin{cases} \delta/t & \text{for even } n \\ 0 & \text{for odd } n \end{cases} \quad (3.29)$$

Contrary to the compression and bending cases, under apparent shear, the vertical displacement u_2 is symmetric whereas the horizontal displacements u_1 and u_3 are antisymmetric about the mid-plane of the layer. That is,

$$u_1^n = u_3^n = 0 \quad \text{and} \quad \bar{u}_2^n = 0 \quad \text{for even } n$$

$$\bar{u}_1^n = \bar{u}_3^n = 0 \quad \text{and} \quad u_2^n = 0 \quad \text{for odd } n \quad (3.30)$$

Following the same procedure employed in Section 3.2.1.1, the governing equations for the apparent shear problem may be obtained as

- weighted form of constitutive equations:

$$\left. \begin{aligned} \tau_{11}^n &= \alpha \partial_1 u_1^n + \lambda \partial_3 u_3^n - \lambda \bar{u}_2^n \\ \tau_{22}^n &= \lambda \partial_1 u_1^n + \lambda \partial_3 u_3^n - \alpha \bar{u}_2^n \\ \tau_{33}^n &= \lambda \partial_1 u_1^n + \alpha \partial_3 u_3^n - \lambda \bar{u}_2^n \\ \tau_{13}^n &= \mu \partial_1 u_3^n + \mu \partial_3 u_1^n \end{aligned} \right\} \text{for even } n$$

$$\left. \begin{aligned} \tau_{12}^n &= \mu \partial_1 u_2^n - \mu \bar{u}_1^n + \mu \frac{\delta}{t} \\ \tau_{23}^n &= \mu \partial_3 u_2^n - \mu \bar{u}_3^n \end{aligned} \right\} \text{for odd } n \quad (3.31)$$

- weighted form of equilibrium equations:

$$\left. \begin{aligned}
 & \left[\begin{aligned}
 & \alpha \partial_{11} u_1^n + \mu \partial_{33} u_1^n + (\lambda + \mu) \partial_{13} u_3^n - \lambda \partial_1 \bar{u}_2^n \\
 & + \frac{4\mu}{t^2} \left(\sum_{k=1,3}^{p'} \gamma_k u_1^k \right) + \frac{4\mu}{t^2} \delta \gamma^-
 \end{aligned} \right] = \bar{\tau}_{21}^n \\
 & \left[\begin{aligned}
 & \alpha \partial_{33} u_3^n + \mu \partial_{11} u_3^n + (\lambda + \mu) \partial_{13} u_1^n - \lambda \partial_3 \bar{u}_2^n \\
 & + \frac{4\mu}{t^2} \left(\sum_{k=1,3}^{p'} \gamma_k u_3^k \right)
 \end{aligned} \right] = \bar{\tau}_{23}^n
 \end{aligned} \right\} \text{for odd } n \quad (3.32)$$

$$\left[\begin{aligned}
 & \mu \partial_{11} u_2^n + \mu \partial_{33} u_2^n - \mu \partial_1 \bar{u}_1^n - \mu \partial_3 \bar{u}_3^n \\
 & + \frac{4\alpha}{t^2} \left(\sum_{k=0,2}^p \gamma_k u_2^k \right)
 \end{aligned} \right] = \bar{\tau}_{22}^n \quad \text{for even } n$$

In Eqs. (3.32), \bar{u}_i^n and $\bar{\tau}_{2i}^n$ are related to u_i^n and τ_{2i}^j by Eq. (3.22) where τ_{2i}^j can be expressed in terms of u_i^n by Eqs. (3.31).

3.2.2 Reduced Governing Equations in Cylindrical Coordinates

For circular cross sections, it is convenient to write the governing equations of the approximate theory in cylindrical coordinates (r, θ, z) . Referring to the cylindrical coordinate system defined in Figure 3.3, the fundamental equations of linear elasticity can be written in cylindrical coordinates as:

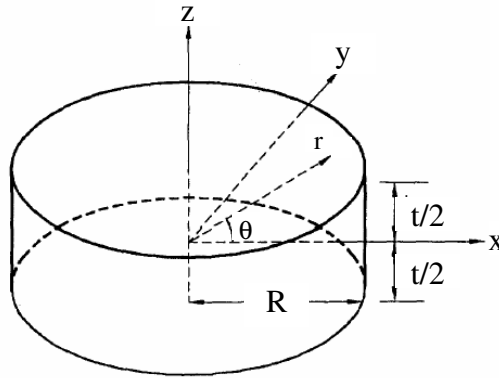


Figure 3.3 Cylindrical coordinate system defined for axisymmetric case (taken from [30])

- equilibrium equations in the absence of body forces:

$$\begin{aligned}
\partial_r \tau_{rr} + \frac{1}{r} \partial_\theta \tau_{r\theta} + \partial_z \tau_{rz} + \frac{1}{r} (\tau_{rr} - \tau_{\theta\theta}) &= 0 \\
\partial_r \tau_{r\theta} + \frac{1}{r} \partial_\theta \tau_{\theta\theta} + \partial_z \tau_{\theta z} + \frac{2}{r} \tau_{r\theta} &= 0 \\
\partial_r \tau_{rz} + \frac{1}{r} \partial_\theta \tau_{\theta z} + \partial_z \tau_{zz} + \frac{1}{r} \tau_{rz} &= 0
\end{aligned} \tag{3.33}$$

- constitutive equations:

$$\begin{aligned}
\tau_{rr} &= \alpha \partial_r u_r + \lambda \left(\frac{1}{r} \partial_\theta u_\theta + \frac{1}{r} u_r + \partial_z u_z \right) \\
\tau_{\theta\theta} &= \alpha \left(\frac{1}{r} \partial_\theta u_\theta + \frac{1}{r} u_r \right) + \lambda (\partial_r u_r + \partial_z u_z) \\
\tau_{zz} &= \alpha \partial_z u_z + \lambda \left(\partial_r u_r + \frac{1}{r} \partial_\theta u_\theta + \frac{1}{r} u_r \right) \\
\tau_{r\theta} &= \mu \left(\frac{1}{r} \partial_\theta u_r + \partial_r u_\theta - \frac{1}{r} u_\theta \right) \\
\tau_{rz} &= \mu (\partial_r u_z + \partial_z u_r) \\
\tau_{\theta z} &= \mu \left(\partial_z u_\theta + \frac{1}{r} \partial_\theta u_z \right)
\end{aligned} \tag{3.34}$$

Following the same procedure used in the derivation of the governing equations in rectangular Cartesian coordinates in Section 3.1, the governing equations of the approximate theory in cylindrical coordinates can be expressed as:

- weighted form of equilibrium equations ($n=0-m$):

$$\begin{aligned}
\partial_r \tau_{rr}^n + \frac{1}{r} \partial_\theta \tau_{r\theta}^n + \frac{1}{r} (\tau_{rr}^n - \tau_{\theta\theta}^n) + (R_r^n - \bar{\tau}_{rz}^n) &= 0 \\
\partial_r \tau_{r\theta}^n + \frac{1}{r} \partial_\theta \tau_{\theta\theta}^n + \frac{2}{r} \tau_{r\theta}^n + (R_\theta^n - \bar{\tau}_{z\theta}^n) &= 0 \\
\partial_r \tau_{rz}^n + \frac{1}{r} \partial_\theta \tau_{\theta z}^n + \frac{1}{r} \tau_{rz}^n + (R_z^n - \bar{\tau}_{zz}^n) &= 0
\end{aligned} \tag{3.35}$$

where

$$R_i^n = \frac{\hat{R}_i^n \phi_n(1)}{2h} \quad \text{where} \quad \hat{R}_i^n = \begin{cases} R_i^- = \tau_{zi}^+ - \tau_{zi}^- & \text{for even } n \\ R_i^+ = \tau_{zi}^+ + \tau_{zi}^- & \text{for odd } n \end{cases} \tag{3.36}$$

and

$$\bar{\tau}_{zi}^n = \bar{L}^n \tau_{zi} \quad \text{where} \quad \bar{L}^n = \frac{1}{2h} \int_{-h}^h (\cdot) \frac{d\phi_n}{dz} dz \quad (i=r, \theta, z) \quad (3.37)$$

- weighted form of constitutive equations ($n=0-m$):

$$\begin{aligned} \tau_{rr}^n &= \alpha \partial_r u_r^n + \lambda \left(\frac{1}{r} \partial_\theta u_\theta^n + \frac{1}{r} u_r^n \right) + \lambda (S_z^n - \bar{u}_z^n) \\ \tau_{\theta\theta}^n &= \alpha \left(\frac{1}{r} \partial_\theta u_\theta^n + \frac{1}{r} u_r^n \right) + \lambda (\partial_r u_r^n) + \lambda (S_z^n - \bar{u}_z^n) \\ \tau_{zz}^n &= \lambda (\partial_r u_r^n + \frac{1}{r} \partial_\theta u_\theta^n + \frac{1}{r} u_r^n) + \alpha (S_z^n - \bar{u}_z^n) \\ \tau_{r\theta}^n &= \mu \left(\frac{1}{r} \partial_\theta u_r^n + \partial_r u_\theta^n - \frac{1}{r} u_\theta^n \right) \\ \tau_{rz}^n &= \mu \partial_r u_z^n + \mu (S_r^n - \bar{u}_r^n) \\ \tau_{\theta z}^n &= \mu \frac{1}{r} \partial_\theta u_z^n + \mu (S_\theta^n - \bar{u}_\theta^n) \end{aligned} \quad (3.38)$$

where

$$S_i^n = \frac{\hat{S}_i^n \phi_n(1)}{2h} \quad \text{where} \quad \hat{S}_i^n = \begin{cases} S_i^- = u_i^+ - u_i^- & \text{for even } n \\ S_i^+ = u_i^+ + u_i^- & \text{for odd } n \end{cases} \quad (i=r, \theta, z) \quad (3.39)$$

- constitutive equations for the face variables:

$$\begin{aligned} R_r^+ &= \mu (\partial_r S_z^+) + \frac{2\mu}{h} \left(\sum_{k=1,3}^{p'} \gamma_k u_r^k + \gamma^- S_r^- \right) \\ R_r^- &= \mu (\partial_r S_z^-) + \frac{2\mu}{h} \left(\sum_{k=0,2}^p \gamma_k u_r^k + \gamma^+ S_r^+ \right) \\ R_z^+ &= \mu \left(\partial_r S_r^+ + \frac{1}{r} \partial_\theta S_\theta^+ + \frac{1}{r} S_r^+ \right) + \frac{2\alpha}{h} \left(\sum_{k=1,3}^{p'} \gamma_k u_z^k + \gamma^- S_z^- \right) \\ R_z^- &= \mu \left(\partial_r S_r^- + \frac{1}{r} \partial_\theta S_\theta^- + \frac{1}{r} S_r^- \right) + \frac{2\alpha}{h} \left(\sum_{k=0,2}^p \gamma_k u_z^k + \gamma^+ S_z^+ \right) \\ R_\theta^+ &= \mu \left(\frac{1}{r} \partial_\theta S_z^+ \right) + \frac{2\mu}{h} \left(\sum_{k=1,3}^{p'} \gamma_k u_\theta^k + \gamma^- S_\theta^- \right) \\ R_\theta^- &= \mu \left(\frac{1}{r} \partial_\theta S_z^- \right) + \frac{2\mu}{h} \left(\sum_{k=0,2}^p \gamma_k u_\theta^k + \gamma^+ S_\theta^+ \right) \end{aligned} \quad (3.40)$$

3.2.2.1 Uniform Compression

Under uniform compression, the deformation of a bonded elastic disc will obviously be axisymmetric, implying that $u_\theta=0$ and that radial and axial displacements are independent of θ ; i.e., $u_r=u_r(r,z)$, $u_z=u_z(r,z)$. It is also clear that u_z is antisymmetric while u_r is symmetric about the mid-plane of the layer which leads, in view of the special properties of the distribution functions, to

$$\begin{aligned} u_r^n &= 0 \quad \text{and} \quad \bar{u}_z^n = 0 \quad \text{for odd } n \\ \bar{u}_r^n &= 0 \quad \text{and} \quad u_z^n = 0 \quad \text{for even } n \end{aligned} \quad (3.41)$$

The boundary conditions at the bonded faces of the layer implies

$$u_r^\pm = 0 \quad \text{and} \quad u_z^\pm = u_z \Big|_{z=\pm t/2} = \mp \frac{\Delta}{2} \quad (3.42)$$

Then, S_i^\pm ($i=r,z$) becomes

$$S_r^\pm = S_z^+ = 0 \quad \text{and} \quad S_z^- = -\Delta \quad (3.43)$$

which leads to

$$S_r^n = 0 \quad \text{for all } n, \quad S_z^n = \begin{cases} -\Delta/t & \text{for even } n \\ 0 & \text{for odd } n \end{cases} \quad (3.44)$$

Then, Eqs. (3.38) and (3.40) reduce to the following uncoupled forms:

- constitutive equations for the face variables:

$$\left. \begin{aligned} \tau_{rr}^n &= \alpha \partial_r u_r^n + \frac{\lambda}{r} u_r^n - \frac{\lambda \Delta}{t} - \lambda \bar{u}_z^n \\ \tau_{\theta\theta}^n &= \lambda \partial_r u_r^n + \frac{\alpha}{r} u_r^n - \frac{\lambda \Delta}{t} - \lambda \bar{u}_z^n \\ \tau_{zz}^n &= \lambda \partial_r u_r^n + \frac{\lambda}{r} u_r^n - \frac{\alpha \Delta}{t} - \alpha \bar{u}_z^n \end{aligned} \right\} \quad \text{for even } n \quad (3.45)$$

$$\tau_{rz}^n = \mu \partial_r u_z^n - \mu \bar{u}_r^n \quad \text{for odd } n$$

- weighted form of constitutive equations:

$$R_r^n = \frac{4\mu}{t^2} \left(\sum_{k=0,2}^p \gamma_k u_r^k \right) \quad \text{for even } n, \quad R_z^n = \frac{4\alpha}{t^2} \left(\sum_{k=1,3}^{p'} \gamma_k u_z^k - \Delta \gamma^- \right) \quad \text{for odd } n \quad (3.46)$$

where other R_i^n and τ_{ij}^n are zero. Through the substitution of Eqs. (3.45) and (3.46) into Eqs.(3.35), one obtains the following governing equations for the weighted displacements u_i^n :

$$\begin{aligned} \alpha \partial_{rr} u_r^n + \frac{\alpha}{r} \partial_r u_r^n - \frac{\alpha}{r^2} u_r^n - \lambda \partial_r \bar{u}_z^n + \frac{4\mu}{t^2} \left(\sum_{k=0,2}^p \gamma_k u_r^k \right) &= \bar{\tau}_{rz}^n \quad \text{for even } n \\ \mu \partial_{rr} u_z^n + \frac{\mu}{r} \partial_r u_z^n - \mu \partial_r \bar{u}_r^n - \frac{\mu}{r} \bar{u}_r^n + \frac{4\alpha}{t^2} \left(\sum_{k=1,3}^{p'} \gamma_k u_z^k \right) - \frac{4\alpha}{t^2} \Delta \mathcal{Y}^- &= \bar{\tau}_{zz}^n \quad \text{for odd } n \end{aligned} \quad (3.47)$$

where

$$(\bar{\tau}_{zi}^n, \bar{u}_i^n) = \frac{2}{t} \sum_{j=0}^m c_{nj} (\tau_{zi}^j, u_i^j) \quad (3.48)$$

in which τ_{zi}^j can be expressed in terms of u_i^n by Eqs.(3.45). Eqs. (3.47) with Eqs. (3.45) and (3.48) constitute the reduced governing equations for the compression problem of bonded elastic discs for any order of the theory.

3.2.2.2 Pure Bending

Under pure bending, u_z is antisymmetric while u_r and u_θ are symmetric about the mid-plane of the layer. Thus, the weighted displacement components have the following properties:

$$\begin{aligned} u_r^n = u_\theta^n = 0 \quad \text{and} \quad \bar{u}_z^n = 0 \quad \text{for odd } n \\ \bar{u}_r^n = \bar{u}_\theta^n = 0 \quad \text{and} \quad u_z^n = 0 \quad \text{for even } n \end{aligned} \quad (3.49)$$

The boundary conditions at the bonded faces of the layer implies that

$$u_r^\pm = u_\theta^\pm = 0 \quad \text{and} \quad u_z^\pm = \pm \frac{\phi}{2} r \cos \theta \quad (3.50)$$

Then,

$$S_r^\pm = S_\theta^\pm = S_z^+ = 0 \quad \text{and} \quad S_z^- = \phi r \cos \theta \quad (3.51)$$

$$S_r^n = S_\theta^n = 0 \quad \text{for all } n, \quad S_z^n = \begin{cases} \phi r \cos \theta / t & \text{for even } n \\ 0 & \text{for odd } n \end{cases} \quad (3.52)$$

Substituting Eqs. (3.49), (3.51) and (3.52) into the governing equations of the theory (Eqs. (3.35), (3.38) and (3.40)) and following the same procedure described in the previous sections, one can obtain the following uncoupled equations for the bending problem:

- weighted constitutive equations:

$$\left. \begin{aligned}
 \tau_{rr}^n &= \alpha \partial_r u_r^n + \frac{\lambda}{r} u_r^n + \frac{\lambda}{r} \partial_\theta u_\theta^n + \frac{\lambda \phi r \cos \theta}{t} - \lambda \bar{u}_z^n \\
 \tau_{\theta\theta}^n &= \lambda \partial_r u_r^n + \frac{\alpha}{r} u_r^n + \frac{\alpha}{r} \partial_\theta u_\theta^n + \frac{\lambda \phi r \cos \theta}{t} - \lambda \bar{u}_z^n \\
 \tau_{zz}^n &= \lambda \partial_r u_r^n + \frac{\lambda}{r} u_r^n + \frac{\lambda}{r} \partial_\theta u_\theta^n + \frac{\alpha \phi r \cos \theta}{t} - \alpha \bar{u}_z^n \\
 \tau_{r\theta}^n &= \frac{\mu}{r} \partial_\theta u_r^n + \mu \partial_r u_\theta^n - \frac{\mu}{r} u_\theta^n
 \end{aligned} \right\} \text{for even } n$$

$$\left. \begin{aligned}
 \tau_{rz}^n &= \mu \partial_r u_z^n - \mu \bar{u}_r^n \\
 \tau_{\theta z}^n &= \frac{\mu}{r} \partial_\theta u_z^n - \mu \bar{u}_\theta^n
 \end{aligned} \right\} \text{for odd } n$$
(3.53)

- weighted equilibrium equations:

$$\left. \begin{aligned}
 &\left[\begin{aligned}
 &\alpha \partial_{rr} u_r^n + \frac{\alpha}{r} \partial_r u_r^n - \frac{\alpha}{r^2} u_r^n + \frac{\mu}{r^2} \partial_{\theta\theta} u_r^n + \frac{\lambda + \mu}{r} \partial_{r\theta} u_\theta^n \\
 &- \frac{\alpha + \mu}{r^2} \partial_\theta u_\theta^n - \lambda \partial_r \bar{u}_z^n + \frac{4\mu}{t^2} \left(\sum_{k=0,2}^p \gamma_k u_r^k \right) \\
 &+ (\lambda + \mu) \frac{\phi}{t} \cos \theta
 \end{aligned} \right] = \bar{\tau}_{rz}^n \\
 &\left[\begin{aligned}
 &\mu \partial_{rr} u_\theta^n + \frac{\mu}{r} \partial_r u_\theta^n - \frac{\mu}{r^2} u_\theta^n + \frac{\alpha}{r^2} \partial_{\theta\theta} u_\theta^n + \frac{\lambda + \mu}{r} \partial_{r\theta} u_r^n \\
 &+ \frac{\alpha + \mu}{r^2} \partial_\theta u_r^n - \frac{\lambda}{r} \partial_\theta \bar{u}_z^n + \frac{4\mu}{t^2} \left(\sum_{k=0,2}^p \gamma_k u_\theta^k \right) \\
 &- (\lambda + \mu) \frac{\phi}{t} \sin \theta
 \end{aligned} \right] = \bar{\tau}_{\theta z}^n
 \end{aligned} \right\} \text{for even } n$$

$$\left[\begin{aligned}
 &\mu \partial_{rr} u_z^n + \frac{\mu}{r} \partial_r u_z^n + \frac{\mu}{r^2} \partial_{\theta\theta} u_z^n - \mu \partial_r \bar{u}_r^n - \frac{\mu}{r} \bar{u}_r^n - \frac{\mu}{r} \partial_\theta \bar{u}_\theta^n \\
 &+ \frac{4\alpha}{t^2} \left(\sum_{k=1,3}^{p'} \gamma_k u_z^k \right) + \frac{4\alpha}{t^2} \gamma^- \phi r \cos \theta
 \end{aligned} \right] = \bar{\tau}_{zz}^n \text{ for odd } n$$
(3.54)

3.2.2.3 Apparent Shear

Under apparent shear, u_z is symmetric whereas u_r and u_θ are antisymmetric about the mid-plane of the layer. That is,

$$\begin{aligned} u_r^n = u_\theta^n = 0 \quad \text{and} \quad \bar{u}_z^n = 0 \quad \text{for even } n \\ \bar{u}_r^n = \bar{u}_\theta^n = 0 \quad \text{and} \quad u_z^n = 0 \quad \text{for odd } n \end{aligned} \quad (3.55)$$

The boundary conditions at the bonded faces, in this case, are

$$u_r^\pm = \pm \frac{\delta}{2} \cos \theta, \quad u_\theta^\pm = \mp \frac{\delta}{2} \sin \theta \quad \text{and} \quad u_z^\pm = 0 \quad (3.56)$$

Then,

$$\begin{aligned} S_r^+ = S_\theta^+ = S_z^\pm = 0, \quad S_r^- = \delta \cos \theta \quad \text{and} \quad S_\theta^- = -\delta \sin \theta \\ S_z^n = 0 \quad \text{for all } n, \end{aligned} \quad (3.57)$$

$$S_r^n = \begin{cases} \delta \cos \theta / t & \text{for even } n \\ 0 & \text{for odd } n \end{cases} \quad \text{and} \quad S_\theta^n = \begin{cases} -\delta \sin \theta / t & \text{for even } n \\ 0 & \text{for odd } n \end{cases}$$

Following the same procedure employed in the previous sections, the governing equations for the apparent shear problem may be obtained, in cylindrical polar coordinates, as

- weighted form of constitutive equations:

$$\left. \begin{aligned} \tau_{rr}^n &= \alpha \partial_r u_r^n + \frac{\lambda}{r} u_r^n + \frac{\lambda}{r} \partial_\theta u_\theta^n - \lambda \bar{u}_z^n \\ \tau_{\theta\theta}^n &= \lambda \partial_r u_r^n + \frac{\alpha}{r} u_r^n + \frac{\alpha}{r} \partial_\theta u_\theta^n - \lambda \bar{u}_z^n \\ \tau_{zz}^n &= \lambda \partial_r u_r^n + \frac{\lambda}{r} u_r^n + \frac{\lambda}{r} \partial_\theta u_\theta^n - \alpha \bar{u}_z^n \\ \tau_{r\theta}^n &= \frac{\mu}{r} \partial_\theta u_r^n + \mu \partial_r u_\theta^n - \frac{\mu}{r} u_\theta^n \end{aligned} \right\} \text{for odd } n \quad (3.58)$$

$$\left. \begin{aligned} \tau_{rz}^n &= \mu \partial_r u_z^n - \mu \bar{u}_r^n + \mu \frac{\delta}{t} \cos \theta \\ \tau_{\theta z}^n &= \frac{\mu}{r} \partial_\theta u_z^n - \mu \bar{u}_\theta^n - \mu \frac{\delta}{t} \sin \theta \end{aligned} \right\} \text{for even } n$$

- weighted form of equilibrium equations:

$$\left. \begin{aligned}
& \left[\begin{aligned}
& \alpha \partial_{rr} u_r^n + \frac{\alpha}{r} \partial_r u_r^n - \frac{\alpha}{r^2} u_r^n + \frac{\mu}{r^2} \partial_{\theta\theta} u_r^n + \frac{\lambda + \mu}{r} \partial_{r\theta} u_\theta^n \\
& - \frac{\alpha + \mu}{r^2} \partial_\theta u_\theta^n - \lambda \partial_r \bar{u}_z^n + \frac{4\mu}{t^2} \left(\sum_{k=1,3}^{p'} \gamma_k u_r^k \right) \\
& + \frac{4\mu}{t^2} \gamma^- \delta \cos \theta
\end{aligned} \right] = \bar{\tau}_{rz}^n \\
& \left[\begin{aligned}
& \mu \partial_{rr} u_\theta^n + \frac{\mu}{r} \partial_r u_\theta^n - \frac{\mu}{r^2} u_\theta^n + \frac{\alpha}{r^2} \partial_{\theta\theta} u_\theta^n + \frac{\lambda + \mu}{r} \partial_{r\theta} u_r^n \\
& + \frac{\alpha + \mu}{r^2} \partial_\theta u_r^n - \frac{\lambda}{r} \partial_\theta \bar{u}_z^n + \frac{4\mu}{t^2} \left(\sum_{k=1,3}^{p'} \gamma_k u_\theta^k \right) \\
& - \frac{4\mu}{t^2} \gamma^- \delta \sin \theta
\end{aligned} \right] = \bar{\tau}_{\theta z}^n
\end{aligned} \right\} \text{for odd } n \quad (3.59)$$

$$\left[\begin{aligned}
& \mu \partial_{rr} u_z^n + \frac{\mu}{r} \partial_r u_z^n + \frac{\mu}{r^2} \partial_{\theta\theta} u_z^n - \mu \partial_r \bar{u}_r^n - \frac{\mu}{r} \bar{u}_r^n - \frac{\mu}{r} \partial_\theta \bar{u}_\theta^n \\
& + \frac{4\alpha}{t^2} \left(\sum_{k=0,2}^p \gamma_k u_z^k \right)
\end{aligned} \right] = \bar{\tau}_{zz}^n \text{ for even } n$$

3.2.3 Determination of Displacement/Stress Distributions

Eqs. (3.21), (3.27) and (3.32) (or Eqs. (3.47),(3.54) and (3.59) in cylindrical coordinates) constitute the three sets of partial differential equations for the weighted displacements u_i^n governing the behavior of a bonded elastic layer under its three basic deformation modes. Necessary boundary conditions for the solution of these differential equations are the traction-free boundary conditions at the lateral bulge-free surfaces. Once the governing equations are solved for u_i^n , determination of displacements and stress distributions is straightforward.

For various orders of the theory, the distributions of the displacements u_i ($i=1-3$, in rectangular coordinates) may be computed in terms of u_i^n and S_i^\pm as, in view of the coefficients in Table 3.2 and of Eq. (3.9),

$$\begin{aligned}
u_i &= u_i^0 + \left(\frac{S_i^-}{2}\right)\left(\frac{2x_2}{t}\right) + \left(\frac{S_i^+}{2} - u_i^0\right)\left(\frac{6x_2^2}{t^2} - \frac{1}{2}\right) \quad (m=0) \\
u_i &= u_i^0 + (3u_i^1)\left(\frac{2x_2}{t}\right) + \left(\frac{S_i^+}{2} - u_i^0\right)\left(\frac{6x_2^2}{t^2} - \frac{1}{2}\right) + \left(\frac{S_i^-}{2} - 3u_i^1\right)\left(\frac{20x_2^3}{t^3} - \frac{3x_2}{t}\right) \quad (m=1) \\
u_i &= \left\{ \begin{aligned} &u_i^0 + (3u_i^1)\left(\frac{2x_2}{t}\right) + (5u_i^2)\left(\frac{6x_2^2}{t^2} - \frac{1}{2}\right) + \left(\frac{S_i^-}{2} - 3u_i^1\right)\left(\frac{20x_2^3}{t^3} - \frac{3x_2}{t}\right) \\ &+ \left(\frac{S_i^+}{2} - u_i^0 - 5u_i^2\right)\left(\frac{70x_2^4}{t^4} - \frac{15x_2^2}{t^2} + \frac{3}{8}\right) \end{aligned} \right\} \quad (m=2)
\end{aligned} \tag{3.60}$$

In cylindrical polar coordinates ($i=r, \theta, z$), Eqs. (3.60) are still valid; only the parameter z must be used in place of x_2 .

Substitution of the displacement components into Eq. (3.2) (or Eq. (3.34)) determines the stress distributions.

3.2.4 Compression, Bending and Apparent Shear Moduli

The effective modulus of the layer under its any deformation state may be determined whenever the stress distributions are obtained. As discussed in CHAPTER 2, the effective compression modulus E_c or effective bending modulus E_b of a bonded elastic layer can easily be obtained from the following equations:

$$E_c = \frac{\sigma_c}{\varepsilon_c} \quad \text{where} \quad \sigma_c = \frac{P}{A} \quad \text{and} \quad \varepsilon_c = \frac{\Delta}{t} \tag{3.61}$$

$$E_b = \frac{K_b}{I} \quad \text{and} \quad K_b = \frac{M}{\kappa} \quad \text{with} \quad \kappa = \frac{\phi}{t} \tag{3.62}$$

where I is the inertia moment of horizontal layer section about the bending axis.

Similarly, the apparent shear modulus μ_a of a bonded elastic layer can be determined from the ratio of nominal shear stress τ to nominal shear strain γ that is,

$$\mu_a = \frac{\tau}{\gamma} \quad \text{where} \quad \tau = \frac{F}{A} \quad \text{and} \quad \gamma = \frac{\delta}{t} \tag{3.63}$$

For any deformation state, the applied load can be computed by integrating the related face stress τ_{2i}^\pm (or τ_{ji}^\pm) over the horizontal section of the layer. Similarly, the applied moment can be determined by integrating, over the horizontal area, the

moment of the related face stress about the bending axis. Since zeroth order theory corresponds to averaging the variables through the layer thickness, τ_{2i}^0 (or τ_{zi}^0), instead of τ_{2i}^\pm (or τ_{zi}^\pm), should be used in the calculation of the forces or moments for this order. Thus, the compressive force P , bending moment M and shear force F in Eqs. (3.61) to (3.63) may be obtained, in Cartesian coordinates, from

$$\begin{aligned} (P, M, F) &= \iint_A (-\tau_{22}^0, \tau_{22}^0 x_1, \tau_{12}^0) dA \quad \text{for } m=0 \\ (P, M, F) &= \iint_A (-\tau_{22}^\pm, \tau_{22}^\pm x_1, \tau_{12}^\pm) dA \quad \text{for } m=1, 2, \dots \end{aligned} \quad (3.64)$$

where, in view of that $R_2^- = \tau_{22}^+ - \tau_{22}^- = 0$ for the uniform compression and pure bending problems, and $R_1^- = \tau_{12}^+ - \tau_{12}^- = 0$ and $R_2^+ = \tau_{22}^+ + \tau_{22}^- = 0$ for the apparent shear problem,

$$\begin{aligned} \tau_{22}^\pm &= \frac{2\alpha}{t} \left(\sum_{k=1,3}^{p'} \gamma_k u_2^k \right) + \frac{2\alpha}{t} \gamma^- \beta, \quad \beta = \begin{cases} -\Delta & \text{for uniform compression} \\ \phi x_1 & \text{for pure bending} \end{cases} \\ \left. \begin{aligned} \tau_{22}^+ &= -\tau_{22}^- = \frac{2\alpha}{t} \left(\sum_{k=0,2}^p \gamma_k u_2^k \right) \\ \tau_{12}^\pm &= \frac{2\mu}{t} \left(\sum_{k=1,3}^{p'} \gamma_k u_1^k \right) + \frac{2\mu}{t} \gamma^- \delta \end{aligned} \right\} \text{for apparent shear} \end{aligned} \quad (3.65)$$

Eqs. (3.64) and (3.65) take the following forms in cylindrical polar coordinates:

$$\begin{aligned} (P, M, F) &= \iint_A (-\tau_{zz}^0, \tau_{zz}^0 r \cos \theta, \tau^\theta) dA \quad \text{for } m=0 \\ (P, M, F) &= \iint_A (-\tau_{zz}^\pm, \tau_{zz}^\pm r \cos \theta, \tau^\pm) dA \quad \text{for } m=1, 2, \dots \end{aligned} \quad (3.66)$$

where, $\tau^0 = \sqrt{(\tau_{rz}^0)^2 + (\tau_{\theta z}^0)^2}$ and $\tau^\pm = \sqrt{(\tau_{rz}^\pm)^2 + (\tau_{\theta z}^\pm)^2}$ are, respectively, the resultant average and face shear stresses. The face stresses (τ_{iz}^\pm) can be determined, in view of that $R_z^- = \tau_{zz}^+ - \tau_{zz}^- = 0$ for the uniform compression and pure bending problems, and $R_r^- = \tau_{rz}^+ - \tau_{rz}^- = 0$, $R_\theta^- = \tau_{\theta z}^+ - \tau_{\theta z}^- = 0$ and $R_z^+ = \tau_{zz}^+ + \tau_{zz}^- = 0$ for the apparent shear problem, as

$$\begin{aligned}
\tau_{zz}^{\pm} &= \frac{2\alpha}{t} \left(\sum_{k=1,3}^{p'} \gamma_k u_z^k \right) + \frac{2\alpha}{t} \gamma^- \beta, & \beta &= \begin{cases} -\Delta & \text{for uniform compression} \\ \phi r \cos \theta & \text{for pure bending} \end{cases} \\
\left. \begin{aligned}
\tau_{zz}^+ &= -\tau_{zz}^- = \frac{2\alpha}{t} \left(\sum_{k=0,2}^p \gamma_k u_z^k \right) \\
\tau_{rz}^{\pm} &= \frac{2\mu}{t} \left(\sum_{k=1,3}^{p'} \gamma_k u_r^k \right) + \frac{2\mu}{t} \gamma^- \delta \cos \theta \\
\tau_{\theta z}^{\pm} &= \frac{2\mu}{t} \left(\sum_{k=1,3}^{p'} \gamma_k u_{\theta}^k \right) - \frac{2\mu}{t} \gamma^- \delta \sin \theta
\end{aligned} \right\} \text{for apparent shear}
\end{aligned} \tag{3.67}$$

3.3 APPLICATION OF THE APPROXIMATE THEORY TO ELASTIC LAYERS BONDED TO FLEXIBLE REINFORCEMENTS

For an elastic layer of uniform thickness t bonded to flexible reinforcements, with equivalent thickness t_f , at its top and bottom faces (Figure 3.4a), three fundamental deformation modes can be defined corresponding to the three fundamental loading types; compression, bending and shear. In the first deformation mode (Figure 3.4b), the layer is compressed uniformly by a uniaxial compressive force P such that the top and bottom reinforcements approach uniformly towards each other with a relative vertical displacement Δ .

While it is possible to apply “uniform” compression to an elastic layer even when it is bonded to extensible reinforcements with no flexural rigidity, it is *not* possible to apply “pure” bending or “apparent” shear to the layer since the flexible reinforcements will induce distortion (warping) in the bonded faces of the layer in these cases. In other words, the second and third modes are indeed much more complex in the flexible-reinforcement case since the influence of “warping” of the reinforcements has to be included in these modes.

From these two complex deformation modes, only the bending mode is considered in this dissertation. Furthermore, in order to obtain comparable results with the previously-analyzed rigid-reinforcement case, and for the simplicity of the analysis, this complex deformation mode is studied as the superposition of the two simpler modes: pure bending and pure warping.

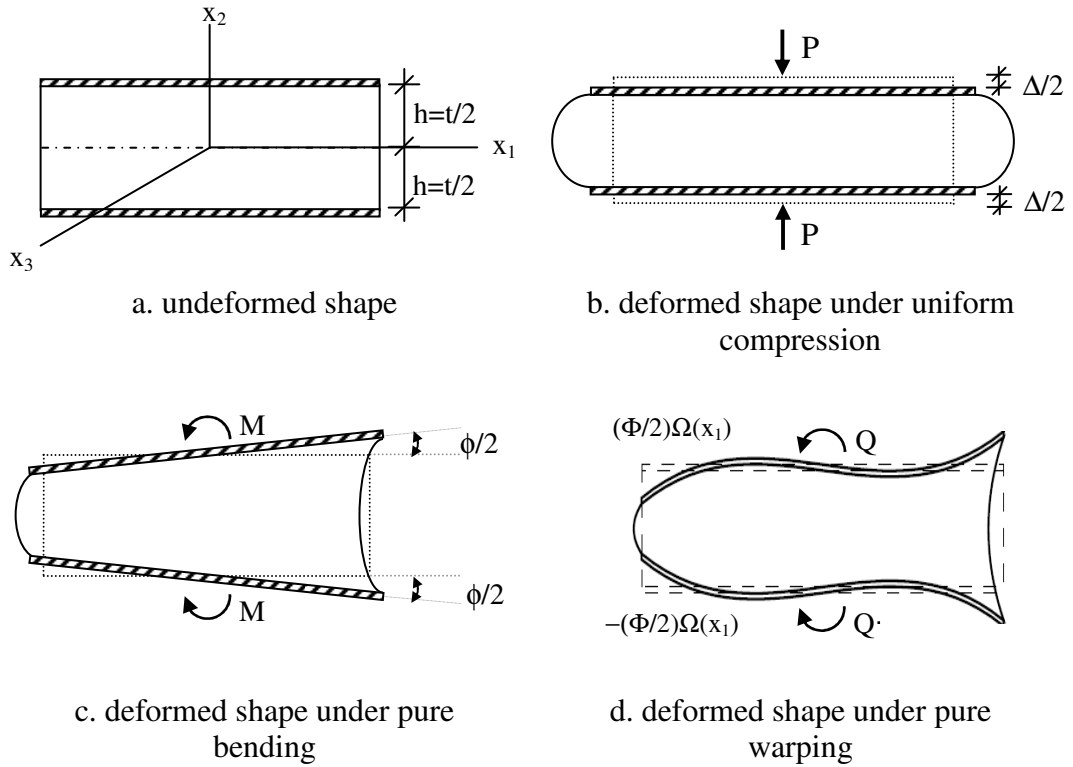


Figure 3.4 Undeformed and deformed configurations for an elastic layer bonded to flexible reinforcements under compression and bending (taken from [46])

In the pure bending mode (Figure 3.4c), the layer is purely bended by bending moments M so that the top and bottom reinforcements *remain plane* and rotate with respect to each other about x_3 axis with a relative angle of rotation ϕ . It is important to note that the reinforcements are not allowed to warp in the pure bending mode; the effect of reinforcement warping is considered in the pure warping mode. In the pure warping mode (Figure 3.4d), the bonded layer is subjected to the warping moment Q so that the top and bottom reinforcements deform about x_3 axis with a warping shape $(\Phi/2)\Omega(x_1)$ with *no rotation* from their plane.

The object in this section is again to formulate and analyze each problem within the framework of the approximate theory presented in Section 3.1. Similar to the rigidly-bonded cases studied in Section 3.2, the layer is referred to the same rectangular frame employed in the approximate theory and Legendre polynomials

are used as the distribution functions in the approximate theory. Thus, for the coefficients c_{nj} , a_k^i , γ_j and γ^\pm of the theory, Table 3.1 and Table 3.2 can be referred to. The formulation uses the two assumptions put forward by **Kelly [10]** on the behavior of the reinforcements: (i) the reinforcements are flexible in extension but have no flexural rigidity and (ii) the displacement field of the reinforcements can be idealized in accordance with the plane state of stress.

3.3.1 Derivation of Reduced Governing Equations

3.3.1.1 Uniform Compression

Figure 3.4b illustrates the deformed shape of an elastic layer bonded to flexible reinforcements under uniform compression. When Figure 3.4b is compared with Figure 3.2b, it can be seen that the main characteristics of the deformation field remains the same even when the reinforcements are flexible: the vertical displacement is antisymmetric and the horizontal displacements are symmetric about the mid-plane of the layer, implying that Eqs. (3.15) are still valid.

While the flexibility of the reinforcement does not affect the form of the “weighted” displacements, it does affect the formulation through the “face” displacements. Since the reinforcing sheets at the top and bottom faces of the layer are no longer rigid, the first of Eqs. (3.16) is longer be valid. Considering that the horizontal displacements are symmetric about the mid-plane of the layer, Eqs. (3.16) can be revised in the following form:

$$u_1^+ = u_1^-, \quad u_3^+ = u_3^- \quad \text{and} \quad u_2^\pm = \mp \frac{\Delta}{2} \quad (3.68)$$

Then, one has

$$S_1^- = S_3^- = S_2^+ = 0, \quad S_1^+ = 2u_1^+ = 2u_1^-, \quad S_3^+ = 2u_3^+ = 2u_3^- \quad \text{and} \quad S_2^- = -\Delta \quad (3.69)$$

It can be inferred from Eqs. (3.69) that when the reinforcement flexibility is included in the formulation, two additional unknowns appear in the governing equations. Any pair from $\{(S_1^+, S_3^+), (u_1^+, u_3^+), (u_1^-, u_3^-)\}$ can equally be selected as

these additional unknowns. In this study, the displacements at the top face of the layer (u_1^+, u_3^+) are used as the additional “unknown face displacements”.

Thus, S_i^n can be written in terms of the displacements at the top face of the layer as

$$S_i^n = \begin{cases} 0 & \text{for even } n \\ 2u_i^+ / t & \text{for odd } n \end{cases} \quad \text{for } (i=1,3) \quad \text{and} \quad S_2^n = \begin{cases} -\Delta / t & \text{for even } n \\ 0 & \text{for odd } n \end{cases} \quad (3.70)$$

Then, the constitutive equations for the face variables and the weighted constitutive equations can be written, in terms of the unknown weighted and face displacements, as

- constitutive equations for face variables:

$$R_i^n = \frac{4\mu}{t^2} \left(\sum_{k=0,2}^p \gamma_k u_i^k \right) + \frac{8\mu}{t^2} \gamma^+ u_i^+ \quad (i=1,3) \quad \text{for even } n,$$

$$R_2^n = \frac{4\alpha}{t^2} \left(\sum_{k=1,3}^{p'} \gamma_k u_2^k - \gamma^- \Delta \right) + \frac{2\lambda}{t} (\partial_1 u_1^+ + \partial_3 u_3^+) \quad \text{for odd } n \quad (3.71)$$

- weighted constitutive equations:

$$\left. \begin{aligned} \tau_{11}^n &= \alpha \partial_1 u_1^n + \lambda \partial_3 u_3^n - \frac{\lambda \Delta}{t} - \lambda \bar{u}_2^n \\ \tau_{22}^n &= \lambda \partial_1 u_1^n + \lambda \partial_3 u_3^n - \frac{\alpha \Delta}{t} - \alpha \bar{u}_2^n \\ \tau_{33}^n &= \lambda \partial_1 u_1^n + \alpha \partial_3 u_3^n - \frac{\lambda \Delta}{t} - \lambda \bar{u}_2^n \\ \tau_{13}^n &= \mu \partial_1 u_3^n + \mu \partial_3 u_1^n \end{aligned} \right\} \quad \text{for even } n \quad (3.72)$$

$$\left. \begin{aligned} \tau_{12}^n &= \mu \partial_1 u_2^n - \mu \bar{u}_1^n + \frac{2\mu}{t} u_1^+ \\ \tau_{23}^n &= \mu \partial_3 u_2^n - \mu \bar{u}_3^n + \frac{2\mu}{t} u_3^+ \end{aligned} \right\} \quad \text{for odd } n$$

where $\alpha = 2\mu + \lambda$, and other R_i^n and τ_{ij}^n being zero.

Substitution of Eqs. (3.71) and (3.72) into Eq. (3.3) gives the following governing equations for the unknown displacements u_i^n and (u_1^+, u_3^+) :

- weighted equilibrium equations:

$$\left. \begin{aligned}
& \left[\begin{aligned}
& \alpha \partial_{11} u_1^n + \mu \partial_{33} u_1^n + (\lambda + \mu) \partial_{13} u_3^n - \lambda \partial_1 \bar{u}_2^n \\
& + \frac{4\mu}{t^2} \left(\sum_{k=0,2}^p \gamma_k u_1^k \right) + \frac{8\mu}{t^2} \gamma^+ u_1^+
\end{aligned} \right] = \bar{\tau}_{21}^n \\
& \left[\begin{aligned}
& \alpha \partial_{33} u_3^n + \mu \partial_{11} u_3^n + (\lambda + \mu) \partial_{13} u_1^n - \lambda \partial_3 \bar{u}_2^n \\
& + \frac{4\mu}{t^2} \left(\sum_{k=0,2}^p \gamma_k u_3^k \right) + \frac{8\mu}{t^2} \gamma^+ u_3^+
\end{aligned} \right] = \bar{\tau}_{23}^n
\end{aligned} \right\} \text{for even } n \quad (3.73)$$

$$\left[\begin{aligned}
& \mu \partial_{11} u_2^n + \mu \partial_{33} u_2^n - \mu \partial_1 \bar{u}_1^n - \mu \partial_3 \bar{u}_3^n + \frac{4\alpha}{t^2} \left(\sum_{k=1,3}^{p'} \gamma_k u_2^k \right) \\
& - \frac{4\alpha}{t^2} \Delta \gamma^- + \frac{2(\lambda + \mu)}{t} (\partial_1 u_1^+ + \partial_3 u_3^+)
\end{aligned} \right] = \bar{\tau}_{22}^n \quad \text{for odd } n$$

where \bar{u}_i^n and $\bar{\tau}_{2i}^n$ are related to u_i^n and τ_{2i}^n by Eq. (3.22), in which τ_{2i}^j can be expressed in terms of u_i^n and (u_1^+, u_3^+) by Eqs. (3.72).

Due to the addition of (u_1^+, u_3^+) , the number of equations in Eqs. (3.73) is now surely not sufficient to determine all the unknowns. Two additional equations for the two additional unknown displacements come from the equilibrium equations written for the reinforcing sheets.

In this study, only the monotonically-deformed ‘‘interior’’ bonded layers are analyzed. In this case, the deformation in a reinforcing sheet is constrained by the deformation of the elastic layers at the top and bottom of the sheet. This constraint is taken accounted for approximately in the present study through the use of the shear stresses at the interfaces between the reinforcing sheet and the layers. Internal forces on an infinitesimal area of a reinforcing sheet bonded to elastic layers at its top and bottom surfaces are illustrated in Figure 3.5, where N_{11} and N_{33} are the stretching forces per unit length in the x_1 and x_3 directions, N_{13} is the in-plane shear force per unit length, and τ_{21}^+ and τ_{21}^- are the bonding shear stresses. It is assumed that the reinforcing sheet is under the influence of the plane state of stress.

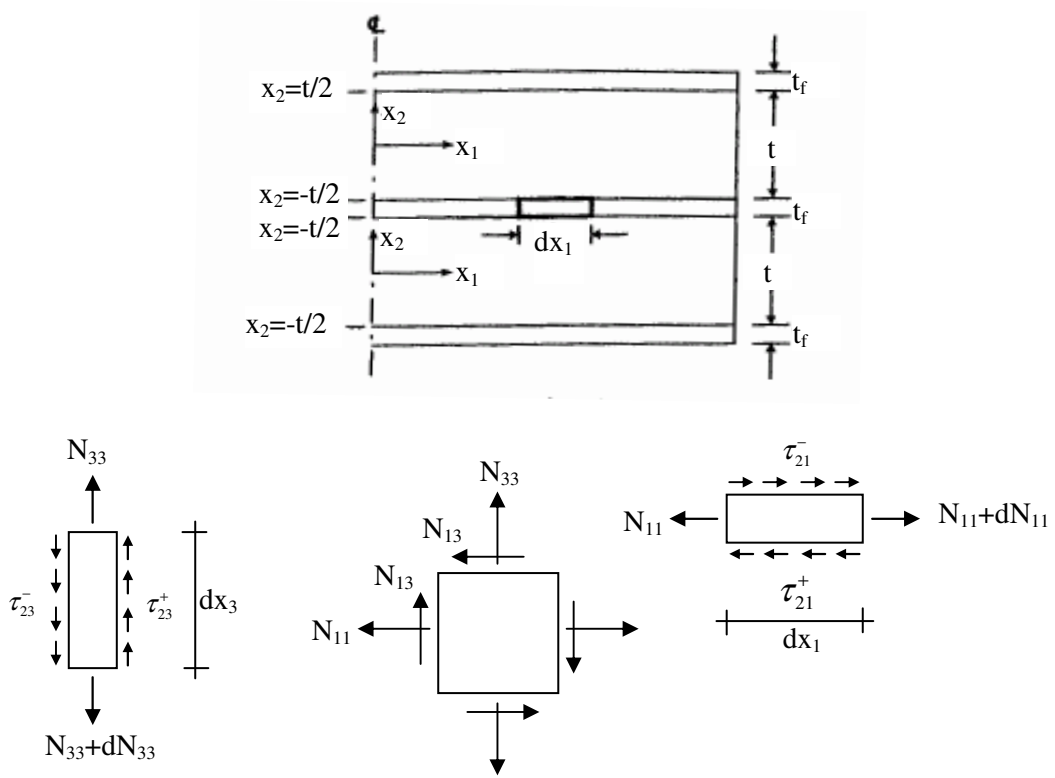


Figure 3.5 Forces on an infinitesimal area of a reinforcing sheet bonded to rubber layers at its top and bottom faces (taken from [47])

As discussed in Section 2.2.1, equilibrium equations for the reinforcing sheet in the two horizontal directions can be written as, in view of the assumption that the deformations and so the face shear stresses are equal at the same level of the top and bottom layers,

$$\begin{aligned} \partial_1 N_{11} + \partial_3 N_{13} &= \tau_{21}^+ - \tau_{21}^- \\ \partial_3 N_{33} + \partial_1 N_{13} &= \tau_{23}^+ - \tau_{23}^- \end{aligned} \quad (3.74)$$

Using the linearly elastic stress strain relations, internal forces N_{11} , N_{33} and N_{13} can be expressed in terms of the displacement components as follows:

$$\begin{aligned} N_{11} &= k_f [\partial_1 u_1^+ + \nu_f \partial_3 u_3^+], \quad N_{33} = k_f [\partial_3 u_3^+ + \nu_f \partial_1 u_1^+] \\ N_{13} &= k_f \left(\frac{1-\nu_f}{2} \right) [\partial_1 u_3^+ + \partial_3 u_1^+] \end{aligned} \quad (3.75)$$

where “in-plane stiffness of the reinforcement” k_f is defined as

$$k_f = \frac{E_f t_f}{1 - \nu_f^2} \quad (3.76)$$

It should be noted that while writing Eqs. (3.75), perfect bond is assumed between the elastic layer and flexible reinforcements. In other words, the extensions of the reinforcing sheet in x_1 and x_3 axes are taken to be equal to the face displacements.

Substituting Eqs. (3.75) and (3.71), in view of that $R_i^- = \tau_{2i}^+ - \tau_{2i}^- = tR_i^n$ for even n , into Eqs. (3.74), the two additional equations in terms of u_i^n and (u_1^+, u_3^+) are obtained as

$$\begin{aligned} \partial_{11}u_1^+ + \frac{1+\nu_f}{2}\partial_{13}u_3^+ + \frac{1-\nu_f}{2}\partial_{33}u_1^+ &= \frac{1}{k_f} \left[\frac{4\mu}{t} \left(\sum_{k=0,2}^p \gamma_k u_1^k \right) + \frac{8\mu}{t} \gamma^+ u_1^+ \right] \\ \partial_{33}u_3^+ + \frac{1+\nu_f}{2}\partial_{13}u_1^+ + \frac{1-\nu_f}{2}\partial_{11}u_3^+ &= \frac{1}{k_f} \left[\frac{4\mu}{t} \left(\sum_{k=0,2}^p \gamma_k u_3^k \right) + \frac{8\mu}{t} \gamma^+ u_3^+ \right] \end{aligned} \quad (3.77)$$

Eqs. (3.73) and (3.77) with Eq. (3.22) and Eqs. (3.72) comprise the reduced governing equations for the problem of uniform compression of elastic layers bonded to flexible reinforcements.

3.3.1.2 Pure Bending

The bending problem can be treated similarly. Since the reinforcement flexibility does not affect the form of the weighted displacements, it is sufficient to replace Eqs. (3.68) with

$$u_1^+ = u_1^-, \quad u_3^+ = u_3^-, \quad \text{and} \quad u_2^\pm = \pm \frac{\phi}{2} x_1 \quad (3.78)$$

Then,

$$\begin{aligned} S_1^- = S_3^- = S_2^+ = 0, \quad S_1^+ = 2u_1^+ = 2u_1^-, \quad S_3^+ = 2u_3^+ = 2u_3^- \quad \text{and} \quad S_2^- = \phi x_1 \\ S_i^n = \begin{cases} 0 & \text{for even } n \\ 2u_i^+ / t & \text{for odd } n \end{cases} \quad \text{for } (i=1,3) \quad \text{and} \quad S_2^n = \begin{cases} \phi x_1 / t & \text{for even } n \\ 0 & \text{for odd } n \end{cases} \end{aligned} \quad (3.79)$$

Following the same procedure described for the compression problem, one can obtain the reduced form of the governing equations for the bending problem as

- weighted constitutive equations:

$$\left. \begin{aligned}
 \tau_{11}^n &= \alpha \partial_1 u_1^n + \lambda \partial_3 u_3^n + \frac{\lambda \phi}{t} x_1 - \lambda \bar{u}_2^n \\
 \tau_{22}^n &= \lambda \partial_1 u_1^n + \lambda \partial_3 u_3^n + \frac{\alpha \phi}{t} x_1 - \alpha \bar{u}_2^n \\
 \tau_{33}^n &= \lambda \partial_1 u_1^n + \alpha \partial_3 u_3^n + \frac{\lambda \phi}{t} x_1 - \lambda \bar{u}_2^n \\
 \tau_{13}^n &= \mu \partial_1 u_3^n + \mu \partial_3 u_1^n
 \end{aligned} \right\} \text{for even } n$$

$$\left. \begin{aligned}
 \tau_{12}^n &= \mu \partial_1 u_2^n - \mu \bar{u}_1^n + \frac{2\mu}{t} u_1^+ \\
 \tau_{23}^n &= \mu \partial_3 u_2^n - \mu \bar{u}_3^n + \frac{2\mu}{t} u_3^+
 \end{aligned} \right\} \text{for odd } n$$
(3.80)

- weighted equilibrium equations:

$$\left. \begin{aligned}
 \left[\begin{aligned}
 &\alpha \partial_{11} u_1^n + \mu \partial_{33} u_1^n + (\lambda + \mu) \partial_{13} u_3^n - \lambda \partial_1 \bar{u}_2^n \\
 &+ \frac{4\mu}{t^2} \left(\sum_{k=0,2}^p \gamma_k u_1^k \right) + (\lambda + \mu) \frac{\phi}{t} + \frac{8\mu}{t^2} \gamma^+ u_1^+
 \end{aligned} \right] &= \bar{\tau}_{21}^n \\
 \left[\begin{aligned}
 &\alpha \partial_{33} u_3^n + \mu \partial_{11} u_3^n + (\lambda + \mu) \partial_{13} u_1^n - \lambda \partial_3 \bar{u}_2^n \\
 &+ \frac{4\mu}{t^2} \left(\sum_{k=0,2}^p \gamma_k u_3^k \right) + \frac{8\mu}{t^2} \gamma^+ u_3^+
 \end{aligned} \right] &= \bar{\tau}_{23}^n
 \end{aligned} \right\} \text{for even } n$$

$$\left[\begin{aligned}
 &\mu \partial_{11} u_2^n + \mu \partial_{33} u_2^n - \mu \partial_1 \bar{u}_1^n - \mu \partial_3 \bar{u}_3^n \\
 &+ \frac{4\alpha}{t^2} \left(\sum_{k=1,3}^{p'} \gamma_k u_2^k \right) + \frac{4\alpha}{t^2} \gamma^- \phi x_1 + \frac{2}{t} (\mu + \lambda) (\partial_1 u_1^+ + \partial_3 u_3^+)
 \end{aligned} \right] = \bar{\tau}_{22}^n \quad \text{for odd } n$$
(3.81)

- additional equations coming from reinforcement equilibrium:

$$\partial_{11} u_1^+ + \frac{1+\nu_f}{2} \partial_{13} u_3^+ + \frac{1-\nu_f}{2} \partial_{33} u_1^+ = \frac{1}{k_f} \left[\frac{4\mu}{t} \left(\sum_{k=0,2}^p \gamma_k u_1^k \right) + \frac{8\mu}{t} \gamma^+ u_1^+ + \mu \phi \right]$$

$$\partial_{33} u_3^+ + \frac{1+\nu_f}{2} \partial_{13} u_1^+ + \frac{1-\nu_f}{2} \partial_{11} u_3^+ = \frac{1}{k_f} \left[\frac{4\mu}{t} \left(\sum_{k=0,2}^p \gamma_k u_3^k \right) + \frac{8\mu}{t} \gamma^+ u_3^+ \right]$$
(3.82)

Eqs. (3.81) and (3.82) with Eq. (3.22) and Eqs. (3.80) comprise the reduced governing equations for the bending problem of elastic layers bonded to flexible reinforcements.

3.3.1.3 Pure Warping

Warping of the layer shown in Figure 3.4a results in the deformed shape illustrated in Figure 3.4d. From Figure 3.4d, it can be seen that the vertical displacement of the layer is antisymmetric while its horizontal displacements are symmetric about the mid-plane of the layer. Thus, the warping problem can be treated similar to the bending problem.

For the warping problem, one has

$$u_1^+ = u_1^-, \quad u_3^+ = u_3^- \quad \text{and} \quad u_2^\pm = \pm \frac{\Phi}{2} \Omega(x_1) \quad (3.83)$$

which leads to

$$S_1^- = S_3^- = S_2^+ = 0, \quad S_1^+ = 2u_1^+ = 2u_1^-, \quad S_3^+ = 2u_3^+ = 2u_3^-, \quad S_2^- = \Phi \Omega(x_1)$$

$$S_i^n = \begin{cases} 0 & \text{for even } n \\ 2u_i^+ / t & \text{for odd } n \end{cases} \quad \text{for } (i=1,3), \quad S_2^n = \begin{cases} \Phi \Omega(x_1) / t & \text{for even } n \\ 0 & \text{for odd } n \end{cases} \quad (3.84)$$

Following the same procedure described for the compression/bending problem, the reduced form of the governing equations for the warping problem can be obtained as

- weighted constitutive equations:

$$\left. \begin{aligned} \tau_{11}^n &= \alpha \partial_1 u_1^n + \lambda \partial_3 u_3^n + \frac{\lambda \Phi}{t} \Omega - \lambda \bar{u}_2^n \\ \tau_{22}^n &= \lambda \partial_1 u_1^n + \lambda \partial_3 u_3^n + \frac{\alpha \Phi}{t} \Omega - \alpha \bar{u}_2^n \\ \tau_{33}^n &= \lambda \partial_1 u_1^n + \alpha \partial_3 u_3^n + \frac{\lambda \Phi}{t} \Omega - \lambda \bar{u}_2^n \\ \tau_{13}^n &= \mu \partial_1 u_3^n + \mu \partial_3 u_1^n \end{aligned} \right\} \quad \text{for even } n \quad (3.85)$$

$$\left. \begin{aligned} \tau_{12}^n &= \mu \partial_1 u_2^n - \mu \bar{u}_1^n + \frac{2\mu}{t} u_1^+ \\ \tau_{23}^n &= \mu \partial_3 u_2^n - \mu \bar{u}_3^n + \frac{2\mu}{t} u_3^+ \end{aligned} \right\} \quad \text{for odd } n$$

- weighted equilibrium equations:

$$\left. \begin{aligned}
& \left[\begin{aligned}
& \alpha \partial_{11} u_1^n + \mu \partial_{33} u_1^n + (\lambda + \mu) \partial_{13} u_3^n - \lambda \partial_1 \bar{u}_2^n \\
& + \frac{4\mu}{t^2} \left(\sum_{k=0,2}^p \gamma_k u_1^k \right) + (\lambda + \mu) \frac{\Phi}{t} \partial_1 \Omega + \frac{8\mu}{t^2} \gamma^+ u_1^+
\end{aligned} \right] = \bar{\tau}_{21}^n \\
& \left[\begin{aligned}
& \alpha \partial_{33} u_3^n + \mu \partial_{11} u_3^n + (\lambda + \mu) \partial_{13} u_1^n - \lambda \partial_3 \bar{u}_2^n \\
& + \frac{4\mu}{t^2} \left(\sum_{k=0,2}^p \gamma_k u_3^k \right) + \frac{8\mu}{t^2} \gamma^+ u_3^+
\end{aligned} \right] = \bar{\tau}_{23}^n
\end{aligned} \right\} \text{for even } n \quad (3.86)$$

$$\left[\begin{aligned}
& \mu \partial_{11} u_2^n + \mu \partial_{33} u_2^n - \mu \partial_1 \bar{u}_1^n - \mu \partial_3 \bar{u}_3^n \\
& + \frac{4\alpha}{t^2} \left(\sum_{k=1,3}^{p'} \gamma_k u_2^k \right) + \frac{4\alpha}{t^2} \gamma^- \Phi \Omega + \frac{2}{t} (\mu + \lambda) (\partial_1 u_1^+ + \partial_3 u_3^+)
\end{aligned} \right] = \bar{\tau}_{22}^n \quad \text{for odd } n$$

- additional equations coming from reinforcement equilibrium:

$$\partial_{11} u_1^+ + \frac{1+\nu_f}{2} \partial_{13} u_3^+ + \frac{1-\nu_f}{2} \partial_{33} u_1^+ = \frac{1}{k_f} \left[\begin{aligned}
& \frac{4\mu}{t} \left(\sum_{k=0,2}^p \gamma_k u_1^k \right) + \frac{8\mu}{t} \gamma^+ u_1^+ \\
& + \mu \Phi \partial_1 \Omega
\end{aligned} \right] \quad (3.87)$$

$$\partial_{33} u_3^+ + \frac{1+\nu_f}{2} \partial_{13} u_1^+ + \frac{1-\nu_f}{2} \partial_{11} u_3^+ = \frac{1}{k_f} \left[\begin{aligned}
& \frac{4\mu}{t} \left(\sum_{k=0,2}^p \gamma_k u_3^k \right) + \frac{8\mu}{t} \gamma^+ u_3^+
\end{aligned} \right]$$

Eqs. (3.86) and (3.87) with Eq. (3.22) and Eqs. (3.85) comprise the reduced governing equations for the warping problem of elastic layers bonded to flexible reinforcements.

3.3.2 Determination of Displacement/Stress Distributions and Effective Moduli of the Layer

Eqs. {(3.73),(3.77)}, or {(3.81),(3.82)} or {(3.86),(3.87)} constitute three sets of differential equations for the unknown weighted and face displacements $\{u_i^n, u_1^+, u_3^+\}$ governing the behavior of an elastic layer bonded to flexible reinforcements under the three studied deformation modes. Necessary boundary conditions for the solution of these equations are the traction-free boundary

conditions at the lateral bulge-free surfaces of the elastic layer and the force-free boundary conditions at the edges of the reinforcing sheets. Once the governing equations are solved for $\{u_i^-, u_1^+, u_3^+\}$, the displacement and stress distributions can be determined as discussed in Section 3.2.3.

Similarly, the effective compression and bending moduli of the layer can be derived by using the Eqs. (3.61) and (3.62) with the Eqs. (3.64). However, in this case, it should be recognized that the face axial stresses τ_{22}^\pm become, in view of that $R_2^- = \tau_{22}^+ - \tau_{22}^- = 0$ for all problems,

$$\tau_{22}^\pm = \lambda \left[\partial_1 u_1^+ + \partial_3 u_3^+ \right] + \frac{2\alpha}{t} \left(\sum_{k=1,3} \gamma_k u_2^k \right) + \frac{2\alpha}{t} \gamma^- \beta \quad \text{where}$$

$$\beta = \begin{cases} -\Delta & \text{for uniform compression} \\ \phi_{x_1} & \text{for pure bending} \\ \Phi \Omega & \text{for warping} \end{cases} \quad (3.88)$$

Thus, in the computation of the force and moment resultants given in the second of Eqs. (3.64), Eqs. (3.88) must be used.

Referring to Section 2.2.3, the warping modulus (E_w) of an elastic layer bonded to flexible reinforcements can be defined as

$$E_w = \frac{K_w}{J} \quad \text{where} \quad K_w = \frac{Q}{\Phi/t} \quad \text{and} \quad J = \int_A \Omega^2 dA \quad (3.89)$$

where the warping moment Q can be computed from

$$Q = \iint_A \tau_{22}^0 \Omega dA \quad \text{for } m=0 \quad \text{and} \quad Q = \iint_A \tau_{22}^\pm \Omega dA \quad \text{for } m=1,2,\dots \quad (3.90)$$

CHAPTER 4

ANALYSIS OF BONDED ELASTIC LAYERS USING THE NEW FORMULATION

The governing equations given in the previous chapter constitute the most general equations derived for a bonded elastic layer with any arbitrary shape. The formulation can easily be applied to a layer of any symmetrical shape to analyze its behavior under its basic deformation modes. In this chapter, the application of the formulation is demonstrated for bonded elastic layers with different cross sectional shapes and/or under different loadings.

The new formulation presented in the previous chapter is first applied to infinite-strip (IS) shaped elastic layers bonded to rigid surfaces. For each deformation mode, the governing equations are solved for the displacements, from which closed form expressions for the displacement/stress distributions and the relevant modulus are derived. The theory is then applied to elastic discs bonded to rigid reinforcements under uniform compression. By solving the governing equations for both circular (C) and hollow circular (HC) shaped layers, closed form expressions are derived for the compression modulus and displacement/stress distributions in a bonded elastic disc with and without a central hole.

The capability of the formulation in analyzing the behavior of bonded elastic layers even when the bonded surfaces are not rigid is also shown by applying the formulation to IS-shaped elastic layers bonded to extensible reinforcements. For each deformation mode, closed form expressions are derived, for this case, for the displacement/stress distributions and relevant modulus.

4.1 ANALYTICAL SOLUTIONS FOR ELASTIC LAYERS BONDED TO RIGID SURFACES

4.1.1 Bonded Elastic Strips

In the analyses presented in this section, it is assumed that the length of the bonded rectangular layer is much longer than its width ($2w$) and thickness (t). Thus, this layer may be approximated by an IS-shaped bonded elastic layer in a state of plane strain. When the centerline of the strip is taken to coincide with x_3 axis, one has $u_3=0$. Moreover, the nonzero displacements are independent of x_3 ; i.e., $u_1=u_1(x_1, x_2)$, $u_2=u_2(x_1, x_2)$. The compression problem is solved by using both zeroth and first order theories. After showing that the zeroth order theory indeed results in the same solutions obtained in literature by the formulations which “average” the variables through the layer thickness, the bending and apparent shear problems are solved by using only the first order theory.

4.1.1.1 Uniform Compression

4.1.1.1.1 Solution for Zeroth Order Theory

For the zeroth order theory ($m=0$, $p=0$ and $p'=-1$), the weighted equilibrium equation in x_2 direction (third of Eqs. (3.21)) is trivially satisfied. In view of Eq. (3.22) and Table 3.1 and Table 3.2 for $m=0$, the weighted form of the equilibrium equation in x_1 direction (first of Eqs. (3.21)) becomes

$$\partial_{11}u_1^0 - \beta_{10}^2 u_1^0 = 0 \quad \text{with} \quad \beta_{10}^2 = \frac{12\mu}{\alpha t^2} \quad (4.1)$$

Since u_1 is antisymmetric about $x_1=0$, the solution of Eq. (4.1) for u_1^0 is

$$u_1^0 = a_{10} \sinh(\beta_{10} x_1) \quad (4.2)$$

where a_{10} is an integration constant which can be determined from the traction-free boundary conditions $\tau_{12}^0|_{x_1=\pm w} = 0$ and $\tau_{11}^0|_{x_1=\pm w} = 0$ at the lateral boundary. While the first condition is trivially satisfied, the second condition requires

$$\left[\partial_1 u_1^0 \right]_{x_1=\pm w} = \frac{\lambda \Delta}{\alpha t} \quad (4.3)$$

which leads to

$$a_{10} = \frac{\lambda \Delta}{\alpha t} \frac{1}{\beta_{10} \cosh(\beta_{10} w)} \quad (4.4)$$

Then, the displacements u_i ($i=1,2$) and the effective compression modulus E_c can be computed from the first of Eqs.(3.60) and Eq. (3.61), in view of the first of Eqs. (3.64) and (3.65), as

$$u_1 = \frac{3 \Delta \lambda}{2 t \alpha \beta_{10}} \frac{\sinh(\beta_{10} x_1)}{\cosh(\beta_{10} w)} \left(1 - \frac{4x_2^2}{t^2} \right), \quad u_2 = -\frac{\Delta}{t} x_2 \quad (4.5)$$

$$E_c = \alpha - \frac{\lambda^2 \tanh(\beta_{10} w)}{\alpha (\beta_{10} w)}$$

It is noteworthy that the effect of compressibility is naturally included in the formulation. The above expressions clearly indicate that the zeroth order theory, which is the lowest order theory, simply corresponds to the averaging the field variables and equations over the layer thickness. Therefore, for the compression modulus, it gives the same expression obtained by Tsai and Lee [30] (Eq. (2.31)). In addition, the selection of polynomial functions as the distribution functions leads to a parabolic bulging shape in the zeroth order theory.

4.1.1.1.2 Solution for First Order Theory

In the first order theory ($m=1$, $p=0$ and $p'=1$), the governing equations should be analyzed both for $n=0$ and $n=1$, separately. It may be seen that, for $n=0$, the governing equations for the first order theory are identical to those derived for the zeroth order theory. That is, the expression obtained for u_1^0 remains unchanged and Eqs. (4.2) and (4.4) are still valid. Considering Eq. (3.22) and Table 3.1 and Table 3.2 for the first order theory and recalling from the zeroth order theory that

$$\tau_{22}^0 = \lambda \partial_1 u_1^0 - \frac{\alpha \Delta}{t} \quad (4.6)$$

the additional variable u_2^1 can be obtained from the solution of the nontrivial equilibrium equation in x_2 direction for $n=1$ (third of Eqs. (3.21)), that is, from

$$\mu(\partial_{11}u_2^1 - \frac{60\alpha}{\mu t^2}u_2^1) - \frac{2}{t}(\lambda + \mu)(\partial_1u_1^0) - \frac{10\alpha\Delta}{\mu t^2} = 0 \quad (4.7)$$

Necessary boundary condition for the solution of the above equation comes from the nontrivial boundary condition that $\tau_{12}^1|_{x_1=\pm w} = 0$, which yields

$$[\partial_1u_2^1]_{x_1=\pm w} = \frac{2}{t} [u_1^0]_{x_1=\pm w} \quad (4.8)$$

Substituting Eqs. (4.2) and (4.4) into Eqs. (4.7) and (4.8), one gets the following governing equation and boundary condition for u_2^1 :

$$\partial_{11}u_2^1 - \beta_{21}^2u_2^1 = \frac{2}{t} \frac{\lambda + \mu}{\mu} \frac{\lambda}{\alpha} \frac{\Delta}{t} \frac{\cosh(\beta_{10}x_1)}{\cosh(\beta_{10}w)} + \frac{10\alpha\Delta}{\mu t^2} \quad (4.9)$$

with

$$[\partial_1u_2^1]_{x_1=\pm w} = \pm \frac{2}{t} \frac{\lambda}{\alpha} \frac{\Delta}{t} \frac{\tanh(\beta_{10}w)}{\beta_{10}} \quad (4.10)$$

where

$$\beta_{10}^2 = \frac{12\mu}{\alpha t^2}, \quad \beta_{21}^2 = \frac{60\alpha}{\mu t^2} \quad (4.11)$$

The solution of Eq. (4.9) for u_2^1 subject to the boundary condition in Eq. (4.10) is

$$u_2^1 = a_{21} \cosh(\beta_{21}x_1) + \frac{2}{t} \frac{\mu + \lambda}{\mu} \frac{\lambda}{\alpha} \frac{\Delta}{t} \frac{1}{\beta_{10}^2 - \beta_{21}^2} \frac{\cosh(\beta_{10}x_1)}{\cosh(\beta_{10}w)} - \frac{\Delta}{6} \quad (4.12)$$

where the integration constant a_{21} is given by

$$a_{21} = \frac{2}{t} \frac{\lambda}{\alpha} \frac{\Delta}{t} \frac{1}{\beta_{10}\beta_{21}} \frac{\tanh(\beta_{10}w)}{\sinh(\beta_{21}w)} \left[1 - \frac{\mu + \lambda}{\mu} \frac{\beta_{10}^2}{\beta_{10}^2 - \beta_{21}^2} \right] \quad (4.13)$$

Then, the displacement distributions and the effective compression modulus can be obtained through the use of the second of Eqs. (3.60) and Eqs. (3.61) as, in view of the second of Eqs. (3.64) and first of Eqs. (3.65),

$$\begin{aligned}
u_1 &= \frac{3 \Delta \lambda}{2 t \alpha} \frac{\sinh(\beta_{10} x_1)}{\beta_{10} \cosh(\beta_{10} w)} \left(1 - \frac{4x_2^2}{t^2}\right) \\
u_2 &= \left[\begin{aligned} &\frac{30 \lambda \Delta x_2}{t \alpha t t} \left(1 - \frac{4x_2^2}{t^2}\right) \\ &\left\{ \frac{1}{\beta_{10} \beta_{21}} \frac{\tanh(\beta_{10} w)}{\sinh(\beta_{21} w)} \left[1 - \frac{\mu + \lambda}{\mu} \frac{\beta_{10}^2}{\beta_{10}^2 - \beta_{21}^2} \right] \cosh(\beta_{21} x_1) \right\} \\ &+ \frac{\mu + \lambda}{\mu} \frac{1}{\beta_{10}^2 - \beta_{21}^2} \frac{\cosh(\beta_{10} x_1)}{\cosh(\beta_{10} w)} \\ &-\frac{\Delta}{t} x_2 \end{aligned} \right] \quad (4.14) \\
E_c &= \alpha - \frac{\lambda^2 \tanh(\beta_{10} w)}{\alpha (\beta_{10} w)}
\end{aligned}$$

When the solutions in Eqs. (4.14) obtained by the first order theory are compared with those derived from the zeroth order theory (Eqs. (4.5)), it may be seen that increasing the order of the theory from zero to one eliminates the common assumption used in literature, namely, plane horizontal section remains plane during deformation. On the other hand, parabolic bulging assumption is still included in the resulting expressions.

4.1.1.2 Pure Bending

For the bending problem, in view of Eqs. (3.15) and (3.27), the first order theory has two nontrivial equations for the two unknown weighted displacements, u_1^0 and u_2^1 . The first equation comes from the first of Eqs. (3.27) with $n=0$, which reduces to the following governing equation for u_1^0 , in view of Eq. (3.22) and Table 3.1 and Table 3.2 for $m=1$,

$$\partial_{11} u_1^0 - \beta_{10}^2 u_1^0 = -\frac{\lambda + \mu \phi}{\alpha} \frac{\phi}{t} \quad \text{where} \quad \beta_{10}^2 = \frac{12\mu}{\alpha t^2} \quad (4.15)$$

Necessary boundary condition for the solution of Eq. (4.15) for u_1^0 is: $\tau_{11}^0 \Big|_{x_1=\pm w} = 0$, which requires

$$\left[\partial_1 u_1^0 \right]_{x_1=\pm w} = -\frac{\lambda \phi}{\alpha t} (\pm w) \quad (4.16)$$

Then, one has, for u_1^0 ,

$$u_1^0 = -\frac{\lambda \phi}{\alpha t} \frac{w \cosh(\beta_{10} x_1)}{\beta_{10} \sinh(\beta_{10} w)} + \frac{\mu + \lambda}{12\mu} \phi t \quad (4.17)$$

The second equation for u_2^1 comes from the third of Eqs. (3.27) for $n=1$. Considering Eq. (3.22) and Table 3.1 and Table 3.2 for $m=1$, the second of Eqs. (3.26) for $n=0$, and Eq. (4.17) for u_1^0 , the equation for u_2^1 reduces to

$$\partial_{11} u_2^1 - \beta_{21}^2 u_2^1 = -\frac{2}{t} \frac{\lambda + \mu}{\mu} \frac{\lambda \phi}{\alpha t} \frac{w \sinh(\beta_{10} x_1)}{\sinh(\beta_{10} w)} - \frac{10\alpha}{\mu t^2} \phi x_1 \quad \text{with} \quad \beta_{21}^2 = \frac{60\alpha}{\mu t^2} \quad (4.18)$$

Nontrivial boundary condition at the lateral sides: $\tau_{12}^1 \Big|_{x_1=\pm w} = 0$ yields

$$\left[\partial_1 u_2^1 \right]_{x_1=\pm w} = -\frac{2}{t} \frac{\lambda \phi}{\alpha t} \frac{w}{\beta_{10} \tanh(\beta_{10} w)} + \frac{\mu + \lambda}{6\mu} \phi \quad (4.19)$$

Using this boundary condition, u_2^1 may be determined as

$$u_2^1 = a_{22} \sinh(\beta_{21} x_1) - \frac{2}{t} \frac{\mu + \lambda}{\mu} \frac{\lambda \phi}{\alpha t} \frac{1}{\beta_{10}^2 - \beta_{21}^2} \frac{w \sinh(\beta_{10} x_1)}{\sinh(\beta_{10} w)} + \frac{\phi}{6} x_1 \quad (4.20)$$

where the constant a_{22} is given by

$$a_{22} = \left\{ \begin{array}{l} -\frac{2}{t} \frac{\lambda \phi}{\alpha t} \frac{w}{\beta_{10} \beta_{21} \cosh(\beta_{21} w)} \left[1 - \frac{\mu + \lambda}{\mu} \frac{\beta_{10}^2}{\beta_{10}^2 - \beta_{21}^2} \right] \\ + \frac{\phi \lambda}{6 \mu \beta_{21} \cosh(\beta_{21} w)} \end{array} \right\} \quad (4.21)$$

Then, the displacement components u_i and the effective bending modulus E_b may be obtained from the second of Eqs. (3.60) and Eqs. (3.62) as, in view of the second of Eqs. (3.64) and first of Eqs.(3.65),

$$\begin{aligned}
u_1 &= \left[-\frac{3}{2} \frac{\lambda \phi}{\alpha t} \frac{w \cosh(\beta_{10} x_1)}{\beta_{10} \sinh(\beta_{10} w)} + \frac{\mu + \lambda}{8\mu} \phi t \right] \left(1 - \frac{4x_2^2}{t^2}\right) \\
u_2 &= \left\{ \begin{aligned} &\frac{x_2}{t} \left(1 - \frac{4x_2^2}{t^2}\right) \\ &\left(-\frac{30}{t} \frac{\lambda \phi}{\alpha t} \frac{w}{\beta_{10} \beta_{21}} \frac{\coth(\beta_{10} w)}{\cosh(\beta_{21} w)} \left[1 - \frac{\mu + \lambda}{\mu} \frac{\beta_{10}^2}{\beta_{10}^2 - \beta_{21}^2} \right] \sinh(\beta_{21} x_1) \right. \\ &\quad \left. + \frac{5\phi \lambda}{2} \frac{\sinh(\beta_{21} x_1)}{\mu \beta_{21} \cosh(\beta_{21} w)} - \frac{30}{t} \frac{\lambda \phi}{\alpha t} \frac{\mu + \lambda}{\mu} \frac{w}{\beta_{10}^2 - \beta_{21}^2} \frac{\sinh(\beta_{10} x_1)}{\sinh(\beta_{10} w)} \right) \\ &\quad \left. - \frac{\phi}{t} x_1 x_2 \right\} \quad (4.22) \\
E_b &= \alpha - \frac{15\lambda\alpha}{\mu} \left\{ \begin{aligned} &\frac{\mu + \lambda}{\mu} \frac{\beta_{10}^2}{\beta_{10}^2 - \beta_{21}^2} \left[\frac{1}{(\beta_{10} w)^2} \left(1 - \frac{\beta_{10} w}{\tanh(\beta_{10} w)}\right) + \right. \\ &\quad \left. \frac{1}{(\beta_{21} w)^2} \frac{\beta_{10} w}{\tanh(\beta_{10} w)} \left(1 - \frac{\tanh(\beta_{21} w)}{\beta_{21} w}\right) \right] \\ &\quad \left. + \frac{1}{(\beta_{21} w)^2} \left(1 - \frac{\beta_{10} w}{\tanh(\beta_{10} w)}\right) \left(1 - \frac{\tanh(\beta_{21} w)}{\beta_{21} w}\right) \right\}
\end{aligned} \right.
\end{aligned}$$

4.1.1.3 Apparent Shear

When the first order theory is applied to the apparent shear problem, one has, in view of Eqs. (3.30), two unknown weighted displacements: u_2^0 and u_1^1 . The governing equation for u_2^0 comes from the third of Eqs. (3.32) for $n=0$, which, in view of Eq. (3.22) and Table 3.1 and Table 3.2 for $m=1$, simplifies to

$$\partial_{11} u_2^0 - \beta_{20}^2 u_2^0 = 0 \quad \text{where} \quad \beta_{20}^2 = \frac{12\alpha}{\mu t^2} \quad (4.23)$$

From the nontrivial boundary condition $\tau_{12}^0|_{x_1=\pm w} = 0$, one also has

$$\left[\partial_1 u_2^0 \right]_{x_1=\pm w} = -\frac{\delta}{t} \quad (4.24)$$

Thus, u_2^0 can be obtained as, through the solution of Eq. (4.23) for becomes u_2^0 in view of the boundary conditions in Eq. (4.24),

$$u_2^0 = -\frac{\delta}{t} \frac{\sinh(\beta_{20}x_1)}{\beta_{20} \cosh(\beta_{20}w)} \quad (4.25)$$

For $n=1$, only nontrivial equation is the first of Eqs. (3.32). Considering Eq. (3.22) and the coefficients in Table 3.1 and Table 3.2 for $m=1$, the second of Eqs. (3.31) for $n=0$, and Eq. (4.25) for u_2^0 , the governing equation for u_1^1 is obtained as

$$\partial_{11}u_1^1 - \beta_{11}^2 u_1^1 = -\frac{2}{t} \frac{\lambda + \mu}{\alpha} \frac{\delta}{t} \frac{\cosh(\beta_{20}x_1)}{\cosh(\beta_{20}w)} - \frac{10\mu}{\alpha t^2} \delta \quad \text{with} \quad \beta_{11}^2 = \frac{60\mu}{\alpha t^2} \quad (4.26)$$

The boundary condition at the lateral sides: $\tau_{11}^1|_{x_1=\pm w} = 0$ requires

$$\left[\partial_1 u_1^1 \right]_{x_1=\pm w} = -\frac{2}{t} \frac{\lambda}{\alpha} \frac{\delta}{t} \frac{\tanh(\beta_{20}w)}{\beta_{20}} \quad (4.27)$$

Then, one obtains u_1^1 as

$$u_1^1 = a_{11} \cosh(\beta_{11}x_1) - \frac{2}{t} \frac{\mu + \lambda}{\alpha} \frac{\delta}{t} \frac{1}{\beta_{20}^2 - \beta_{11}^2} \frac{\cosh(\beta_{20}x_1)}{\cosh(\beta_{20}w)} + \frac{\delta}{6} \quad (4.28)$$

where

$$a_{11} = -\frac{2}{t} \frac{\lambda}{\alpha} \frac{\delta}{t} \frac{1}{\beta_{11}\beta_{20}} \frac{\tanh(\beta_{20}w)}{\sinh(\beta_{11}w)} \left[1 - \frac{\mu + \lambda}{\lambda} \frac{\beta_{20}^2}{\beta_{20}^2 - \beta_{11}^2} \right] \quad (4.29)$$

Consequently, the displacement components u_i and the apparent shear modulus μ_a are evaluated from the second of Eqs. (3.60) and Eqs.(3.63), in view of the second of Eqs. (3.64) and (3.65), as

$$u_1 = \left(\begin{array}{l} -\frac{30}{t} \frac{\lambda}{\alpha} \frac{\delta}{t} \frac{\tanh(\beta_{20}w)}{\beta_{11}\beta_{20}} \frac{\cosh(\beta_{11}x_1)}{\sinh(\beta_{11}w)} \left[1 - \frac{\mu + \lambda}{\lambda} \frac{\beta_{20}^2}{\beta_{20}^2 - \beta_{11}^2} \right] \\ -\frac{30}{t} \frac{\mu + \lambda}{\alpha} \frac{\delta}{t} \frac{1}{\beta_{20}^2 - \beta_{11}^2} \frac{\cosh(\beta_{20}x_1)}{\cosh(\beta_{20}w)} \end{array} \right) \frac{x_2}{t} \left(1 - \frac{4x_2^2}{t^2} \right) + \frac{\delta}{t} x_2 \quad (4.30)$$

$$u_2 = \left[-\frac{3}{2} \frac{\delta}{t} \frac{\sinh(\beta_{20}x_1)}{\beta_{20} \cosh(\beta_{20}w)} \right] \left(1 - \frac{4x_2^2}{t^2} \right)$$

$$\mu_a = \mu \left[1 - \frac{\tanh(\beta_{20}w)}{(\beta_{20}w)} \right]$$

4.1.2 Bonded Elastic Discs

4.1.2.1 Uniform Compression

Figure 4.1a and Figure 4.1c show the undeformed configurations of a bonded disc of thickness t and radius R respectively in the absence and presence of a central hole of radius a . When compressed by the amount Δ by a uniaxial compressive force P , the bonded discs have the deformed shapes illustrated in Figure 4.1b and Figure 4.1d, respectively.

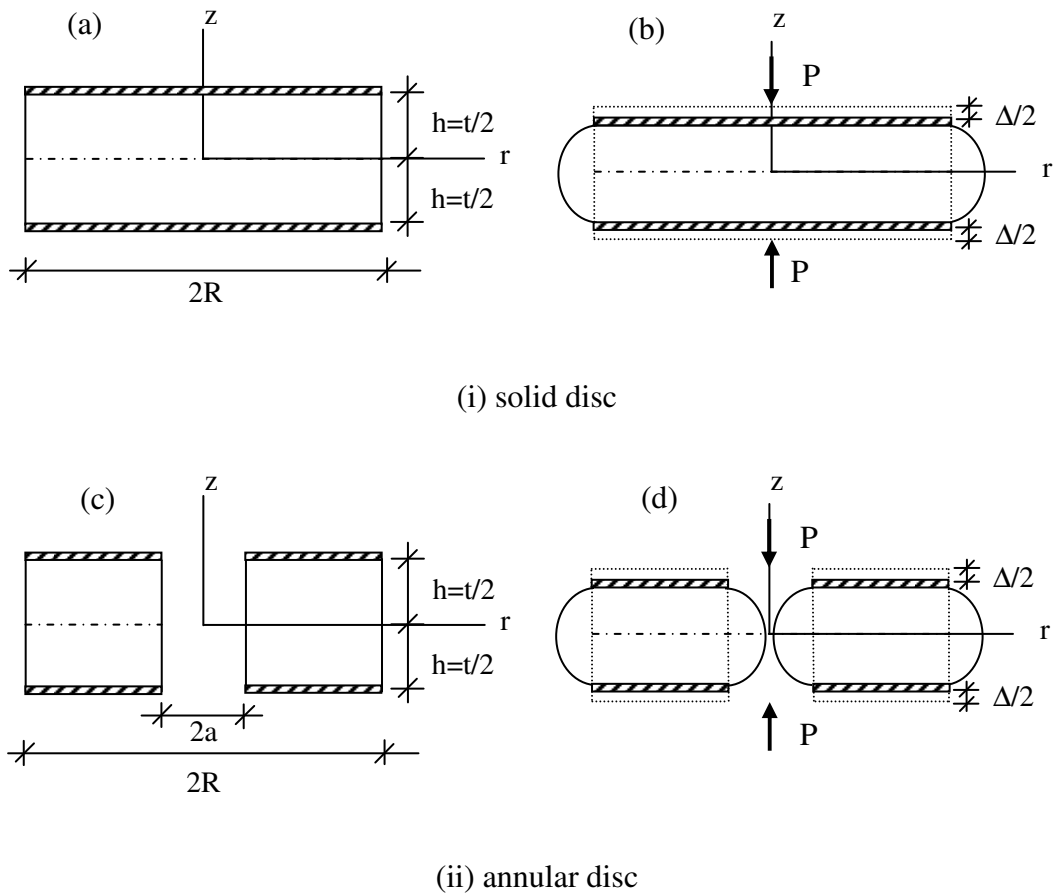


Figure 4.1 Undeformed and deformed configurations of a bonded disc (i) without and (ii) with a central hole under uniform compression

It can be recalled from Section 3.2.2.1, Eqs. (3.47) with Eqs. (3.45) and (3.48) constitute the reduced governing equations for the problem of uniform compression of bonded elastic discs for any order of the theory. The presence of a central hole does not change these equations but influences the solutions through the boundary conditions. For the solution of the differential equations given in Eqs. (3.47), necessary boundary conditions are the traction-free boundary conditions at the lateral bulge-free surfaces, which can be formulated as

$$\tau_{rr}^n \Big|_{r=r^*} = 0 \quad \text{for even } n \quad \text{and} \quad \tau_{rz}^n \Big|_{r=r^*} = 0 \quad \text{for odd } n$$

$$\text{where } r^* = \begin{cases} R & \text{for solid sections} \\ a, R & \text{for hollow sections} \end{cases} \quad (4.31)$$

which are still not sufficient to obtain solutions for the solid sections. For C-shaped layers, the additional conditions come from the fact that displacements must be finite at the centroid, i.e., at $r=0$.

4.1.2.1.1 Solid Circular Sections

If the compression problem for the bonded solid disc illustrated in Figure 4.1a-b is formulated using the first order theory ($m=1$, $p=0$ and $p'=1$), in view of Eqs. (3.41), there will be two nonzero weighted displacements, u_r^0 and u_z^1 , which can be determined by solving Eqs. (3.47) for both $n=0$ and $n=1$.

For $n=0$, the first of Eqs. (3.47) directly provides the governing equation for u_r^0 . Using the relation given in Eq. (3.48) and the coefficients in Table 3.1 and Table 3.2 for $m=1$, this equation can be simplified as

$$\partial_{rr} u_r^0 + \frac{1}{r} \partial_r u_r^0 - \left(\frac{1}{r^2} + \beta_{r0}^2 \right) u_r^0 = 0 \quad \text{where} \quad \beta_{r0}^2 = \frac{12\mu}{\alpha t^2} \quad (4.32)$$

the solution of which is in the form:

$$u_r^0 = a_{r0} I_1(\beta_{r0} r) + a_{r1} K_1(\beta_{r0} r) \quad (4.33)$$

where a_{r0} and a_{r1} are constants to be determined from the boundary conditions, and, I_1 and K_1 represent the modified Bessel functions of first and second kind of order

one, respectively. As already mentioned, for a solid circular section, u_r^0 must be finite at $r=0$, which implies that a_{r1} is zero. The other integration constant, a_{r0} , can be obtained from the boundary condition that $\tau_{rr}^0|_{r=R} = 0$. In view of the first of Eqs. (3.45) with $n=0$, this equation requires

$$\left[\partial_r u_r^0 + \frac{\lambda}{\alpha} \frac{u_r^0}{r} \right]_{r=R} = \frac{\lambda \Delta}{\alpha t} \quad (4.34)$$

Then, the constants appearing in Eq. (4.33) would be

$$a_{r0} = \frac{\lambda \Delta}{\alpha t} \frac{1}{\beta_{r0} I_0(\beta_{r0} R) - \frac{2\mu}{\alpha R} I_1(\beta_{r0} R)} \quad \text{and} \quad a_{r1} = 0 \quad (4.35)$$

For $n=1$, the nontrivial equation comes from the weighted equilibrium equation along z direction, i.e., the second of Eqs. (3.47), which simplifies, in view of the coefficients given in Table 3.2, as

$$\mu \partial_{rr} u_z^1 + \frac{\mu}{r} \partial_r u_z^1 - \mu \partial_r \bar{u}_r^1 - \frac{\mu}{r} \bar{u}_r^1 - \frac{60\alpha}{t^2} u_z^1 - \frac{12\alpha}{t^2} \Delta = \bar{\tau}_{zz}^1 \quad (4.36)$$

Considering the relation in Eq. (3.48), and using the third of Eqs. (3.45) with $n=0$, for τ_{zz}^0 , Eq. (4.36) can further be reduced, in view of Table 3.1, to

$$\partial_{rr} u_z^1 + \frac{1}{r} \partial_r u_z^1 - \beta_{z1}^2 u_z^1 = \frac{2}{t} \left(\frac{\lambda + \mu}{\mu} \right) \left[\partial_r u_r^0 + \frac{1}{r} u_r^0 \right] + \frac{10\alpha \Delta}{\mu t^2} \quad \text{where} \quad \beta_{z1}^2 = \frac{60\alpha}{\mu t^2} \quad (4.37)$$

From the the boundary condition at the lateral sides, one has, in view of the second of Eqs. (4.31) for $n=1$, $\tau_{rz}^1|_{r=R} = 0$, which implies

$$\left[\partial_r u_z^1 \right]_{r=R} = \frac{2}{t} \left[u_r^0 \right]_{r=R} \quad (4.38)$$

Finally, substitution of Eq. (4.33) with Eqs. (4.35) into Eqs. (4.37) and (4.38) leads to the following governing equation and boundary condition for u_z^1 :

$$\partial_{rr} u_z^1 + \frac{1}{r} \partial_r u_z^1 - \beta_{z1}^2 u_z^1 = \frac{2}{t} \frac{\lambda + \mu}{\mu} \left[a_{r0} \beta_{r0} I_0(\beta_{r0} r) \right] + \frac{10\alpha \Delta}{\mu t^2} \quad (4.39)$$

with

$$\left[\partial_r u_z^1 \right]_{r=R} = \frac{2a_{r0}}{t} I_1(\beta_{r0}R) \quad (4.40)$$

The solution of Eq. (4.39) subject to the boundary condition in Eq. (4.40) with the condition that u_z^1 must be finite at $r=0$ gives

$$u_z^1 = a_{z1} I_0(\beta_{z1}r) + \frac{2}{t} \frac{\mu + \lambda}{\mu} \frac{\beta_{r0}}{\beta_{r0}^2 - \beta_{z1}^2} a_{r0} I_0(\beta_{r0}r) - \frac{\Delta}{6} \quad (4.41)$$

where

$$a_{z1} = \frac{2a_{r0}}{t} \frac{I_1(\beta_{r0}R)}{\beta_{z1} I_1(\beta_{z1}R)} \left[1 - \frac{\mu + \lambda}{\mu} \frac{\beta_{r0}^2}{\beta_{r0}^2 - \beta_{z1}^2} \right] \quad (4.42)$$

Consequently, u_r and u_z can be determined, as defined in Section 3.2.3, as

$$u_r = \frac{3}{2} a_{r0} I_1(\beta_{r0}r) \left(1 - \frac{4z^2}{t^2} \right) \quad (4.43)$$

$$u_z = \frac{30}{t} a_{r0} \left\{ \begin{array}{l} \frac{I_1(\beta_{r0}R) I_0(\beta_{z1}r)}{\beta_{z1} I_1(\beta_{z1}R)} \left[1 - \frac{\mu + \lambda}{\mu} \frac{\beta_{r0}^2}{\beta_{r0}^2 - \beta_{z1}^2} \right] \\ + I_0(\beta_{r0}r) \frac{\mu + \lambda}{\mu} \frac{\beta_{r0}}{\beta_{r0}^2 - \beta_{z1}^2} \end{array} \right\} \left(\frac{z}{t} \left(1 - \frac{4z^2}{t^2} \right) - \Delta \frac{z}{t} \right)$$

In addition, using Eqs. (3.61), the second of (3.66) and the first of (3.67), one can obtain the effective compression modulus for bonded elastic discs as

$$E_c = \alpha - \frac{\lambda^2}{\alpha(\beta_{r0}R) \frac{I_0(\beta_{r0}R)}{2I_1(\beta_{r0}R)} - \mu} \quad (4.44)$$

It is to be noted that the first order theory leads to the same expression derived by Tsai and Lee [30] (Eq. (2.32)). Also, it can be verified that this expression is the same as the prediction of the zeroth order theory for E_c . This is also the case for the horizontal displacement. Thus, similar to the strip case, the main contribution of the use of the first order theory in the formulation is to eliminate the commonly used assumption that plane sections remain plane during deformation. Removal of this assumption leads to an improved expression for the axial displacement u_z , which, in turn, improves the stress expressions, enabling one to study the stress distributions over any section of the layer thoroughly.

4.1.2.1.2 Hollow Circular Sections

As already mentioned, the solution of annular discs differs from the solution of solid discs only with regard to the boundary conditions. That is, for the first order theory, the governing equations derived for the unknown weighted displacements u_r^0 and u_z^1 , i.e., Eqs. (4.32) and (4.37), are valid also for the hollow sections; but, in this case, instead of vanishing the weighted displacements at the centroid, one has, in view of Eqs. (4.31), the following two boundary conditions in addition to the ones in Eqs. (4.34) and (4.38):

$$\begin{aligned} \left[\partial_r u_r^0 + \frac{\lambda}{\alpha} \frac{u_r^0}{r} \right]_{r=a} &= \frac{\lambda \Delta}{\alpha t} \\ \left[\partial_r u_z^1 \right]_{r=a} &= \frac{2}{t} \left[u_r^0 \right]_{r=a} \end{aligned} \quad (4.45)$$

From the boundary conditions given in Eq. (4.34) and the first of Eqs. (4.45), the integration constants a_{r0} and a_{r1} appearing in Eq. (4.33) can be determined as

$$a_{r0} = \frac{\lambda \Delta}{t} \frac{A_4 - A_2}{A_1 A_4 - A_2 A_3} \quad \text{and} \quad a_{r1} = \frac{\lambda \Delta}{t} \frac{A_3 - A_1}{A_1 A_4 - A_2 A_3} \quad (4.46)$$

where

$$\begin{aligned} A_1 &= \alpha \beta_{r0} I_0(\beta_{r0} R) - 2\mu \frac{I_1(\beta_{r0} R)}{R} \\ A_2 &= \alpha \beta_{r0} K_0(\beta_{r0} R) + 2\mu \frac{K_1(\beta_{r0} R)}{R} \\ A_3 &= \alpha \beta_{r0} I_0(\beta_{r0} a) - 2\mu \frac{I_1(\beta_{r0} a)}{a} \\ A_4 &= \alpha \beta_{r0} K_0(\beta_{r0} a) + 2\mu \frac{K_1(\beta_{r0} a)}{a} \end{aligned} \quad (4.47)$$

Substitution of Eq. (4.33) with Eqs. (4.46) into Eqs. (4.37), (4.38) and the second of Eqs. (4.45) gives the following governing equation and the boundary conditions for u_z^1 for the case of hollow circular sections:

$$\partial_{rr} u_z^1 + \frac{1}{r} \partial_r u_z^1 - \beta_{z1}^2 u_z^1 = \frac{2}{t} \frac{\lambda + \mu}{\mu} [a_{r0} \beta_{r0} I_0(\beta_{r0} r) - a_{r1} \beta_{r0} K_0(\beta_{r0} r)] + \frac{10\alpha \Delta}{\mu t^2} \quad (4.48)$$

with

$$\begin{aligned} \left[\partial_r u_z^1 \right]_{r=R} &= \frac{2}{t} [a_{r0} I_1(\beta_{r0} R) + a_{r1} K_1(\beta_{r0} R)] \\ \left[\partial_r u_z^1 \right]_{r=a} &= \frac{2}{t} [a_{r0} I_1(\beta_{r0} a) + a_{r1} K_1(\beta_{r0} a)] \end{aligned} \quad (4.49)$$

By solving Eq. (4.48) with the conditions given in Eqs. (4.49), one can obtain u_z^1 as

$$u_z^1 = a_{z1} I_0(\beta_{z1} r) + a_{z2} K_0(\beta_{z1} r) + B [a_{r0} I_0(\beta_{r0} r) - a_{r1} K_0(\beta_{r0} r)] - \frac{\Delta}{6} \quad (4.50)$$

where

$$B = \frac{2}{t} \frac{\mu + \lambda}{\mu} \frac{\beta_{r0}}{\beta_{r0}^2 - \beta_{z1}^2} \quad (4.51)$$

and

$$\begin{aligned} a_{z1} &= \frac{C_1 K_1(\beta_{z1} a) - C_2 K_1(\beta_{z1} R)}{\beta_{z1} [I_1(\beta_{z1} R) K_1(\beta_{z1} a) - I_1(\beta_{z1} a) K_1(\beta_{z1} R)]} \\ a_{z2} &= \frac{C_1 I_1(\beta_{z1} a) - C_2 I_1(\beta_{z1} R)}{\beta_{z1} [I_1(\beta_{z1} R) K_1(\beta_{z1} a) - I_1(\beta_{z1} a) K_1(\beta_{z1} R)]} \end{aligned} \quad (4.52)$$

with

$$\begin{aligned} C_1 &= [a_{r0} I_1(\beta_{r0} R) + a_{r1} K_1(\beta_{r0} R)] \times \left[\frac{2}{t} - B \beta_{r0} \right] \\ C_2 &= [a_{r0} I_1(\beta_{r0} a) + a_{r1} K_1(\beta_{r0} a)] \times \left[\frac{2}{t} - B \beta_{r0} \right] \end{aligned} \quad (4.53)$$

Then, the displacements u_r and u_z for bonded annular discs subject to uniform compression become

$$\begin{aligned} u_r &= \frac{3}{2} [a_{r0} I_1(\beta_{r0} r) + a_{r1} K_1(\beta_{r0} r)] \left(1 - \frac{4z^2}{t^2} \right) \\ u_z &= 15 \left\{ \begin{aligned} &a_{z1} I_0(\beta_{z1} r) + a_{z2} K_0(\beta_{z1} r) \\ &+ B [a_{r0} I_0(\beta_{r0} r) - a_{r1} K_0(\beta_{r0} r)] \end{aligned} \right\} \left(\frac{z}{t} \right) \left(1 - \frac{4z^2}{t^2} \right) - \Delta \frac{z}{t} \end{aligned} \quad (4.54)$$

Substituting the expression for u_z^1 in the first of Eqs. (3.67) and then using the second of Eqs. (3.66) and Eqs. (3.61), E_c for a bonded disc with a central circular hole can be determined as

$$E_c = \alpha - \frac{2\lambda}{\frac{\Delta}{t}(R^2 - a^2)} \left\{ \begin{array}{l} a_{r0} [RI_1(\beta_{r0}R) - aI_1(\beta_{r0}a)] \\ -a_{r1} [RK_1(\beta_{r0}R) - aK_1(\beta_{r0}a)] \end{array} \right\} \quad (4.55)$$

It can be shown that the above expression for E_c is identical to the expression predicted by the zeroth order theory. However, it may be noted that, similar to the solid case, the first order theory removes the assumption that plane sections remain plane and leads to improved expressions for the axial displacement, in turn, for the stress distributions.

4.2 ANALYTICAL SOLUTIONS FOR ELASTIC LAYERS BONDED TO FLEXIBLE REINFORCEMENTS

4.2.1 Bonded Elastic Strips

As discussed in Section 4.1.1, a bonded elastic layer whose length is much larger than its width ($2w$) and thickness (t) can be approximated as an IS-shaped bonded elastic layer in a state of plane strain. Thus, for an elastic strip bonded to flexible reinforcements, the displacement along the “infinite” length of the layer vanishes, i.e., $u_3=0$, implying that $u_3^\pm = 0$. Moreover, the nonzero displacements u_1 , u_2 and the stretching of the reinforcements in the direction of finite length of the layer u_1^\pm are independent of x_3 , i.e., $u_1=u_1(x_1, x_2)$, $u_2=u_2(x_1, x_2)$ and $u_1^\pm = u_1^\pm(x_1)$.

As in the case of rigidly-bonded layers, only the compression problem is solved by using both the zeroth and first order theories. After showing that the zeroth order theory results in the same solutions obtained in literature by the formulations which “average” the variables through the layer thickness, the bending and warping problems are solved by using only the first order theory.

4.2.1.1 Uniform Compression

4.2.1.1.1 Solution for Zeroth Order Theory

When the zeroth order theory ($m=0$, $p=0$ and $p'=-1$) is applied to the compression problem, one has, in view of Eqs. (3.15) and (3.68), two unknown

displacements: one weighted displacement u_1^0 and one face displacement u_1^+ . The first equation for these two unknowns comes from the first of Eqs. (3.73), which in view of Eq. (3.22) and Table 3.1 and Table 3.2 for $m=0$, can be simplified as

$$\partial_{11}u_1^0 - \beta_{10}^2 [u_1^0 - u_1^+] = 0 \quad \text{where} \quad \beta_{10}^2 = \frac{12\mu}{\alpha t^2} \quad (4.56)$$

The equilibrium of the forces in the reinforcing sheet in x_1 direction generates the second equation for the unknown displacements. Thus, from the first of Eqs. (3.77), in view of Table 3.2, one has

$$\partial_{11}u_1^+ - \beta_{11}^2 [u_1^+ - u_1^0] = 0 \quad \text{where} \quad \beta_{11}^2 = \frac{12\mu}{k_f t} \quad (4.57)$$

From Eqs. (4.56), it is clear that

$$[u_1^0 - u_1^+] = -\frac{1}{\beta_{10}^2} \partial_{11}u_1^0 \quad (4.58)$$

Substituting Eq. (4.58) into Eq. (4.57), one obtains

$$\partial_{11}u_1^+ = -\frac{\beta_{11}^2}{\beta_{10}^2} \partial_{11}u_1^0 \quad (4.59)$$

whose solution can be written, in view of that the horizontal displacement u_1 is antisymmetric about $x_1=0$, in the form of

$$u_1^+ = -\frac{\beta_{11}^2}{\beta_{10}^2} u_1^0 + d_1 x_1 \quad (4.60)$$

where d_1 is an integration constant to be determined from the boundary conditions. Substitution of Eq. (4.60) into Eq. (4.56) gives the following differential equation for the unknown weighted displacement u_1^0 :

$$\partial_{11}u_1^0 - \beta_1^2 u_1^0 = -\beta_{10}^2 d_1 x_1 \quad \text{where} \quad \beta_1^2 = \beta_{10}^2 + \beta_{11}^2 \quad (4.61)$$

When Eq. (4.61) is solved for u_1^0 and then the solution is substituted into Eq. (4.60) to determine u_1^+ , the following expressions are obtained for the unknown displacements in terms of the two integration constants d_1 and a_{10} :

$$\begin{aligned}
u_1^0 &= a_{10} \sinh(\beta_1 x_1) + \frac{\beta_{10}^2}{\beta_{11}^2} d_1 x_1 \\
u_1^+ &= -\frac{\beta_{11}^2}{\beta_{10}^2} a_{10} \sinh(\beta_1 x_1) + \frac{\beta_{10}^2}{\beta_{11}^2} d_1 x_1
\end{aligned} \tag{4.62}$$

Noting that the force displacement relations given in Eqs. (3.75) reduce, for the simple strip case, to a single equality: $N_{11} = k_f (\partial_1 u_1^+)$, the constants d_1 and a_{10} can be related by using the force-free boundary condition at the edges of the reinforcement, i.e., by the condition $N_{11}|_{x_1=\pm w} = 0$, as

$$d_1 = a_{10} \frac{\beta_{11}^2 \beta_1^3}{\beta_{10}^4} \cosh(\beta_1 w) \tag{4.63}$$

The second condition for the determination of the unknown constants comes from the stress-free boundary conditions at the lateral faces of the layer. While the condition that $\tau_{12}^0|_{x_1=\pm w} = 0$ is satisfied trivially, the condition that $\tau_{11}^0|_{x_1=\pm w} = 0$ implies, in view of the first of Eqs. (3.72) with $n=0$,

$$\left[\partial_1 u_1^0 \right]_{x_1=\pm w} = \frac{\lambda \Delta}{\alpha t} \tag{4.64}$$

which leads to

$$a_{10} = \frac{\lambda \Delta \beta_{10}^2}{\alpha t \beta_1^2} \frac{1}{\cosh(\beta_1 w)} \tag{4.65}$$

Thus, the unknown displacements u_1^0 and u_1^+ can be expressed as

$$\begin{aligned}
u_1^0 &= \frac{\lambda \Delta \beta_{11}^2}{\alpha t \beta_1^2} \left[x_1 + \frac{\beta_{10}^2}{\beta_{11}^2} \frac{\sinh(\beta_1 x_1)}{\beta_1 \cosh(\beta_1 w)} \right] \\
u_1^+ &= \frac{\lambda \Delta \beta_{11}^2}{\alpha t \beta_1^2} \left[x_1 - \frac{\sinh(\beta_1 x_1)}{\beta_1 \cosh(\beta_1 w)} \right]
\end{aligned} \tag{4.66}$$

Then, the displacements u_i ($i=1,2$) can be computed from the first of Eqs. (3.60) as

$$u_1 = \left\{ \begin{array}{l} \frac{3}{2} \frac{\Delta}{t} \frac{\lambda}{\alpha} \frac{\beta_{11}^2}{\beta_1^2} \left[x_1 + \frac{\beta_{10}^2}{\beta_{11}^2} \frac{\sinh(\beta_1 x_1)}{\beta_1 \cosh(\beta_1 w)} \right] \left(1 - \frac{4x_2^2}{t^2} \right) \\ + \frac{\Delta}{t} \frac{\lambda}{\alpha} \frac{\beta_{11}^2}{\beta_1^2} \left[x_1 - \frac{\sinh(\beta_1 x_1)}{\beta_1 \cosh(\beta_1 w)} \right] \left(\frac{6x_2^2}{t^2} - \frac{1}{2} \right) \end{array} \right\} \quad (4.67)$$

$$u_2 = -\frac{\Delta}{t} x_2$$

The first of Eqs. (4.67) can be further simplified as

$$u_1 = \frac{3}{2} \frac{\Delta}{t} \frac{\lambda}{\alpha} \frac{\sinh(\beta_1 x_1)}{\beta_1 \cosh(\beta_1 w)} \left(1 - \frac{4x_2^2}{t^2} \right) + \frac{\Delta}{t} \frac{\lambda}{\alpha} \frac{\beta_{11}^2}{\beta_1^2} \left(x_1 - \frac{\sinh(\beta_1 x_1)}{\beta_1 \cosh(\beta_1 w)} \right) \quad (4.68)$$

Realizing that the second term on the right hand side of Eq. (4.68) equals u_1^+ (refer to the second of Eqs. (4.66)), one, thus, has

$$u_1 = \frac{3}{2} \frac{\Delta}{t} \frac{\lambda}{\alpha} \frac{\sinh(\beta_1 x_1)}{\beta_1 \cosh(\beta_1 w)} \left(1 - \frac{4x_2^2}{t^2} \right) + u_1^+ \quad (4.69)$$

When Eq. (4.69) and the second of Eqs. (4.67) are compared with the first and second of Eqs. (4.5), it can be concluded that the reinforcement flexibility mainly affects the horizontal displacement of the layer. An additional displacement term appears in u_1 expression. In fact, this term simply equals to the extension of the reinforcement due to the tension generated by the shear stresses developed at the bonded faces of the layer. It may also be noted that this additional term is independent of x_2 . In other words, it is constant through the layer thickness.

It is worth noting that the inclusion of the effect of the reinforcement flexibility in the expression for the horizontal displacement through an additional term which is constant over the layer thickness is *not* an initial *assumption* used in the formulation; it is the *conclusion* drawn when the formulation is applied by using the zeroth order theory and by selecting polynomial functions as the distribution functions. On the other hand, as it can easily be recalled from Section 2.2.1, this was an initial assumption on the displacement field of the layer in the formulations of Kelly [10] or Tsai [48]. Keeping in mind that the zeroth order theory simply corresponds to averaging the field variables and equations over the layer thickness,

as roughly done in these studies, it can be deduced that this assumption seems to be as realistic as the parabolic bulging assumption.

From the comparison of Eq. (4.69) with the first of Eqs. (4.5), it can also be seen that the appearance of the second term, u_1^+ in Eq. (4.69), is not the only change in the expression of the horizontal displacement in the flexible-reinforcement case. To include the effect of the reinforcement flexibility properly, it is also necessary to replace the parameter β_{10} by $\beta_1 = \sqrt{\beta_{10}^2 + \beta_{11}^2}$, where β_{11} depends on geometrical and material properties of both the layer (μ, t) and the reinforcing sheets (E_f, ν_f, t_f).

After deriving the displacement distributions, it is not difficult to derive the effective compression modulus for the layer. Using Eqs. (3.61), with the first of Eqs. (3.64) and Eq. (3.88), one can obtain the following closed-form expression for the compression modulus E_c :

$$E_c = \alpha - \frac{\lambda^2 \beta_{10}^2 \tanh(\beta_1 w)}{\alpha \beta_1^2 (\beta_1 w)} - \frac{\lambda^2 \beta_{11}^2}{\alpha \beta_1^2} \quad (4.70)$$

It is to be noted that this expression is different from Kelly's expression (i.e., Eq. (2.71)) because the pressure method is based on the pressure assumption. In addition, it should not be forgotten that the expression derived by Kelly [13] considers only the second stage deformations ignoring the first stage deformations coming from homogenous compression of the layer. On the other hand, it can be shown that the E_c expression derived using the zeroth order theory (i.e., Eq. (4.70)) is the same as that derived by Tsai [48] (i.e., Eq. (2.73)), who eliminated the pressure assumption in his formulation.

4.2.1.1.2 Solution for First Order Theory

When the order of the theory is increased from zero to one ($m=1, p=0$ and $p'=1$), the number of the unknown displacements increases from two to three. In addition to u_1^0 and u_1^+ , one also has u_2^1 as an unknown function. As in the case of the rigid reinforcement, for $n=0$, the governing equations for the first order theory are identical to those derived from the zeroth order theory. Thus, the expressions

derived for u_1^0 and u_1^+ , i.e., Eqs. (4.66), remain the same in the first order theory. Using Eq. (3.22) with Table 3.1 and Table 3.2 for $m=1$ and recalling from the zeroth order theory that

$$\tau_{22}^0 = \lambda \partial_1 u_1^0 - \frac{\alpha \Delta}{t} \quad (4.71)$$

the additional variable u_2^1 can be obtained from the solution of the nontrivial equilibrium equation in x_2 direction for $n=1$ (third of Eqs. (3.73)), that is, from

$$\partial_{11} u_2^1 - \frac{60\alpha}{\mu t^2} u_2^1 = \frac{2}{t} \frac{(\lambda + \mu)}{\mu} [\partial_1 u_1^0 - \partial_1 u_1^+] + \frac{10\alpha \Delta}{\mu t^2} \quad (4.72)$$

From Eqs. (4.66), one has, for the difference $[u_1^0 - u_1^+]$,

$$[u_1^0 - u_1^+] = \frac{\lambda \Delta}{\alpha t} \frac{\sinh(\beta_1 x_1)}{\beta_1 \cosh(\beta_1 w)} \quad (4.73)$$

which when inserted into Eq. (4.72) gives the following equation for u_2^1

$$\partial_{11} u_2^1 - \beta_{21}^2 u_2^1 = \frac{2}{t} \frac{\lambda + \mu}{\mu} \frac{\lambda \Delta}{\alpha t} \frac{\cosh(\beta_1 x_1)}{\cosh(\beta_1 w)} + \frac{10\alpha \Delta}{\mu t^2} \quad \text{where} \quad \beta_{21}^2 = \frac{60\alpha}{\mu t^2} \quad (4.74)$$

Necessary boundary condition for the solution of Eq. (4.74) comes from the condition that $\tau_{12}^1|_{x_1=\pm w} = 0$, which yields

$$[\partial_1 u_2^1]_{x_1=\pm w} = \frac{2}{t} [u_1^0 - u_1^+]_{x_1=\pm w} \quad (4.75)$$

which becomes, in view of Eq. (4.73),

$$[\partial_1 u_2^1]_{x_1=\pm w} = \pm \frac{2}{t} \frac{\lambda \Delta}{\alpha t} \frac{\tanh(\beta_1 w)}{\beta_1} \quad (4.76)$$

Before trying to solve this equation, it seems to be beneficial to compare Eqs. (4.74) and (4.76) with Eqs. (4.9) and (4.10), i.e., with the equations obtained for the rigid-reinforcement case. From the comparison of Eq. (4.74) with Eq. (4.9), one can see that the governing equation for u_2^1 for the flexible-reinforcement case remains almost the same as that when the reinforcing sheets are rigid. The only difference is

on the coefficient in the cosh terms. The flexibility of the reinforcements changes the coefficient from β_{10} to β_1 . Thus, there is no need to solve Eq. (4.74). Instead, the solution derived for the rigid-reinforcement case can be adapted to this problem. However, for such an adaptation, it is necessary to show that the boundary conditions of the problems are also similar. From the comparison of Eq. (4.76) with Eq. (4.10), one can see that the boundary conditions for the governing equations of the problems are in fact similar. Thus, the solution derived for u_2 for the rigid-reinforcement cases, i.e., the second of Eq. (4.14), can be used also for the case where the reinforcements are flexible provided that β_1 is used in place of β_{10} .

As far as the horizontal displacement is concerned, since the expressions derived for u_1^0 and u_1^+ by using the zeroth order theory remains unchanged in the first order theory, Eq. (4.68) also remains the same. One can also show that the E_c expression predicted by the zeroth order theory also remains unchanged when the order of the theory is increased from zero to one. Thus, for an IS-shaped elastic layer bonded to flexible reinforcements at its top and bottom faces, the predictions of the first order theory for the displacement distributions and the effective modulus of the layer under uniform compression are

$$\begin{aligned}
u_1 &= \frac{3}{2} \frac{\Delta}{t} \frac{\lambda}{\alpha} \frac{\sinh(\beta_1 x_1)}{\beta_1 \cosh(\beta_1 w)} \left(1 - \frac{4x_2^2}{t^2} \right) + \frac{\Delta}{t} \frac{\lambda}{\alpha} \frac{\beta_{11}^2}{\beta_1^2} \left(x_1 - \frac{\sinh(\beta_1 x_1)}{\beta_1 \cosh(\beta_1 w)} \right) \\
u_2 &= \left[\begin{array}{l} \frac{30}{t} \frac{\lambda}{\alpha} \frac{\Delta}{t} \frac{x_2}{t} \left(1 - \frac{4x_2^2}{t^2} \right) \\ \left\{ \begin{array}{l} \frac{1}{\beta_1 \beta_{21}} \frac{\tanh(\beta_1 w)}{\sinh(\beta_{21} w)} \left[1 - \frac{\mu + \lambda}{\mu} \frac{\beta_1^2}{\beta_1^2 - \beta_{21}^2} \right] \cosh(\beta_{21} x_1) \\ + \frac{\mu + \lambda}{\mu} \frac{1}{\beta_1^2 - \beta_{21}^2} \frac{\cosh(\beta_1 x_1)}{\cosh(\beta_1 w)} \end{array} \right\} \\ -\frac{\Delta}{t} x_2 \end{array} \right] \quad (4.77) \\
E_c &= \alpha - \frac{\lambda^2}{\alpha} \frac{\beta_{10}^2}{\beta_1^2} \frac{\tanh(\beta_1 w)}{(\beta_1 w)} - \frac{\lambda^2}{\alpha} \frac{\beta_{11}^2}{\beta_1^2}
\end{aligned}$$

4.2.1.2 Pure Bending

When the formulation is applied to the bending problem by using directly the first order theory, one has, similar to the compression problem, three unknown displacements, u_1^0 , u_2^1 and u_1^+ . For these three unknowns, two equations come from the weighted equilibrium equations: the first of Eqs. (3.81) with $n=0$ and the third of Eqs. (3.81) with $n=1$. The third equation is obtained from the equilibrium equation written for the reinforcing sheets: the first of Eqs. (3.82). Of these three equations, two equations are independent of u_2^1 , as in the compression case. Thus, u_1^0 and u_1^+ can be determined first.

The first of Eqs. (3.81) with $n=0$ can be reduced, in view of Eq. (3.22) and Table 3.1 and Table 3.2 for $m=1$, to the following equation:

$$\partial_{11}u_1^0 - \beta_{10}^2 [u_1^0 - u_1^+] = -\frac{\lambda + \mu \phi}{\alpha t} \quad \text{where} \quad \beta_{10}^2 = \frac{12\mu}{\alpha t^2} \quad (4.78)$$

In a similar way, using the coefficients given in Table 3.2 for $m=1$, the first of Eqs. (3.82) can be simplified as

$$\partial_{11}u_1^+ - \beta_{11}^2 [u_1^+ - u_1^0] = \frac{\beta_{11}^2 \mu \phi}{\beta_{10}^2 \alpha t} \quad \text{where} \quad \beta_{11}^2 = \frac{12\mu}{k_f t} \quad (4.79)$$

Similar to the compression problem, by eliminating the terms in the brackets in Eqs. (4.78) and (4.79) and then by integrating the resulting equation twice in x_1 , the following relation can be obtained between u_1^0 and u_1^+ :

$$u_1^+ = -\frac{\beta_{11}^2}{\beta_{10}^2} u_1^0 - \frac{\beta_{11}^2}{\beta_{10}^2} \frac{\lambda \phi}{\alpha t} \frac{x_1^2}{2} + d_2 \quad (4.80)$$

where d_2 is an integration constant. It is to be noted that unlike the compression problem, in bending problem the horizontal displacement is symmetric about $x_1=0$. Thus, for the weighted displacement u_1^0 , one has the following equation:

$$\partial_{11}u_1^0 - \beta_{11}^2 u_1^0 = \beta_{11}^2 \frac{\lambda \phi}{\alpha t} \frac{x_1^2}{2} - \beta_{10}^2 d_2 - \frac{\lambda + \mu \phi}{\alpha t} \quad \text{where} \quad \beta_{11}^2 = \beta_{10}^2 + \beta_{11}^2 \quad (4.81)$$

from which one can obtain u_1^0 and u_1^+ , in view of Eq. (4.80), as

$$u_1^0 = a_{11} \cosh(\beta_1 x_1) - \frac{\beta_{11}^2 \lambda \phi x_1^2}{\beta_1^2 \alpha t 2} + \frac{1}{\beta_1} \frac{\lambda \phi}{\alpha t} \left[\frac{\beta_{10}^2}{\beta_1^2} + \frac{\mu}{\lambda} \right] + \frac{\beta_{10}^2}{\beta_1^2} d_2 \quad (4.82)$$

$$u_1^+ = -\frac{\beta_{11}^2}{\beta_{10}^2} a_{11} \cosh(\beta_1 x_1) - \frac{\beta_{11}^2 \lambda \phi x_1^2}{\beta_1^2 \alpha t 2} - \frac{\beta_{11}^2 \lambda \phi}{\beta_{10}^2 \beta_1^2 \alpha t} \left[\frac{\beta_{10}^2}{\beta_1^2} + \frac{\mu}{\lambda} \right] + \frac{\beta_{10}^2}{\beta_1^2} d_2$$

where a_{11} is the second integration constant to be determined from the boundary conditions. The condition $N_{11}|_{x_1=\pm w} = 0$, implying $[\partial_1 u_1^+]_{x_1=\pm w} = 0$, leads to

$$a_{11} = -\frac{\beta_{10}^2 \lambda \phi \beta_1 w}{\beta_1^4 \alpha t \sinh(\beta_1 w)} \quad (4.83)$$

It should be noted that the nontrivial boundary condition at the lateral bulge-free faces of the layer for $n=0$, i.e., $\tau_{11}^0|_{x_1=\pm w} = 0$, results in the same expression for a_{11} . The remaining constant d_2 can be obtained from the condition that $[u_1^+]_{x_1=0} = 0$, which yields

$$d_2 = \frac{\beta_{11}^2 \lambda \phi}{\beta_{10}^4 \alpha t} \left[\frac{\beta_{10}^2}{\beta_1^2} + \frac{\mu}{\lambda} \right] - \frac{\beta_{11}^2 \lambda \phi \beta_1 w}{\beta_{10}^2 \beta_1^2 \alpha t \sinh(\beta_1 w)} \quad (4.84)$$

Then, u_1^0 and u_1^+ become

$$u_1^0 = \left\{ \begin{array}{l} -\frac{\beta_{10}^2 \lambda \phi \beta_1 w}{\beta_1^4 \alpha t \sinh(\beta_1 w)} \left[\frac{\beta_{11}^2}{\beta_{10}^2} + \cosh(\beta_1 x_1) \right] \\ -\frac{\beta_{11}^2 \lambda \phi x_1^2}{\beta_1^2 \alpha t 2} + \frac{1}{\beta_{10}^2} \frac{\mu \phi}{\alpha t} \left[1 + \frac{\beta_{10}^2 \lambda}{\beta_1^2 \mu} \right] \end{array} \right\} \quad (4.85)$$

$$u_1^+ = -\frac{\beta_{11}^2 \lambda \phi \beta_1 w}{\beta_1^4 \alpha t \sinh(\beta_1 w)} [1 - \cosh(\beta_1 x_1)] - \frac{\beta_{11}^2 \lambda \phi x_1^2}{\beta_1^2 \alpha t 2}$$

As already mentioned, the third equation for the solution of u_2^1 comes from the third of Eqs. (3.81) with $n=1$, which can be simplified, in view of Eq. (3.22) and Table 3.1 and Table 3.2 for $m=1$, as

$$\partial_{11} u_2^1 - \frac{60\alpha}{\mu t^2} u_2^1 = \frac{2(\lambda + \mu)}{t \mu} [\partial_1 u_1^0 - \partial_1 u_1^+] - \frac{10\alpha\phi}{\mu t^2} x_1 \quad (4.86)$$

From Eqs. (4.85), it follows that

$$\left[u_1^0 - u_1^+ \right] = a_{11} \frac{\beta_1^2}{\beta_{10}^2} \cosh(\beta_1 x_1) + \frac{1}{\beta_{10}^2} \frac{\mu \phi}{\alpha t} \left[1 + \frac{\beta_{10}^2 \lambda}{\beta_1^2 \mu} \right] \quad (4.87)$$

Using Eq. (4.87), Eq. (4.86) can be simplified further to

$$\partial_{11} u_2^1 - \beta_{21}^2 u_2^1 = \frac{2}{t} \frac{\lambda + \mu}{\mu} \frac{\lambda \phi}{\alpha t} \frac{w \sinh(\beta_1 x_1)}{\sinh(\beta_1 w)} - \frac{10\alpha}{\mu t^2} \phi x_1 \quad \text{where} \quad \beta_{21}^2 = \frac{60\alpha}{\mu t^2} \quad (4.88)$$

The boundary condition for Eq. (4.88) for u_2^1 is $\tau_{12}^1 \Big|_{x_1=\pm w} = 0$, which implies

$$\left[\partial_1 u_2^1 \right]_{x_1=\pm w} = \frac{2}{t} \left[u_1^0 - u_1^+ \right]_{x_1=\pm w} \quad (4.89)$$

which in turn becomes, in view of Eq. (4.87),

$$\left[\partial_1 u_2^1 \right]_{x_1=\pm w} = -\frac{2}{t} \frac{\lambda \phi}{\alpha t} \frac{w}{\beta_1 \tanh(\beta_1 w)} + \frac{\phi}{6} \left(1 + \frac{\beta_{10}^2 \lambda}{\beta_1^2 \mu} \right) \quad (4.90)$$

Similar to the compression problem, the governing equation for u_2^1 in the case of the flexible reinforcements is almost the same as that derived for the rigid case. Thus, the solution remains unchanged formwise. Only the coefficient β_{10} should be replaced with β_1 , which yields, for u_2^1 ,

$$u_2^1 = a_{22} \sinh(\beta_{21} x_1) - \frac{2}{t} \frac{\mu + \lambda}{\mu} \frac{\lambda \phi}{\alpha t} \frac{1}{\beta_1^2 - \beta_{21}^2} \frac{w \sinh(\beta_1 x_1)}{\sinh(\beta_1 w)} + \frac{\phi}{6} x_1 \quad (4.91)$$

When the boundary conditions in Eq. (4.19) and (4.90) are compared, a slight difference is observed in their last terms. This results in a small change in the expression for a_{22} , which becomes, for the flexible-reinforcement flexibility case,

$$a_{22} = \left\{ \begin{array}{l} -\frac{2}{t} \frac{\lambda \phi}{\alpha t} \frac{w}{\beta_1 \beta_{21}} \frac{\coth(\beta_1 w)}{\cosh(\beta_{21} w)} \left[1 - \frac{\mu + \lambda}{\mu} \frac{\beta_1^2}{\beta_1^2 - \beta_{21}^2} \right] \\ + \frac{\phi \lambda \beta_{10}^2}{6 \mu \beta_1^2} \frac{1}{\beta_{21} \cosh(\beta_{21} w)} \end{array} \right\} \quad (4.92)$$

Then, the displacement components u_i and the effective bending modulus E_b may be obtained from the second of Eqs. (3.60) and Eqs. (3.62) as, in view of second of Eqs. (3.64) and Eq. (3.88),

$$\begin{aligned}
u_1 &= \left[-\frac{3 \lambda \phi w \cosh(\beta_1 x_1)}{2 \alpha t \beta_1 \sinh(\beta_1 w)} + \frac{3 \mu \phi}{2 \alpha t \beta_{10}^2} \left(1 + \frac{\beta_{10}^2 \lambda}{\beta_1^2 \mu} \right) \right] \left(1 - \frac{4x_2^2}{t^2} \right) + u_1^+ \\
u_2 &= \left. \begin{aligned} &\left[\frac{x_2}{t} \left(1 - \frac{4x_2^2}{t^2} \right) \right. \\ &\left. \left(-\frac{30 \lambda \phi w \coth(\beta_1 w)}{t \alpha t \beta_1 \beta_{21} \cosh(\beta_{21} w)} \left[1 - \frac{\mu + \lambda}{\mu} \frac{\beta_1^2}{\beta_1^2 - \beta_{21}^2} \right] \sinh(\beta_{21} x_1) \right. \right. \\ &\left. \left. + \frac{5 \phi \lambda \beta_{10}^2}{2 \mu \beta_1^2 \beta_{21} \cosh(\beta_{21} w)} - \frac{30 \lambda \phi \mu + \lambda}{t \alpha t \mu} \frac{w}{\beta_1^2 - \beta_{21}^2} \frac{\sinh(\beta_1 x_1)}{\sinh(\beta_1 w)} \right) \right. \\ &\left. + \frac{\phi}{t} x_1 x_2 \right] \end{aligned} \right\} \quad (4.93)
\end{aligned}$$

$$\begin{aligned}
E_b &= \left[\alpha - \frac{15 \lambda \alpha}{\mu} \left\{ \frac{\mu + \lambda}{\mu} \frac{\beta_{10}^2}{\beta_1^2 - \beta_{21}^2} \left[\frac{1}{(\beta_1 w)^2} \left(1 - \frac{\beta_1 w}{\tanh(\beta_1 w)} \right) + \right. \right. \right. \\ &\quad \left. \left. \frac{1}{(\beta_{21} w)^2} \frac{\beta_1 w}{\tanh(\beta_1 w)} \left(1 - \frac{\tanh(\beta_{21} w)}{\beta_{21} w} \right) \right] \right. \\ &\quad \left. \left. + \frac{1}{(\beta_{21} w)^2} \frac{\beta_{10}^2}{\beta_1^2} \left(1 - \frac{\beta_1 w}{\tanh(\beta_1 w)} \right) \left(1 - \frac{\tanh(\beta_{21} w)}{\beta_{21} w} \right) \right\} \right. \\ &\quad \left. - \frac{\lambda^2 \beta_{11}^2}{\alpha \beta_1^2} \left\{ 1 + \frac{3}{(\beta_1 w)^2} \left(1 - \frac{\beta_1 w}{\tanh(\beta_1 w)} \right) \right\} \right]
\end{aligned}$$

It is worth noting that the prediction of the zeroth order theory for the effective bending modulus of the layer has the following simpler form:

$$E_b = \alpha - \frac{3 \lambda^2 \beta_{10}^2}{\alpha \beta_1^2} \frac{1}{(\beta_1 w)^2} \left[\frac{(\beta_1 w)}{\tanh(\beta_1 w)} - 1 \right] - \frac{\lambda^2 \beta_{11}^2}{\alpha \beta_1^2} \quad (4.94)$$

It is to be noted that Eq. (4.94) reduces to the following equation when $\beta_{11} \rightarrow \infty$, i.e., $\beta_1 \rightarrow \beta_{10}$,

$$E_b = \alpha - \frac{3 \lambda^2}{\alpha} \frac{1}{(\beta_{10} w)^2} \left[\frac{(\beta_{10} w)}{\tanh(\beta_{10} w)} - 1 \right] \quad (4.95)$$

which is the prediction of the zeroth order theory for the bending modulus of an IS-shaped layer bonded to rigid surfaces.

4.2.1.3 *Pure Warping*

For the warping problem, it seems to be beneficial to define the warping shape $\Omega(x_1)$ at the beginning of the analysis, instead of keeping it as an additional unknown function through the derivations. For the selection of the appropriate warping function, the studies of Kelly [44] and Tsai and Kelly [45,46], who investigated *indirectly* the warping behavior of short uniform beams and elastomeric bearings, can be referred to. It is worth noting that these studies are, in fact, the only studies (to the knowledge of the author) in literature on the warping behavior of bonded elastic layers.

It can be recalled from Section 2.2.3, Tsai and Kelly [46] selected the cubic function given in Eq. (2.89) as their warping function since it is the simplest function that permits uncoupling of the constitutive equations for axial load and warping moment. Similarly, they determined the constant f appearing in the cubic function such that the constitutive equations for bending moment and warping moment were also uncoupled. It is important to note that Tsai and Kelly [45, 46] used such an uncoupling in their virtual work expression in order to simplify their stability analysis.

As mentioned previously, this dissertation aims to study the behavior of bonded elastic layers under three simple deformation modes so that the individual expressions derived for each deformation mode can later be superposed directly to be able to obtain closed form expressions for the behavior of bonded elastic layers under the combined effects of compression and bending. Since the uniform compression and pure bending problems are studied separately, it seems to be appropriate to study the pure warping problem in a way that it is independent from the compression and bending problems. Thus, instead of trying to satisfy the uncoupling conditions used by Tsai and Kelly [46], selecting a warping shape in such a way that the resultant axial force P and the bending moment M would be uncoupled from pure warping deformation seems to be practical and feasible for the warping problem studied in this section.

Selecting the simplest cubic function is still possible for this case since this assures that the resultant axial force on the layer will be zero. It is to be noted that the cubic expression in Eq. (2.89) can be written, in the notation of the present formulation, in the following form:

$$\Omega(x) = \left(\frac{x_1}{w}\right)^3 + f\left(\frac{x_1}{w}\right) \quad (4.96)$$

The second condition, the condition that the resultant moment on the layer should be zero, then enables one to compute the unknown constant f in Eq. (4.96). However, it can easily be realized that f cannot be determined at the beginning of the analysis since its computation necessitates knowledge on the stress distributions, which can be obtained only when the analytical solutions are derived for the displacement components. For this reason, in the following derivations, the constant f is kept as an unknown warping-related parameter until the closed form expressions are obtained for the stress distributions.

When the governing equations for the warping problem (Eqs. {(3.86),(3.87)}), are compared with those of the bending problem (Eqs. {(3.81),(3.82)}), it can be seen that these problems can be handled in a very similar way. Thus, for the warping problem, there are again three unknown displacements u_1^0 , u_2^1 and u_1^+ when the first order theory is applied directly. In addition, from these unknowns, u_1^0 and u_1^+ , can again be solved independent from u_2^1 . Coupled differential equations for u_1^0 and u_1^+ can be obtained from the first of Eqs. (3.86) with $n=0$ and the first of Eqs. (3.87) using the relation given in Eq. (3.22) and the coefficients and constants given in Table 3.1 and Table 3.2 for $m=1$. In view of Eq. (4.96), these equations are

$$\partial_{11}u_1^0 - \beta_{10}^2 [u_1^0 - u_1^+] = -\frac{\lambda + \mu}{\alpha} \frac{\Phi}{t} \left(\frac{3x_1^2}{w^3} + \frac{f}{w} \right) \quad \text{where} \quad \beta_{10}^2 = \frac{12\mu}{\alpha t^2} \quad (4.97)$$

$$\partial_{11}u_1^+ - \beta_{11}^2 [u_1^+ - u_1^0] = \frac{\beta_{11}^2}{\beta_{10}^2} \frac{\mu}{\alpha} \frac{\Phi}{t} \left(\frac{3x_1^2}{w^3} + \frac{f}{w} \right) \quad \text{where} \quad \beta_{11}^2 = \frac{12\mu}{k_f t} \quad (4.98)$$

Eliminating the terms in the brackets in the above equations leads to the following equation:

$$\partial_{11}u_1^+ = -\frac{\beta_{11}^2}{\beta_{10}^2}\partial_{11}u_1^0 - \frac{\beta_{11}^2}{\beta_{10}^2}\frac{\lambda}{\alpha}\frac{\Phi}{t}\left(\frac{3x_1^2}{w^3} + \frac{f}{w}\right) \quad (4.99)$$

Keeping in mind that u_1 is an even function of x_1 and integrating Eq. (4.99) twice in x_1 , one can obtain the following relation between u_1^+ and u_1^0 :

$$u_1^+ = -\frac{\beta_{11}^2}{\beta_{10}^2}u_1^0 - \frac{\beta_{11}^2}{\beta_{10}^2}\frac{\lambda}{\alpha}\frac{\Phi}{t}\left(\frac{x_1^4}{4w^3} + f\frac{x_1^2}{2w}\right) + d_2 \quad (4.100)$$

where d_2 is an integration constant to be determined from the boundary/symmetry conditions. Substituting Eq. (4.100) into Eq. (4.97), the governing equation for u_1^0 is obtained as

$$\partial_{11}u_1^0 - \beta_1^2 u_1^0 = \beta_{11}^2 \frac{\lambda}{\alpha} \frac{\Phi}{t} \left(\frac{x_1^4}{4w^3} + f \frac{x_1^2}{2w} \right) - \frac{\lambda + \mu}{\alpha} \frac{\Phi}{t} \left(\frac{3x_1^2}{w^3} + \frac{f}{w} \right) - \beta_{10}^2 d_2 \quad (4.101)$$

where $\beta_1^2 = \beta_{10}^2 + \beta_{11}^2$. From the solution of Eq. (4.101), one can obtain u_1^0 and u_1^+ , in view of Eq. (4.100), as

$$u_1^0 = \left\{ \begin{aligned} & a_{11} \cosh(\beta_1 x_1) - \frac{\beta_{11}^2}{\beta_1^2} \frac{\Phi}{t} \frac{\lambda}{\alpha} \left[\frac{x_1^4}{4w^3} + \frac{f x_1^2}{2w} \right] \\ & + \frac{1}{\beta_1^2} \frac{\lambda}{\alpha} \frac{\Phi}{t} \left[\frac{\mu}{\lambda} + \frac{\beta_{10}^2}{\beta_1^2} \right] \left[\frac{3x_1^2}{w^3} + \frac{f}{w} + \frac{6}{w(\beta_1 w)^2} \right] + \frac{\beta_{10}^2}{\beta_1^2} d_2 \end{aligned} \right\} \quad (4.102)$$

$$u_1^+ = \left\{ \begin{aligned} & -\frac{\beta_{11}^2}{\beta_{10}^2} a_{11} \cosh(\beta_1 x_1) - \frac{\beta_{11}^2}{\beta_1^2} \frac{\Phi}{t} \frac{\lambda}{\alpha} \left[\frac{x_1^4}{4w^3} + \frac{f x_1^2}{2w} \right] \\ & - \frac{\beta_{11}^2}{\beta_{10}^2 \beta_1^2} \frac{\lambda}{\alpha} \frac{\Phi}{t} \left[\frac{\mu}{\lambda} + \frac{\beta_{10}^2}{\beta_1^2} \right] \left[\frac{3x_1^2}{w^3} + \frac{f}{w} + \frac{6}{w(\beta_1 w)^2} \right] + \frac{\beta_{10}^2}{\beta_1^2} d_2 \end{aligned} \right\}$$

where a_{11} is the second integration constant to be determined from the boundary/symmetry conditions. Similar to the bending problem, either the force-free boundary conditions at the edges of the reinforcing sheets $N_{11}|_{x_1=\pm w} = 0$ or the stress-free boundary conditions at the lateral surfaces of the elastic layer $\tau_{11}^0|_{x_1=\pm w} = 0$ can be used to determine a_{11} , which gives, for a_{11} ,

$$a_{11} = -\frac{\beta_{10}^2 \Phi \lambda}{\beta_1^2 t \alpha \beta_1 \sinh(\beta_1 w)} \frac{1}{\left[1 + f + \frac{6}{(\beta_1 w)^2} \left(1 + \frac{\mu \beta_1^2}{\lambda \beta_{10}^2}\right)\right]} \quad (4.103)$$

The additional condition for the remaining constant d_2 comes from the condition that $[u_1^+]_{x_1=0} = 0$, which results in

$$d_2 = a_{11} \frac{\beta_{11}^2 \beta_1^2}{\beta_{10}^4} + \frac{\beta_{11}^2 \lambda \Phi}{\beta_{10}^4 \alpha t} \left[\frac{\beta_{10}^2}{\beta_1^2} + \frac{\mu}{\lambda} \right] \left[\frac{f}{w} + \frac{6}{w(\beta_1 w)^2} \right] \quad (4.104)$$

Then, the weighted displacement u_1^0 and the face displacement u_1^+ become

$$u_1^0 = \left\{ \begin{aligned} & a_{11} \cosh(\beta_1 x_1) + a_{11} \frac{\beta_{11}^2}{\beta_{10}^2} - \frac{\beta_{11}^2 \lambda \Phi}{\beta_1^2 \alpha t} \left[\frac{x_1^4}{4w^3} + \frac{fx_1^2}{2w} \right] \\ & + \frac{1}{\beta_1^2} \frac{\mu \Phi}{\alpha t} \left[1 + \frac{\beta_{10}^2 \lambda}{\beta_1^2 \mu} \right] \left[\frac{3x_1^2}{w^3} \right] \\ & + \frac{1}{\beta_{10}^2} \frac{\mu \Phi}{\alpha t} \left[1 + \frac{\beta_{10}^2 \lambda}{\beta_1^2 \mu} \right] \left[\frac{f}{w} + \frac{6}{w(\beta_1 w)^2} \right] \end{aligned} \right\} \quad (4.105)$$

$$u_1^+ = \left\{ \begin{aligned} & -a_{11} \frac{\beta_{11}^2}{\beta_{10}^2} \cosh(\beta_1 x_1) + a_{11} \frac{\beta_{11}^2}{\beta_{10}^2} - \frac{\beta_{11}^2 \lambda \Phi}{\beta_1^2 \alpha t} \left[\frac{x_1^4}{4w^3} + \frac{fx_1^2}{2w} \right] \\ & - \frac{\beta_{11}^2 \mu \Phi}{\beta_{10}^2 \beta_1^2 \alpha t} \left[1 + \frac{\beta_{10}^2 \lambda}{\beta_1^2 \mu} \right] \left[\frac{3x_1^2}{w^3} \right] \end{aligned} \right\}$$

The third equation for the remaining unknown u_2^1 comes from the third of Eqs. (3.86) with $n=1$, which can be written in view of Eq. (3.22) and Table 3.1 and Table 3.2 for $m=1$, as

$$\partial_{11} u_2^1 - \beta_{21}^2 u_2^1 = \frac{2(\lambda + \mu)}{t} \frac{1}{\mu} [\partial_1 u_1^0 - \partial_1 u_1^+] - \frac{10\alpha}{\mu t^2} \Phi \Omega \quad \text{where} \quad \beta_{21}^2 = \frac{60\alpha}{\mu t^2} \quad (4.106)$$

From Eqs. (4.105), one has

$$\partial_1 [u_1^0 - u_1^+] = a_{11} \frac{\beta_1^3}{\beta_{10}^2} \sinh(\beta_1 x_1) + \frac{1}{\beta_{10}^2} \frac{\mu \Phi}{\alpha t} \left[1 + \frac{\beta_{10}^2 \lambda}{\beta_1^2 \mu} \right] \left[\frac{6x_1}{w^3} \right] \quad (4.107)$$

Then, u_2^1 has the following form for the warping shape given in Eq. (4.96):

$$u_2^1 = a_{22} \sinh(\beta_{21} x_1) + A \sinh(\beta_1 x_1) + B x_1^3 + C x_1 \quad (4.108)$$

where the constants A, B and C (coming from the particular solution) are

$$A = \frac{2(\mu + \lambda) \beta_1^3}{\mu t} \frac{a_{11}}{\beta_{10}^2 \beta_1^2 - \beta_{21}^2}, \quad B = \frac{1}{\beta_{21}^2} \frac{10\alpha \Phi}{\mu t} \frac{1}{w^3}$$

$$C = \frac{6B}{\beta_{21}^2} - \frac{12}{\beta_{21}^2 \beta_{10}^2} \frac{\mu + \lambda}{\mu t} \frac{\mu \Phi}{\alpha t} \left[1 + \frac{\lambda \beta_{10}^2}{\mu \beta_1^2} \right] \frac{1}{w^3} + \frac{1}{\beta_{21}^2} \frac{10\alpha \Phi}{\mu t} \frac{f}{w}$$
(4.109)

and the constant a_{22} can be obtained from the condition that $\tau_{12}^1|_{x_1=\pm w} = 0$, which yields

$$a_{22} = \frac{1}{\beta_{21} \cosh(\beta_{21}w)} \left\{ \begin{aligned} & \left[a_{11} \frac{2 \beta_1^2}{t \beta_{10}^2} - A \beta_1 \right] \cosh(\beta_1 w) - 3Bw^2 - C \\ & + \frac{2}{\beta_{10}^2 t} \frac{\mu \Phi}{\alpha t} \left[1 + \frac{\lambda \beta_{10}^2}{\mu \beta_1^2} \right] \left[\frac{3+f}{w} + \frac{6}{w(\beta_1 w)^2} \right] \end{aligned} \right\}$$
(4.110)

Then, the displacement components u_i ($i=1,2$) become, in view of the second of Eqs. (3.60),

$$u_1 = \frac{3}{2} \left\{ \begin{aligned} & a_{11} \frac{\beta_1^2}{\beta_{10}^2} \cosh(\beta_1 x_1) + \\ & \frac{1}{\beta_{10}^2} \frac{\mu \Phi}{\alpha t} \left[1 + \frac{\lambda \beta_{10}^2}{\mu \beta_1^2} \right] \left[\frac{3x_1^2}{w^3} + \frac{f}{w} + \frac{6}{w(\beta_1 w)^2} \right] \end{aligned} \right\} \left(1 - \frac{4x_2^2}{t^2} \right) + u_1^+$$

$$u_2 = \left\{ \begin{aligned} & 15 \left[a_{22} \sinh(\beta_{21} x_1) + A \sinh(\beta_1 x_1) + Bx_1^3 + Cx_1 \right] \left[\frac{x_2}{t} - \frac{4x_2^3}{t^3} \right] \\ & + \Phi \left[\frac{x_1^3}{w^3} + f \frac{x_1}{w} \right] \left[\frac{10x_2^3}{t^3} - \frac{3x_2}{2t} \right] \end{aligned} \right\}$$
(4.111)

Since the expression for the warping modulus of the layer using the first order theory is too lengthy and complex, only the prediction of the zeroth order theory for E_w is presented here. By determining Q from the first of Eqs. (3.90) and using the relation defined in Eqs. (3.89), one can compute the warping modulus for an IS-shaped layer bonded to flexible reinforcements as

$$E_w = \frac{\lambda^2 \beta_{10}^2}{\alpha \beta_1^2 (\beta_1 w)^2} \left\{ \begin{aligned} & \left[\frac{\alpha^2 \beta_1^2}{\lambda^2 \beta_{10}^2} - \frac{\beta_{11}^2}{\beta_{10}^2} \right] (\beta_1 w)^2 \left(\frac{1}{7} + \frac{2f}{5} + \frac{f^2}{3} \right) \\ & + \left(1 + \frac{\mu \beta_1^2}{\lambda \beta_{10}^2} \right) \left(\frac{6}{5} + 2f \right) \\ & + \left[\left(1 + f + \frac{6}{(\beta_1 w)^2} \right) \left(1 - \frac{\beta_1 w}{\tanh(\beta_1 w)} \right) + 2 \right] \\ & \cdot \left[1 + f + \frac{6}{(\beta_1 w)^2} \left(1 + \frac{\mu \beta_1^2}{\lambda \beta_{10}^2} \right) \right] \end{aligned} \right\} \quad (4.112)$$

Finally, since the stress distributions are known now, the constant f appearing in the warping function Ω in Eq. (4.96) can be determined from the condition that resultant bending moment must be zero in the layer. Similar to the warping modulus, for f , only the prediction of the zeroth order theory is presented here. From the condition $M = \iint_A (\tau_{22}^0 x_1) dA = 0$, f may be determined as

$$f = - \frac{\left\{ \left[1 - \frac{\beta_1 w}{\tanh(\beta_1 w)} \right] \left[1 + \frac{6}{(\beta_1 w)^2} \left(1 + \frac{\mu \beta_1^2}{\lambda \beta_{10}^2} \right) \right] \right\}}{\left\{ 1 - \frac{\beta_1 w}{\tanh(\beta_1 w)} \right\} - \frac{(\beta_1 w)^2 \beta_{11}^2}{3 \beta_{10}^2} \left(1 - \frac{\beta_1^2 \alpha^2}{\beta_{11}^2 \lambda^2} \right)} + 2 \frac{\left(1 + \frac{\mu \beta_1^2}{\lambda \beta_{10}^2} \right) - \frac{(\beta_1 w)^2 \beta_{11}^2}{5 \beta_{10}^2} \left(1 - \frac{\beta_1^2 \alpha^2}{\beta_{11}^2 \lambda^2} \right)}{\left\{ 1 - \frac{\beta_1 w}{\tanh(\beta_1 w)} \right\} - \frac{(\beta_1 w)^2 \beta_{11}^2}{3 \beta_{10}^2} \left(1 - \frac{\beta_1^2 \alpha^2}{\beta_{11}^2 \lambda^2} \right)} \quad (4.113)$$

CHAPTER 5

ASSESSMENT OF THE FORMULATION

Experimental studies conducted on bonded rubber layers have shown that the determination of stresses and even displacements in a bonded rubber layer experimentally is considerably difficult [1,17]. For this reason, the verification of the analytical solutions obtained in literature has usually been done by comparing the results with the numerical ones. Similarly, to assess the new formulation proposed in this dissertation, the analytical solutions derived using this new formulation are compared with the numerical solutions. For this purpose, some simple ‘numerical’ problems are designed and analyzed using a widely used numerical technique: BEM (boundary element method).

As pointed out by Fenner and Remzi [38], BEM is a practical numerical technique which can be used in linear analysis of bonded elastic layers. Since BEM is a semi-analytical method requiring the discretization of only the boundary of the solution domain, accurate solutions can be obtained by BEM using much simpler elements than finite element method (FEM). As an example, if BEM is used to analyze a plane strain problem, such as an IS-shaped bonded elastic layer, it is adequate to discretize the layer boundary using simple line elements, which reduces the number of the elements used in the model, thus, also the computing cost, considerably compared to FEM. Preparation of the input data and processing the output data are also usually much easier in BEM, compared to FEM.

In the following sections, the analytical solutions derived for IS, C and HC-shaped elastic layers bonded to rigid surfaces by using the first order theory (FOT)

are compared with the numerical solutions obtained using BEM for different values of shape factor and Poisson's ratio. It should be noted that it has already been verified by several researchers that the pressure method (PM) can accurately predict the linear behavior of bonded elastic layers under uniform compression/pure bending for HSF layers of nearly incompressible materials [3,40]. It is not difficult to show that the FOT predictions satisfactorily converge to the PM predictions as the material compressibility decreases and the shape factor increases (see e.g., Ref. [49]). Thus, in this chapter, it seems to be adequate to assess the FOT solutions by comparing their predictions with the BEM results obtained for LSF layers (e.g., $S=1,2,5$) of compressible or slightly compressible materials (e.g., $\nu=0.3,0.45,0.49$).

5.1 PROBLEM 1: A C-SHAPED LAYER UNDER COMPRESSION

This first problem is designed to verify the success of the FOT solutions in predicting the compressive behavior of a C-shaped bonded elastic layer of compressible material ($\nu=0.45$) with a relatively low shape factor ($S=2$). During the comparisons, particular emphasis is given to the displacement and stress distributions at different sections of the layer.

5.1.1 BEM Model

In this problem, BEM analysis is performed using the FORTRAN program AXI, developed by Ozkan [50] for the elastodynamic analysis of axisymmetric bodies. Since the program is capable of expanding the boundary quantities in the angular θ -direction, it is sufficient to discretize only the half of the boundary in the r - z plane as shown in Figure 5.1. For easier evaluation, the same coordinate system that has been used in the derivation of the FOT solutions are adapted in the BEM model (Figure 5.1). In addition to the displacement BC's at the top and bottom bonded faces ($u_z=\pm\Delta/2$, $u_r=u_\theta=0$), the problem has stress (traction) BC's at the lateral traction-free boundary ($t_i=0$, $i=r,\theta,z$).

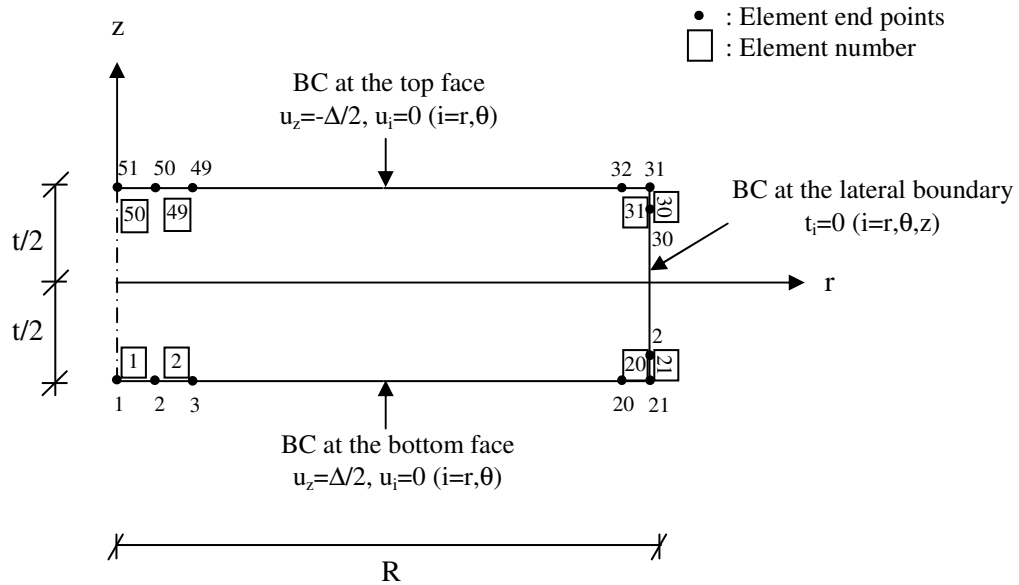


Figure 5.1 Discretization of the bonded elastic disc in r-z plane for axisymmetric BEM solution (Boundary conditions (BC's) are also specified)

Since in BEM, only the boundary of the layer is discretized, at the end of the analysis, only the displacements and tractions at the boundary elements are obtained unless some interior points are specified in the input file. For this reason, the program is executed for a number of times to be able to obtain displacement and stress distributions at different interior sections.

The sections over which the displacement and/or stress distributions are investigated are illustrated in Figure 5.2. From the figure, it can be seen that the section AB represents the top face of the layer ($z=+t/2$). Parallel to this section, the sections CD and EF are defined respectively at $z=+t/4$ and at the centroidal plane $z=0$. Due to the symmetry, only the top-right quarter of the layer is investigated for the distributions in the radial direction. Besides these sections in the radial direction, four vertical sections are considered: the traction-free surface of the layer, i.e., the section HB at $r=R$, the centroidal section GA at $r=0$ and the additional vertical sections JI and LK at $r=R/2$ and $r=0.9R$.

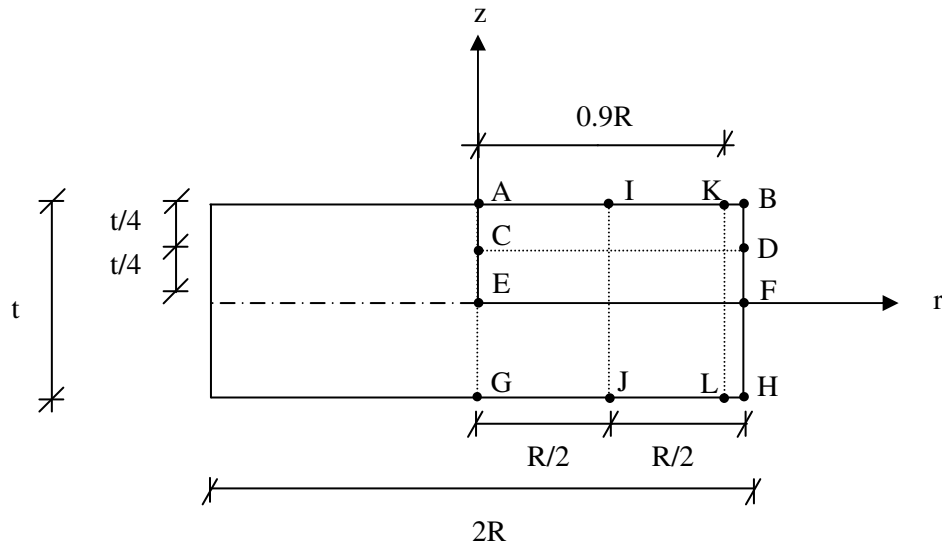


Figure 5.2 Definition of the sections in the bonded elastic disc over which the displacement and stress distributions are plotted

5.1.2 Compression Modulus

The program used in the BEM analysis is also capable of computing the total vertical load P at the bonded faces, from which the compression modulus of the layer is determined, by using Eqs. (2.3) and (2.4), as $E_{c,BEM}=7.788\mu$. The prediction of FOT for a bonded elastic disc with $S=2$ and $\nu=0.45$ is $E_{c,FOT}=7.812\mu$, indicating a very good agreement with the BEM result as far as the compression modulus of the layer is concerned.

5.1.3 Displacement Distributions

The distributions of the nondimensional displacement components (u_i/Δ , $i=r,z$) over the sections defined in Figure 5.2 are presented in Figure 5.3 to Figure 5.6, where the FOT predictions are shown by continuous lines while the BEM results are plotted as discrete points.

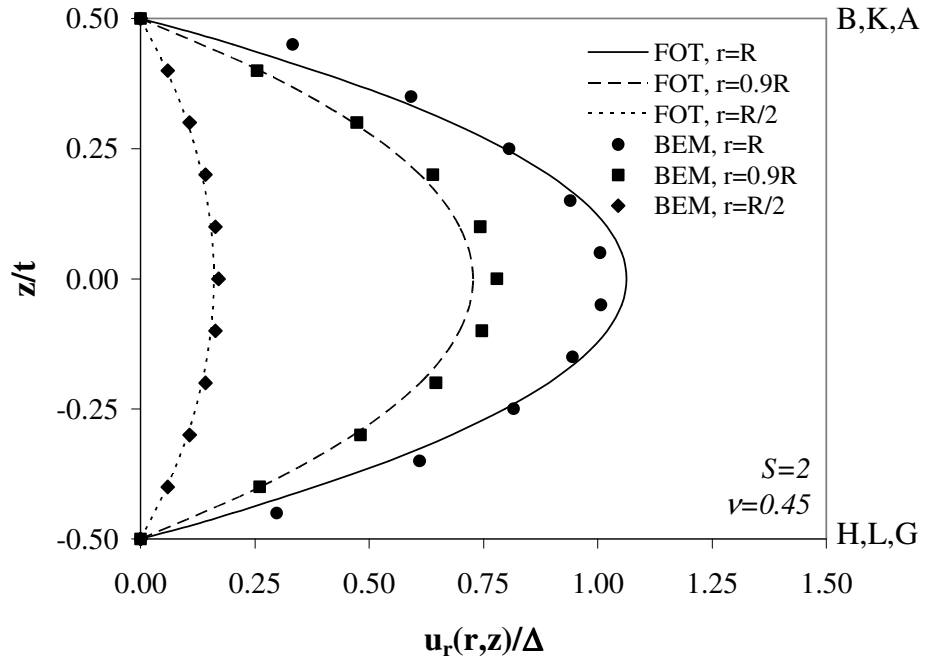


Figure 5.3 Variation of normalized radial displacement through the layer thickness at various sections

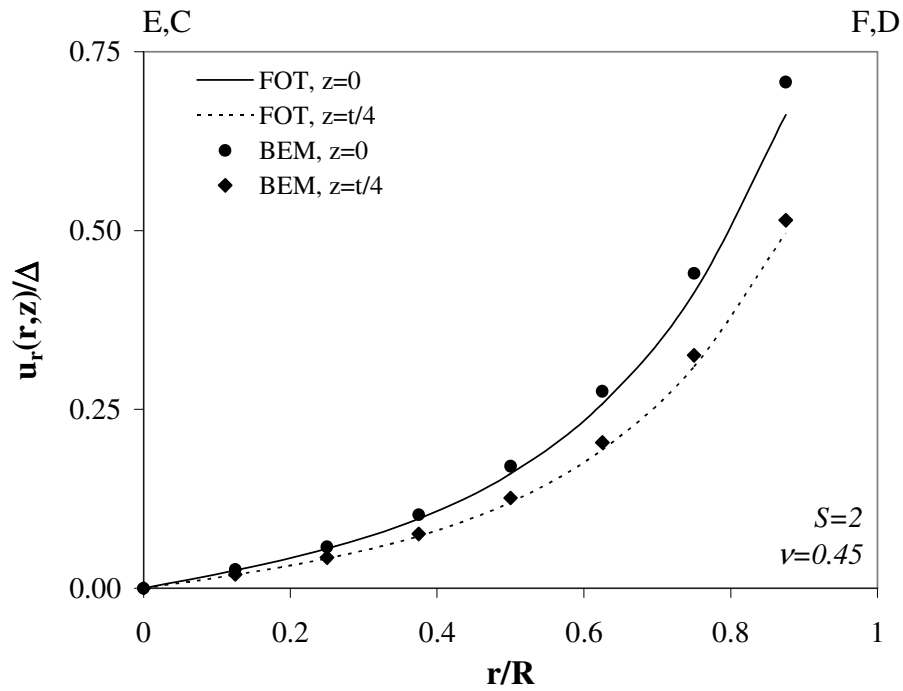


Figure 5.4 Variation of normalized radial displacement through the radius at $z=0, t/4$

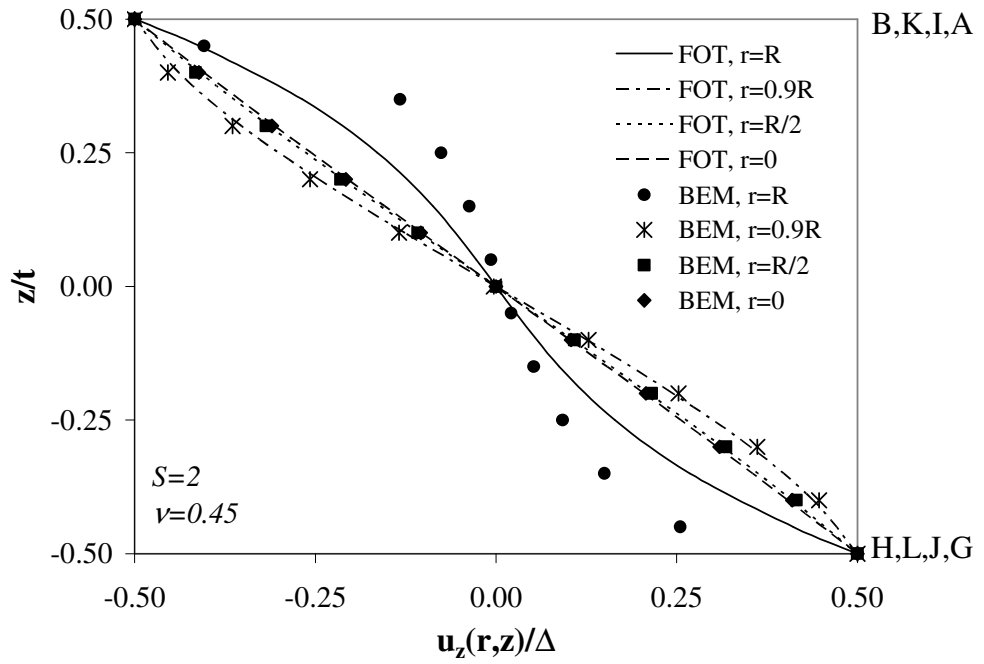


Figure 5.5 Variation of normalized axial displacement through the layer thickness at various sections

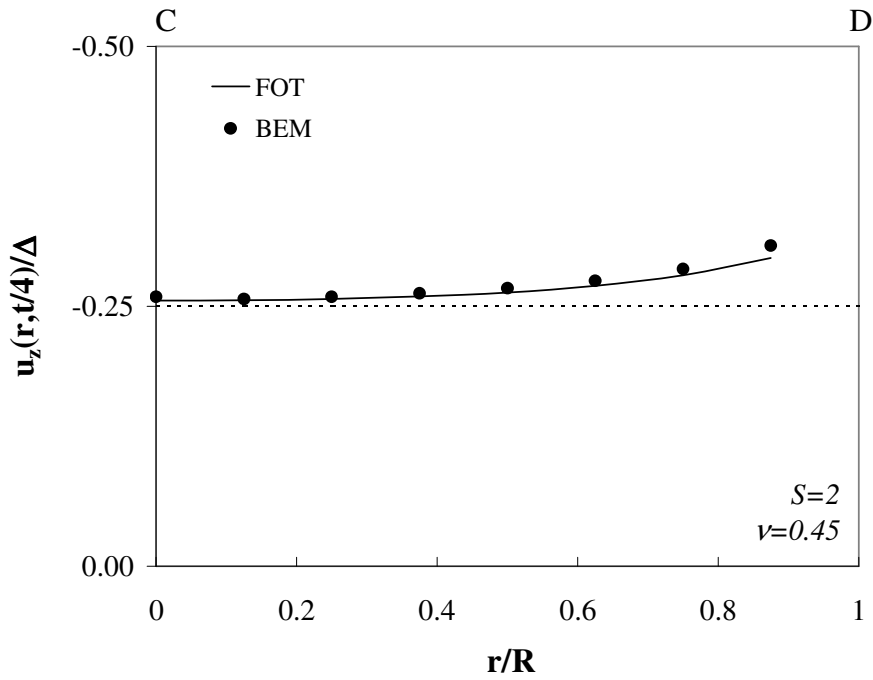


Figure 5.6 Variation of normalized axial displacement through the radius at $z=t/4$

Figure 5.3 shows the bulging pattern of the layer in the radial direction at three different sections. As expected, maximum bulging occurs at the center of the layer, $z=0$. When the predictions of the two methods at $r=R$ are compared, it is seen that the FOT results are slightly larger than the BEM results in the range of about $-0.25t < z < +0.25t$, while the reverse is true for the points closer to the bonded faces. The difference between the predictions of the two methods seems to reduce as the considered vertical section moves towards the center. In Figure 5.4, the distribution of the normalized radial displacement along the radial direction is plotted at two different sections. When the figure is closely examined, it is seen that the FOT predictions are slightly lower than the BEM results. However, the difference is not significant.

The distributions of the axial displacement over different vertical sections are plotted in Figure 5.5. As shown in the figure, the FOT predictions seem to deviate from the BEM results considerably at the lateral face of the layer (i.e., at $r=R$). It may be noted that despite this great difference at the lateral boundary, the results almost coincide for the other sections ($r=0$ and $r=R/2$) even in the vicinity of the boundary ($r=0.9R$).

Figure 5.6 exhibits the distribution of the axial displacement over the horizontal section CD at $z=t/4$. This figure shows that the assumption “the plane sections remain plane during compressional deformation” is not correct, especially for the horizontal sections away from the bonded and centroidal horizontal sections. While the values obtained by BEM appear to be slightly larger than those of FOT, it may be observed that the predictions of the two methods are close.

5.1.4 Stress Distributions

Similar to the displacement distributions, the stress distributions can be plotted over various sections in the layer. Some example plots are presented in Figure 5.7 to Figure 5.13. It should be noted that in these plots stress values are nondimensionalized by dividing them by $\mu\epsilon_c$.

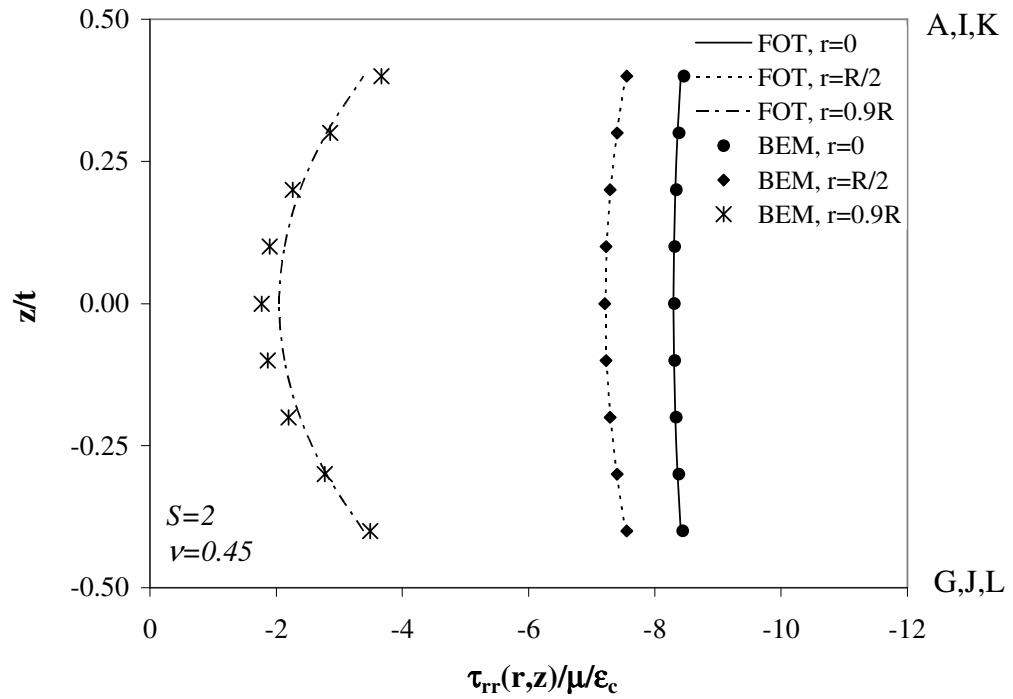


Figure 5.7 Variation of normalized radial stress through the layer thickness

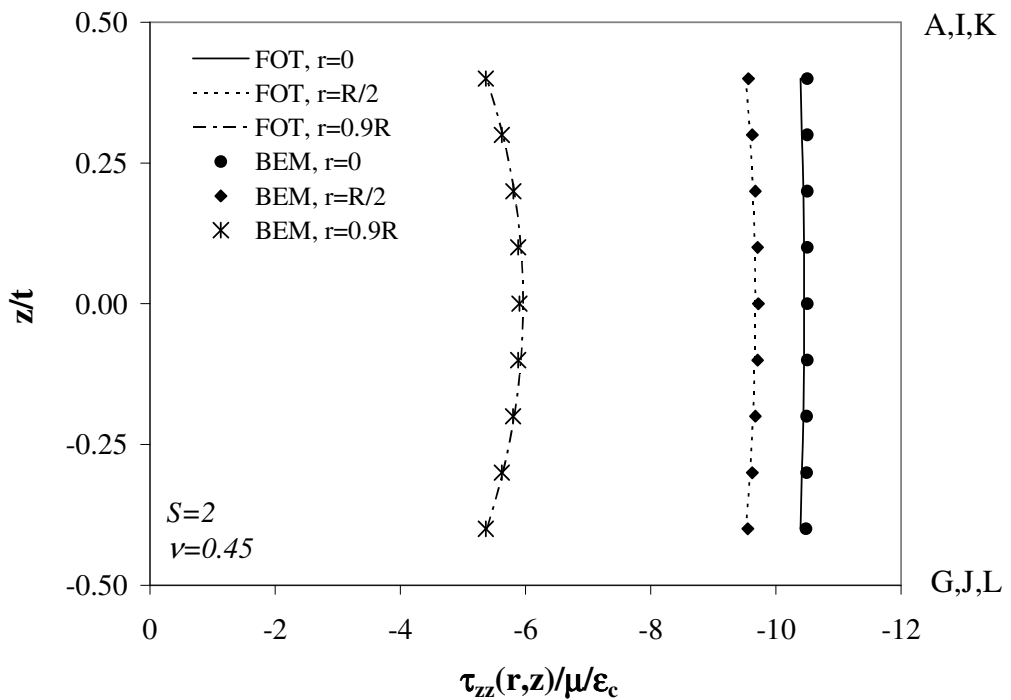


Figure 5.8 Variation of normalized axial stress through the layer thickness

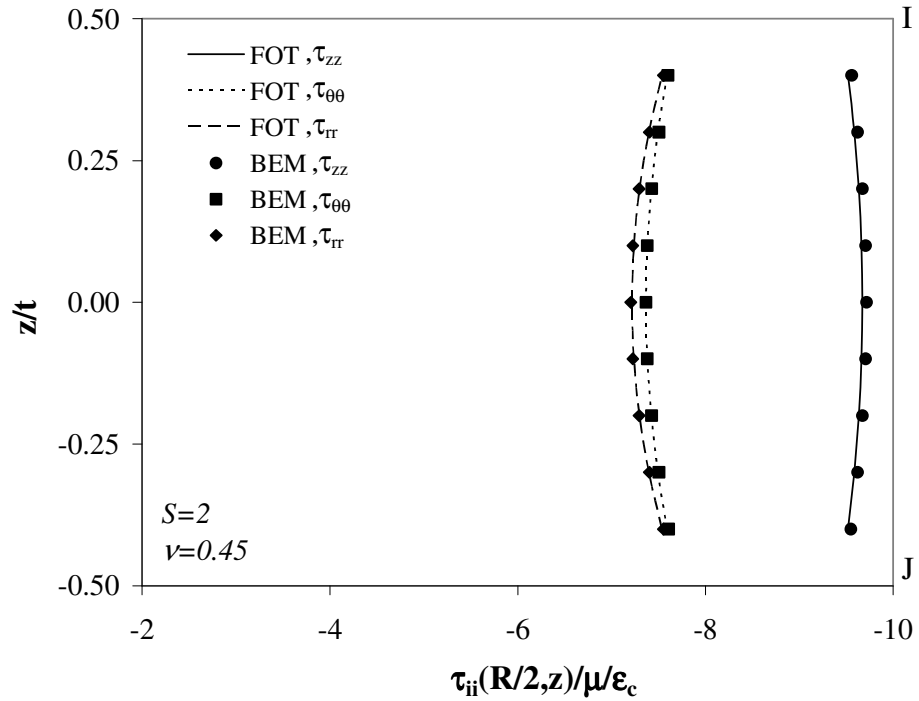


Figure 5.9 Variation of normalized radial, circumferential and axial stresses ($\tau_{ii}/\mu\epsilon_c$ for $i=r,\theta,z$) through the layer thickness at $r=R/2$

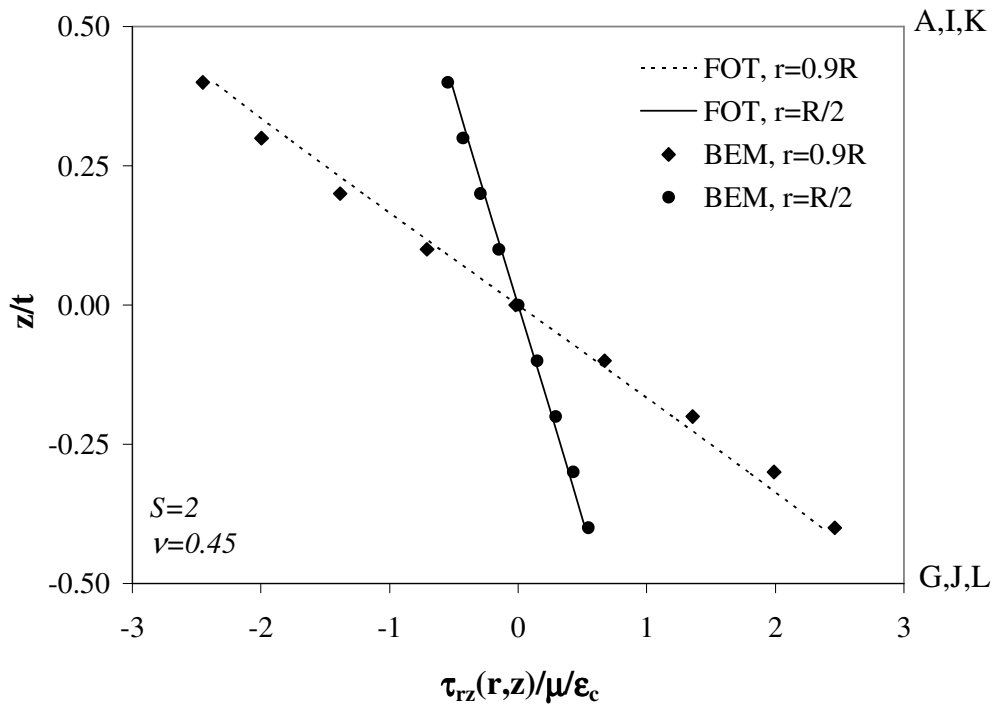


Figure 5.10 Variation of normalized shear stress through the layer thickness

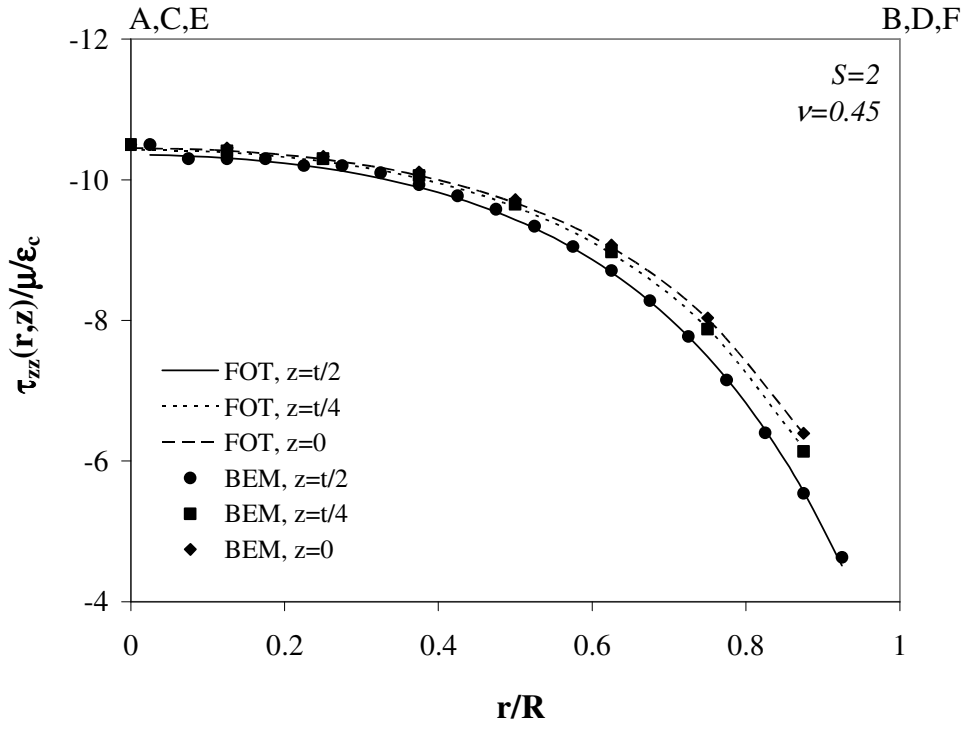


Figure 5.11 Variation of normalized axial stress through the radius

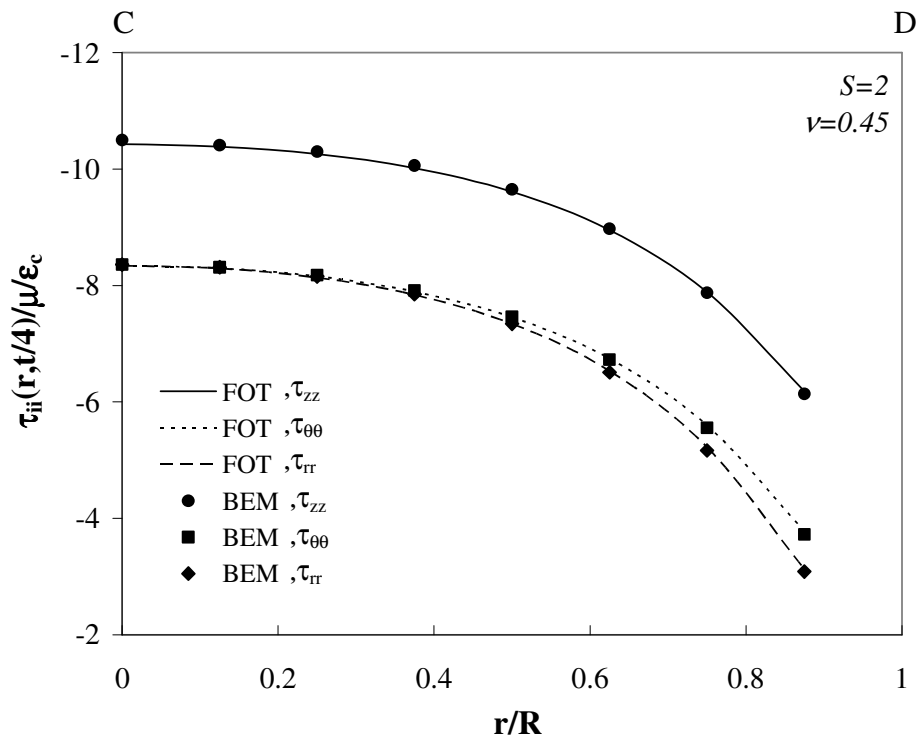


Figure 5.12 Variation of normalized radial, circumferential and axial stresses ($\tau_{ii}/\mu\epsilon_c$ for $i=r,\theta,z$) through radius at $z=t/4$

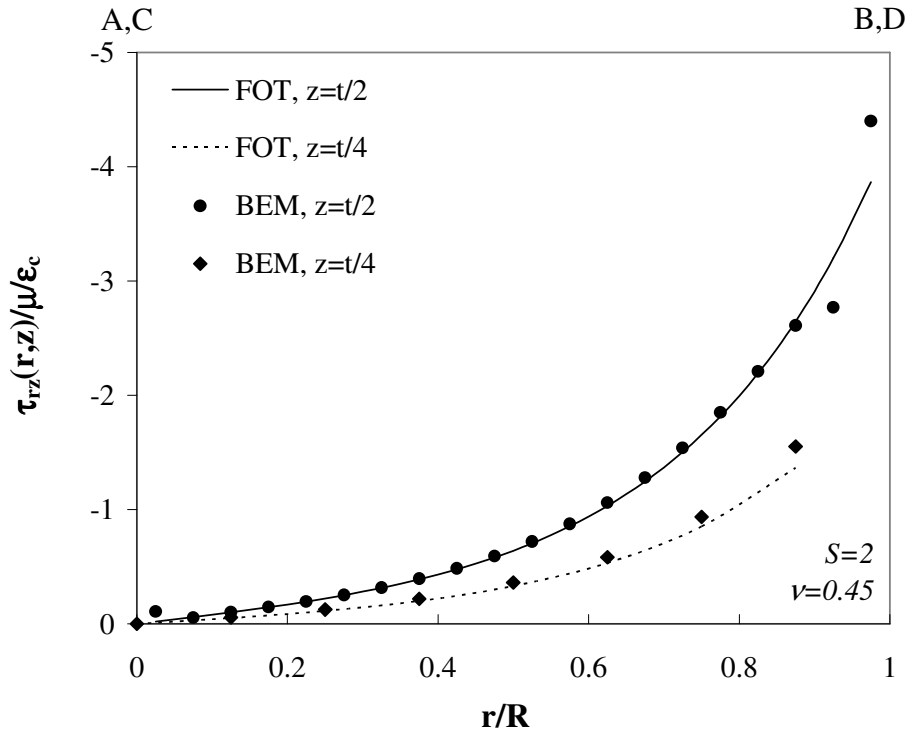


Figure 5.13 Variation of normalized shear stress through the radius

Figure 5.7 and Figure 5.8 demonstrate the distributions of the radial stress τ_{rr} and axial stress τ_{zz} in the axial direction over three different sections, $r=0$, $R/2$, $0.9R$. From the plots, it can be seen that both radial and axial stresses reach their peak values at the center, at $r=0$. Their distributions over the central section are more or less uniform while this uniformity seems to be lost near the lateral surface. To compare the variation of all components of the normal stress, namely, radial, circumferential and axial stresses, at a particular section, stress distributions are also determined at $r=R/2$ and plotted in a single graph presented in Figure 5.9. This figure reveals that axial stress is larger than radial and circumferential stresses, which are almost equal. Axial stress is different from radial and circumferential stress also in its variation pattern: while maximum value of axial stress occurs at the center of the layer ($z=0$), peak values of the other normal stress components occur at the bonded faces ($z=\pm t/2$). The variation of the shear stress through the layer thickness is plotted in Figure 5.10, which shows that the shear stress increases from

the center to the bonded edges almost linearly; the variation is linear even when the vertical section is very close to the lateral surface.

The distributions of normal and shear stresses in the radial direction are plotted over various sections in the layer and presented in Figure 5.11 to Figure 5.13. From these graphs, it may be observed that while normal stresses decrease, the shear stress increases along the radial direction. It should be noted that the variation of shear stress is *not* linear as predicted by the “incompressible” theory. It is also noticeable that the FOT predictions for the stress distributions are close to the BEM results for all studied cases.

5.1.5 Effect of Mesh Size

The effect of the mesh size on the BEM results is also investigated by analyzing this specific compression problem ($S=2$, $\nu=0.45$) using several models with different meshing properties (Table 5.1). As it can be inferred from this table, the initial coarse mesh with only 25 elements is increased step by step to a considerably fine mesh consisting of 100 elements in the fifth model. The prediction of each model for the compression modulus of the layer is also given in Table 5.1. As it can be understood from the tabulated values, even the coarsest mesh predicts the compression modulus of the layer with relatively good accuracy.

Table 5.1 Definition of BEM models with different mesh sizes and their predictions for compression modulus ($S=2$, $\nu=0.45$)

Model Number (n)	Model Name	# of elements			$(E_c)_n/\mu$	$(E_c)_n/(E_c)_{n-1}$	$(E_c)_n/(E_c)_{FOT}$
		along width	along thickness	total			
1	BEM/25	10	5	25	7.724	-	0.989
2	BEM/38	15	8	38	7.762	1.005	0.994
3	BEM/50	20	10	50	7.788	1.003	0.997
4	BEM/75	30	15	75	7.816	1.004	1.000
5	BEM/100	40	20	100	7.821	1.000	1.001

The effect of the mesh size on the BEM results is also investigated by comparing the predictions of each model for the stress distributions. Figure 5.14 illustrates two of such comparisons. As shown in the plots, the stress values predicted by the model with the coarsest mesh deviate from the predictions of the other models considerably particularly for the radial stress distribution given in Figure 5.14a. On the other hand, the predictions of the models with finer meshes almost coincide. It is also noticeable from Figure 5.14a that as the mesh size increases, the BEM results come closer to the FOT prediction.

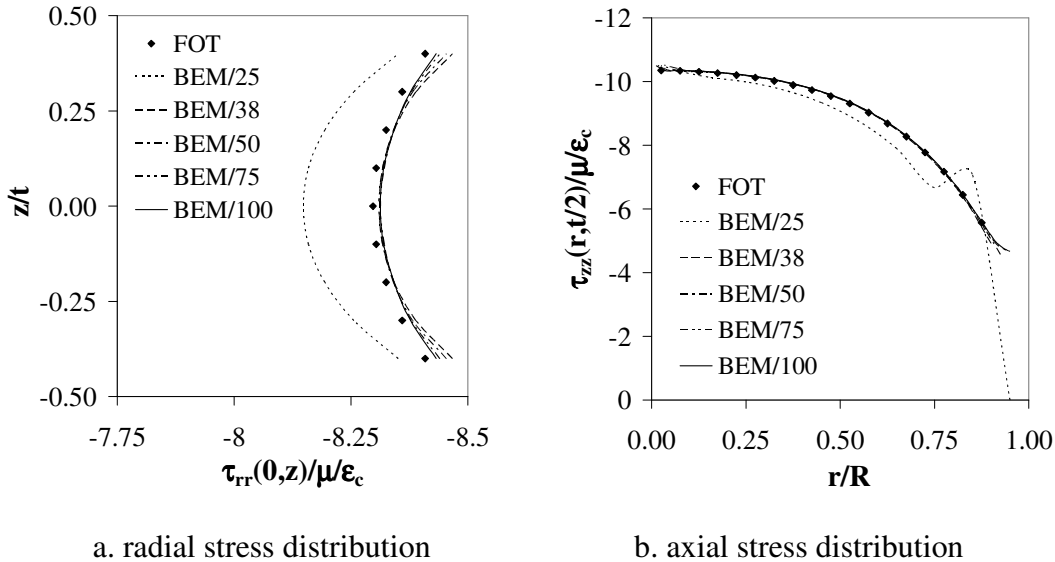


Figure 5.14 Effect of mesh size on BEM predictions for stress distributions

From Table 5.1 and Figure 5.14, it is clear that even the use of the model with 38 elements is sufficient to obtain “mesh-size-independent” BEM results. However, as already illustrated in Figure 5.1, for the results presented in the preceding sections, the model with 50 elements is used. This selection is mainly dictated by the desire to have somewhat more elements at the boundaries so that the displacement/stress distributions can be plotted accurately using more points.

5.2 PROBLEM 2: AN HC-SHAPED LAYER UNDER COMPRESSION

The expressions derived for HC-shaped bonded elastic layers are verified by comparing the FOT predictions with the BEM results for an LSF layer of $S_0=R/t=4$ with two different values of hole diameter; $a/t=0.4$ and 2, corresponding to the radius ratios $\beta=R/a=0.1$ and 0.5, respectively. The predictions for a C-shaped layer of $S=2$, corresponding to the radius ratio $\beta=0$, are also included in the stress plots so that the effect of the presence of a central hole on the compressive behavior of a bonded disc can also be examined. A relatively high value of Poisson's ratio, 0.499, is selected in this study to simulate the problem of a bonded rubber layer.

5.2.1 BEM Model

BEM analysis of the considered HC-shaped layer is performed using the same program used in the analysis of the C-shaped layer studied in the first problem. The discretization of the layer boundary in this problem, shown in Figure 5.15, is very similar to that defined in Figure 5.1.

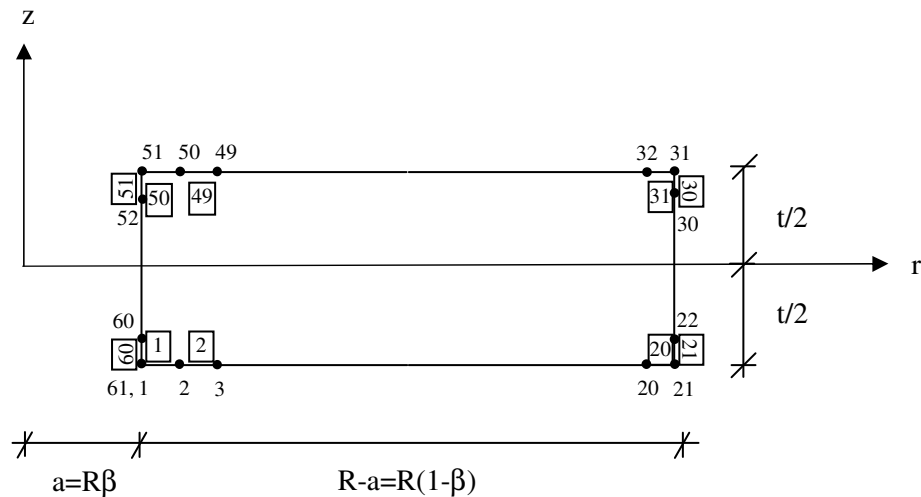


Figure 5.15 Discretization of the HC-shaped bonded elastic layer for BEM analysis

The major difference between the models in Figure 5.1 and Figure 5.15 is that while only the outer boundary is discretized in the C-shaped layer, the inner boundary is also discretized in the HC-shaped layer due to the presence of the hole. The BC's in this case are similar to the previous problem: as the displacement BC's at the bonded faces, $u_z = \pm \Delta/2$ and $u_r = u_\theta = 0$, and as the stress (traction) BC's at the lateral traction-free boundaries, i.e., at both $r=a$ and $r=R$, $t_i = 0$, $i=r, \theta, z$.

5.2.2 Compression Modulus

The predictions of both FOT and BEM for the compression modulus of the analyzed layers are given in Table 5.2. From the table, it is seen that the FOT results are very close to the BEM results for all studied cases. To investigate the effect of the presence of a central hole in the layer on its compression modulus, the ratios of the results obtained for HC-sections to those for C-section are also listed in the last column of the table. It may be observed that the presence of even a small hole ($a/t=0.4$) in the layer reduces the compression stiffness of the layer by about 25%. When the radius ratio reaches to the value of 0.5, the compression stiffness of the layer becomes even smaller than one-third of its corresponding solid value. In fact, due to the presence of such a large hole in the layer, the layer starts to behave as if it were an IS-shaped bonded elastic layer with $w/t=1$. The FOT prediction for E_c of an IS-shaped layer with $S=1$ and $\nu=0.499$ is 7.923μ , which is indeed close to the value determined from the boundary element analysis of the HC-shaped layer with $\beta=0.5$.

Table 5.2 BEM and FOT predictions for compression modulus of the HC-shaped layer ($S_0=2$, $\nu=0.499$) with different hole sizes

Model Number (n)	a	β	$(E_c)_{\text{BEM}}/\mu$	$(E_c)_{\text{FOT}}/\mu$	$(E_c)_{\text{BEM}}/(E_c)_{\text{FOT}}$	$(E_c)_{\text{n,BEM}}/(E_c)_{\text{1,BEM}}$
1	0	0	25.48	25.47	1.00	1.00
2	0.4	0.1	19.20	19.35	0.99	0.75
3	2.0	0.5	8.126	8.070	1.00	0.32

5.2.3 Stress Distributions

Stress distributions in an HC-shaped bonded rubber layer of $R/t=4$ with different radius ratios are plotted in Figure 5.16 to Figure 5.18. The agreement of the FOT predictions with the BEM results is considerably good in all of these plots. These graphs also show the effect of the hole size on the distribution of stress components in the layer, which will be discussed later in more detail. The only thing that is worth noting at this point is that, as discussed in the previous section, the compressive behavior of an HC-shaped bonded elastic layer approaches the compressive behavior of an IS-shaped bonded elastic layer as the hole diameter increases. In fact, the curves for $\beta=0.5$ in Figure 5.16 to Figure 5.18 are very close to those of strip layers.

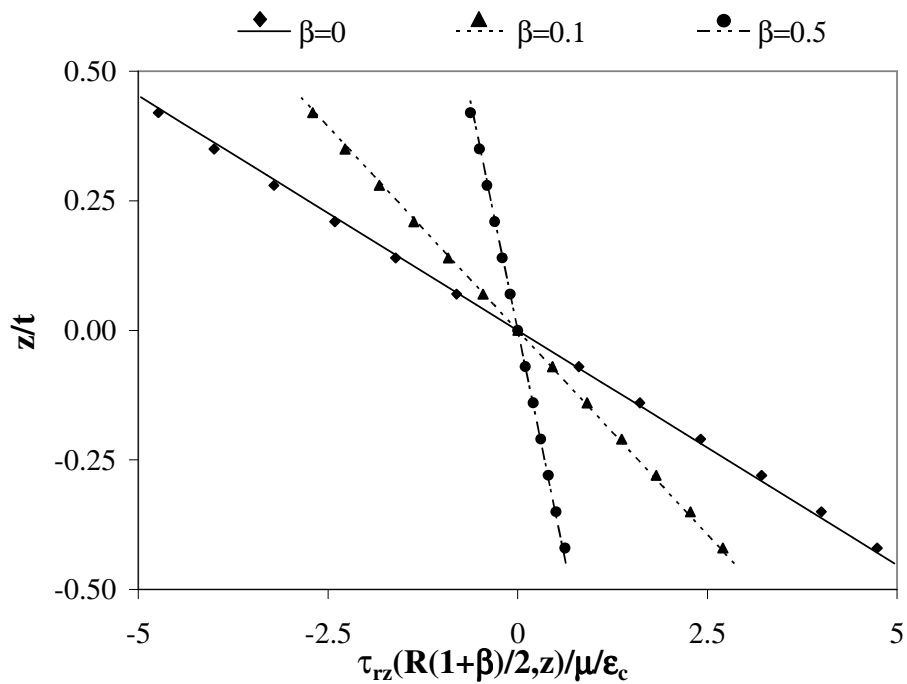


Figure 5.16 Variation of shear stress through the layer thickness in the HC-shaped layer ($S_0=2$, $\nu=0.499$) with different radius ratios predicted by FOT (continuous lines) and BEM (discrete points)

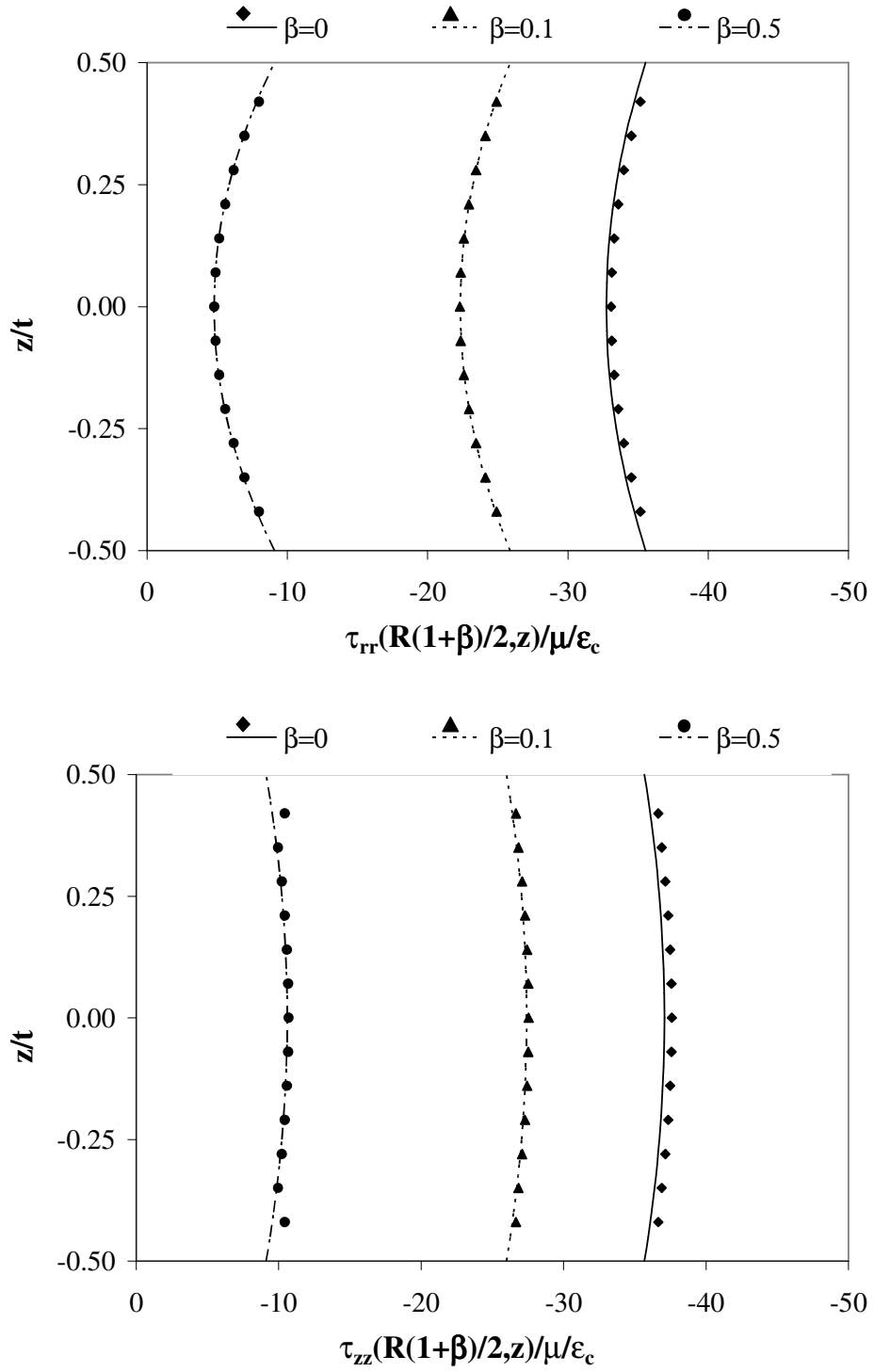


Figure 5.17 Normal stress distributions through the layer thickness in the HC-shaped layer ($S_0=2$, $\nu=0.499$) with different radius ratios predicted by FOT (continuous lines) and BEM (discrete points)

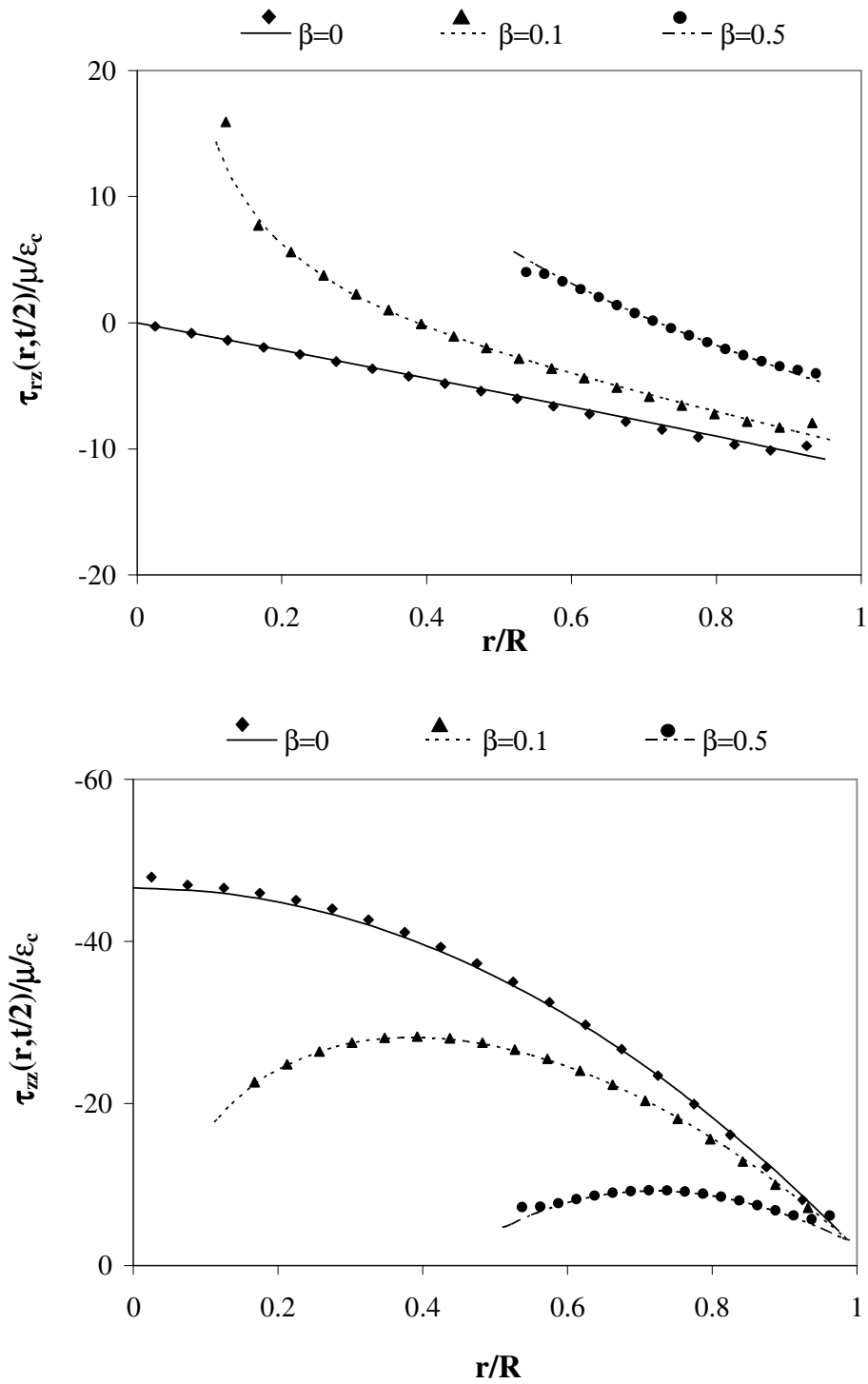


Figure 5.18 Stress distributions over the bonded faces in the HC-shaped layer ($S_0=2$, $\nu=0.499$) with different radius ratios predicted by FOT (continuous lines) and BEM (discrete points)

5.3 PROBLEM 3: AN IS-SHAPED LAYER UNDER COMPRESSION

As already mentioned, FOT eliminates one of the two commonly used kinematics assumptions: the assumption that plane sections remain plane. On the other hand, parabolic bulging assumption is still included in the expressions. Thus, it is valuable to check the validity of these two assumptions through BEM. In this problem, the analyses are conducted for an IS-shaped layer with $S=5$. Displacement distributions are plotted for $\nu=0.3, 0.45, 0.49, 0.499$, so that the effect of ν can also be studied. FOT predictions are also added to the plots to assess the formulation.

5.3.1 BEM Model

BEM analysis is performed using the FORTRAN program D2D, which was developed by Mengi et al. [51] for two dimensional (2-D) dynamic analysis of elastic bodies. The discretization of the layer boundary using simple line elements in x_1 - x_2 plane is illustrated in Figure 5.19.

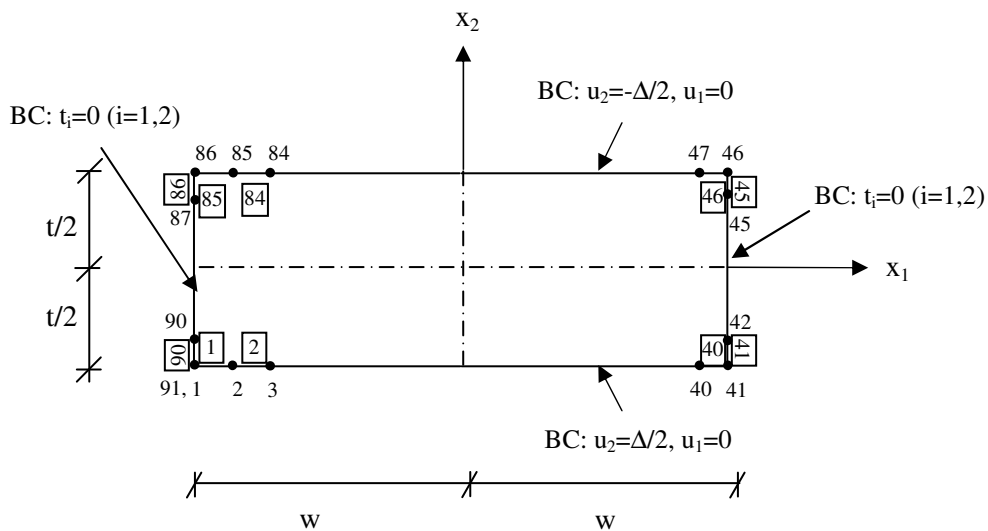


Figure 5.19 Discretization of the IS-shaped bonded elastic layer for the compression problem (Boundary conditions (BC's) are also specified)

5.3.2 Compression Modulus

Similar to the program used in the axisymmetric problems (AXI), the program used in the plane-strain problems (D2D) is capable of computing the resulting forces acting at the boundaries. The compression modulus of the analyzed layer, thus, can easily be computed once the resultant axial force P is determined at the bonded faces. The predictions of both FOT and BEM for the compression modulus of the analyzed layer are tabulated in Table 5.3.

Table 5.3 BEM and FOT predictions for compression modulus of the IS-shaped layer of $S=5$ with different compressibility characteristics

Model Number (n)	ν	$(E_c)_{BEM}/\mu$	$(E_c)_{FOT}/\mu$	$(E_c)_{BEM}/(E_c)_{FOT}$	$(E_c)_{n,BEM}/(E_c)_{1,BEM}$
1	0.3	3.4209	3.4305	0.997	1.00
2	0.45	9.5212	9.5901	0.993	2.78
3	0.49	31.446	31.890	0.986	9.19
4	0.499	81.939	84.069	0.975	23.95

As it can be concluded from Table 5.3, FOT yields results close to those of BEM. The difference between the predictions of the two methods, which is not more than 3%, seems to increase as the value of Poisson's ratio increases. Considering that the same meshing is used in the analyses of all layers with different compressibility characteristics, this deviation can be attributed to the meshing effects in BEM. The results presented in the table also show that the compression modulus of the layer increases as the material compressibility decreases. Even though the shape factor of the layer is not too large, the compression modulus of the layer with $\nu=0.499$ is 24 times larger than that with $\nu=0.3$.

5.3.3 Displacement Distributions

Assessment of the two kinematics assumptions commonly used in the analysis of bonded elastic layers; namely, the parabolic bulging assumption and the assumption “the plane sections remain plane” is considered in Figure 5.20a-b for an IS-shaped bonded elastic layer with a shape factor $S=5$ subjected to uniform compression. Besides the BEM results (plotted as discrete points), the FOT predictions (plotted in continuous lines) are also included in Figure 5.20a-b. Since both over the bonded faces and at the central plane, plane sections remain plane, it is quite reasonable to investigate the axial displacement distribution along the width of the layer at the level of quarter thickness (i.e., at $x_2=\pm t/4$).

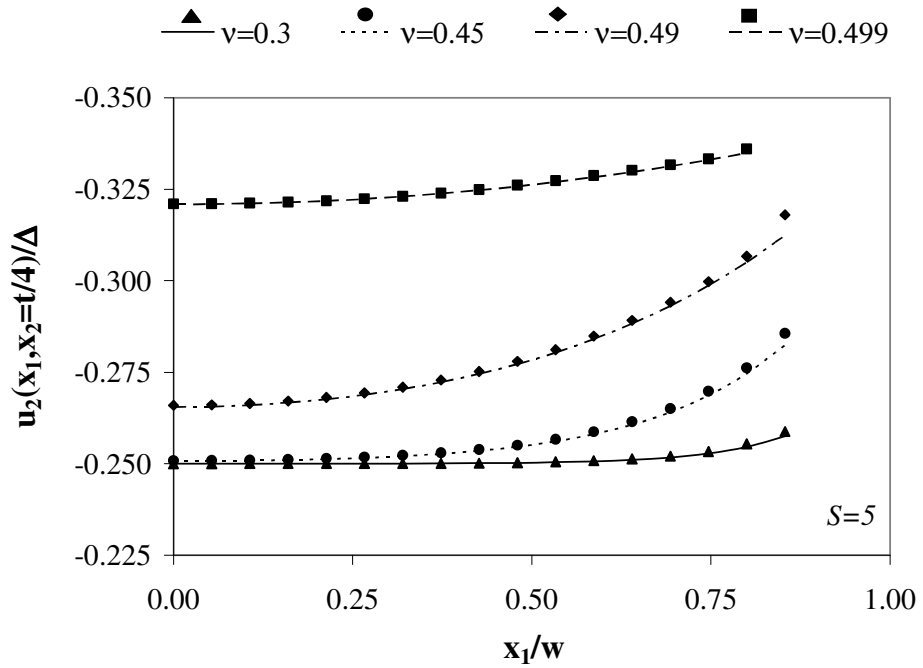
From Figure 5.20a, one can conclude that while the assumption that plane sections remain plane is somewhat reasonable for highly compressible ($\nu=0.3$) materials, for materials with larger Poisson’s ratio, this assumption is not valid. On the other hand, the parabolic bulging assumption can be accepted as a very realistic assumption as shown in Figure 5.20b for the studied S value. In addition, the plots presented in Figure 5.20 clearly show good agreement between the FOT and BEM predictions for all studied values of Poisson’s ratio.

5.4 PROBLEM 4: AN IS-SHAPED LAYER UNDER BENDING

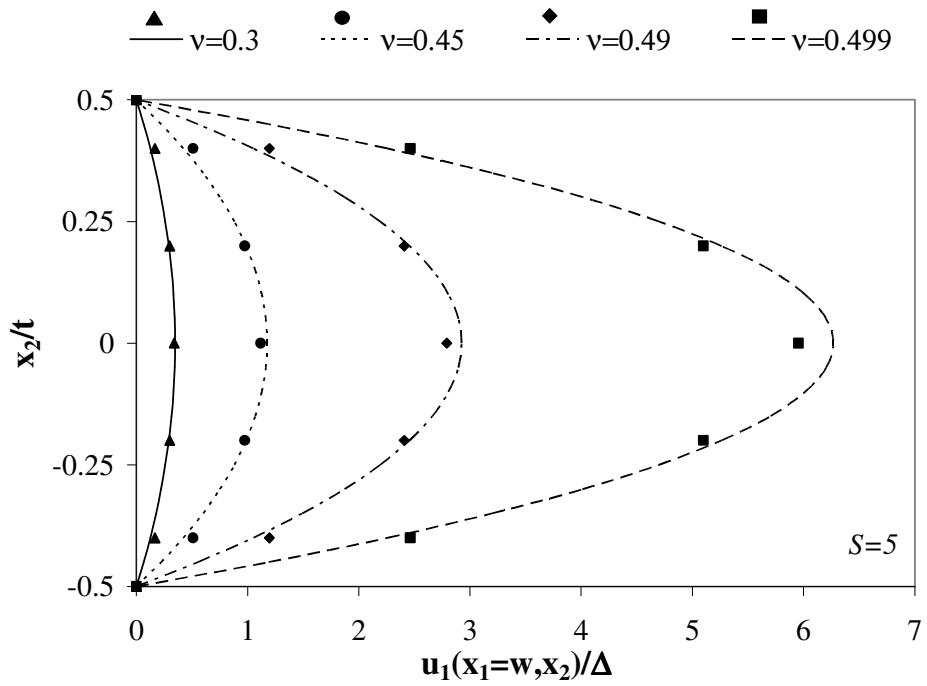
For the assessment of the analytical solutions obtained for IS-shaped bonded elastic layers under pure bending, a strip shaped layer with a shape factor of $S=2.5$ and Poisson’s ratio of $\nu=0.49$ is modeled and analyzed using BEM.

5.4.1 BEM Model

Similar to the previous compression problem, the BEM analysis of this bending problem is performed using the program D2D. The discretization of the layer is shown in Figure 5.21. The boundary conditions at the bonded faces are $u_2=\pm\phi x_1/2$, $u_1=0$.



a. assumption that plane sections remain plane



b. parabolic bulging assumption

Figure 5.20 Assessment of the validity of two basic assumptions through the comparison of FOT (continuous lines) and BEM (discrete points) predictions

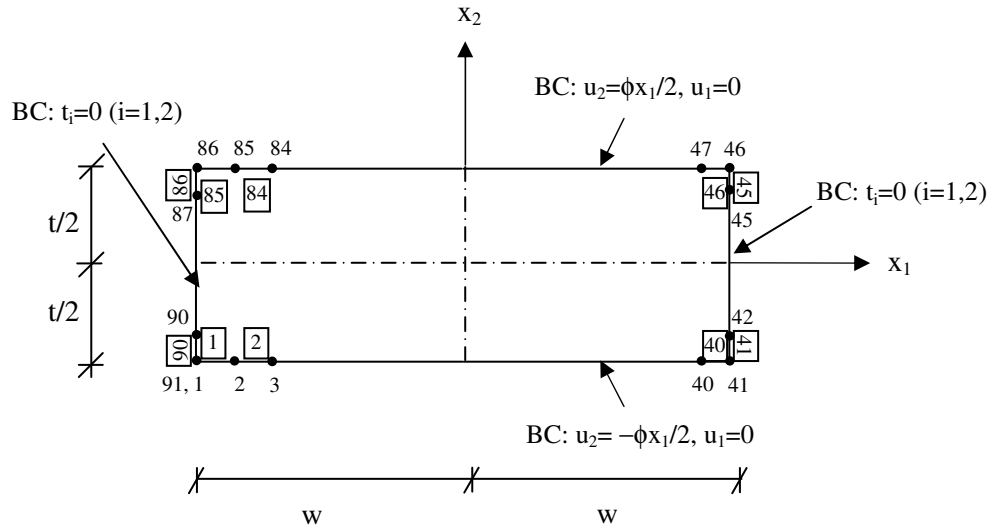


Figure 5.21 Discretization of the IS-shaped bonded elastic layer for the bending problem (Boundary conditions (BC's) are also specified)

5.4.2 Bending Modulus

The program used in the analysis is capable of computing the resulting moments acting at the boundaries, which permits the evaluation of the bending modulus of the layer by Eqs. (3.62). The prediction of FOT for an IS-shaped layer with $S=2.5$ and $\nu=0.49$ is $E_{b,FOT}=7.975\mu$, which is in a good agreement with the BEM result $E_{b,BEM}=7.953\mu$.

5.4.3 Displacement and Stress Distributions

Displacement and stress distributions over various sections in the layer are plotted in Figure 5.22 to Figure 5.24. Since the bending behavior of IS-shaped bonded elastic layers will be studied in more detail in the subsequent chapter, here only the assessment of the formulation will be considered. As it can be seen from the graphs in Figure 5.22 to Figure 5.24, the new formulation proposed in this dissertation leads to the derivation of analytical solutions which are in good agreement with the numerical results obtained by BEM.

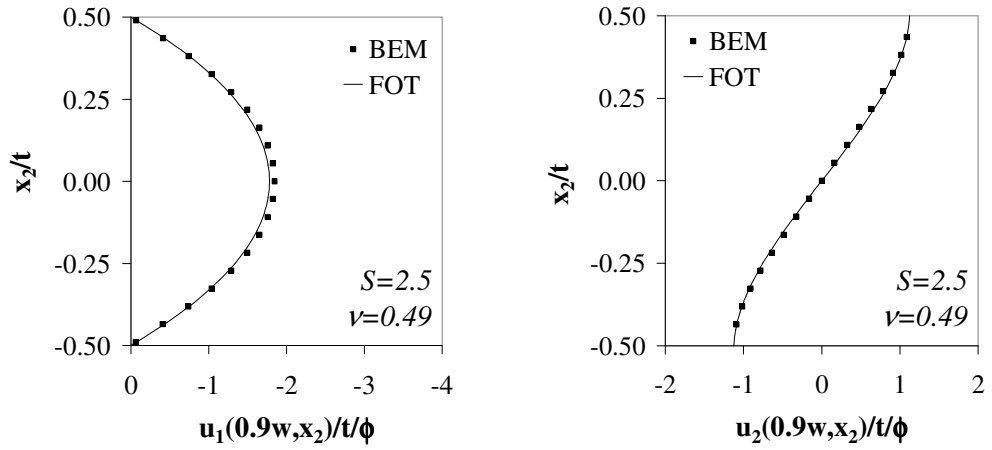


Figure 5.22 Displacement distributions through the layer thickness under pure bending

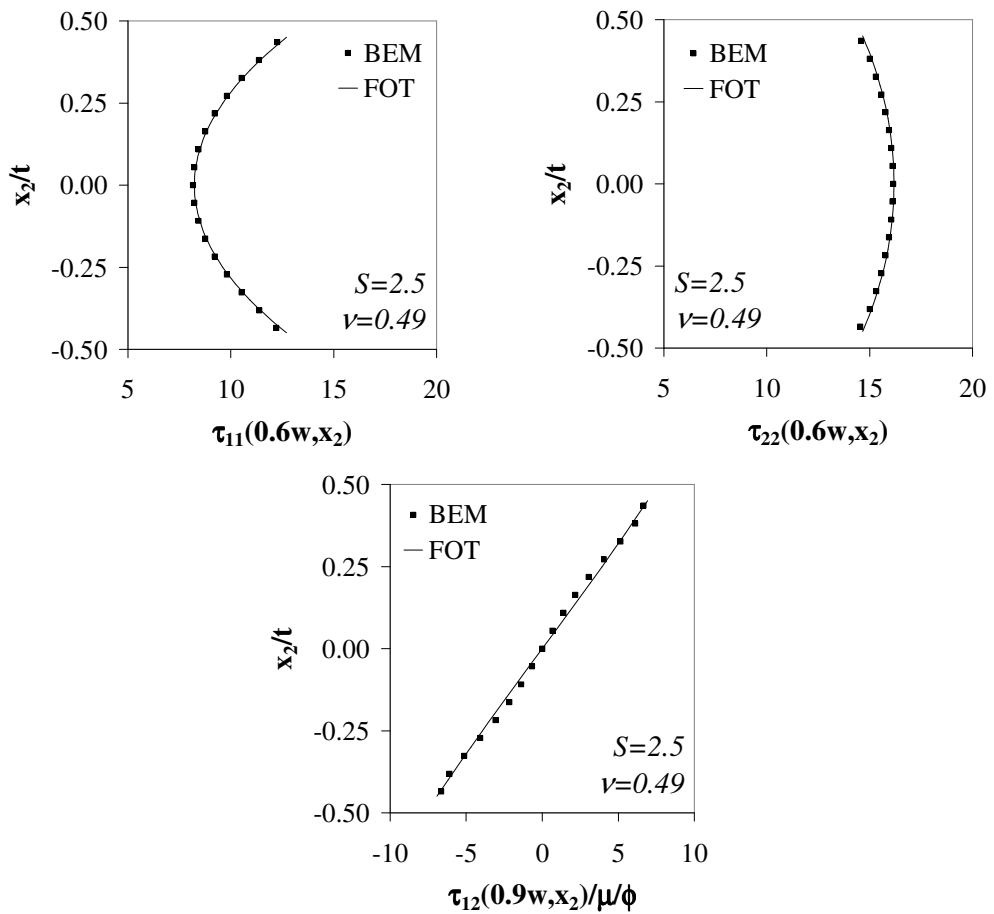


Figure 5.23 Stress distributions through the layer thickness under pure bending

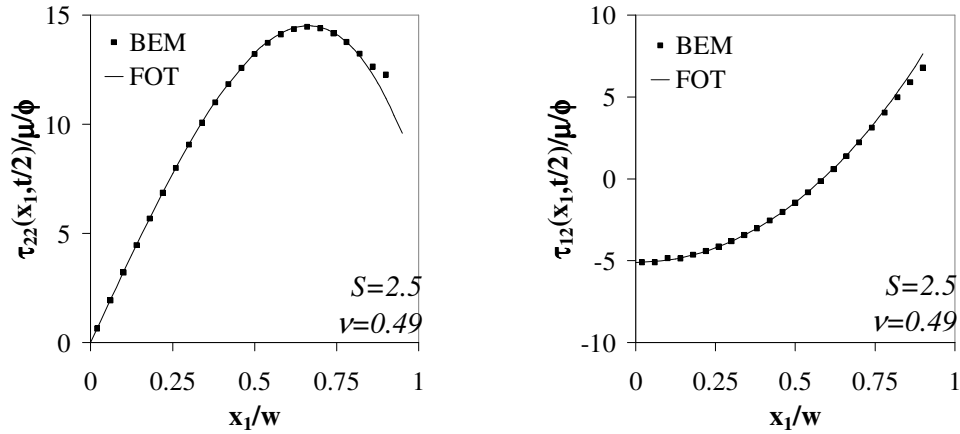


Figure 5.24 Stress distributions at the bonded faces under pure bending

5.5 PROBLEM 5: AN IS-SHAPED LAYER UNDER APPARENT SHEAR

The behavior of an IS-shaped bonded elastic layer under apparent shear can also be investigated using BEM. Since the effect of the bonded faces to the shear behavior of the layer becomes noticeable only when the thickness of the layer is large and when the layer material is compressible, a soft ($\nu=0.3$) layer with a relatively low shape factor, $S=1$, is selected for the analysis.

5.5.1 BEM Model

The discretization of the layer boundary for the apparent shear problem is similar to the compression problem (see Figure 5.25). The main difference between these two problems is the displacement BC's at the bonded faces, which move, in shear problem, in horizontal direction without any movement in vertical direction.

5.5.2 Apparent Shear Modulus

The apparent shear modulus can be computed from the shear force by using Eqs. (3.63). The BEM result $\mu_{a,BEM}=0.848$ is close to the FOT prediction $\mu_{a,FOT}=0.846$ for the considered S and ν values.

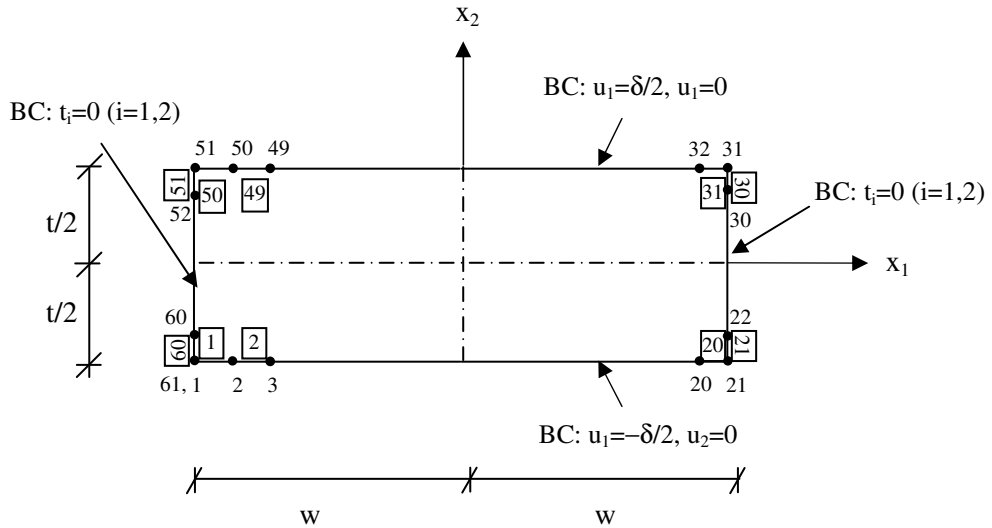


Figure 5.25 Discretization of the IS-shaped bonded elastic layer for apparent shear problem (Boundary conditions (BC)'s) are also specified

5.5.3 Displacement and Stress Distributions

Figure 5.26 and Figure 5.27 present typical displacement and stress distributions in the analyzed layer. As shown in the figures, FOT predictions fit closely the BEM results.

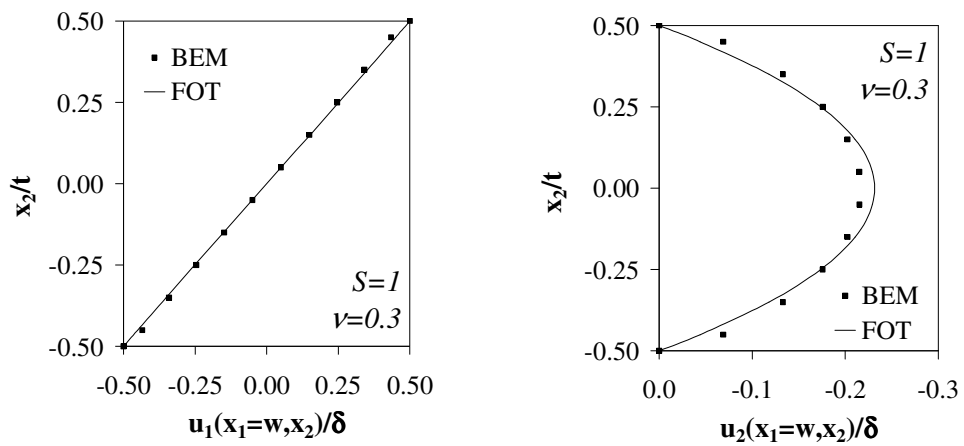


Figure 5.26 Displacement distributions under apparent shear

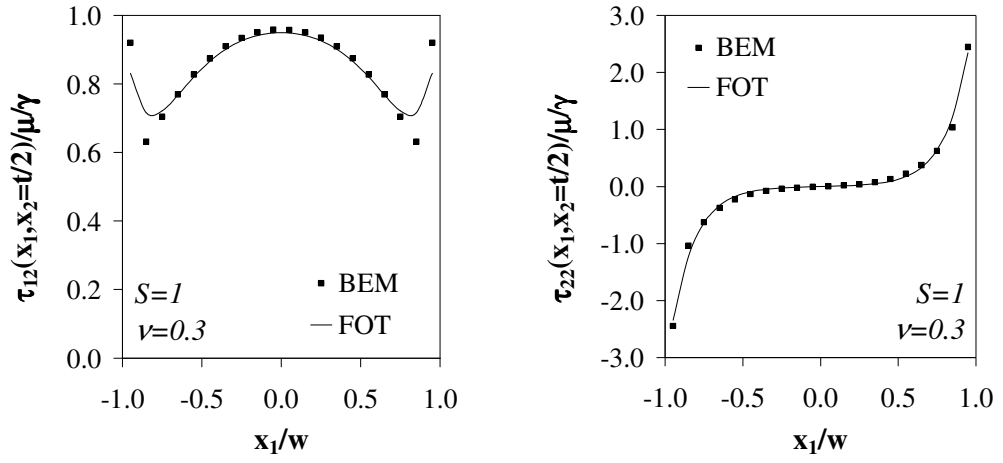


Figure 5.27 Stress distributions at the bonded faces under apparent shear

CHAPTER 6

EFFECT OF POISSON'S RATIO AND SHAPE FACTOR ON BEHAVIOR OF BONDED ELASTIC LAYERS

The behavior of an elastic layer bonded to rigid surfaces is mainly controlled by two basic parameters characterizing the geometrical and material properties of the layer: shape factor (S) and Poisson's ratio (ν). Eliminating most of the assumptions used in literature for the displacement and stress distributions in the layer, the new formulation proposed in this dissertation has lead, with the use of the first order theory (FOT), to quite realistic expressions, which can be used to study the effects of these two important parameters on behavior of bonded elastic layers thoroughly.

Since the effect of the reinforcement flexibility is examined in a later chapter, in this chapter only the layers bonded to rigid reinforcements are studied. Moreover, to have a complete study comprising not only the compressive but also the bending and apparent shear behavior of bonded elastic layers, the discussions in this chapter are devoted to IS-shaped layers, for which the closed form expressions have been derived for all three fundamental deformation modes.

6.1 COMPRESSIVE BEHAVIOR

Figure 6.1 shows the effects of shape factor and Poisson's ratio on compression modulus E_c . As it is seen from the plots, E_c of an HSF rubber layer, for which ν is very close to 0.5, may be thousands times of its shear modulus μ .

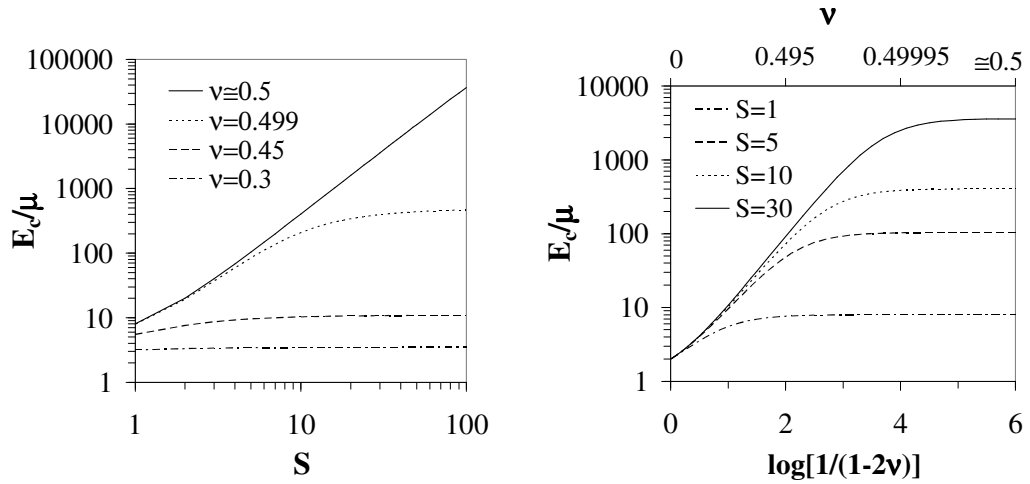


Figure 6.1 Effect of shape factor and Poisson's ratio on compression modulus

Figure 6.2 shows the effect of Poisson's ratio on displacement distributions over the finite width of the layer under uniform compression for two different shape factors; $S=1$, representing LSF layers, and $S=30$, representing HSF layers. To study the behavior of the layers over a wide range of material compressibility, the displacement distributions are plotted for four different values of ν ; 0.5, 0.499, 0.45 and 0.3. Since the maximum bulging occurs at the central plane, the lateral displacement (u_1) distributions are plotted at $x_2=0$. For the axial displacement component (u_2), it is realistic to plot the variation over the section at the quarter thickness ($x_2=t/4$) since both at the central plane ($x_2=0$) and over the bonded faces ($x_2=\pm t/2$), horizontal plane sections remain plane and horizontal.

From Figure 6.2a, it is seen that, for the normalized lateral displacement ($u_1/S\Delta$), FOT prediction satisfactorily converges, as predicted by the incompressible theory [2], to the linear variation as the compressibility of the layer decreases. This linear behavior is valid also for nearly incompressible materials for the LSF layer ($S=1$). Linearity is lost when the material compressibility is increased. On the other hand, for the HSF layer ($S=30$), the linearity is not achieved even for nearly incompressible materials ($\nu=0.499$).

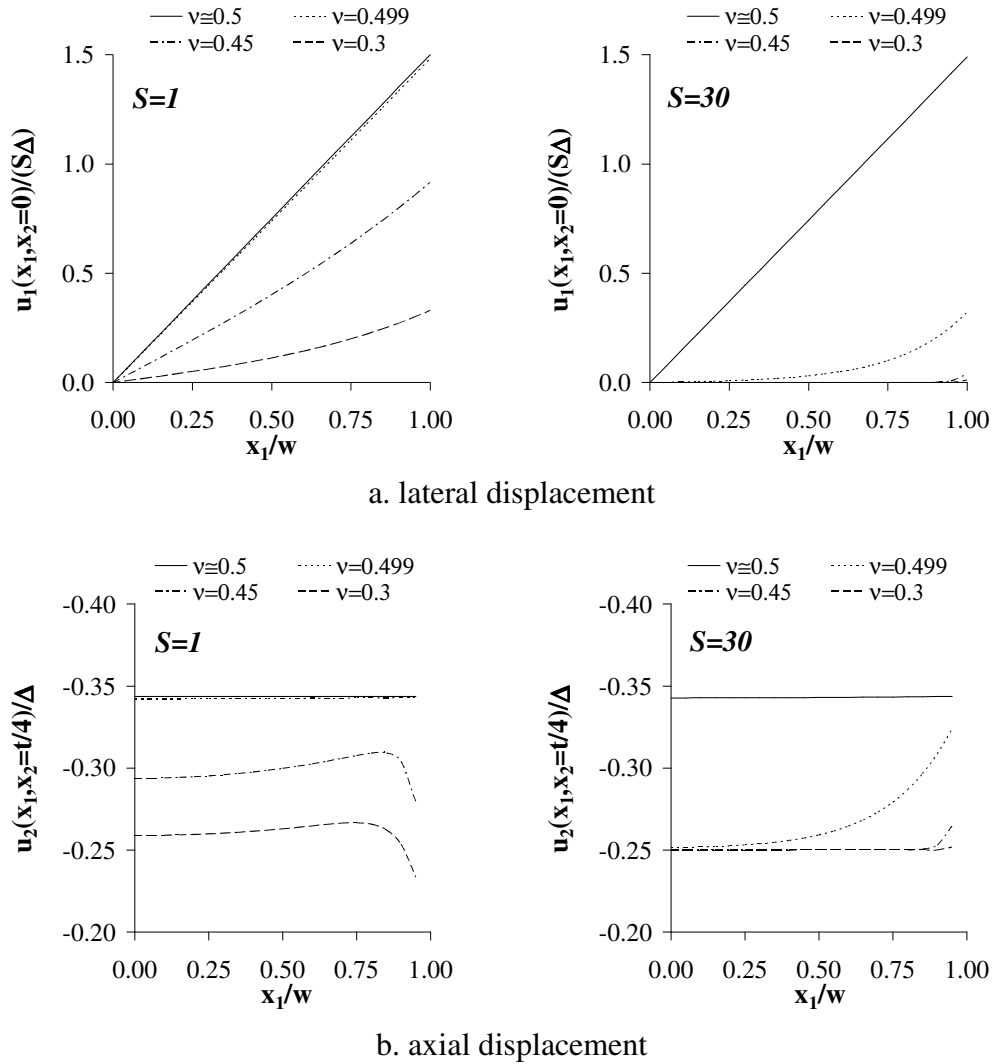


Figure 6.2 Effect of Poisson's ratio on displacement distributions in lateral direction under uniform compression

As far as the axial displacement is concerned (Figure 6.2b), “the plane sections remain plane” assumption seems to be valid for strictly incompressible materials regardless of the value of S . For $S=1$, it is also valid for nearly incompressible materials while it starts to lose its validity for more compressible materials. For $S=30$, the axial displacement distribution deviates from uniform distribution considerably even for $\nu=0.499$. It is also noteworthy that plane sections remain plane in the HSF layer if the layer material is highly compressible materials.

It is to be noted that the discontinuities observed in u_2 distributions are natural consequence of using an approximate theory (FOT) in the formulation.

Figure 6.3 shows the displacement distributions through the layer thickness. u_1 distributions in Figure 6.3a are plotted at $x_1=w$, where the bulging is maximum. From Figure 6.3a, it may be observed that the normalized curves for $S=1$ and $S=30$ are identical for incompressible materials. On the other hand, the displacement values are influenced from S considerably for even slightly compressible materials.

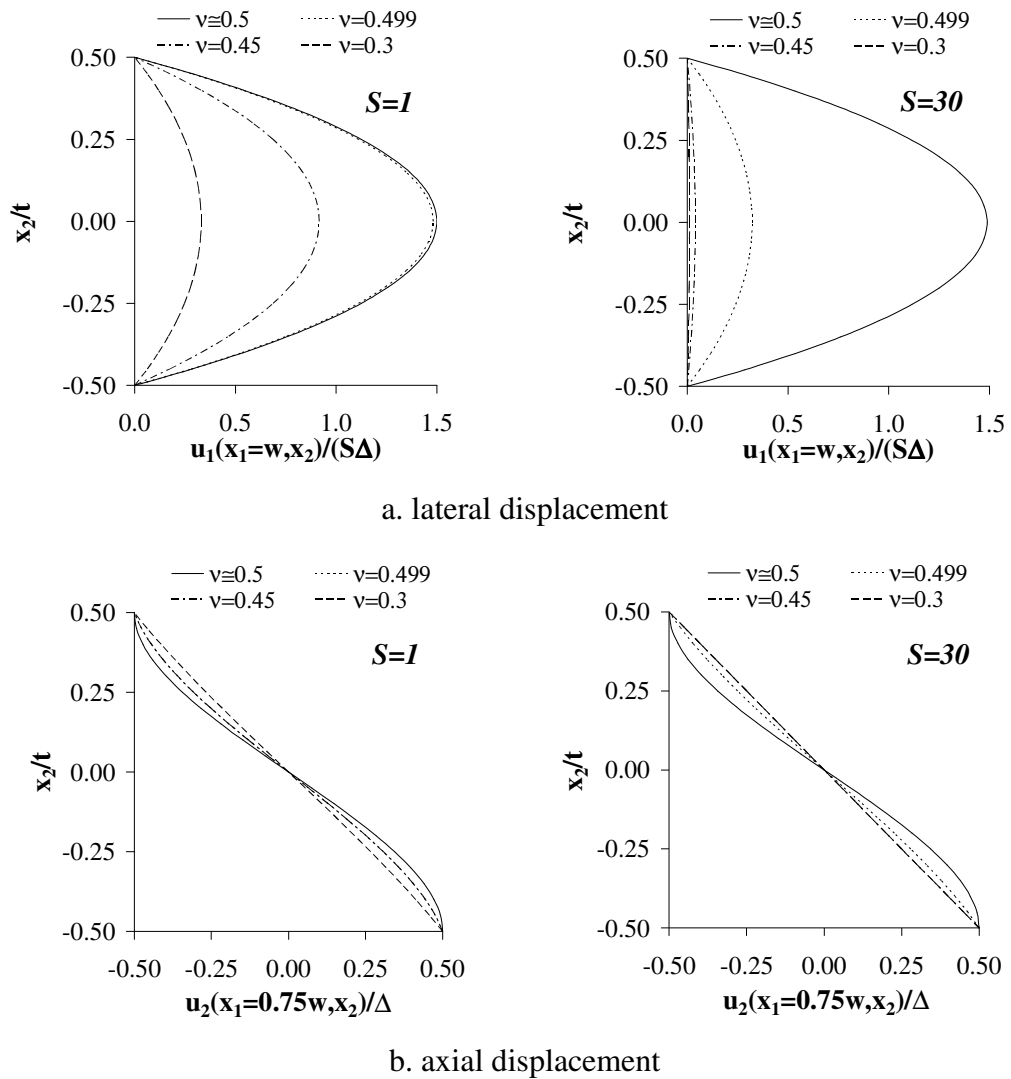


Figure 6.3 Effect of Poisson's ratio on displacement distributions through the layer thickness under uniform compression

Since u_2 distributions have discontinuities near the edges, the variations presented in Figure 6.3b are plotted at a vertical section at $x_1=0.75w$, which is thought to be sufficiently away from the region having discontinuities. The most important conclusion that can be drawn from Figure 6.3b may be the fact that while u_2 distribution is almost linear through the layer thickness for highly compressible materials ($\nu=0.3$), it is nonlinear for incompressible materials.

Maximum bulging, which occurs at $x_1=\pm w$ and $x_2=0$, may be a matter of concern in the design of bonded elastic layers. To investigate the effects of shape factor and Poisson's ratio on maximum bulging in more detail, the normalized maximum bulging is plotted with respect to each parameter separately in Figure 6.4. Except the incompressible case, when the maximum bulging is equal, regardless of the value of the shape factor, to $1.5w\epsilon_c$, the normalized maximum bulging decreases as the shape factor of the layer increases. For a specific value of shape factor, the maximum bulging increases as the material compressibility decreases until the asymptotic incompressible value, i.e., $1.5w\epsilon_c$, is approached. HSF layers attain their asymptotic values at much larger values of Poisson's ratio.

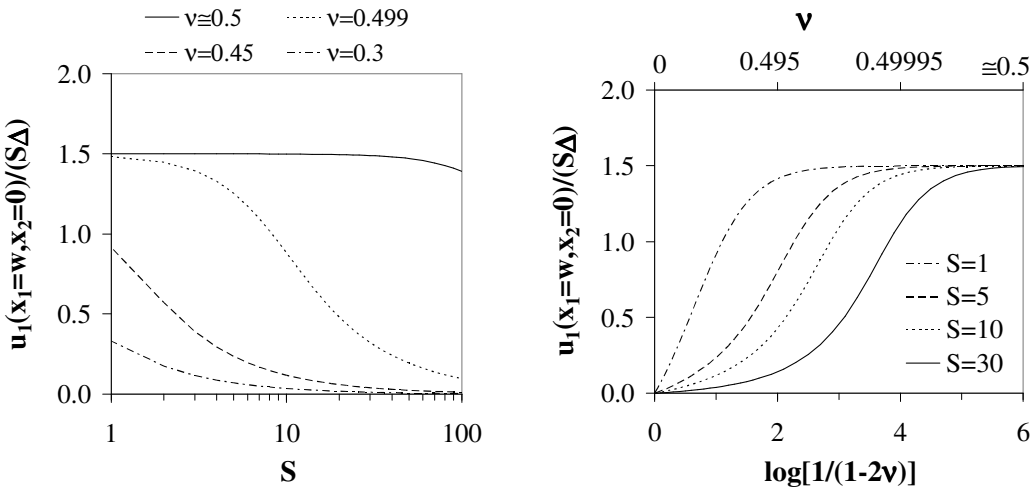


Figure 6.4 Effect of shape factor and Poisson's ratio on maximum bulging under uniform compression

It may also be valuable to investigate the effects of shape factor and Poisson's ratio on the axial displacement at the quarter thickness of the layer. Since u_2 is not constant in general along x_1 direction, the graphs in Figure 6.5 are plotted at two different sections, $x_1=0, 0.75w$. Comparison of these two graphs also enables one to assess the validity of "the plane sections remain plane" assumption. From the graphs, it is seen that, for highly compressible materials, u_2 at the quarter-thickness is constant and equal to the quarter of the applied displacement, i.e., 0.25Δ . Plane sections also remain plane in layers of incompressible materials, for which the axial displacement is about 0.34Δ . In between these two limiting cases, the assumption that plane sections remain plane is not valid in general. The displacement values at $x_1=0$ and $x_1=0.75w$ may deviate considerably especially for HSF layers.

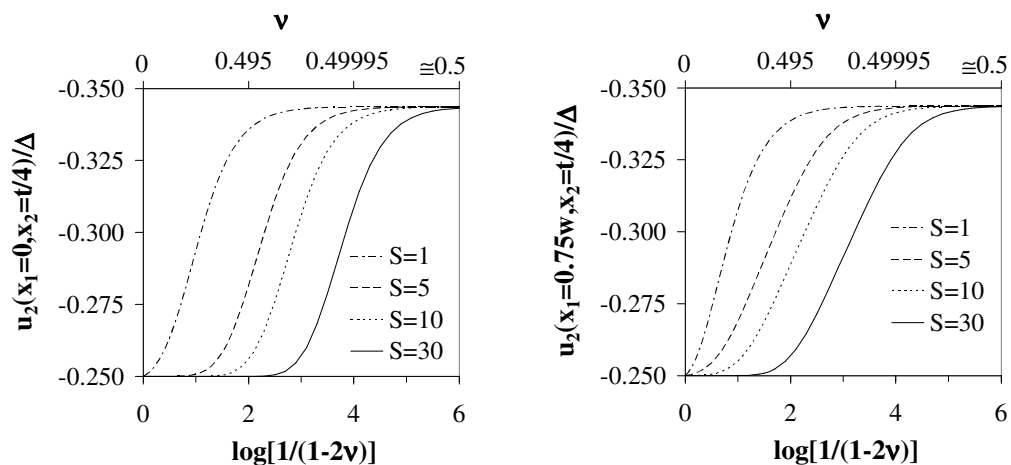
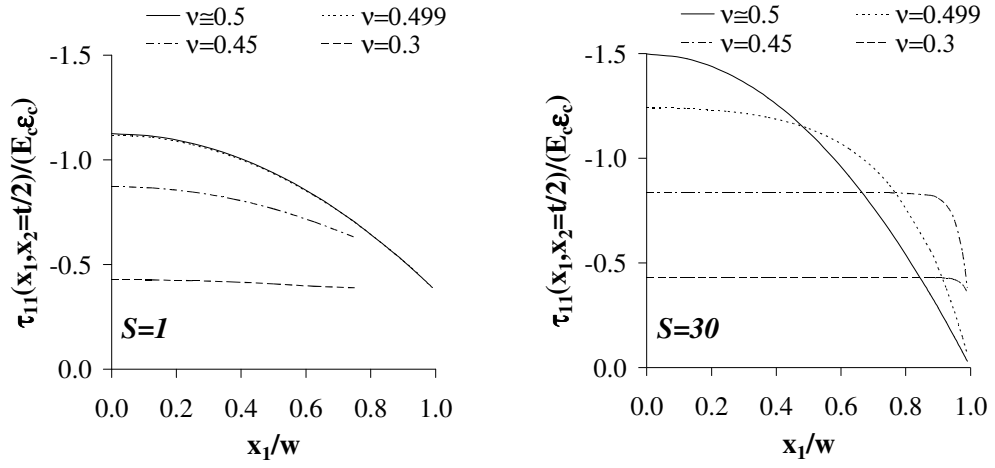
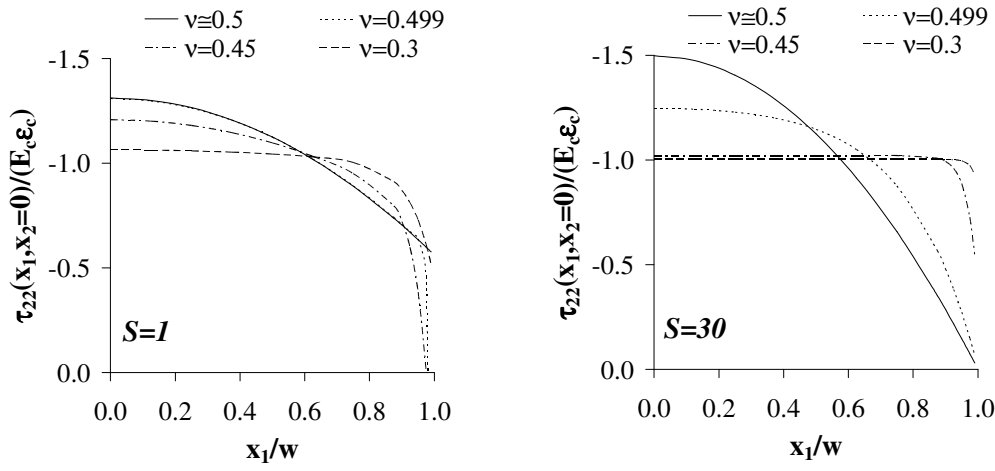


Figure 6.5 Effect of shape factor and Poisson's ratio on axial displacement of the layer at the quarter thickness under uniform compression

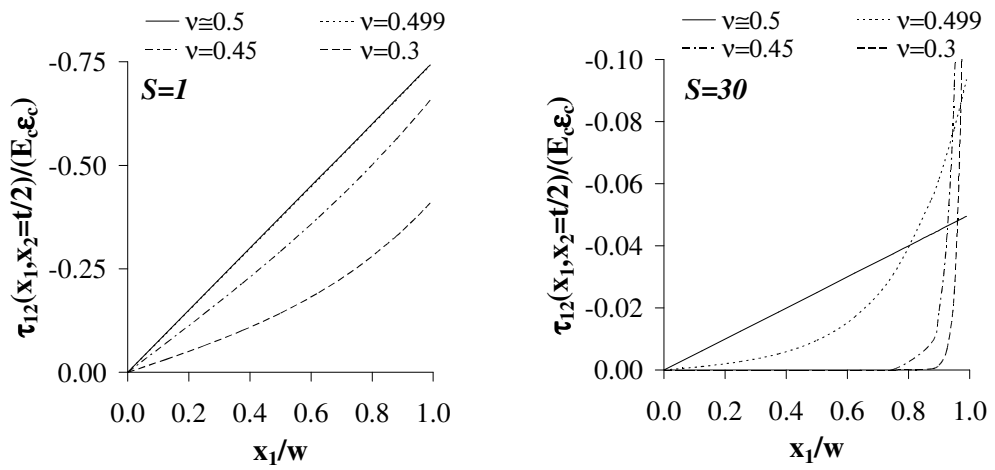
The graphs in Figure 6.6 and Figure 6.7 illustrate the effects of shape factor and Poisson's ratio on the stress distributions in lateral direction in an IS-shaped bonded elastic layer under uniform compression. In the graphs, the distributions are plotted over the most critical sections, i.e., at $x_2=t/2$ for τ_{11} and τ_{12} , and at $x_2=0$ for τ_{22} , and the stress values are normalized with respect to the uniform pressure $E_c \epsilon_c$.



a. lateral normal stress

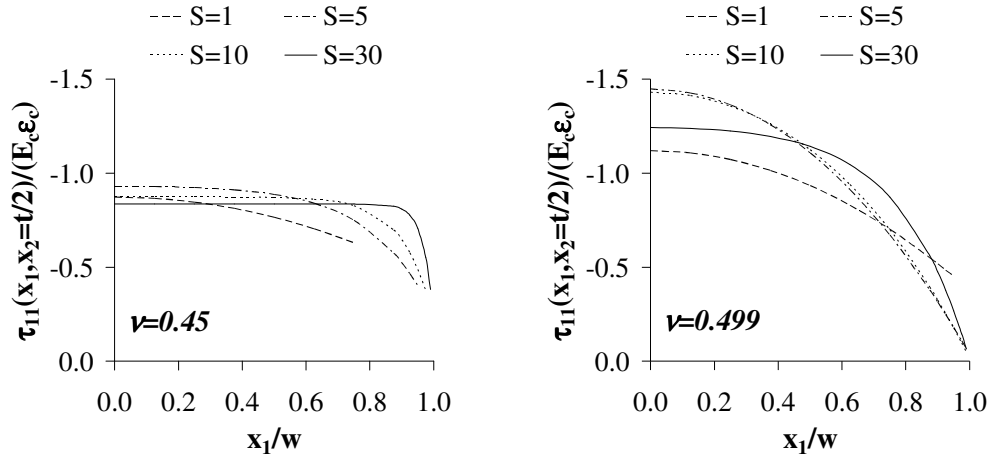


b. axial stress

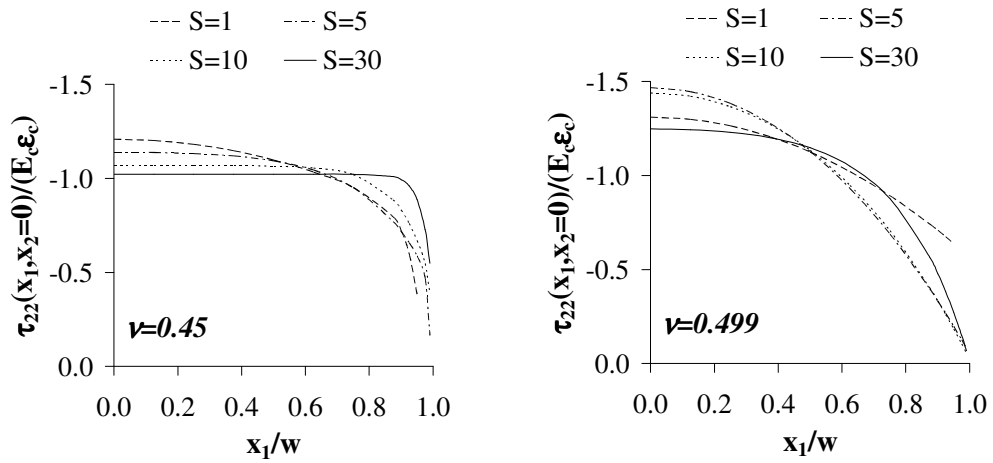


c. shear stress

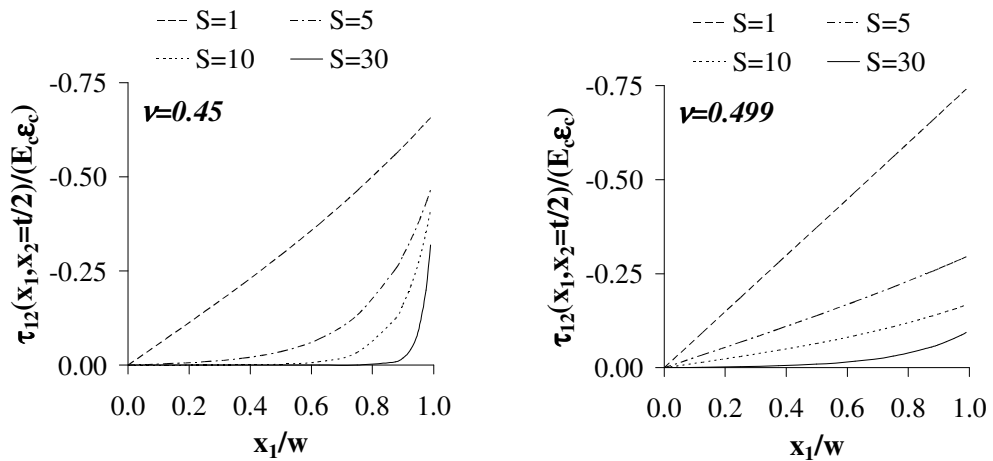
Figure 6.6 Effect of Poisson's ratio on stress distributions in lateral direction in bonded IS-shaped layers with $S=1$ (left hand side) and $S=30$ (right hand side)



a. lateral normal stress



b. axial stress



c. shear stress

Figure 6.7 Effect of shape factor on stress distributions in lateral direction in bonded IS-shaped layers for $\nu=0.45$ (left hand side), $\nu=0.499$ (right hand side)

The graphs in Figure 6.6 and Figure 6.7 show that, independent of the geometrical and material properties, in a bonded elastic layer subjected to uniform compression, the normal stresses take their maximum values at the center ($x_1=0$) and the shear stress takes its maximum value at the edges ($x_1=\pm w$) over their critical horizontal sections. It is to be noted that the stress discontinuities observed in the normal stress distributions near the edges of the layer are due to the approximate nature of FOT expressions and are more noticeable in compressible LSF layers. The graphs in Figure 6.6a,b for $S=1$ are plotted by eliminating these artificial unrealistic discontinuities. For $S=30$, these discontinuities seem to be confined to a very limited region close to the edges. It is surprising that despite the approximate nature of the analytical solutions, no discontinuity is observed in the shear stress distributions even for $S=1$. This conclusion is in agreement with the experimental results obtained by Gent et al. [17], who found that shear stress does not “approach zero toward the edges of the bonded surfaces for the well-bonded blocks” and concluded that “the effects of the edge singularity must be confined to extremely small regions in the neighborhood of the edges”.

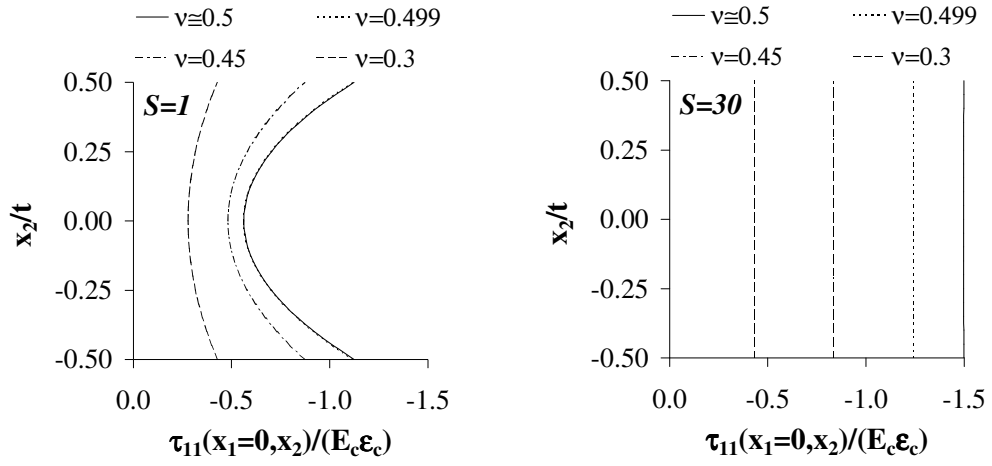
As far as the normal stresses are concerned, for $S=30$, as ν decreases, $(\tau_{22})_{\max}$ decreases from the incompressible value of $1.5E_c\varepsilon_c$ to $E_c\varepsilon_c$ for highly compressible materials. The variation of τ_{11} is similar but τ_{11} approaches to zero as the material compressibility increases. For $S=1$, the upper limits for the peak normal stresses are smaller, less than $1.5E_c\varepsilon_c$, while the lower limits remain the same. For both $S=1$ and $S=30$, as ν approaches 0.5, the distributions for normal stresses become much closer to a well-defined parabolic shape. On the other hand, the material compressibility smoothes the parabolic shape and make the normal stress distributions more uniform over the central part. It is worth noting that similar to the displacement distributions, the stress distributions in the horizontal direction are insensitive to the changes in Poisson’s ratio beyond $\nu=0.499$ for the LSF layer.

The effect of shape factor on the stress distributions is more apparent in the graphs presented in Figure 6.7, where the distributions are plotted for various values of shape factor and two specific values of Poisson’s ratio, 0.45 and 0.499. From

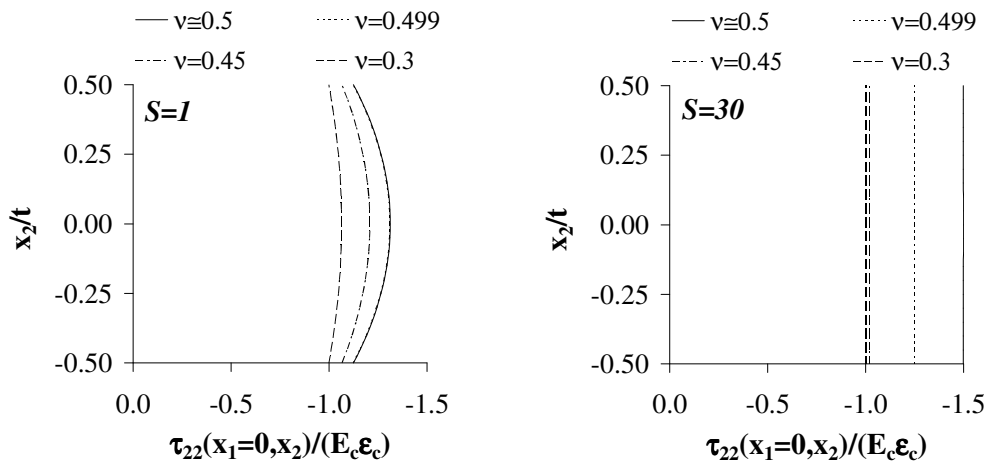
Figure 6.7a,b, it can be concluded that for $\nu=0.45$, as S increases, the maximum axial stress decreases and the stress distributions become more uniform. On the other hand, these conclusions are not valid for $\nu=0.499$.

For the shear stress distributions in the lateral direction (Figure 6.6c and Figure 6.7c), it can be seen that the distribution in the LSF layer ($S=1$) is almost linear for nearly incompressible materials while the distributions becomes nonlinear for smaller values of ν . It can also be observed that, for the HSF layer ($S=30$), the stress values are *comparatively* small. However, it should be noted that, in the graphs, the stress values are normalized with respect to E_c , and E_c of an HSF layer can be much larger than that of an LSF layer. Thus, the apparently small values in the second of Figure 6.6c may indeed correspond to very large values of shear stress in the HSF layer especially if ν is close to 0.5. One can also note that the nonlinear behavior is noticeable in the HSF layer even when $\nu=0.499$. Figure 6.7c shows that, as far as the normalized shear stress is concerned, the effects of the bonded surfaces appear to be most pronounced for the critical shape factor of $S=1$ among the studied values of S . Behavior is almost linear for $S \leq 10$ for $\nu=0.499$ while nonlinearity is observable even for $S=5$ and $\nu=0.45$.

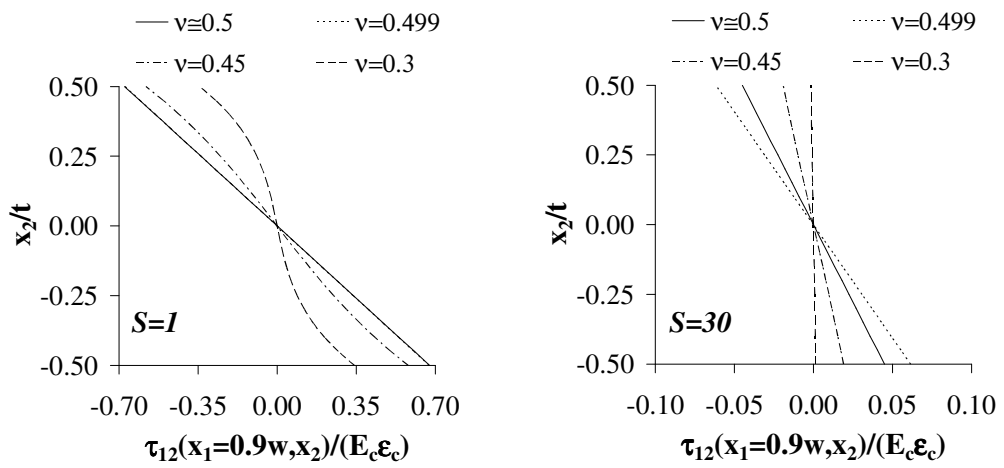
The graphs presented in Figure 6.8 and Figure 6.9 show the effects of shape factor and Poisson's ratio on the stress distributions in axial direction in IS-shaped bonded elastic layers subject to uniform compression. In the graphs, the normal stress distributions are plotted along the centerline ($x_1=0$), where they take their maximum values. As for the shear stress distributions, it is known that, under uniform compression, shear stress increases in the horizontal direction as moved toward the edges, where it suddenly drops to zero due to the stress-free boundary conditions. It is also known that the stress singularities observed at the edges are usually confined to a very limited region [17]. For this reason, the distributions given in Figure 6.8c and Figure 6.9c are plotted along the vertical axis at $x_1=0.9w$, which is thought to be sufficiently away from the edge and at the same time adequately close to the point where shear stress is maximum.



a. lateral normal stress

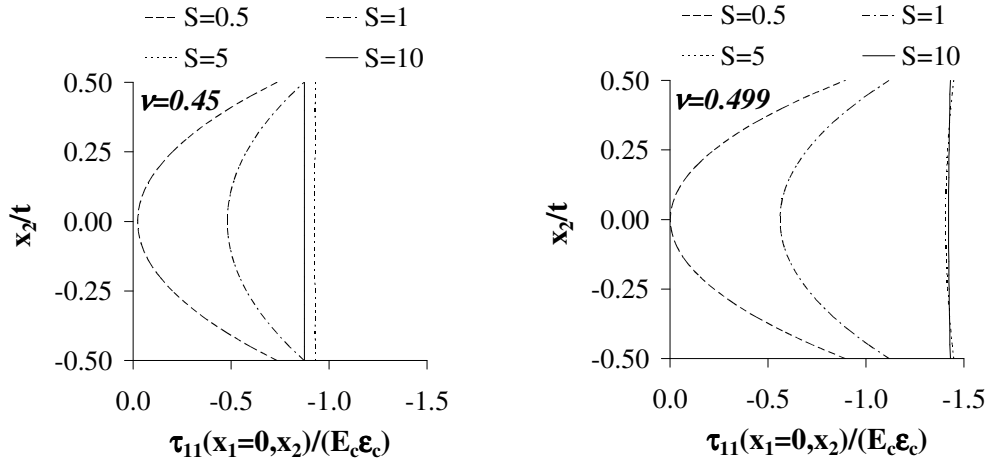


b. axial normal stress

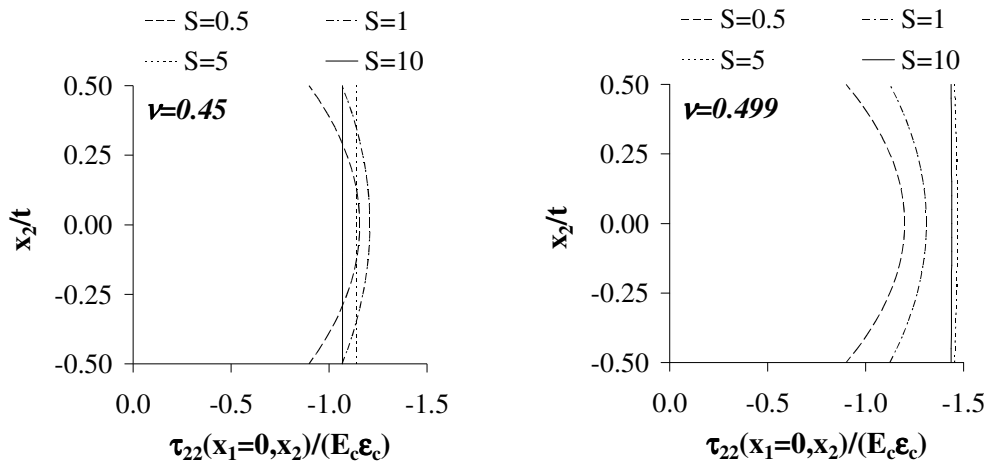


c. shear stress

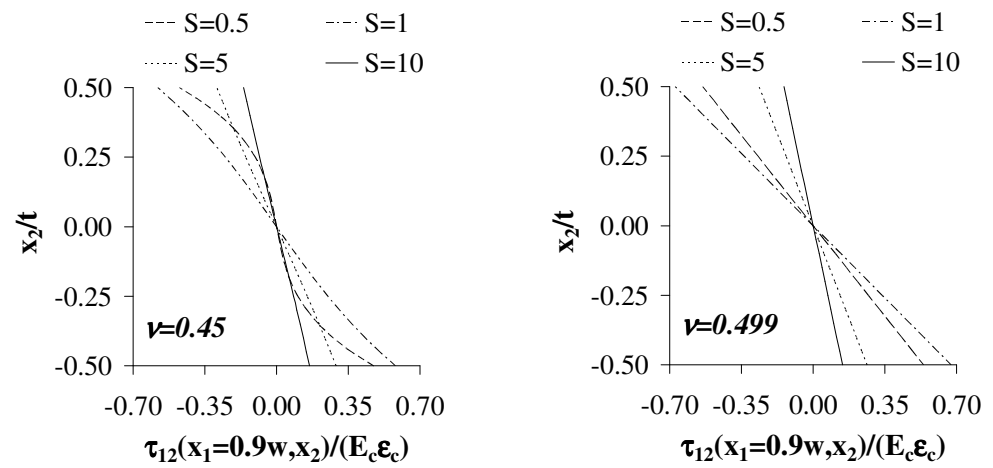
Figure 6.8 Effect of Poisson's ratio on stress distributions in axial direction in bonded IS-shaped layers with $S=1$ (left hand side) and $S=30$ (right hand side)



a. lateral normal stress



b. axial stress



c. shear stress

Figure 6.9 Effect of shape factor on stress distributions in axial direction in bonded IS-shaped layers for $\nu=0.45$ (left hand side), $\nu=0.499$ (right hand side)

From Figure 6.8a,b, it can be concluded that while the normal stresses have uniform variation through the layer thickness for $S=30$, they have parabolic variations for $S=1$. In the LSF layer, τ_{11} reaches its maximum value at the bonded faces ($x_2=\pm t/2$) while τ_{22} has its maximum value at the centroid ($x_2=0$). It can also be observed that the incompressible behavior has already attained at $\nu=0.499$ for $S=1$ while the stress values are sensitive to the changes in ν near 0.5 for $S=30$. The graphs also show that the pressure assumption (i.e., $\tau_{11}=\tau_{22}=\tau_{33}=-p$) used in the pressure method is valid only for the HSF layer and only for nearly/strictly incompressible materials.

At this point, it seems to be valuable to assess the stress predictions of the widely-used pressure method (PM). In Figure 6.10, the predictions of FOT are compared with those of PM for the variation of the lateral normal stress through the thickness of an IS-shaped bonded elastic layer for two different shape factors (1 and 30) and various material compressibilities.

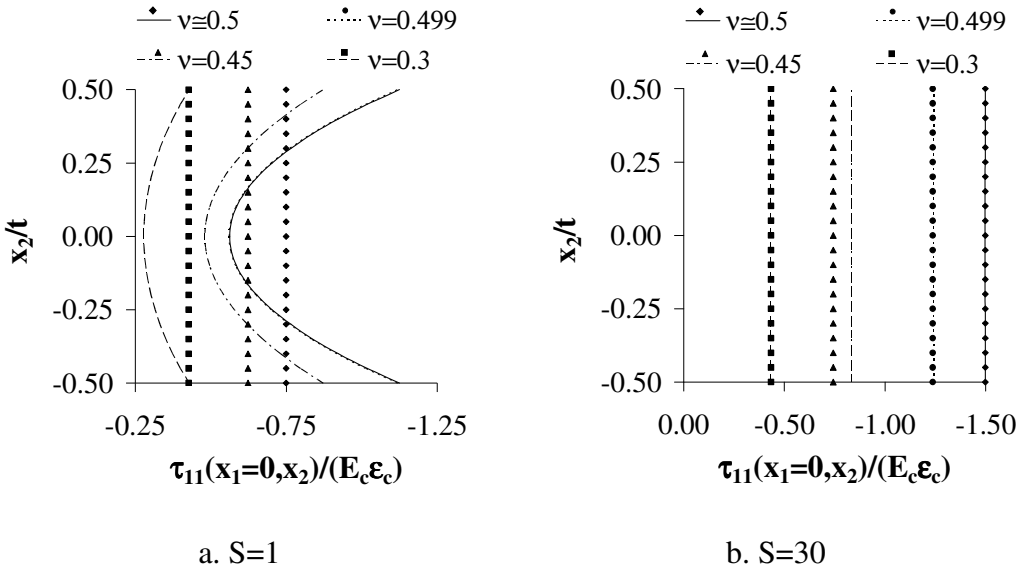


Figure 6.10 Comparison of the predictions of FOT (continuous lines) and PM (discrete points) for lateral normal stress distribution in the axial direction

It is to be noted that while calculating τ_{11} using PM, it is sufficient to consider only the second stage deformations. In other words, $\tau_{11}=-p$, where p can be computed from the first of Eqs. (2.22). On the other hand, while calculating the compression modulus E_c , to which the stress values are normalized, the effect of the first stage deformations should also be considered. In other words, $(E_c)_0$, defined in Eq. (2.5), has to be added to the E_c expression in the first of Eqs. (2.23). The addition of $(E_c)_0$ is essential especially for compressible materials and for the LSF layer.

As shown in Figure 6.10b, although the normal stress distributions in the HSF layer are uniform, as assumed by PM, even for compressible materials, the stress value predicted by PM for $\nu=0.45$ deviate from the FOT prediction considerably. Interestingly, the predictions of both theory coincide also when $\nu=0.3$. On the other hand, as shown in Figure 6.10a, PM fails to predict nonuniform stress distributions in the LSF layer for all studied values of ν .

The effect of shape factor on the normal stress distributions in vertical direction is more apparent in the graphs presented in Figure 6.9a,b. The parabolic stress distributions observed in LSF layers are smoothed as S increases. The normal stresses are almost constant for $S \geq 5$. It can also be observed that the deviation from the uniform stress distribution is more pronounced in the lateral normal stress.

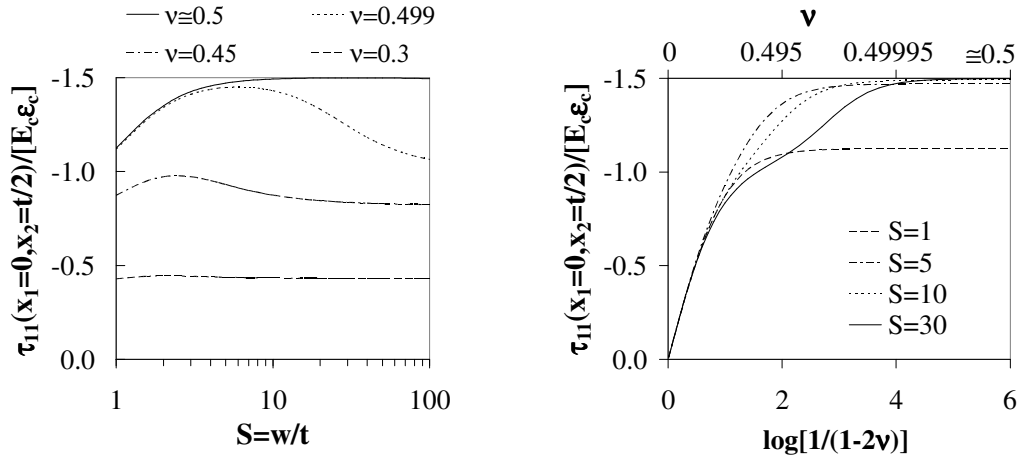
The behavior of the LSF layer is different from that of the HSF layer also in that while considerable shear stress develops in the region close to the outer boundary in the LSF layer, the normalized stress values are comparatively small in the HSF layer, as shown in Figure 6.8c. Shear stress distribution is linear for nearly incompressible materials, even for $S=1$. On the other hand, as the material compressibility increases, the distribution loses its linearity for the LSF layer. From Figure 6.9c, it can be concluded that the normalized shear stress in the considered section is largest in the layer with $S=1$ (within the studied range). Nonlinearity observed in bonded layers of very low shape factors (e.g., for $S=0.5$) are more pronounced for more compressible materials. For $\nu=0.499$, shear stress distributions are almost linear for all studied values of S .

From Figure 6.6 to Figure 6.9, it can be concluded that in a bonded elastic layer subjected to uniform compression, the maximum values of the stresses are experienced at some fixed locations: $(\tau_{22})_{\max}$ occurs at $(x_1=0, x_2=0)$, $(\tau_{11})_{\max}$ at $(x_1=0, x_2=\pm t/2)$ and $(\tau_{12})_{\max}$ at $(x_1=\pm w, x_2=\pm t/2)$. It can also be observed that while their locations are fixed, their magnitudes depend on the aspect ratio of the layer and the compressibility of the layer material considerably.

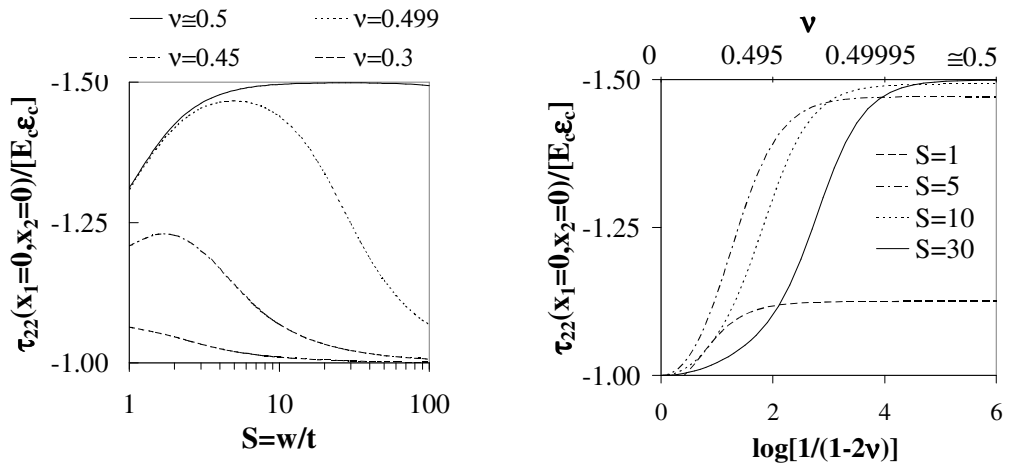
The plots in Figure 6.11 study the effects of shape factor and Poisson's ratio on the maximum values of the normalized stresses, i.e., $(\tau_{ij})_{\max}/E_c \epsilon_c$ ($i, j, :1, 2$), which is simply denoted, in the text, as $(\tau^*_{ij})_{\max}$.

For an incompressible layer, $(\tau^*_{11})_{\max}$ and $(\tau^*_{22})_{\max}$ increase with increasing S until a peak value of 1.5 is reached at about $S=10$ (Figure 6.11a,b). On the other hand, in a compressible layer, $(\tau^*_{11})_{\max}$ and $(\tau^*_{22})_{\max}$ reach their peak values at some critical shape factors and beyond these critical values, they decrease with increasing S . The deviation of the nearly incompressible behavior ($\nu=0.499$) from the strictly incompressible behavior is remarkable for HSF layers. The effect of S on the maximum stresses decreases as ν decreases; for $\nu=0.3$, the maximum stresses are almost independent of the shape factor. For a specific value of S , $(\tau^*_{11})_{\max}$ and $(\tau^*_{22})_{\max}$ are observed to increase with increasing ν until the limiting incompressible values are reached. The lower the shape factor, the lower the value of Poisson's ratio at which the plateau is reached. This is consistent with the earlier conclusion that the stresses in LSF layers are not influenced from the changes in Poisson's ratio in the vicinity of 0.5.

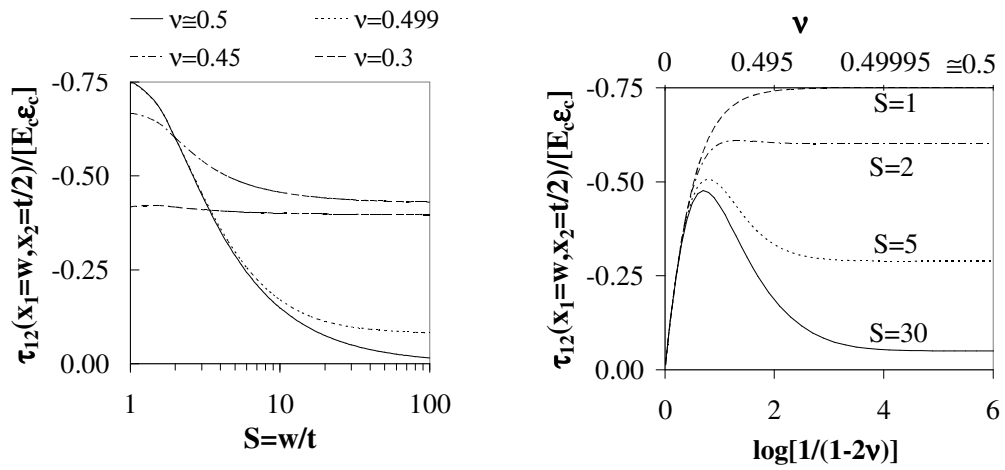
The graphs plotted for the maximum normalized shear stress in Figure 6.11c show that $(\tau^*_{12})_{\max}$ attains its peak value at very low shape factors, typically at $S=1$. For $S>1$, $(\tau^*_{12})_{\max}$ decreases with increasing S . The amount of decrease is much higher in nearly incompressible materials. When the effect of Poisson's ratio on $(\tau^*_{12})_{\max}$ is studied carefully, it is seen that, for about $\nu \geq 0.4$, $(\tau^*_{12})_{\max}$ in an elastic bonded layer of $S=1$ is always the highest in the range of $S \geq 1$. For $S>1$, $(\tau^*_{12})_{\max}$ starts to decrease with increasing ν until the incompressible value is reached.



a. lateral normal stress



b. axial stress



c. shear stress

Figure 6.11 Effect of shape factor and Poisson's ratio on maximum normalized stresses under uniform compression

6.2 BENDING BEHAVIOR

Although the derivation is not included in Section 4.1.1.2, it can be shown that the zeroth order theory (ZOT) leads to the same expression for the bending modulus of IS-shaped bonded elastic layers derived by Tsai and Lee [40] (refer to Eqs. (2.45) and (4.95)). Figure 6.12 compares the predictions of ZOT ($m=0$) and FOT ($m=1$) for bending modulus. As shown in the figure, the predictions of both theories exactly match in the studied range of parameters. Considering the complexity of the expression obtained from FOT, it seems to be more practical to use the simpler formula obtained from ZOT in design calculations.

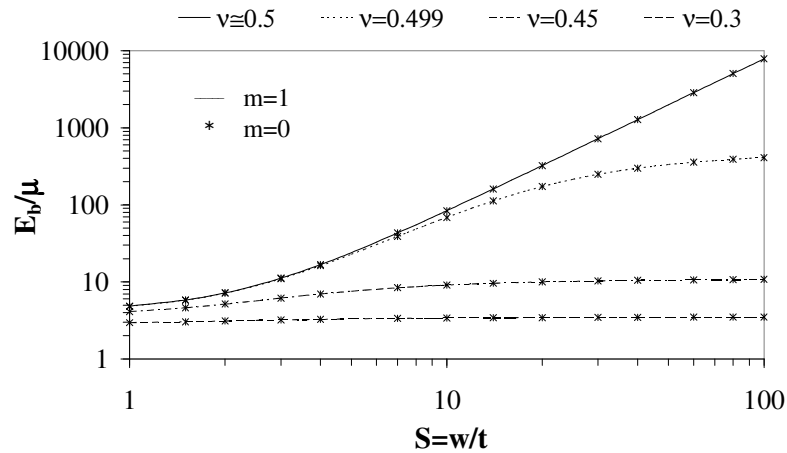


Figure 6.12 Predictions of zeroth and first order theories for bending modulus

In design calculations, it is a common practice to represent the effective bending modulus E_b of a bonded elastic layer in terms of its compression modulus E_c . A factor of five is used for the ratio of E_c to E_b for IS-shaped bonded elastic layers [28]. In Figure 6.13, the E_c/E_b ratio is plotted for various shape factors and Poisson's ratios for IS-shaped layers. As shown in the figure, the above-mentioned value of five is valid only for strictly incompressible materials and for considerably

high shape factors. For instance, for $\nu=0.499$ and for $S>5$, as S increases, this value of the ratio significantly underestimates the true value of the bending modulus.

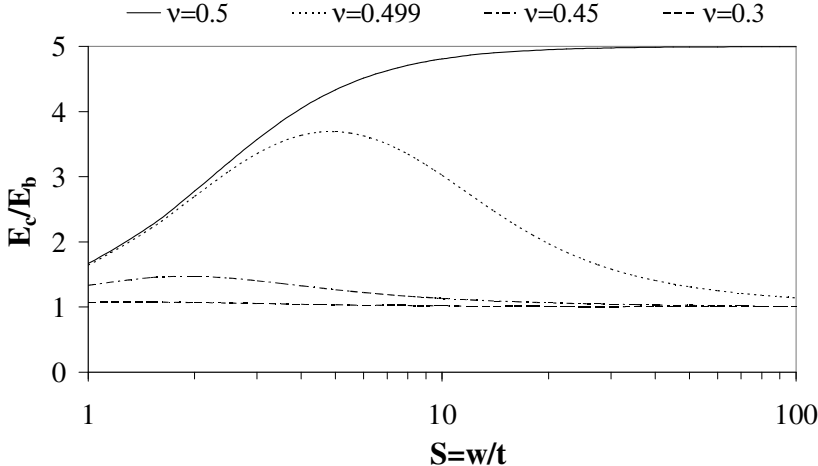
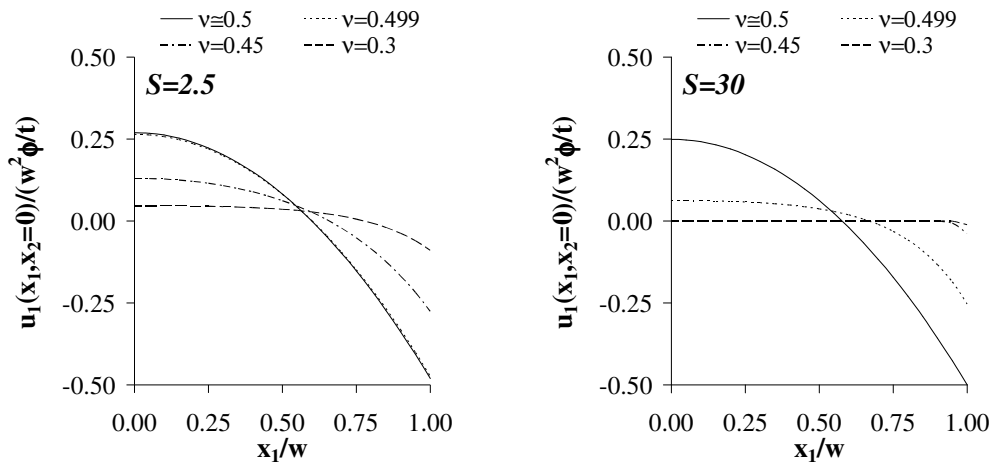


Figure 6.13 Effect of Poisson’s ratio and shape factor on E_c/E_b ratio

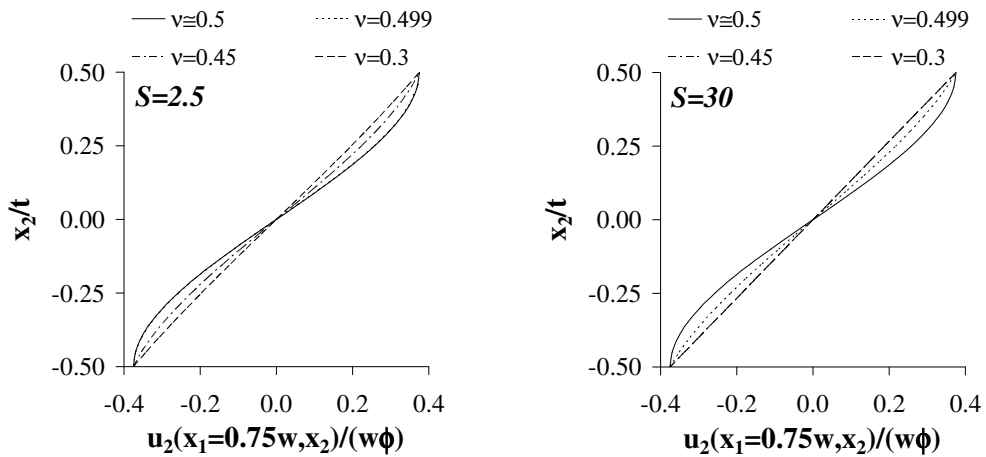
Figure 6.14a shows the effect of Poisson’s ratio on the lateral displacement distributions over the central plane ($x_2=0$) in IS-shaped bonded elastic layers under pure bending for two specific values of shape factor $S=2.5$, representing LSF layers, and $S=30$, representing HSF layers. It can be recalled that while studying the compressive behavior of the layers in the previous section, the value of S for the LSF layer has been selected as 1.0. This selection has been done due to the fact $S=1$ is the most critical shape factor for IS-shaped bonded elastic layers subject to uniform compression as far as the maximum normalized shear stress is concerned. As it will be verified later, such a critical S value also exists for IS-shaped bonded elastic layers subject to pure bending and it equals to 2.5. For this reason, the value of the shape factor of the LSF layer is changed in this section from 1.0 to 2.5.

From Figure 6.14a, it is seen that the lateral displacement attains its critical values at the center ($x_1=0$) and at the edges ($x_1=\pm w$). The absolute maximum occurs at the bulge-free lateral surfaces. One can also note that bulging changes its

direction over the width of the layer. The location of the “neutral” point is not constant in general; it depends on S and ν . Similar to the compression case, the incompressible curves for the normalized lateral displacement $[u_1/(w^2\phi/t)]$ in the LSF and HSF layers almost coincide. As ν decreases, the parabolic distribution becomes more uniform. For $S=30$, the lateral displacement of nearly incompressible material ($\nu=0.499$) differ significantly from that of incompressible material.



a. lateral displacement distribution in lateral direction



b. axial displacement distribution in axial direction

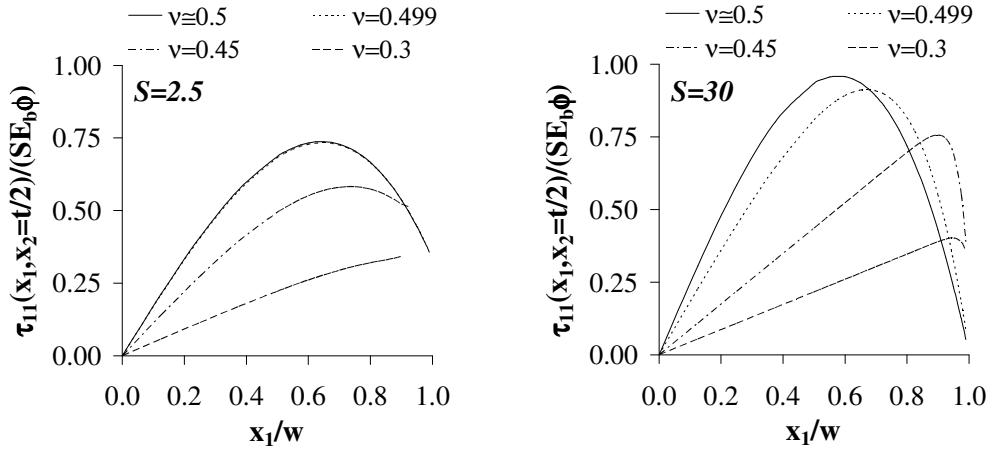
Figure 6.14 Effects of shape factor and Poisson's ratio on displacement distributions under pure bending

The effects of S and ν on the axial displacement distribution in the axial direction at $x_2=0.75w$ are shown in Figure 6.14b. When the graphs given in this figure are compared with those in Figure 6.3b, it may be concluded that the effects of these two parameters on the axial displacement distribution under pure bending are very similar to those of the compression case.

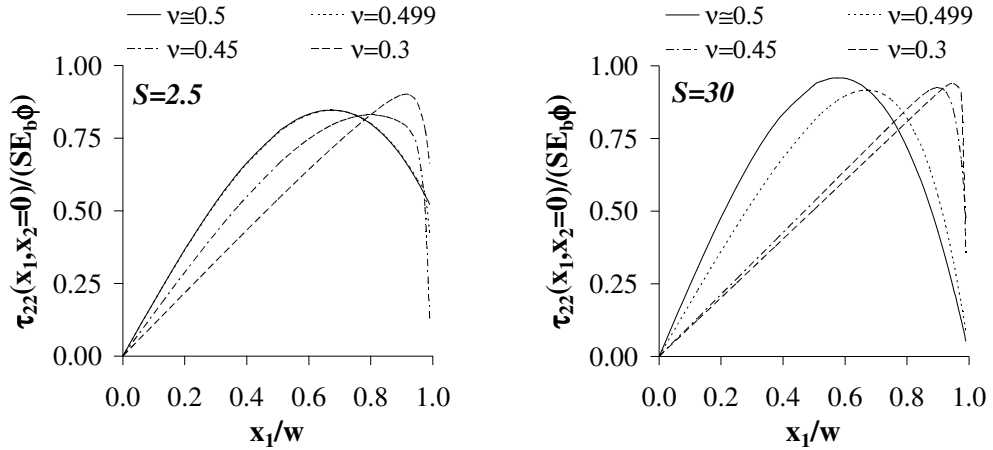
The graphs in Figure 6.15a,b show the normal stress distributions over their most critical horizontal sections (i.e., τ_{11} at the top bonded surface, $x_2=t/2$, and τ_{22} at the centroid, $x_2=0$) for two specific values of shape factor, 2.5 and 30, and various Poisson's ratios. To obtain comparable quantities, stress values are normalized by $SE_b\phi$, which corresponds to the maximum bending stress developing in the corresponding unbonded layer as predicted by the simple beam theory [41].

As in the compression case, the stress discontinuities near the edges, which are not included in the graphics, become noticeable in the LSF layer of compressible material (Figure 6.15a,b). When these singularities are ignored, it can be said that, as ν increases, the normalized lateral normal stress increases. For the normalized axial stress, the effect of ν seems to be more complex. The location of the maximum normalized axial stress moves towards the edge as ν decreases, which is also valid for the normalized lateral stress. Furthermore, the distribution approaches linear distribution, as in the case of the simple beam theory, as the material compressibility increases.

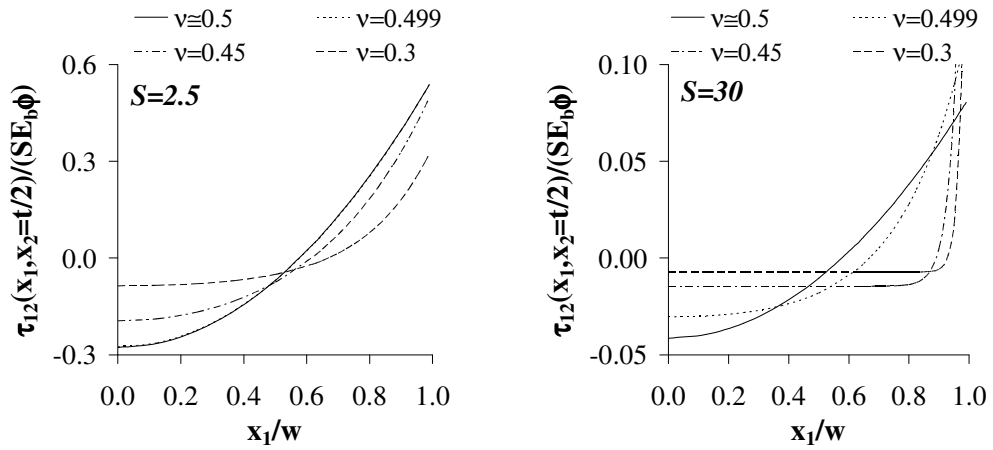
Unlike normal stresses, it is easier to study the effects of S and ν on shear stress distribution in the lateral direction. Since the maximum shear stress occurs at the bonded faces, the shear stress distributions presented in Figure 6.15c are plotted at $x_2=t/2$. The graphs show that the normalized shear stress is much larger in the LSF layer than in the HSF layer. At this point, it is worth reemphasizing that since E_b of an HSF layer can be considerably large, these small values can indeed correspond to significant stress values in the HSF layer. From the figures, it can also be recognized that the shear stress distribution in the lateral direction has a parabolic shape with maximum values experienced at the edges and that the distribution becomes more uniform at the central region as ν decreases.



a. lateral normal stress



b. axial stress



c. shear stress

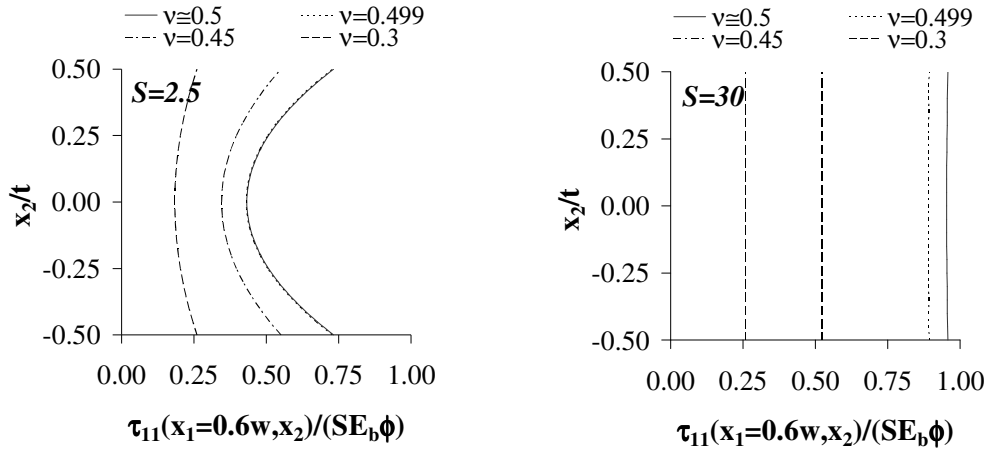
Figure 6.15 Effect of Poisson's ratio on stress distributions in lateral direction in bonded IS-shaped layers with $S=2.5$ (left hand side) and $S=30$ (right hand side)

The behavior of a bonded elastic layer subject to pure bending differs from its behavior under uniform compression in that while normal stresses are known to be maximum at $x_1=0$ under uniform compression, they vanish at this location under pure bending. As shown in Figure 6.15, over a specific horizontal cross section, normal stresses reach their maximum values at different locations under pure bending and the exact locations of these maximum stresses highly depend on both ν and S .

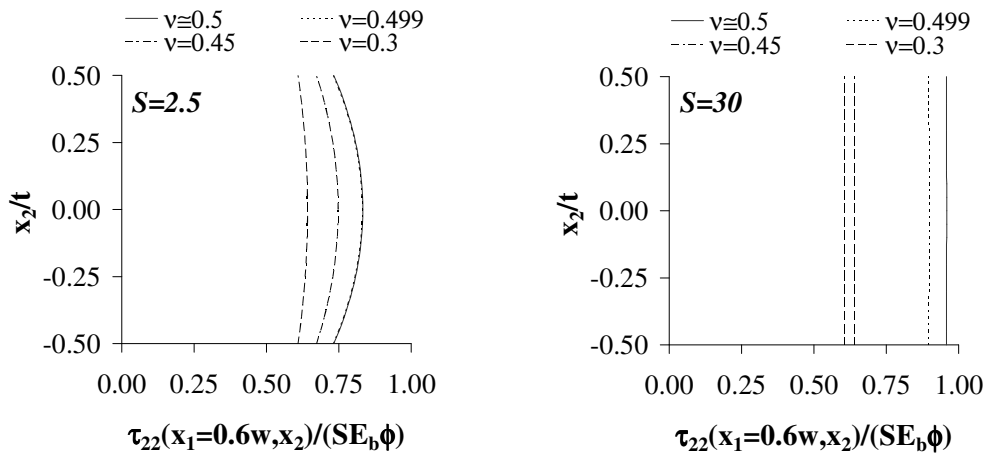
The graphs in Figure 6.16a,b are plotted along the vertical section at $x_1=0.6w$, which is found to be very close to the section where normal stresses maximize for incompressible materials, for two different shape factors ($S=2.5,30$) and various Poisson's ratios. The graphs illustrate the behavior difference between LSF and HSF layers under pure bending. As in the compression case, while normal stresses are constant through the layer thickness for HSF layers, they are not so for LSF layers under pure bending. In addition, the pressure assumption is valid only for the HSF layer of nearly incompressible materials. From the graphs, it is also seen that, for $S=2.5$, the stress values increase with increasing ν and the shape of the stress distributions becomes more parabolic.

The effect of S on the normal stress distributions is more apparent in the graphs presented in Figure 6.17a,b, which show that for a specific value of ν , as S increases, the well-defined parabolic shape tends to be more uniform. For $\nu=0.45$, the distribution is almost uniform for $S \geq 5$. Uniform stress distribution is reached at higher shape factors (practically, at $S=10$) for $\nu=0.499$.

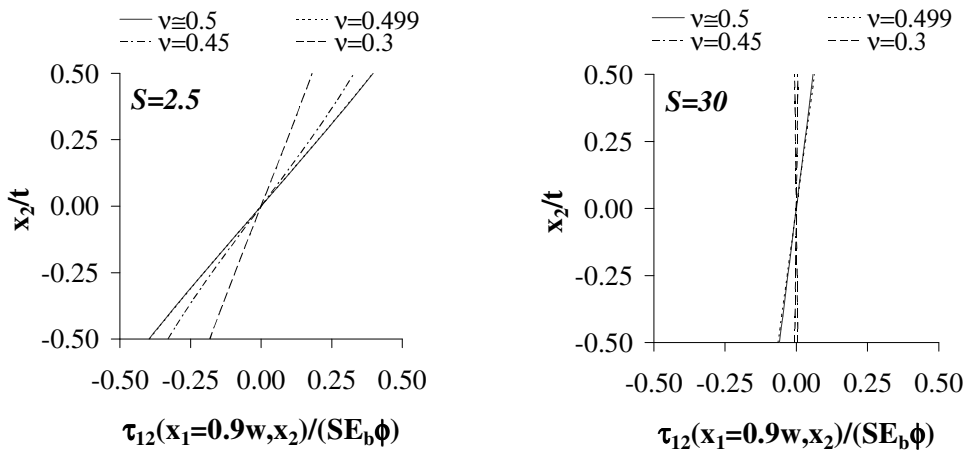
Similar graphs are plotted for the shear stress distributions in Figure 6.16c and Figure 6.17c, where the distributions are plotted, as in the compression case, along the vertical axis at $x_1=0.9w$, which is considered to be sufficiently away from the stress singularities at the edge. It is noteworthy that the shear stress distribution along the considered section is almost linear for all studied values of S and ν . The graphs in in Figure 6.16c and Figure 6.17c also show that, as far as the normalized shear stress is concerned, the effects of the bonded surfaces appear to be most pronounced for the critical shape factor of $S=2.5$ among the studied values of S .



a. lateral normal stress

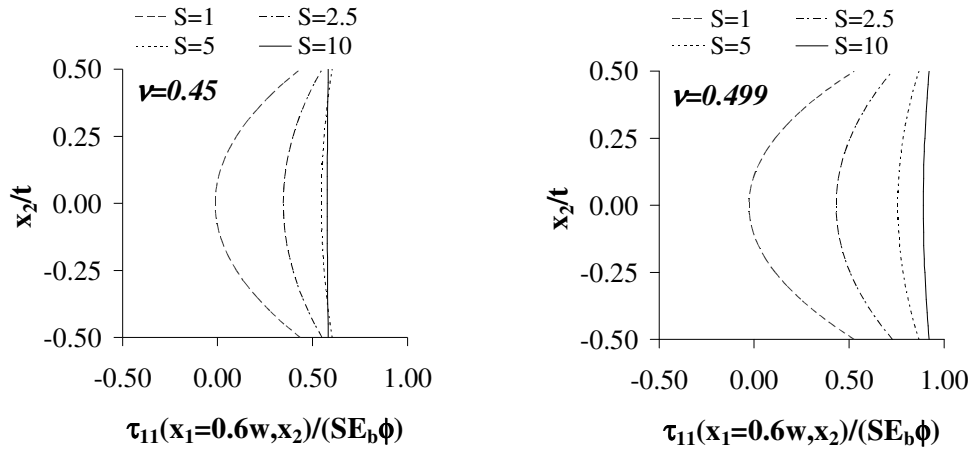


b. axial stress

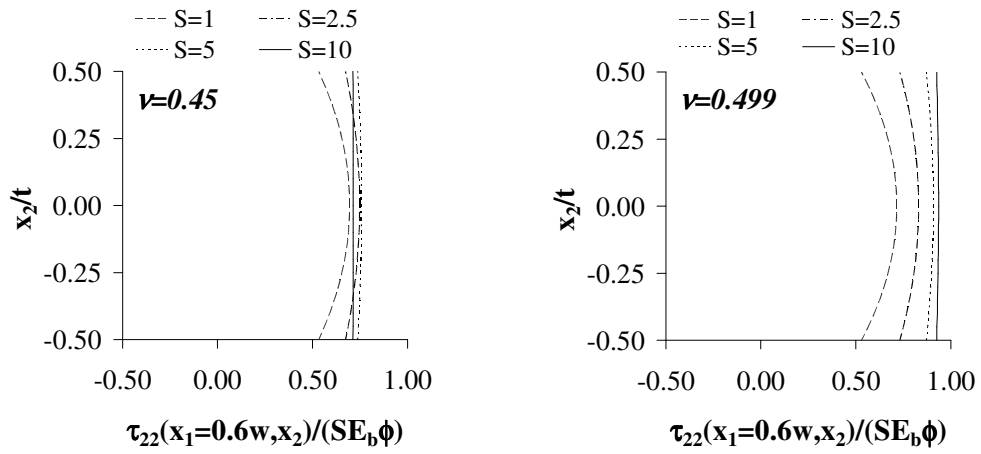


c. shear stress

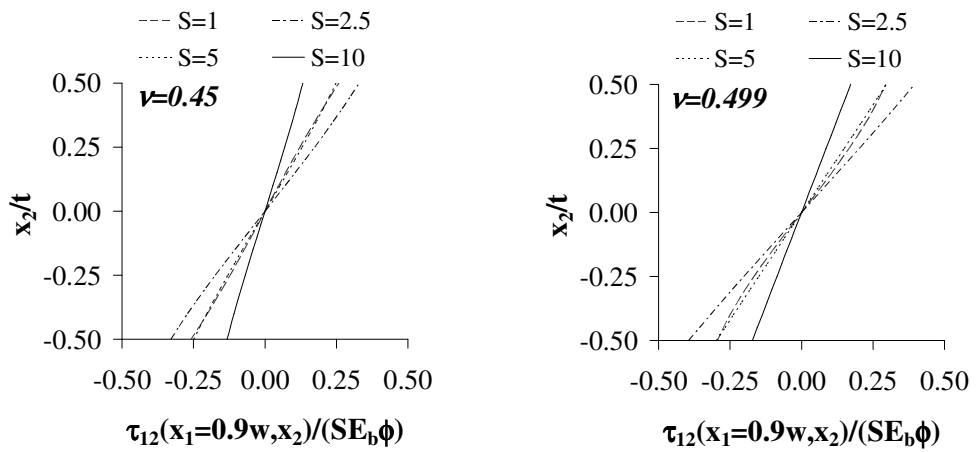
Figure 6.16 Effect of Poisson's ratio on stress distributions in axial direction in bonded IS-shaped layers with $S=2.5$ (left hand side) and $S=30$ (right hand side)



a. lateral normal stress



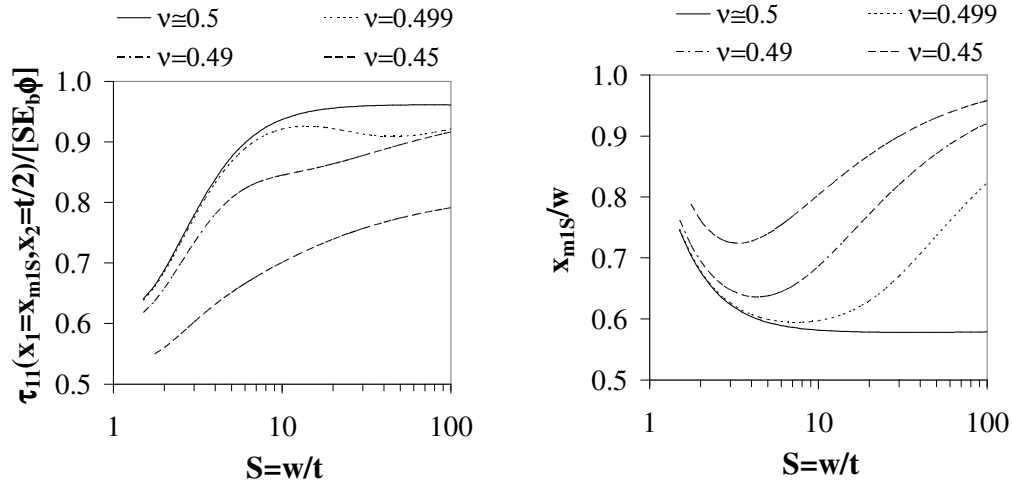
b. axial stress



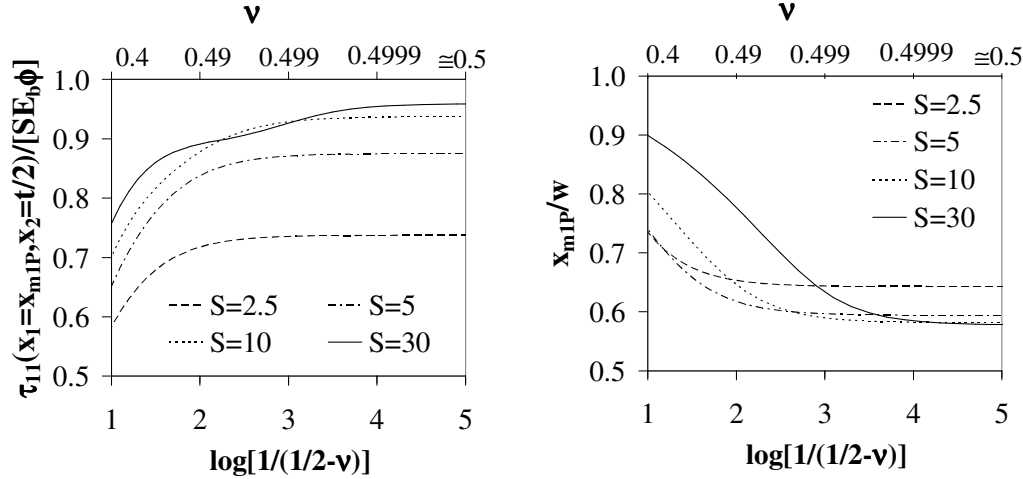
c. shear stress

Figure 6.17 Effect of shape factor on stress distributions in axial direction in bonded IS-shaped layers for $\nu=0.45$ (left hand side), $\nu=0.499$ (right hand side)

Figure 6.18 illustrates how shape factor and Poisson's ratio affect the location and magnitude of the maximum normalized lateral normal stress, denoted, in the text, as $(\tau_{11}^*)_{\max}$, that develops in an IS-shaped bonded elastic layer under pure bending.



a. variation with respect to shape factor



b. variation with respect to Poisson's ratio

Figure 6.18 Effect of shape factor and Poisson's ratio on magnitude and location of maximum lateral normal stress under pure bending

Figure 6.18a depicts the effect of S on $(\tau_{11}^*)_{\max}$ for fixed values of ν . Each curve, corresponding to a fixed value of ν , is plotted for numerous values of S . For each value of S , first the value of x_1 where the normalized lateral normal stress attains its maximum value, which is denoted as x_{m1S} , is determined. Knowing the location of the maximum, the magnitude of the normalized lateral normal stress is computed. In the case of bending, it may not always be possible to determine the exact locations of the maximum normal stresses, especially for very low shape factors and Poisson's ratios due to the stress singularities near the edges. For this reason, the graphs in Figure 6.18 are plotted for Poisson's ratio between 0.4 and 0.5.

Before analyzing the effect of S on the magnitude of $(\tau_{11}^*)_{\max}$, it is wise to study the effect of S on the location of $(\tau_{11}^*)_{\max}$. As shown in the second of Figure 6.18a, for incompressible materials, as S increases, x_{m1S} moves towards the center of the layer until it reaches the asymptotic value of $x_1 \cong 0.58w$ at about $S=10$. The material compressibility changes the shape of the curve considerably: the plateau disappears; after reaching a minimum at a critical shape factor, x_{m1S} starts to increase again. It can also be concluded that x_{m1S} for compressible materials are always equal or greater than the incompressible value, i.e., $x_1 \geq 0.58w$.

The first of Figure 6.18a indicates that, for incompressible materials, as S increases, $(\tau_{11}^*)_{\max}$ increases until it reaches the limiting value of $0.96SE_b\phi$ at about $S=10$. The curve for $\nu=0.499$ almost coincides with the curve for incompressible materials up to about $S=10$. For $S>10$, the effect of ν becomes apparent: as S increases, $(\tau_{11}^*)_{\max}$ decreases. On the other hand, for $\nu=0.49$ and $\nu=0.45$, $(\tau_{11}^*)_{\max}$ is observed to increase with increasing S .

The effect of ν on both the location and magnitude of $(\tau_{11}^*)_{\max}$ is more apparent from Figure 6.18b. For the studied values of shape factors, it can be concluded that for a fixed value of S , as ν increases, the location of $(\tau_{11}^*)_{\max}$, denoted as x_{m1P} , moves from the edge towards the center (second of Figure 6.18b). No further shift is observed after the asymptotic value (i.e., $x_1 \cong 0.58w$) is attained. From the first of Figure 6.18b, it may be concluded that unless the shape factor of

the layer is quite large (e.g., $S=30$), as ν increases, the magnitude of $(\tau_{11}^*)_{\max}$ increases uniformly until the asymptotic incompressible value is attained.

As far as the maximum normalized axial stress, denoted as $(\tau_{22}^*)_{\max}$, is concerned, similar graphs are plotted. From these graphs, it is concluded that although the effect of S or ν on the location and magnitude of $(\tau_{22}^*)_{\max}$ is much more complex than that of $(\tau_{11}^*)_{\max}$, it can be said that the magnitude of $(\tau_{22}^*)_{\max}$ remains approximately in the range of 0.8-1.0.

Maximum hydrostatic tension developing in an IS-shaped bonded elastic layer under pure bending is also investigated for the study of the ‘‘internal rupture’’ phenomena, which is one of the failure modes a bonded rubber layer can undergo under pure bending [20]. A comprehensive study on the pressure distributions over different sections in an IS-shaped bonded elastic layer indicates that the maximum pressure occurs at the same location where the maximum lateral normal stress takes place, i.e. at $x_1=x_{m1S}$ (or $x_1=x_{m1P}$) and $x_2=t/2$. Thus, the seconds of the Figure 6.18a-b are also valid for the maximum pressure. Figure 6.19 shows the effects of S and ν on the magnitude of the maximum normalized pressure, denoted, in the text, as p_{\max}^* . As shown in the figure, p_{\max}^* may deviate from the incompressible value considerably for compressible materials.

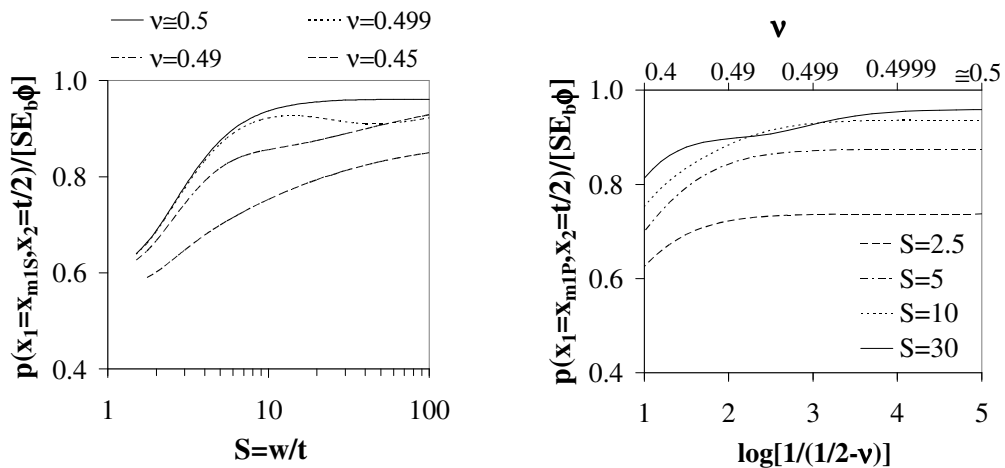


Figure 6.19 Maximum pressure in a bonded elastic layer under pure bending

At this stage, it is worth assessing the values proposed by Gent and Meinecke [20] for the “critical” rotation at which an IS-shaped bonded rubber layer fails due to internal rupture under pure bending (Eqs. (2.40)). It should be noted that the values in Eqs. (2.40) are derived based on the incompressibility assumption and using the pressure method (PM). The graphs in Figure 6.20 are obtained by adding the PM predictions for the location and magnitude of the maximum normalized pressure into the second plot in Figure 6.18a and into the first plot in Figure 6.19, respectively. From Figure 6.20a, it is seen that $x_{m1S} = x_1^*$ only for considerably high shape factors and incompressible materials. For lower S values, the site of failure moves towards the edge of the layer. Similarly, PM can predict the magnitude of the critical pressure accurately only when S is sufficiently large and $\nu=0.5$ (Figure 6.20b). The deviation of the PM curve from the FOT curves is noticeable for $S \leq 10$.

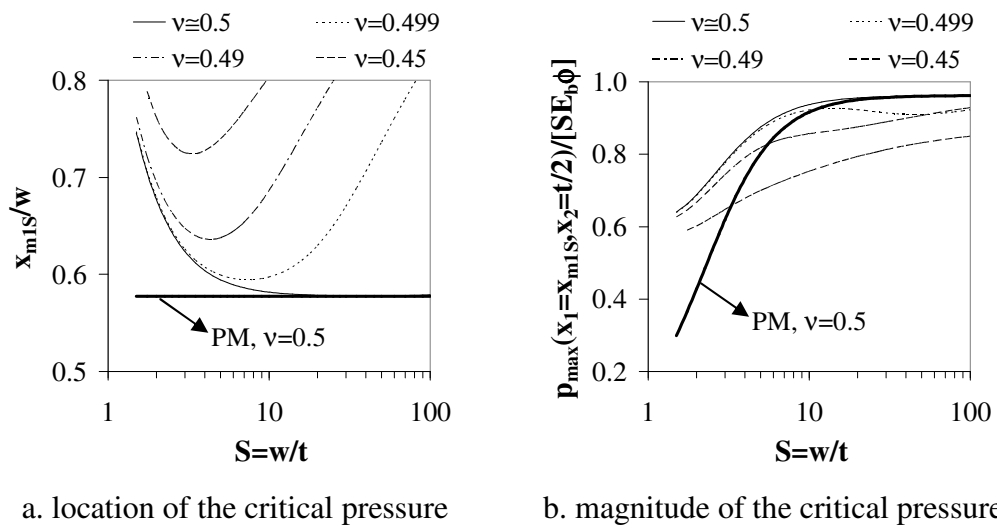


Figure 6.20 Assessment of the predictions of the pressure method (PM) for the “critical” pressure in an IS-shaped layer under pure bending

The effects of shape factor and Poisson’s ratio on the normalized maximum shear stress, denoted, in the text, as $(\tau_{12}^*)_{\max}$, are shown in Figure 6.21. It can be

seen that the effects of S and ν on $(\tau_{12}^*)_{\max}$ under pure bending is almost the same as in the uniform compression case (see Figure 6.11c). The critical shape factor where $(\tau_{12}^*)_{\max}$ reaches its peak value is approximately $S=2.5$ for under pure bending. For $S=2.5$, as ν increases $(\tau_{12}^*)_{\max}$ increases until the plateau is reached. On the other hand, for $S>2.5$, as ν increases, $(\tau_{12}^*)_{\max}$ increases to a peak value, then decreases until the incompressible value is attained.

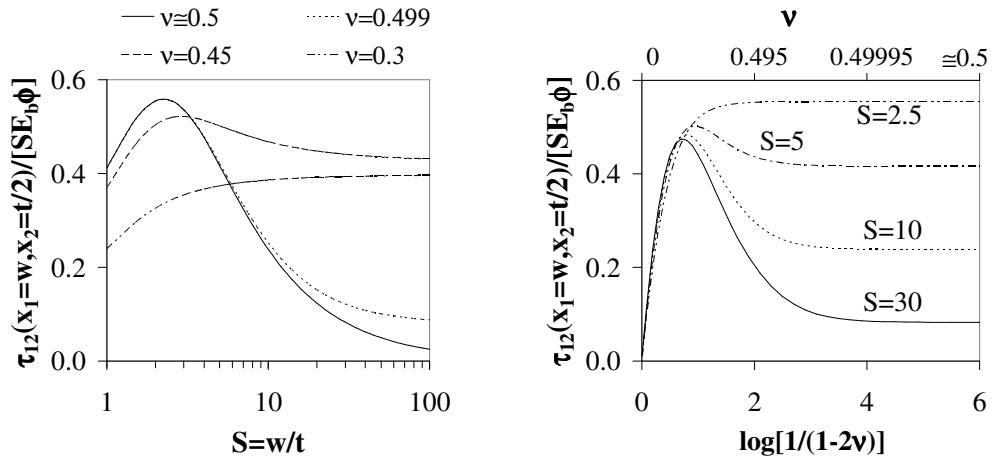


Figure 6.21 Effect of shape factor and Poisson's ratio on maximum shear stress under pure bending

6.3 APPARENT SHEAR BEHAVIOR

As mentioned previously, although some researchers [20,43] proposed approximate expressions for the apparent shear modulus of bonded elastic layers, these expressions were all derived based on the assumption that plane sections remain plane. Moreover, they considered only incompressible materials. Using the new formulation proposed in this dissertation with FOT, both of these assumptions are eliminated. The resulting expression for the apparent shear modulus is functions of both shape factor and Poisson's ratio.

Figure 6.22 shows the effects of shape factor and Poisson's ratio on the ratio of the apparent shear modulus of an IS-shaped bonded elastic layer to its true shear modulus (μ_a/μ). It is clear that for incompressible materials, the apparent shear modulus of a bonded elastic layer almost equals to its true shear modulus. The effect of the material compressibility becomes important only when S and ν are small. This result is compatible with the common acceptance that while the compressive and bending behavior of a bonded rubber layer can be considerably different than the behavior of corresponding unbonded layer, the effect of the bonded surfaces to shear behavior is negligible.

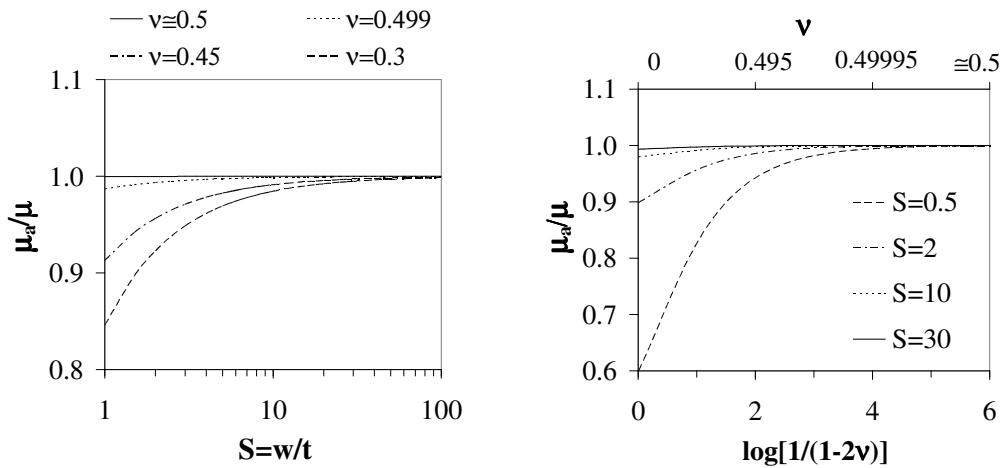


Figure 6.22 Effect of shape factor and Poisson's ratio on apparent shear modulus

Figure 6.23 compares the prediction of FOT for the “incompressible” apparent shear modulus of a bonded IS-shaped layer with the predictions of the expressions proposed by Rivlin and Saunders [43] and Gent and Meinecke [20], i.e., Eqs. (2.47) and (2.48). It is to be noted that although Horton et al. [42] also proposed an expression for μ_a , which is in the form of Eq. (2.48), it is not possible to apply their formula to IS-shaped layers because they did not derive an expression for the bending modulus of IS-shaped layers.

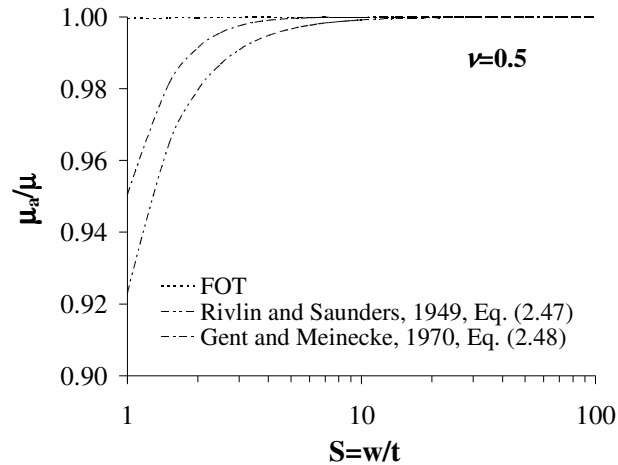


Figure 6.23 Comparison of the prediction of FOT for apparent shear modulus of an IS-shaped layer with the predictions of the other expressions in literature

As shown in Figure 6.23, all expressions converge to the true shear modulus as S increases. Eq. (2.47) starts to deviate from the other two expressions at approximately $S=10$. The deviation increases as S decreases. It is important to note that the basic difference between Eqs. (2.47) and (2.48) is that in Eq. (2.48), the effective bending modulus E_b is used instead of the elastic modulus E . In other words, Eq. (2.48) accounts for the effects of the bonded surfaces, as in the FOT solution. Thus, as shown in Figure 6.23, when the effects of the rigid surfaces are considered, the expression proposed by Rivlin and Saunders [43] approaches towards the FOT expression. From the figure, it can also be seen that the predictions of FOT and the results computed from Eq. (2.48) are almost identical for $S \geq 4$. The deviation observed in the lower S values can be attributed to the fact that while the expression in Eq. (2.48) is derived based on “the plane sections remain plane” assumption, this assumption is removed in the FOT expression.

The plots in Figure 6.24 show the effects of shape factor and Poisson’s ratio on the displacement distributions over the vertical section at $x_1=0.75w$ in an IS-shaped bonded elastic layer under apparent shear for two different shape factors; $S=1$ and $S=5$. As it is seen from the graphs, the effects of the bonded surfaces to the displacement distributions are negligible even for $S=1$.

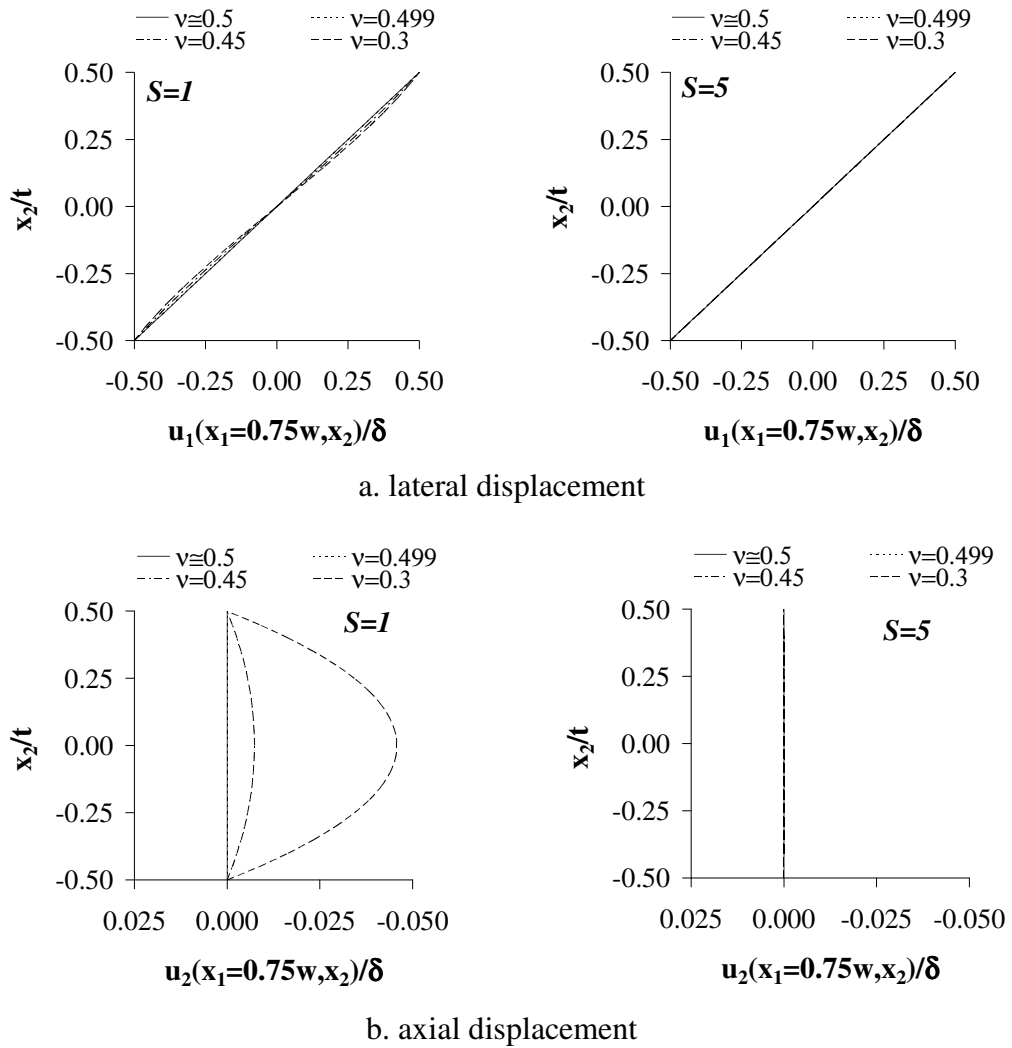
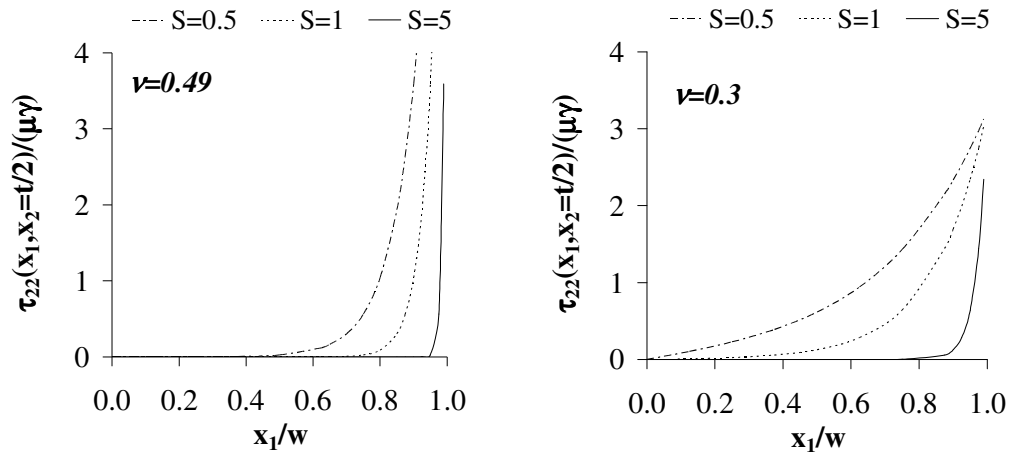
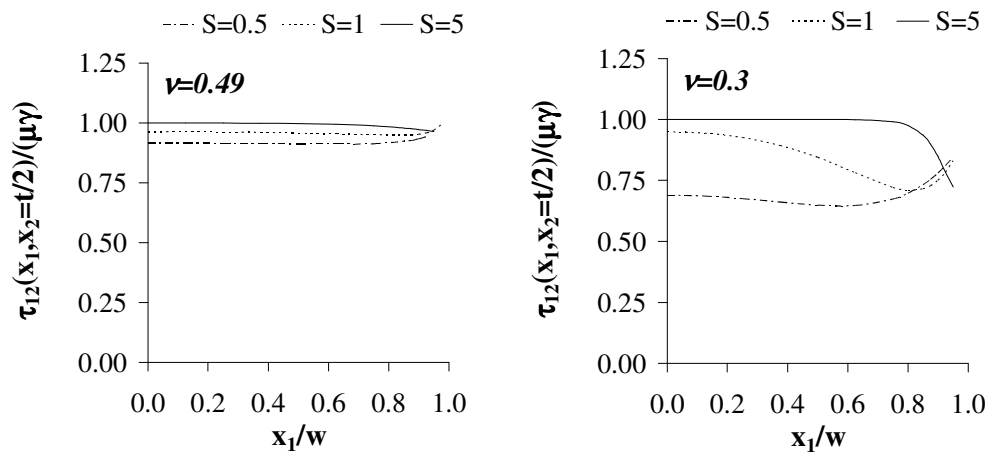


Figure 6.24 Displacement distributions in axial direction under apparent shear

The graphs in Figure 6.25 show the variation of the axial and shear stresses over the top bonded face of an IS-shaped bonded elastic layer under apparent shear for various shape factors and two specific values of Poisson's ratio: $\nu=0.49$, 0.3 . Parallel to the conclusions derived so far, it may be stated that unless S and ν are considerably small, the effect of bonded surfaces to the shear behavior of an elastic layer is negligible.



a. axial stress



b. shear stress

Figure 6.25 Axial and shear stress distribution in lateral direction under apparent shear

CHAPTER 7

EFFECT OF THE PRESENCE OF A CENTRAL HOLE ON COMPRESSIVE BEHAVIOR OF BONDED DISCS

When the earlier studies conducted on bonded elastic layers are investigated, it can be realized that little attention has been given to the layers in the shape of annular discs. Most of the studies have been conducted on “infinitely” long rectangular strips and solid discs. Very interestingly, these two cases are, in fact, the special limiting cases for a bonded elastic layer with a central hole.

In this chapter, the compressive behavior of annular discs bonded to rigid reinforcements is studied comprehensively using the closed form expressions derived from the first order theory (FOT). Since solid circular discs are a special type of annular discs, these discussions inherently include discussions on circular discs with no hole.

It is important to recognize that, as far as the bonded annular discs are concerned, the formulation proposed in this dissertation differs from the others in literature in three main aspects. First, the formulation is complete in itself; in other words, there is no need to try to find the most “successful” method to compute the constants of the theory (as done in [36]). Second, the material compressibility is included in the formulation naturally. For this reason, the solutions are valid not only for nearly or strictly incompressible materials (as in [16] or [52]), but, also for compressible materials. Thirdly, the expressions derived using FOT are free from the two fundamental assumptions of the pressure method: (i) the assumption that the plane sections remain plane and (ii) the pressure assumption. For this reason, the

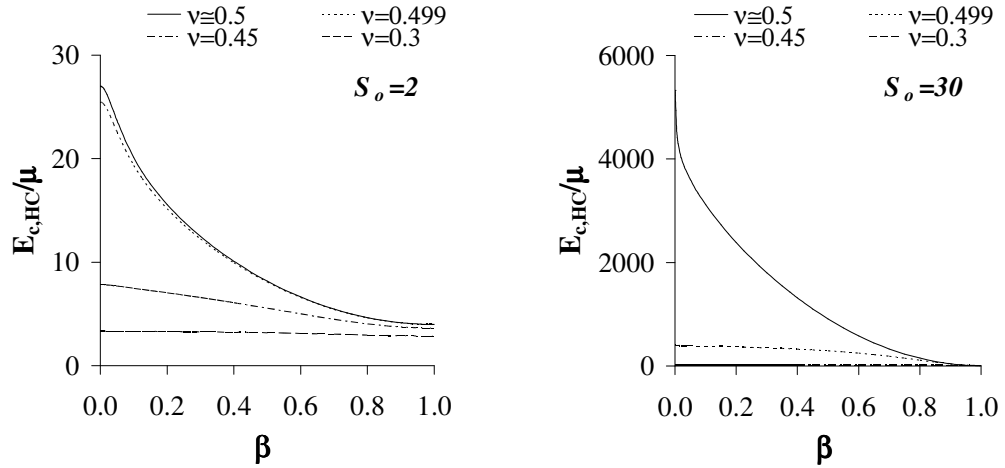
solutions are valid not only for HSF layers but also for LSF layers. Thus, the expressions derived from FOT are, in fact, useful tools to investigate the effect of the presence of a central hole on the compressive behavior of bonded circular discs and to assess the conclusions drawn by the earlier studies.

From the FOT expressions derived for HC-shaped layers (Section 4.1.2.1.2), it can be recognized that the compressive behavior of a bonded annular disc with outside radius R , inside radius a and thickness t depends on three main parameters: the radius ratio of the centrally placed hole $\beta=a/R$, Poisson's ratio of the elastic material ν and the aspect ratio of the layer R/t . Unlike a C-shaped layer, for which $S=R/(2t)$, it is not possible to relate the shape factor of an HC-shaped layer directly to its aspect ratio. On the other hand, it can be realized that the shape factor of an HC-shaped bonded elastic layer can be expressed as $S=S_o(1-\beta)$, where S_o equals to the shape factor of the corresponding solid disc with the same external radius and thickness. In this dissertation, besides β and ν , S_o , which is called "initial shape factor" as proposed in [52], is taken as a key parameter controlling the compressive behavior of bonded annular discs.

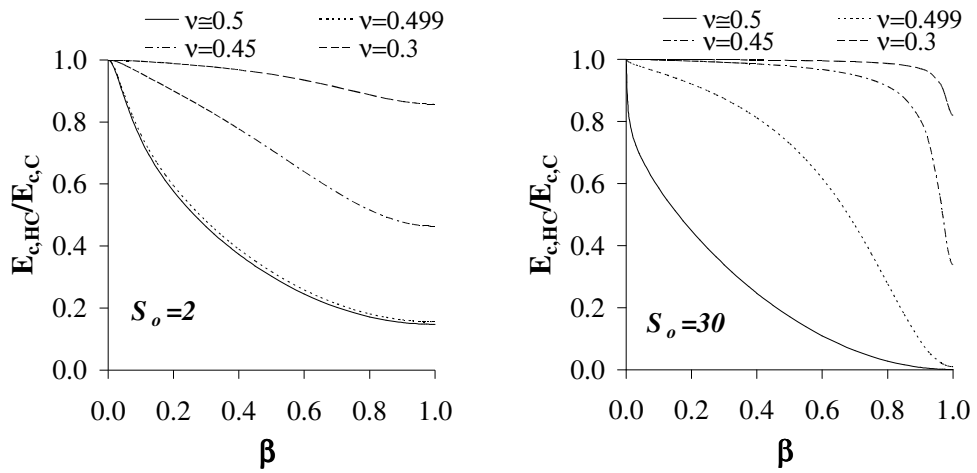
Thus, in the following sections, the effect of the presence of a central hole on the compressive behavior of bonded circular discs is investigated thoroughly by studying the effects of three key parameters; radius ratio β , initial shape factor S_o and Poisson's ratio ν ; on compression modulus, stress distributions and maximum shear stress/strain.

7.1 COMPRESSION MODULUS

The graphs presented in Figure 7.1a illustrate the effect of the radius ratio on compression modulus of bonded HC-shaped layers, denoted as $E_{c,HC}$, for two specific values of initial shape factor; $S_o=2$, representing LSF layers and $S_o=30$, representing HSF layers. To study the behavior of the layers over a wide range of compressibility, the variations are plotted for four different levels of material compressibility; $\nu \cong 0.5, 0.499, 0.45, 0.3$.



a. $E_{c,HC}$, normalized with respect to μ



b. $E_{c,HC}$, normalized with respect to $E_{c,C}$

Figure 7.1 Effect of radius ratio on $E_{c,HC}$, normalized with respect to (a) μ and (b) $E_{c,C}$, for two different initial shape factors $S_o=2,30$

The graphs in Figure 7.1a clearly show that the compression modulus of a bonded circular disc with a central hole can be much smaller than that of a solid disc. However, since the $E_{c,HC}$ values for different S_o and/or ν values can be considerably different, it is logical to replot these graphs in a somewhat normalized manner. The graphs presented in Figure 7.1b are plotted by normalizing $E_{c,HC}$ with respect to the compression modulus of the corresponding C-shaped layer with the same aspect ratio and material properties, which is called, in this chapter, $E_{c,C}$. The

normalized plots given in Figure 7.1b are also valuable in that they directly show the amount of reduction in compression modulus of a bonded circular disc if it has a central hole with a radius ratio β .

It should be noted that FOT may not predict $E_{c,HC}$ accurately for very large values of β ($\beta \approx 1$), when the actual shape factor of the layer tends to zero, in which case the parabolic bulging assumption is not valid. This is especially true if S_o is considerably small. For example, when $\beta=0.90$, the shape factor the layer with $S_o=2$ reduces to 0.2, for which the accuracy of the FOT predictions is questionable. On the other hand, realizing that the presence of even a very large hole, say a hole with a radius ratio of as large as 0.975, reduces the shape factor of the layer with $S_o=30$ to not less than 0.75, it can be said that the graphs plotted in Figure 7.1 for the HSF layer are realistic even for very small values of β .

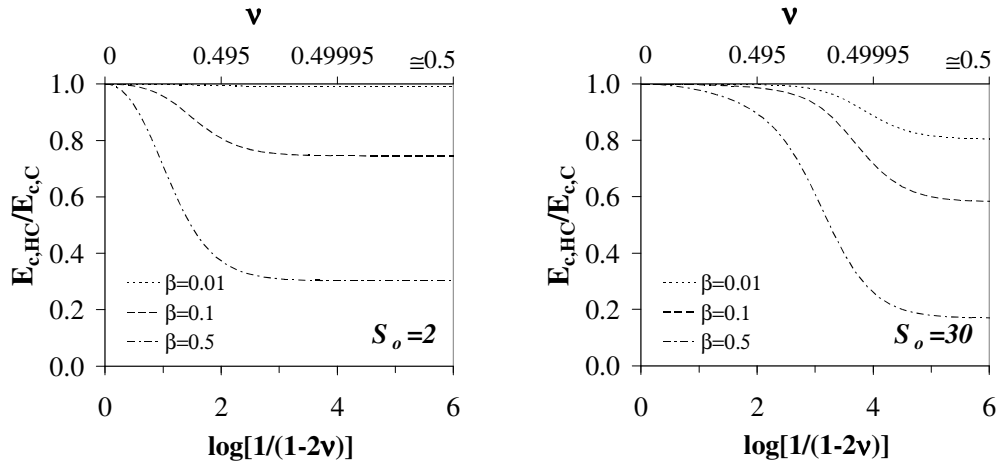
As it can be seen from Figure 7.1, the reduction in $E_{c,HC}$ with increasing β is drastic for a layer of strictly incompressible material. This is mainly due to the fact that the presence of even a very small hole in the center of the layer modifies the axial stress distribution over the cross section enormously due to the stress-free boundary condition at the center of the layer. It is important to note that the decrease in $E_{c,HC}$ with increasing β is *not* linear in general. For incompressible materials, $E_{c,HC}$ reduces abruptly near $\beta=0$ especially if S_o is high. It is interesting to realize that while the presence of a hole with $\beta=0.01$ does not influence the “incompressible” compression modulus of the LSF layer, the reduction in the modulus of the HSF layer is significant, almost 20%, for such a small hole. This behavior difference between the LSF and HSF layers is mainly due to the fact that although a “jump-like” decrease is observed at very small values of β for $S_o=30$, a somewhat more gradual decrease is started to be observed when the size of the hole reaches a critical β value for $S_o=2$.

The behavior of the HSF layer is different from the behavior of the LSF layer also in that while the LSF layer is not affected from the existence of slight compressibility ($\nu=0.499$), the HSF layer is influenced considerably. It is striking to observe that, for $S_o=30$ and $\beta=0.1$, the reduction in the compression modulus when

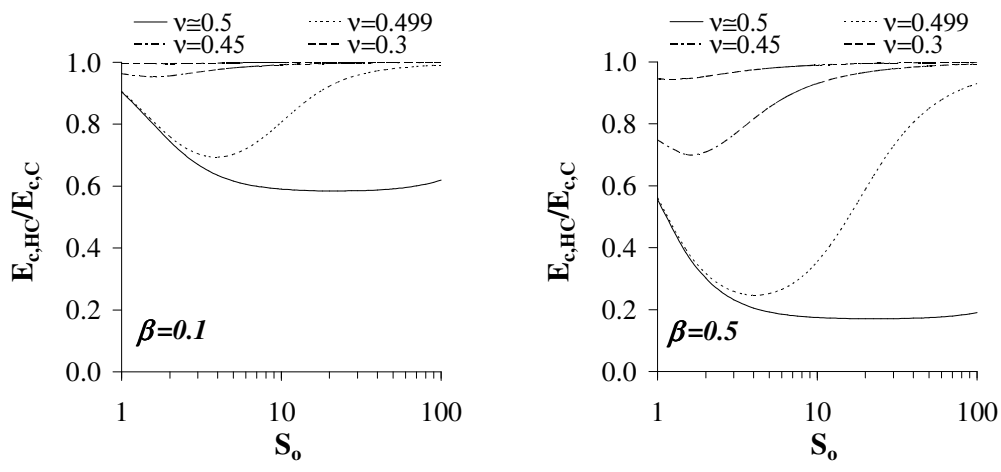
$\nu \cong 0.5$, which is more than 40%, is less than 13% if $\nu = 0.499$. Another important conclusion that can be drawn from the graphs in Figure 7.1 is that for a highly compressible layer ($\nu = 0.3$), the compression modulus of a bonded circular disc is almost independent from the radius ratio of the hole unless the hole size is too large. Therefore, one can conclude that, for $\nu = 0.3$, $E_{c,HC} = E_{c,C}$.

The graphs in Figure 7.2a are plotted for two specific values of shape factor, similar to those in Figure 7.1, and three specific values of radius ratio: $\beta = 0.01, 0.1$ and 0.5 , representing, respectively, a very small hole, a moderate-size hole and a fairly large hole. It is seen that the shapes of the curves for $E_{c,HC}/E_{c,C}$ versus ν are very similar for all studied values of S_o and β ; the ratio $E_{c,HC}/E_{c,C}$ decreases with increasing ν until the asymptotic incompressible value is attained. As the shape factor of the layer decreases, the value of ν at which the limiting value is reached also decreases. The most striking conclusion that can be drawn from the graphs in Figure 7.2a is, perhaps, that while $E_{c,HC}$ of the HSF layer may decrease considerably due to the existence of a very small central hole ($\beta = 0.01$), $E_{c,HC}$ of the LSF layer is not influenced from the presence of such a small hole in its center.

The effect of S_o on $E_{c,HC}$ is more apparent in the graphs presented in Figure 7.2b, which are plotted for two different β values, $\beta = 0.1, 0.5$. The graphs show that the incompressible theory predicts $E_{c,HC}$ for a layer of slightly compressible material satisfactorily only when S_o is considerably small, practically $S_o \leq 2$. For larger values of S_o , the incompressible theory starts to overestimate $E_{c,HC}$ and, for HSF layers, its prediction deviates from the actual modulus enormously especially if β is also large. In fact, the variation of the ratio $E_{c,HC}/E_{c,C}$ with S_o has an interesting shape for $\nu = 0.499$ and is worth mentioning here: the ratio $E_{c,HC}/E_{c,C}$ first decreases, thereby attaining a minimum value, and then increases with increasing S_o . From the second of Figure 7.2b, it can be seen that, for $\beta = 0.5$, the critical value of S_o where the ratio reaches its minimum value is about 4.0 and for this critical shape factor, the presence of the central hole reduces the compression modulus of the disc to quarter of its “initial” compression modulus.



a. variation with Poisson's ratio



b. variation with initial shape factor

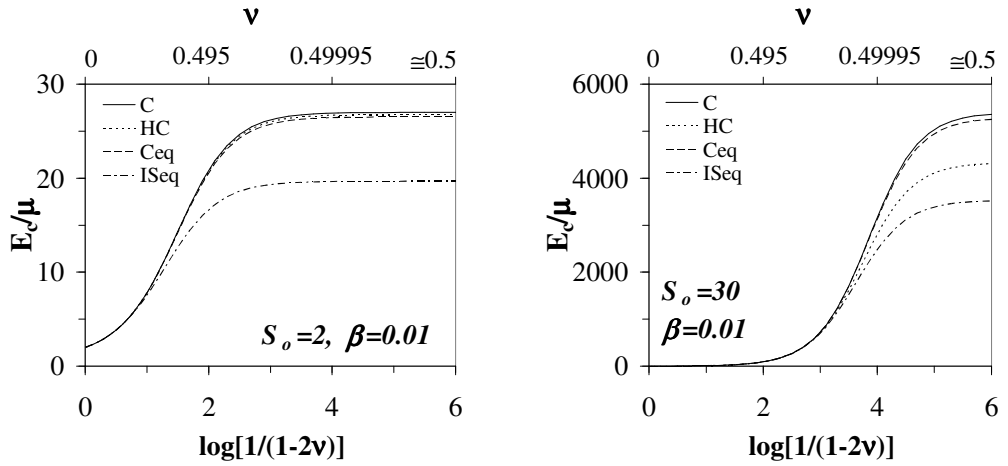
Figure 7.2 Effect of Poisson's ratio and initial shape factor on $E_{c,HC}$, normalized with respect to $E_{c,C}$, for two different initial shape factors

As discussed in Section 5.2, the behavior of a bonded HC-shaped layer approaches to the behavior of the bonded IS-shaped layer with the same S as $\beta \rightarrow 1$. Thus, E_c of a bonded annular disc with a “large” central hole can be computed from the E_c expression derived for the IS-shaped layer, as proposed by Gent and Lindley [2], who also recommended the use of the expression for the C-shaped layer if β is “small”. Since the conclusion of Gent and Lindley [2] was based on a limited number of *rubber* blocks with only a few values of β , they could not define the

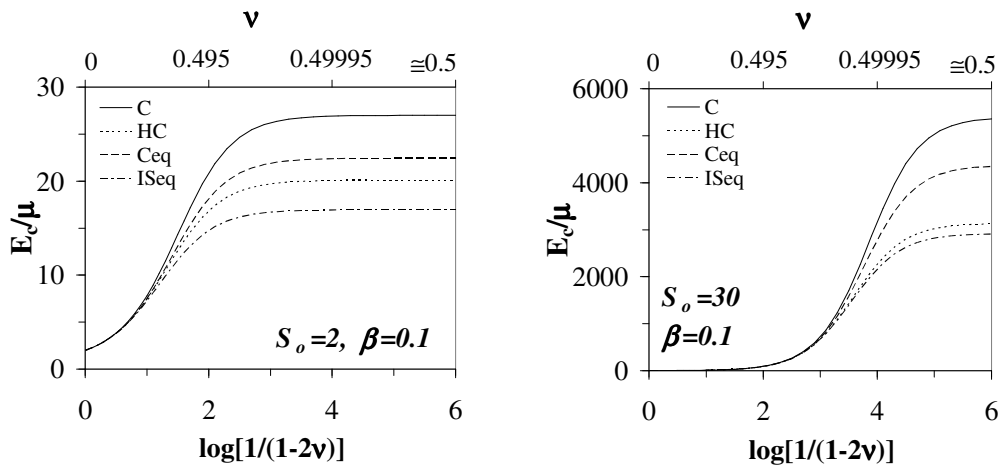
terms “small” and “large” they used for the hole sizes. Similarly, Constantinou et al. [16] proposed to calculate E_c of an HC-shaped layer from the E_c expression derived for a C-shaped layer by using the shape factor of the annular layer.

The validity of these proposals are examined in Figure 7.3 for different values of S_o (2, 30) and β (0.01, 0.1, 0.5). In these graphs, $E_{c,C}$ values are computed from the E_c expression derived for C-shaped layers (i.e., Eq. (4.44)) by using $S=S_o$, i.e., by ignoring the presence of the hole. The “equivalent” E_c values, denoted as $E_{c,ISeq}$ and $E_{c,Ceq}$ values, are computed from the E_c expressions derived for C and IS-shaped layers (i.e., Eq. (4.44) and third of Eqs. (4.14)) by using the actual shape factor of the layer as an “equivalent” shape factor, i.e., $S_{eq} = S_o(1 - \beta)$. In this chapter, these expressions are called “equivalent” C or “equivalent” IS expressions.

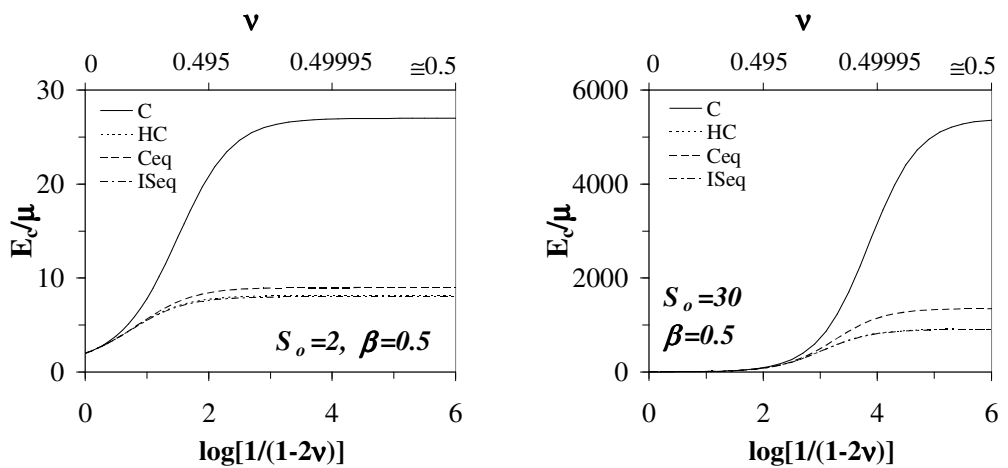
Since the presence of a very small hole does not affect the compression modulus of the LSF layer significantly (the first of Figure 7.3a), both the $E_{c,C}$ and $E_{c,Ceq}$ values are very close to the $E_{c,HC}$ values for $S_o=2$ and $\beta=0.01$. On the other hand, the $E_{c,HC}$ values for the HSF layer can be much smaller than the $E_{c,C}$ and $E_{c,Ceq}$ values when $\beta=0.01$ especially for nearly and strictly incompressible materials (the second of Figure 7.3a). Yet, the behavior of the HSF layer is not sufficiently close to the behavior of its “equivalent” IS-shaped layer, either. Thus, it is essential to use the exact HC expression (i.e., Eq. (4.55)) for the HSF layer when $\beta=0.01$. From the second of Figure 7.3b, it is seen that, for $S_o=30$, when β increases from 0.01 to 0.1, the $E_{c,HC}$ values becomes closer to the $E_{c,ISeq}$ values. Thus, for an annular layer with $S_o=30$ and $\beta=0.1$, the “equivalent” IS expression can be used for the prediction of the E_c of the layer. On the other hand, for the same layer, the use of the $E_{c,C}$ or $E_{c,Ceq}$ values leads to the overestimation of the actual modulus especially if ν is close to 0.5. For the same radius ratio ($\beta=0.1$), the behavior of the LSF layer is very different: the $E_{c,HC}$ curve lies in between the $E_{c,Ceq}$ and $E_{c,ISeq}$ curves so it does not seem to be proper to use any of the approximate expressions for the prediction of the E_c of the LSF layer when $\beta=0.1$. However, when the radius ratio is sufficiently large (e.g., $\beta=0.5$), as shown in the graphs given in Figure 7.3c, the $E_{c,HC}$ curves almost coincide with the $E_{c,ISeq}$ curves not only for $S_o=30$ but also for $S_o=2$.



a. $\beta=0.01$



b. $\beta=0.1$



c. $\beta=0.5$

Figure 7.3 E_c predictions computed from (solid) C, exact HC, “equivalent” C and “equivalent” IS expressions for $S_o=2$ (left hand side) and $S_o=30$ (right hand side)

Since the graphs given in Figure 7.3 are plotted for only three different values of β , it is useful to replot the $E_{c,HC}$, $E_{c,Ceq}$ and $E_{c,ISeq}$ curves as a function of β . The graphs presented in Figure 7.4 are plotted in such a way that they show the variations of the ratios $E_{c,ISeq}/E_{c,HC}$ and $E_{c,Ceq}/E_{c,HC}$ with β . Since the behavior of an LSF layer is very different from that of an HSF layer, the curves for $S_o=10$ are also included in Figure 7.4b.

As expected, for very large values of β , the equivalent IS expression satisfactorily predicts the annular modulus. However, a similar conclusion cannot be drawn for the equivalent C expression and small β values. The value of the ratio $E_{c,Ceq}/E_{c,HC}$ deviates from unity considerably for small values of β especially if $\nu=0.5$. For example, for $S_o=10$ and $\nu=0.499$, the prediction of the equivalent C expression highly overestimates the real modulus for almost all values of β . Surprisingly, for the same value of Poisson's ratio, the prediction of the equivalent C expression is fairly successful for $S_o=30$. This is an important conclusion in view of that it confirms one of the earlier conclusions; that the assumption of incompressibility overestimates the effect of the central hole on E_c of HSF layers.

The graphs presented in Figure 7.4 clearly show that it is in fact rather difficult to define the terminology "small" or "large" used for the size of the central hole in a bonded annular layer since such definitions also highly depend on the initial shape factor of the layer and Poisson's ratio of the layer material. One possible way of making such definitions can be to determine the range of the β values for which the use of the "equivalent" expressions leads to unacceptably large error in the computation of E_c for fixed values of S_o and ν . This can be done from the plots given in Figure 7.4. Table 7.1 presents limiting β values, denoted as β_{Ceq} and β_{ISeq} , computed for an error limit of 1%, for various shape factors and Poisson's ratios. For example, for $S_o=2$ and $\nu=0.499$, the limiting β values are 0.03 and 0.6. In other words, for $S_o=2$ and $\nu=0.499$, it is necessary to use the "exact" HC expression in the range of $0.03 \leq \beta \leq 0.6$; on the other hand, the use of the "equivalent" C expression for $\beta < \beta_{Ceq}=0.03$ or of the "equivalent" IS expression for $\beta > \beta_{ISeq}=0.6$ produces no more than 1% error for the specified values of S_o and ν .

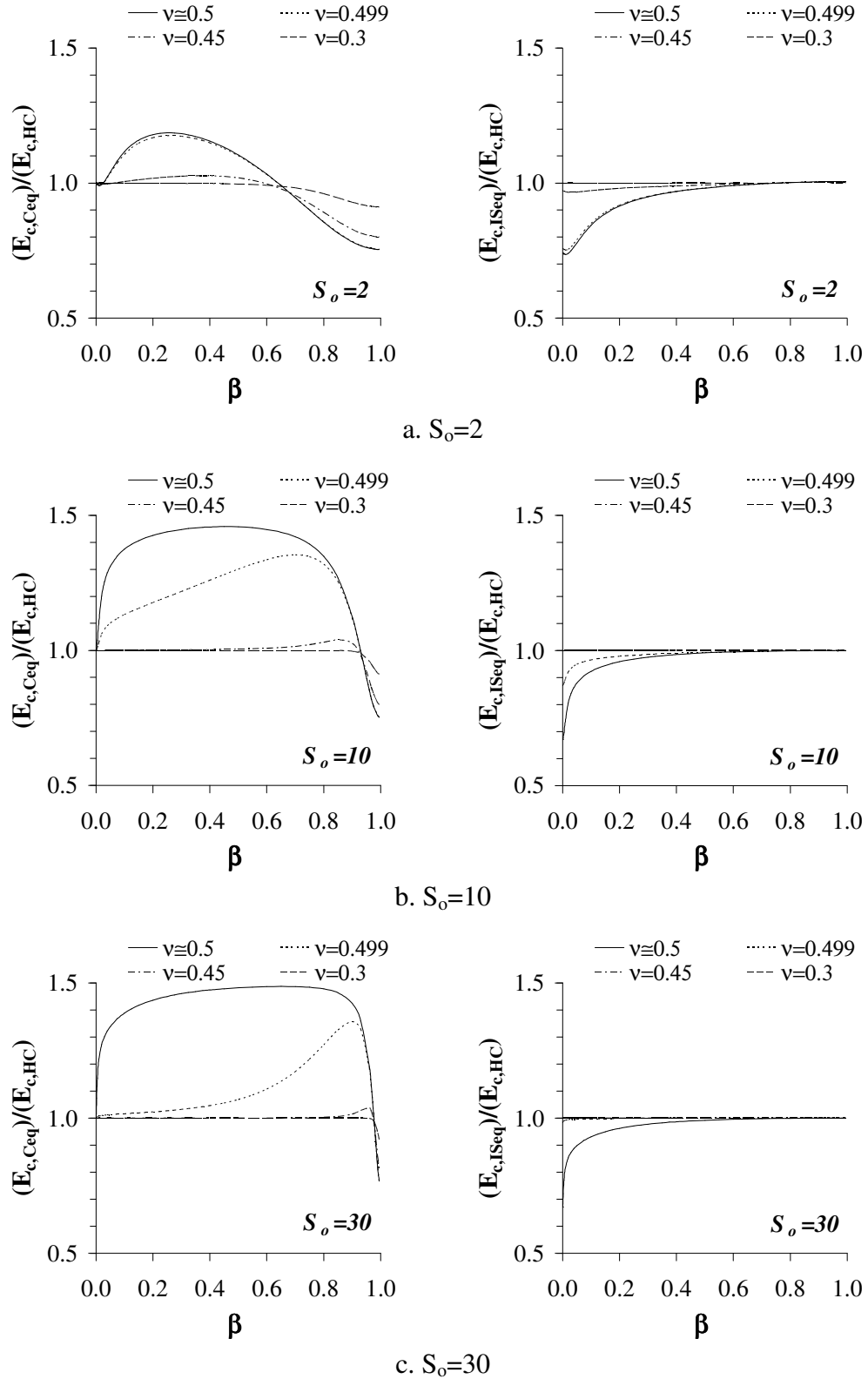


Figure 7.4 Assessment of the success of the “equivalent” C (left hand side) and “equivalent” IS (right hand side) expressions in predicting $E_{c,HC}$

Table 7.1 Limiting β values, denoted as β_{Ceq} and β_{ISeq} , computed for 1% error in the prediction of compression modulus

S_o	$\nu=0.5$		$\nu=0.499$		$\nu=0.45$		$\nu=0.3$	
	β_{Ceq}	β_{ISeq}	β_{Ceq}	β_{ISeq}	β_{Ceq}	β_{ISeq}	β_{Ceq}	β_{ISeq}
2	0.03	0.6	0.03	0.6	0.125	0.4	0.6	$\cong 0$
5	0.005	0.55	0.075	0.55	0.3	$\cong 0$	0.85	$\cong 0$
10	0.001	0.5	0.0025	0.4	0.6	$\cong 0$	0.9	$\cong 0$
15	0.001	0.5	0.0025	0.225	0.75	$\cong 0$	0.93	$\cong 0$
30	0.0001	0.5	0.01	0.005	0.975	$\cong 0$	0.975	$\cong 0$

From Table 7.1, it can also be seen that, for $S_o=30$ and $\nu=0.499$, there is no need to use the exact HC expression. For $\beta \leq 0.005$, it is proper to use the equivalent C expression while the expression must be changed to the equivalent IS expression for $\beta \geq 0.005$. It is interesting to see that for the same S_o value, the incompressibility assumption necessitates the calculation of E_c using the exact HC expression for the β values in the range $0.0001 \leq \beta \leq 0.5$. It is also worth mentioning that for $\nu=0.3$, the error due to the use of the equivalent IS expression is less than 1% for all of the studied S_o values.

7.2 STRESS DISTRIBUTIONS

The analytical expressions derived from FOT can also be used to plot the stress distributions over any section of a bonded annular disc. The graphs presented in Figure 7.5 illustrate how the axial stress distribution in radial direction changes with the size of the central hole for a bonded annular disc subjected to uniform compression. To compare the effect of the radius ratio on layers of different geometrical properties, the graphs are plotted side by side for two different values of initial shape factor: those on the left hand sides of Figure 7.5 are plotted for an LSF layer ($S_o=2$) and those on the right hand sides of Figure 7.5 are plotted for an HSF layer ($S_o=30$).

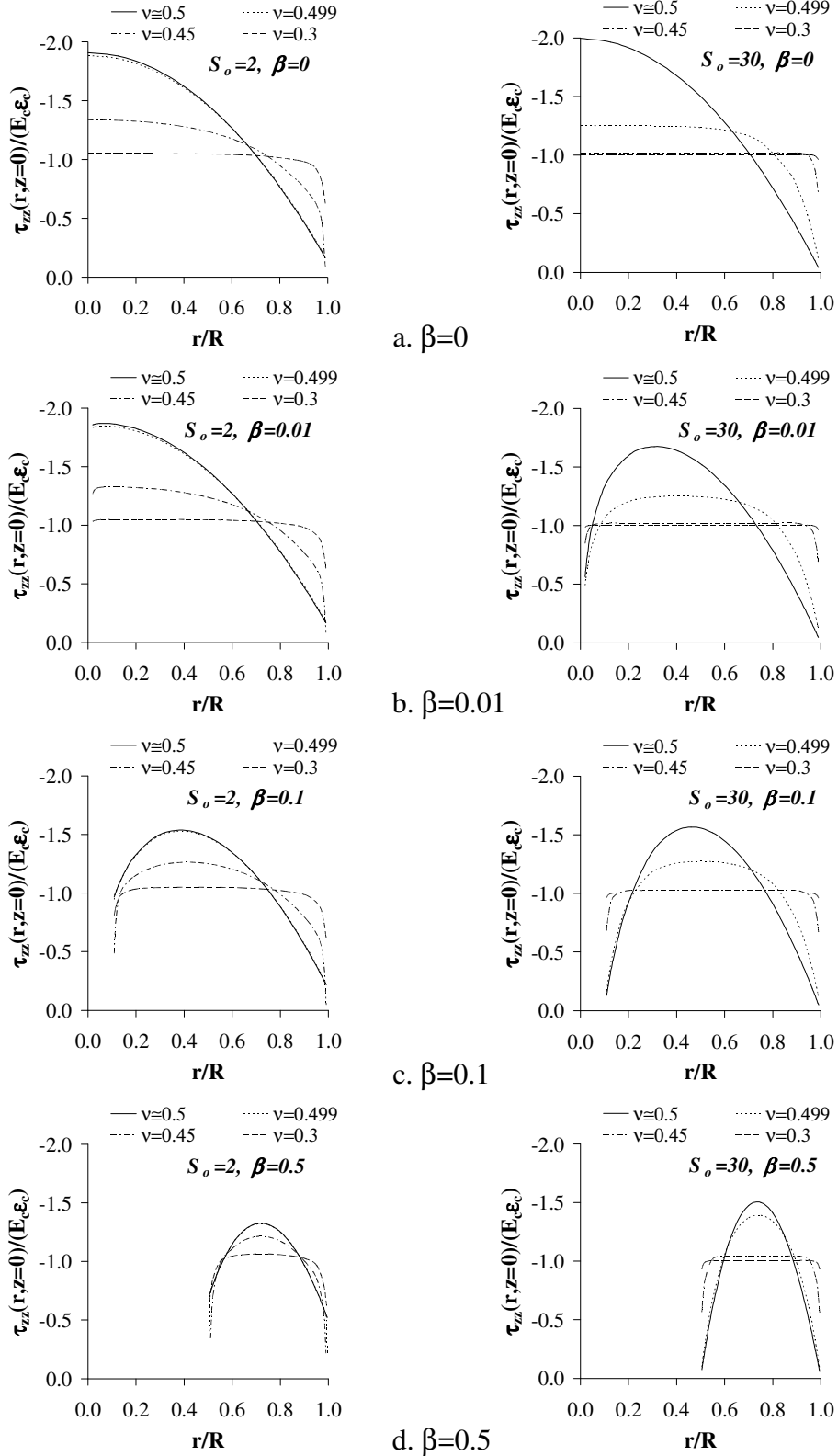


Figure 7.5 Effect of radius ratio on axial stress distribution in radial direction in bonded annular layers with $S_o=2$ (left hand side) and $S_o=30$ (right hand side)

Furthermore, since the effect of the radius ratio on the compressive behavior of a bonded annular disc also highly depends on the Poisson's ratio of the layer material, each graphic presented in Figure 7.5 is plotted for four different levels of material compressibility; $\nu=0.5, 0.499, 0.45, 0.3$. It is to be noted that the effect of the radius ratio on the axial stress distributions is investigated by plotting the distributions for four different values of radius ratio; $\beta=0, 0.01, 0.1$ and 0.5 . The value of $\beta=0$, implying a solid section, is included in the plots so that the behavior of HC-shaped layers can be compared with that of C-shaped layers. It should also be noted, that in Figure 7.5, the stress distributions are plotted over the central plane ($z=0$), where the axial stress (τ_{zz}) takes its maximum value at any vertical section in the layer, and that the stress values are normalized with respect to the uniform pressure, i.e. $E_c \varepsilon_c$.

From the firsts of Figure 7.5a,b, it is seen that the axial stress distribution in the LSF layer is not influenced from the presence of a very small hole ($\beta=0.01$) significantly. On the other hand, from the seconds of Figure 7.5a,b, it is clear that the presence of even a very small hole ($\beta=0.01$) causes a drastic change on the axial stress distribution in the HSF layer. The major effect of the hole is to shift the location of the maximum axial stress toward the center of the "ring" ($r=R(1+\beta)/2$) and to decrease the stress values near the inner edge noticeably. As expected, such a modification in the axial stress distribution is accompanied with a decrease in the peak value of the stress if $\nu \cong 0.5$. What is less expected is perhaps that even though the shape of the axial stress distribution is affected from the presence of a very small hole in the center of the HSF layer considerably, the value of the maximum axial stress does not change significantly if the layer material has slight compressibility. In fact, for compressible and highly compressible materials ($\nu \leq 0.45$), it can even be concluded that the presence of a central hole in a bonded circular disc does not affect the axial stress distribution in the layer, neither its shape nor its peak value.

Although the axial stress distribution in the LSF layer seems to be insensitive to the presence of a very small hole in its center, it surely starts to "sense" the existence of the hole when β is "sufficiently" large. This can be seen from the first

of Figure 7.5c easily. The effect of the presence of a moderate size hole in the LSF layer is very similar to the effect of the presence of a small size hole in the HSF layer: the axial stress distribution changes in a way that its peak value moves toward the center of the “ring” and the stress values drop rapidly near the inner boundary. Still, there is an important difference between the behavior the LSF and HSF layers: while the behavior of a slightly compressible HSF layer is considerably different from its incompressible behavior, the behavior of the LSF layer is not affected significantly from the existence of slight compressibility in the layer material.

From the graphs plotted for $\beta=0.5$, i.e., those in Figure 7.5d, another important conclusion can be drawn: the shape of the axial stress distribution in a bonded circular disc, which is symmetric about the center of the disc when it is solid (Figure 7.5a), changes with increasing radius ratio in such a way that for a sufficiently large value of β , the stress distribution becomes, again, symmetric, but now, about the center of the “ring”. Recalling the earlier conclusion derived in the previous section for the compression modulus, i.e., that E_c of an HC-shaped layer approaches to that of an “equivalent” IS-shaped layer with increasing radius ratio, it seems to be valuable to assess the validity of a similar conclusion for the stress distributions.

Such comparisons are made in the graphs given in Figure 7.6 for the axial stress distribution in radial direction for $S_o=2,30$ and $\beta=0.5$. It can easily be recognized that the graphs in the firsts of Figure 7.6a are simply replotting of the graphs in Figure 7.5d in such a way that the origin of the radial axis is shifted from the center of the layer to the center of the “ring”, i.e., $r=0.75R$ for $\beta=0.5$. It should also be noted that the stress values in the graphs plotted in the seconds of Figure 7.6 for the “equivalent” IS-shaped layers are computed from the axial stress expression derived for IS-shaped bonded elastic layers by using the “equivalent” shape factor of the layer, as defined in the previous section for the “equivalent” compression modulus computations.

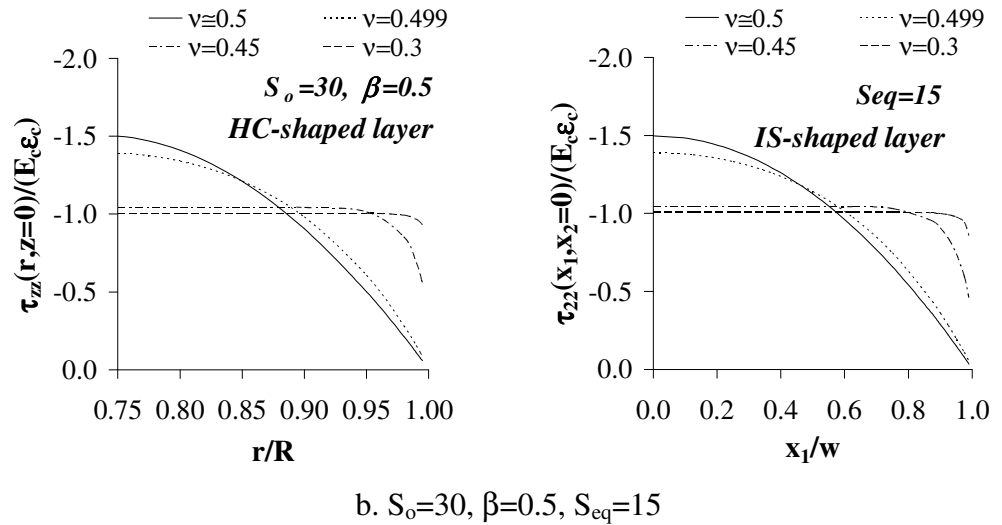
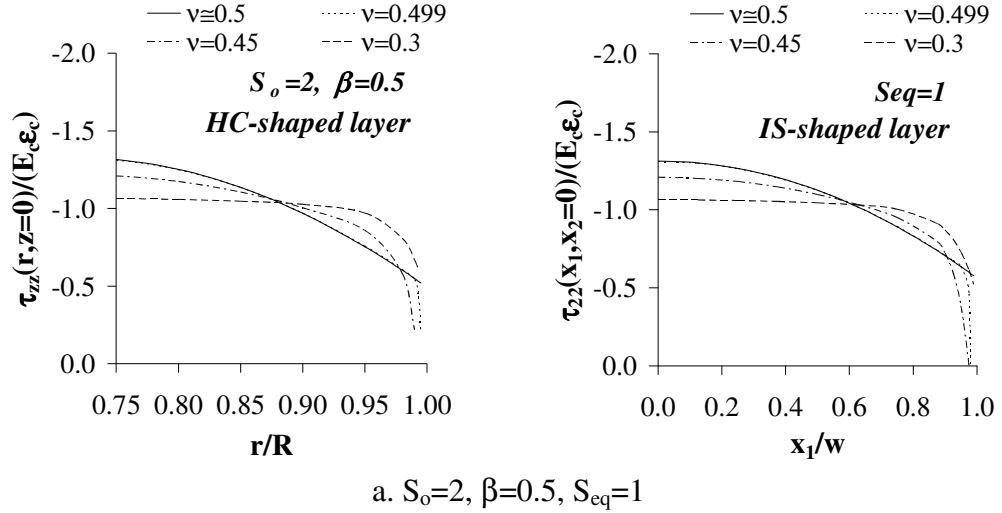


Figure 7.6 Comparison of the predictions of the exact HC expression and the “equivalent” IS expression for axial stress distribution in radial direction in an HC-shaped layer with $\beta=0.5$ for two different initial shape factors

From the comparison of the graphs in Figure 7.6b, it can be concluded that, as far as the axial stress distribution in radial direction is concerned, equivalent IS-shaped layer behavior is attained in the HSF layer when $\beta=0.5$. This means that for an HC-shaped layer to behave as if it were an IS-shaped layer, there is no need to have a β value very close to 1.0; HSF layers reach their equivalent IS-shaped layer behavior even when $\beta=0.5$. However, it is rather difficult to say exactly at which value of β this equivalence occurs since, such a value highly depends on both ν and

S_o . While the graphs for the LSF layer are also very close, one can infer from Figure 7.6a that the equivalent radius ratio for $S_o=2$ is slightly larger than $\beta=0.5$.

It is to be noted that very similar graphics can be plotted for the other stress components. The graphs plotted for the radial stress distributions indicated that the effects of the existence of a central hole on the radial stress distribution in the radial direction are very similar to those discussed above for the axial component.

The graphs presented in Figure 7.7 are plotted to study the effect of the radius ratio on the shear stress distribution in the radial direction in an HC-shaped layer composed of a nearly incompressible material ($\nu=0.499$) for a wide range of initial shape factors. It is to be noted that shear stress attains its maximum value over the bonded faces ($z=\pm t/2$) in any vertical section. For this reason, the shear stress distributions presented in Figure 7.7 are plotted over the top face of the layer ($z=t/2$). Furthermore, to have comparable results, shear stress values are also normalized with respect to the uniform pressure, i.e. $E_c \epsilon_c$.

The earlier conclusion that the normal stress distributions are not affected significantly from the existence of a very small hole in the center of the LSF layer while those in the HSF layer are influenced considerably, appears to be valid also for the shear stress distribution (Figure 7.7b). However, the effect of β on the shear stress distribution is completely different. Opposite to the normal stresses, which decrease noticeably near $r=\beta R$, the shear stress increases with increasing β . What is considerably important for $\tau_{rz}(\beta R, t/2)/E_c \epsilon_c$, which can be denoted, in the text, as $\tau_{rz}^*(\beta R)$, is that it may become even larger than $\tau_{rz}(R, t/2)/E_c \epsilon_c$, denoted, in the text, as $\tau_{rz}^*(R)$. When the graphs in Figure 7.7c are studied, it can be observed that $\tau_{rz}^*(\beta R)$ is larger than $\tau_{rz}^*(R)$ for all studied values of S_o when $\beta=0.1$.

Another important observation is that $\tau_{rz}^*(R)$ also increases with increasing β . It is interesting to see that while a moderate size hole results in considerable increase in $\tau_{rz}^*(\beta R)$, it does not cause significant change on $\tau_{rz}^*(R)$. On the other hand, $\tau_{rz}^*(R)$ increases significantly when β becomes 0.5. In fact, as β increases $\tau_{rz}^*(R)$ approaches to the value of $\tau_{rz}^*(\beta R)$ and in the limiting case they become equal, which occurs when the layer starts to behave as if it were an IS-shaped layer.

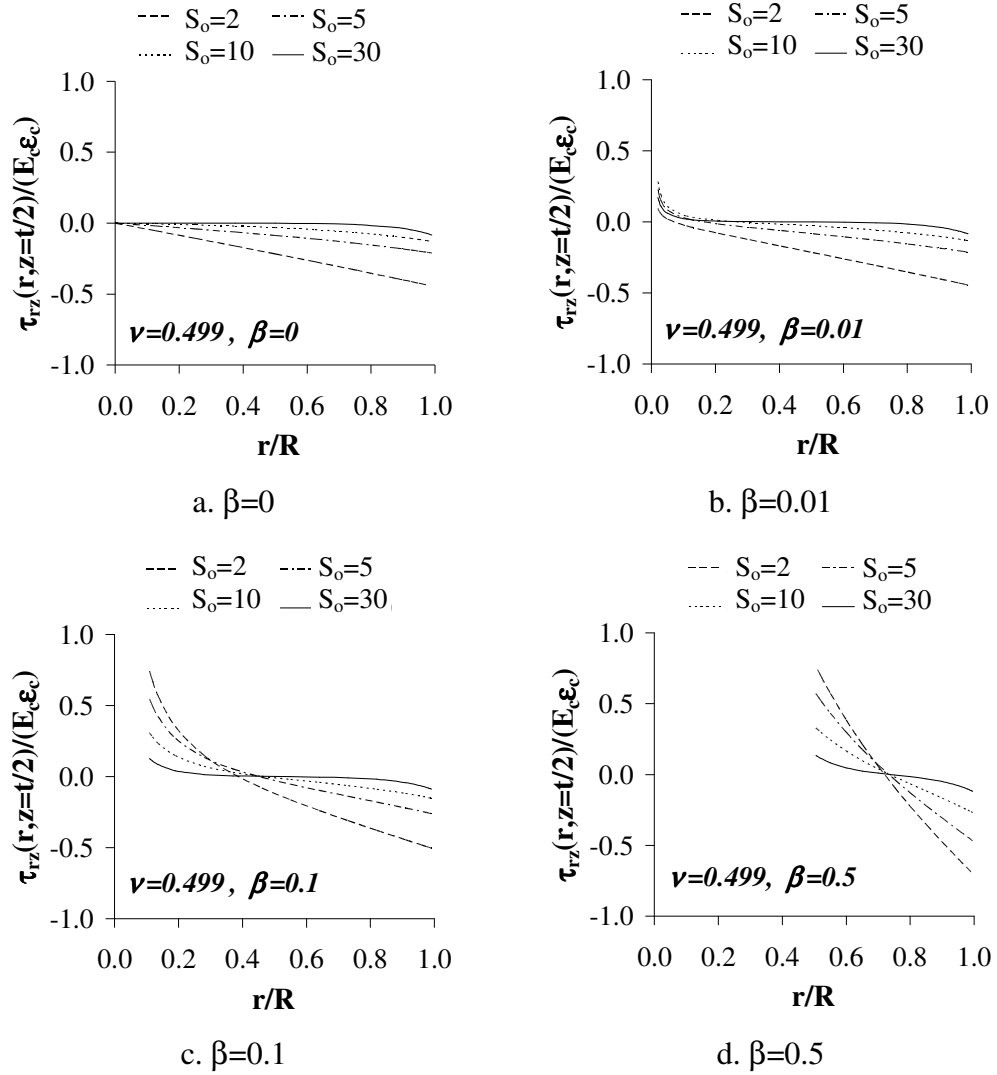


Figure 7.7 Effect of initial shape factor on shear stress distribution in radial direction in a bonded annular layer of slightly compressible material ($\nu=0.499$)

The effect of the radius ratio on the stress distributions through the layer thickness can also be studied in a similar way. As an example, the distributions given in Figure 7.8 show the variation of the radial stress over the layer thickness at the center of the “ring” i.e., at $r=(R+\beta R)/2$. As expected, the radial stress is constant through the layer thickness for the HSF layer. On the other hand, the radial stress distributions are nonuniform in the LSF layer especially if ν is close to 0.5.

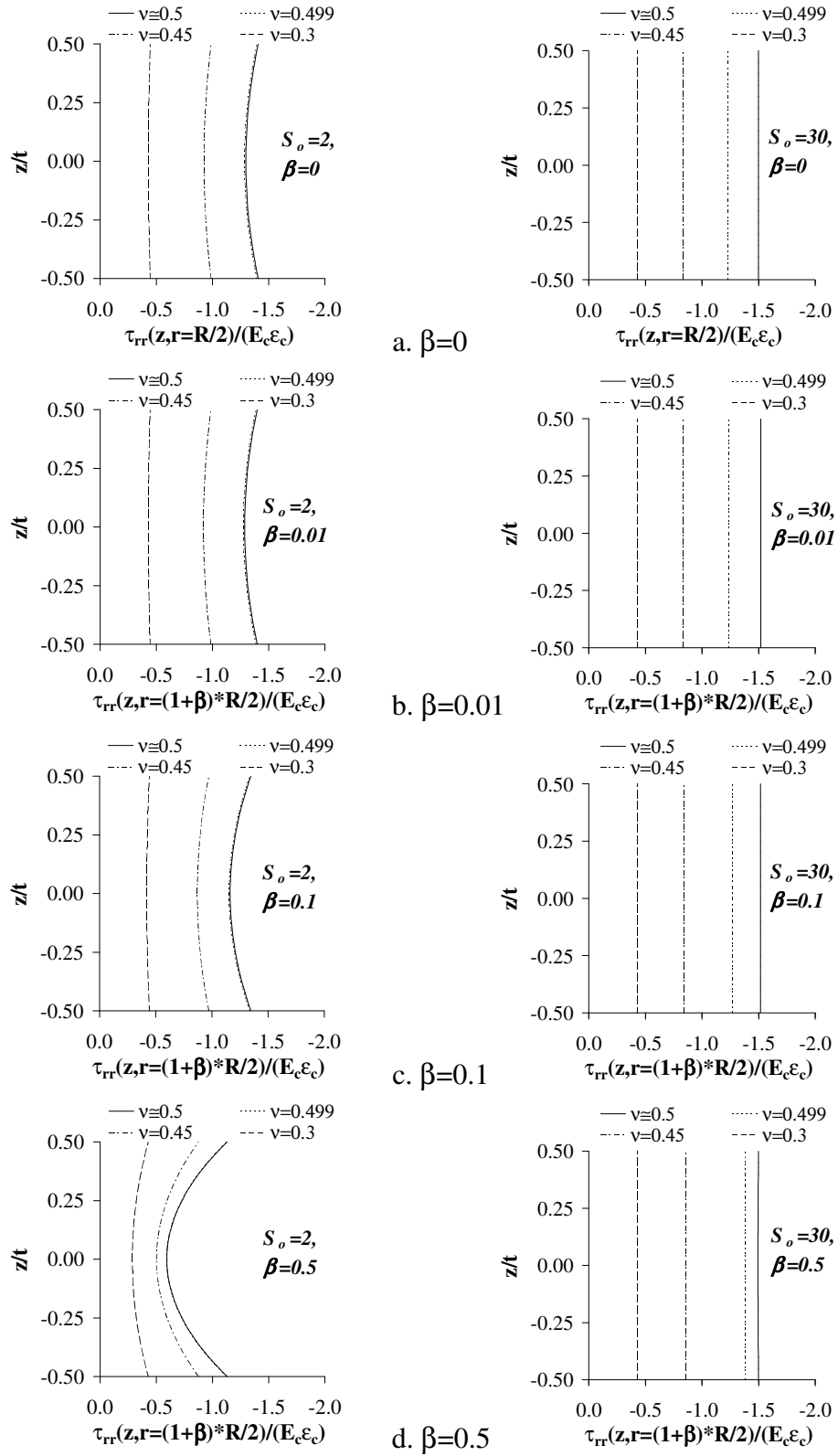


Figure 7.8 Effect of radius ratio on radial stress distribution in axial direction in bonded annular layers with $S_o=2$ (left hand side) and $S_o=30$ (right hand side)

From Figure 7.8, it can also be observed that stress distributions over the studied section remain almost the same when the size of the hole is small or moderate. For $S_o=30$, the stress distributions seem to be almost unaffected from the presence of a central hole even when $\beta=0.5$. On the other hand, for the LSF layer with $\beta=0.5$, even the curves plotted for $\nu=0.3$ are observed to change slightly. It can easily be noticed that for $S_o=2$ and $\beta=0.5$, the radial stress decrease considerably especially if the layer material is nearly or strictly incompressible.

7.3 MAXIMUM SHEAR STRESS AND SHEAR STRAIN

From the graphs presented in Figure 7.7, it can be recognized that one of the major effects of the existence of a central hole in a bonded circular disc is to increase the shear stress in the layer. Thus, it seems to be valuable to study the maximum shear stress developing in bonded elastic discs in some detail.

The graphs given in Figure 7.9 show the effect of shape factor and Poisson's ratio on the normalized maximum shear strain $(\tau_{rz})_{max}/E_c \mathcal{E}_c$, denoted as $(\tau_{rz}^*)_{max}$, in a C-shaped bonded elastic layer. It is to be noted that the maximum shear stress occurs at $(r=R, z=\pm t/2)$ in a bonded solid circular disc.

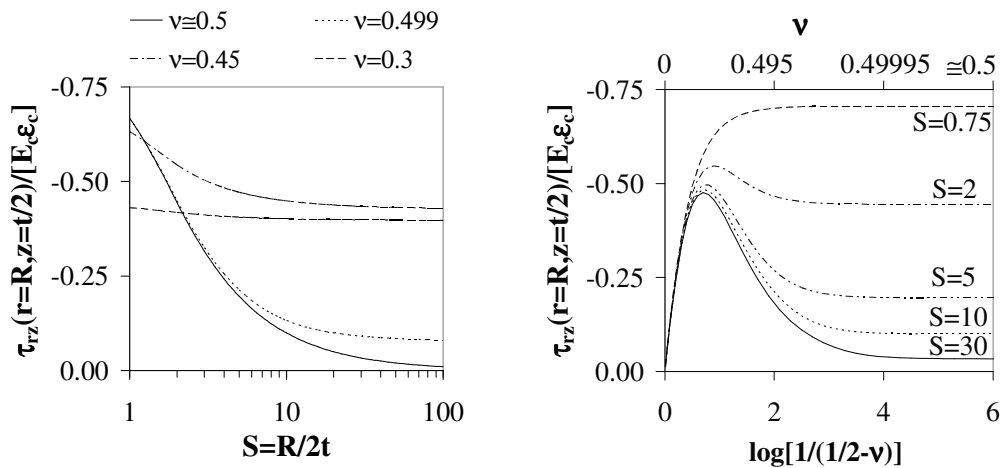
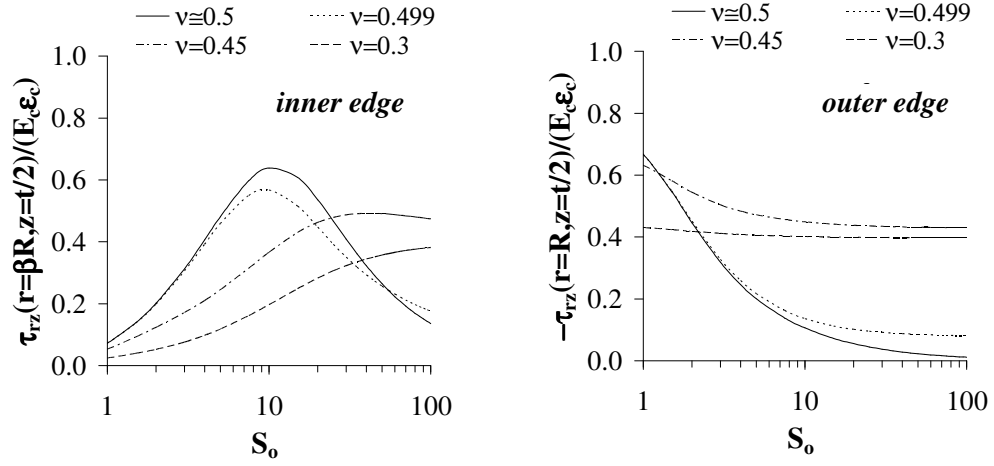


Figure 7.9 Effect of shape factor and Poisson's ratio on maximum shear stress in C-shaped bonded elastic layers

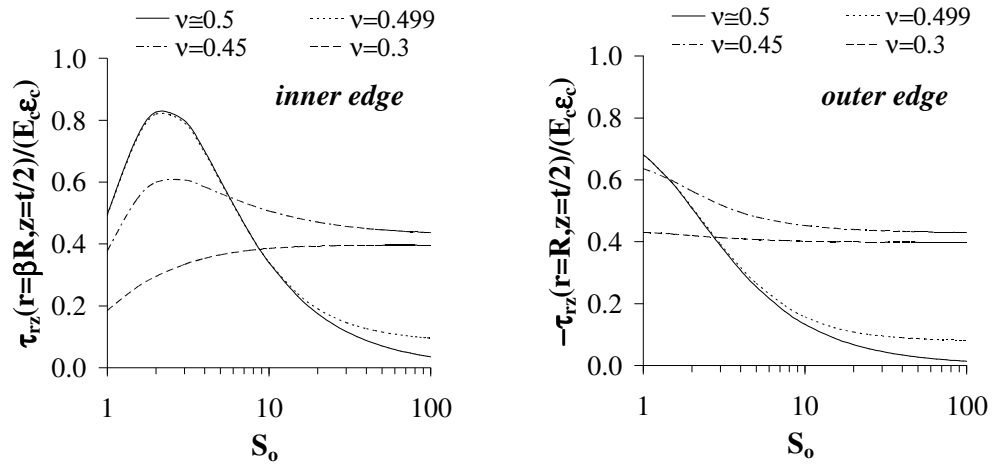
When the graphs presented in Figure 7.9 are compared with the similar graphs plotted for IS-shaped layers (Figure 6.11c (page 155)), it can be seen that the effects of S and ν on $\tau_{rz}^*(R)$ in a bonded solid disc are very similar to their effects on the normalized peak shear stress in a bonded strip. The shapes of the curves for fixed values of S or ν are almost the same. It can also be recognized that similar to IS-shaped layers, for which the critical shape factor at which $(\tau_{rz}^*)_{\max}$ attains its maximum value is 1.0, a critical value of shape factor also exists for C-shaped layers and is approximately equal to 0.75 (the second of Figure 7.9).

As already mentioned, there are two possible locations for the maximum shear stress in a bonded annular disc: either the inner edge or the outer edge over the bonded surfaces ($z=\pm t/2$). However, it is rather difficult to say exactly at which point the maximum shear stress occurs since this directly depends on β , S_o and ν . Thus, it seems to be wise to study the effects of all three parameters on the shear stresses at the edges of a bonded annular layer.

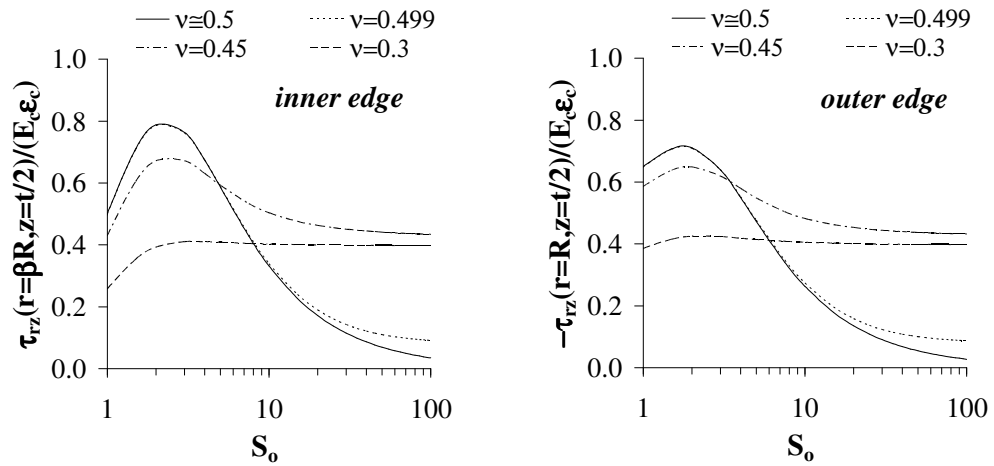
The graphs presented in Figure 7.10 plot the normalized shear stresses at the inner and outer edges of bonded annular discs subject to uniform compression as a function of S_o for three different values of β . When the second of Figure 7.10a is compared with the first of Figure 7.9, it can be realized that the existence of a very small central hole ($\beta=0.01$) does not influence $\tau_{rz}^*(R)$ significantly. On the other hand, keeping in mind that $\tau_{rz}^*(\beta R)$ equals to zero for a solid circular disc ($\beta=0$), one can easily notice the drastic effect of the existence of such a small hole on $\tau_{rz}^*(\beta R)$. It should be noted that the effect of the hole on $\tau_{rz}^*(\beta R)$ also depends on ν considerably. For compressible materials ($\nu \leq 0.45$), $\tau_{rz}^*(\beta R)$ increases with increasing S_o when $\beta=0.01$. For $\nu=0.45$, the curve seems to reach an asymptotic value at very large values of S_o . On the other hand, for nearly and strictly incompressible materials, the variation of $\tau_{rz}^*(\beta R)$ with S_o seems to have a “bell” shape when $\beta=0.01$; after increasing to a peak value at a critical S_o value, it decreases with increasing S_o . This critical S_o value is approximately 10 for nearly and strictly incompressible materials.



a. $\beta=0.01$



b. $\beta=0.1$



c. $\beta=0.5$

Figure 7.10 Variation of shear stress at the inner (left hand side) and outer (right hand side) faces of a bonded annular layer with initial shape factor

The comparison of the seconds of Figure 7.10a,b shows that $\tau_{rz}^*(R)$ is not influenced from the existence of even a moderate size hole in the center of the layer. On the other hand, the graphs given in the firsts of Figure 7.10a,b are considerably different, showing the significant effect of β on $\tau_{rz}^*(\beta R)$. The curves are still dependent on ν . For $\nu=0.3$, $\tau_{rz}^*(\beta R)$ increases with increasing S_o until an asymptotic value is reached. On the other hand, the bell-shaped variation is noticeable even for $\nu=0.45$ when $\beta=0.1$. It is noteworthy that when $\beta=0.1$, the critical S_o value for nearly and strictly incompressible materials is about 2, much smaller than 10. It should also be noted that the value of $\tau_{rz}^*(\beta R)$ at this critical S_o value also increases considerably. In fact, from the first of Figure 7.10b, one important conclusion can be drawn on the maximum shear stress developing in a bonded annular layer: the peak value of $(\tau_{rz})_{max}^*$ in an HC-shaped layer can even be larger than the peak values observed in IS or C-shaped layers.

When the graphs in Figure 7.10b are compared with those in Figure 7.10c, it can be seen that the shapes of the curves remain almost the same for $\tau_{rz}^*(\beta R)$ while the shapes of the curves for $\tau_{rz}^*(R)$ change slightly when β is *further* increased to 0.5 especially for LSF layers. It can be noted that the peak value for $\tau_{rz}^*(\beta R)$ at the critical S_o value also decreased slightly for nearly and strictly incompressible materials, while it increased a little for a relatively lower value of Poisson's ratio ($\nu=0.45$). When the first of Figure 7.10c is compared with the second one, it can also be seen that the stress values at the both edges become almost equal for HSF layers when $\beta=0.5$, as expected.

Considering that the maximum shear strain $(\gamma)_{max}$ is a special concern in the design of bonded elastic layers, it seems to be valuable to investigate the effect of the presence of a hole in the center of a bonded elastic disc on $(\gamma)_{max}$ developing in the elastic material due to compression. The graphs given in Figure 7.11 plot the ratio of the maximum shear strain in an HC-shaped layer, $(\gamma)_{max,HC}$, to that in a C-shaped layer with the same R/t value, $(\gamma)_{max,C}$, as a function of β for several values of S_o and ν .

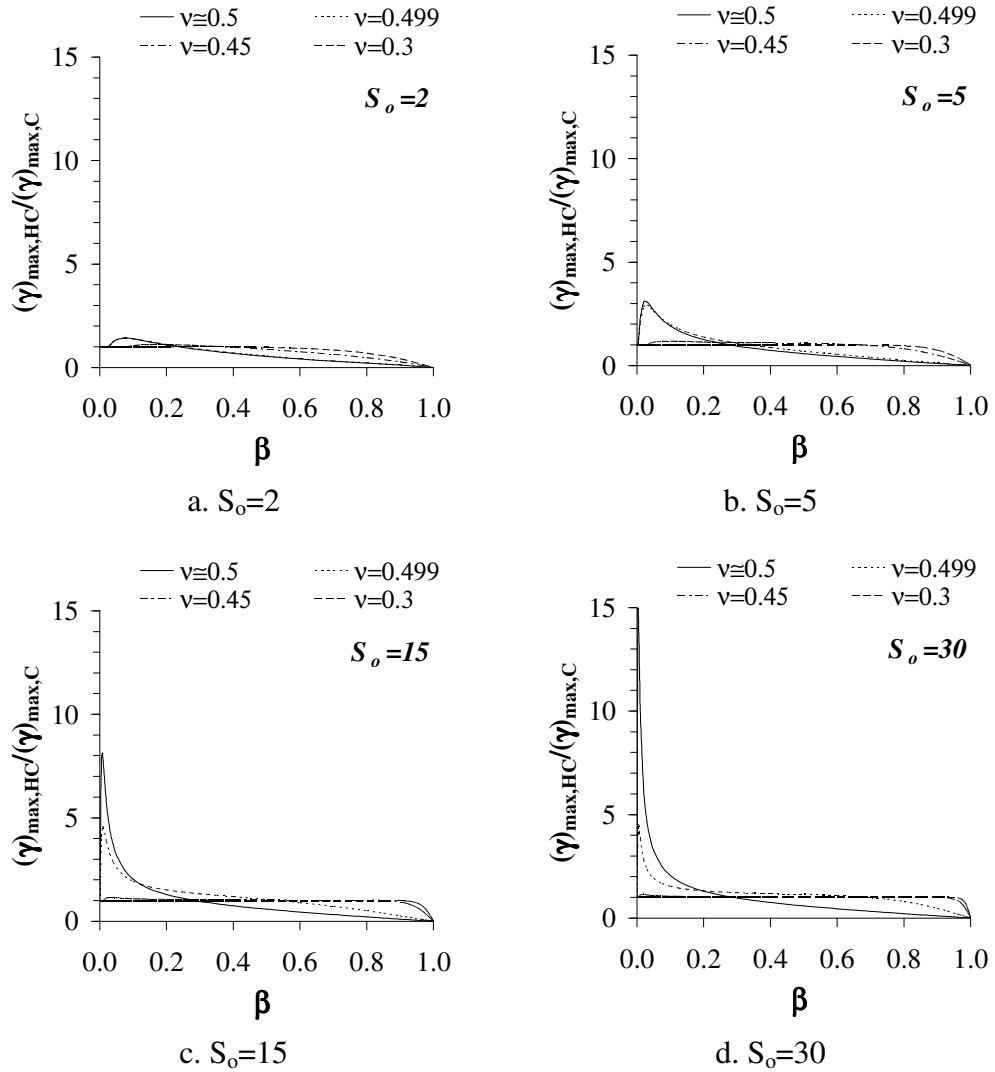


Figure 7.11 Magnification of maximum shear strain due to the existence of a hole in the center of a bonded circular disc as a function of radius ratio

When the graphs given in Figure 7.11 are studied carefully, it can be observed that $(\gamma)_{\max,HC}$ is not influenced significantly from the existence of a central hole in a bonded elastic layer of compressible ($\nu \leq 0.45$) material unless β is too large. On the other hand, the maximum shear strain ratio can reach very large values for HSF layers especially if $\nu \approx 0.5$. For $S_o=30$, it is possible to have a maximum shear strain ratio of as large as 15. It is striking to observe that the existence of even very slight compressibility in the layer material can reduce the peak value of the ratio. For

$S_o=30$, the ratio $(\gamma)_{max,HC}/(\gamma)_{max,C}$ has a peak value of 4.5 when $\nu=0.499$, which is much smaller than the incompressible value of 15.

For nearly and strictly incompressible materials, the variation of the maximum shear strain ratio with the radius ratio can be defined as follows: the ratio $(\gamma)_{max,HC}/(\gamma)_{max,C}$ first increases with increasing β until a peak value is reached, then, it decreases as β increases. In fact, there is also an initial “ β -insensitive” region at very small values of β . This can be observed from the graph in Figure 7.11a for the layer with $S_o=2$. Even though it is quite difficult to detect such regions from the plots presented in Figure 7.11b-d for the layers with larger initial shape factors, one can easily see them if the graphs are plotted using a logarithmic scale for the horizontal axis.

Another important conclusion that can be drawn from the graphs in Figure 7.11 is that for nearly and strictly incompressible materials, the layer with a larger initial shape factor reaches the peak value of the maximum shear strain ratio at a smaller radius ratio. For strictly incompressible materials, it can also be concluded that the peak value of the ratio $(\gamma)_{max,HC}/(\gamma)_{max,C}$ also increases as S_o increases.

At this point, it is worth mentioning that Constantinou et al. [16] state that the maximum shear strain ratio is “in the range 1.4-2.2” for the range of parameters that “cover almost the complete range of interest in applications of elastomeric bearings in base isolation”. In fact, the range of parameters they considered were $5 \leq S_o \leq 20$, $K/\mu=1000, 4000$ (corresponding to $\nu=0.4995, 0.499875$) and $D_o/D_i=5, 7.5, 10$ (corresponding to $\beta=0.1, 0.133, 0.2$). It is worth noting that they used a different parameter for the hole size: “diameter ratio” D_o/D_i , where D_o and D_i are respectively external and internal diameters for the disc. D_o and D_i can be written in terms of the notation used in this dissertation as $D_o=2R/t$ and $D_i=2a/t$. Thus, the diameter ratio D_o/D_i simply equals to $1/\beta$. Based on their approximate analysis, Constantinou et al. [16] proposed the following simple expression for the maximum shear strain ratio in terms of the radius ratio β :

$$\frac{(\gamma)_{max,HC}}{(\gamma)_{max,C}} = 0.9 + \frac{0.12}{\beta} \quad (7.1)$$

While deriving this formula, they pointed out that the ratio $(\gamma)_{max,HC}/(\gamma)_{max,C}$ “has a rather complex dependency on the shape factor and ratio K/G but primarily depends on the diameter ratio D_o/D_i . Conservatively, it may be assumed independent of S_o and K/G with a value equal to the maximum for each value of D_o/D_i ”.

The graphs in Figure 7.12 plot the variation of the ratio $(\gamma)_{max,HC}/(\gamma)_{max,C}$ with β for strictly ($\nu \cong 0.5$) and nearly incompressible ($\nu = 0.499$) materials. The predictions of the expression proposed in [16] also included in the graphs in the form of discrete points in filled triangular shapes. From Figure 7.12, it can be seen that the curve plotted from the simple formula proposed by Constantinou et al. [16] almost fits to the curve plotted for $S_o=30$ and $\nu \cong 0.5$ until the curve approaches to the peak point at a very small value of β . In fact, this is also the case for $S_o=5$ and $S_o=15$ provided that the layer material is strictly incompressible. On the other hand, the simple formula can overestimate the maximum shear strain ratio drastically for very small holes especially if the layer material has slight compressibility. Thus, the simple expression proposed in [16] should be used with care in bonded annular discs especially if the radius ratio is smaller than 0.1.

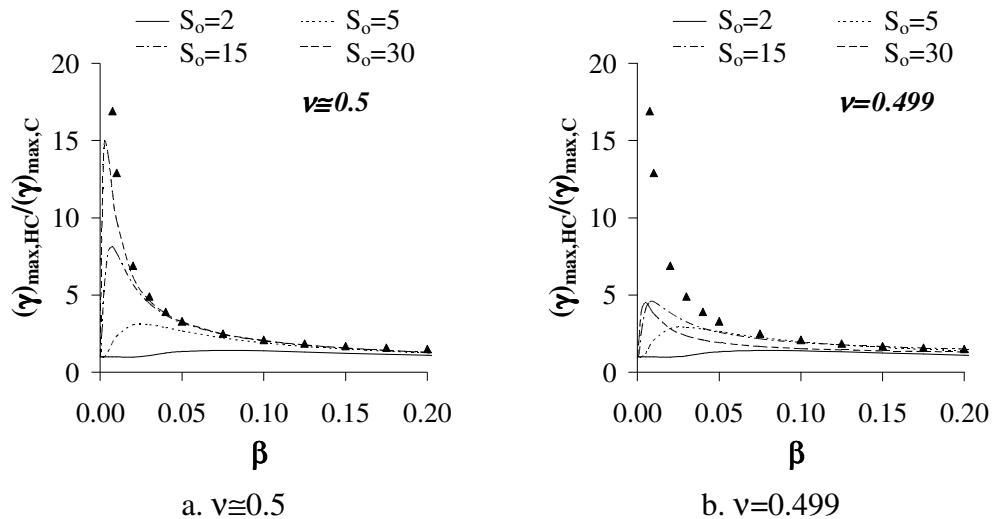


Figure 7.12 Assessment of the success of the simple expression proposed by Constantinou et al. [16] for the maximum shear strain ratio (discrete points in filled triangular shapes)

CHAPTER 8

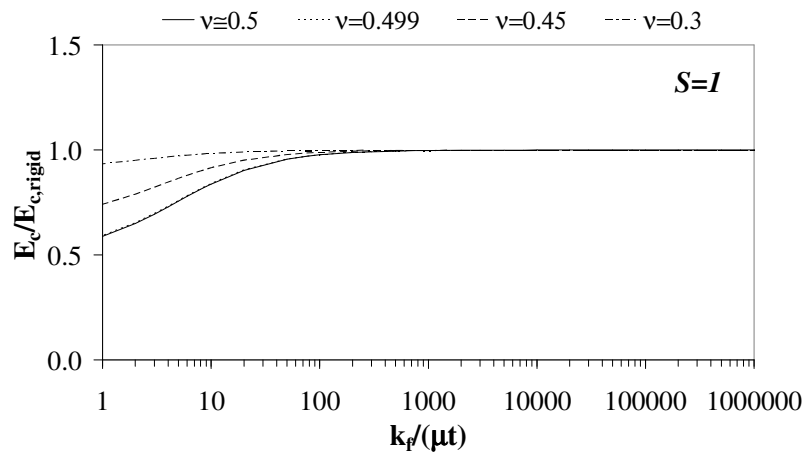
EFFECT OF REINFORCEMENT FLEXIBILITY ON BEHAVIOR OF BONDED ELASTIC LAYERS

For a bonded elastic layer, there are two limiting cases on the basis of the flexibility of the reinforcing sheets to which the layer is bonded at its top and bottom faces: (i) unbonded and (ii) rigidly-bonded cases. The behavior of a bonded elastic layer approaches to its unbonded behavior when the stiffness ratio of the reinforcing sheets and the layer tends to zero and approaches to its rigidly-bonded behavior when the ratio tends to infinity. Considering that the rigidly-bonded behavior of an elastic layer can be significantly different from its unbonded behavior, it can be concluded that the behavior of a bonded elastic layer is in fact controlled by three main parameters: aspect ratio of the layer, compressibility of the layer material and flexibility of the reinforcing sheets.

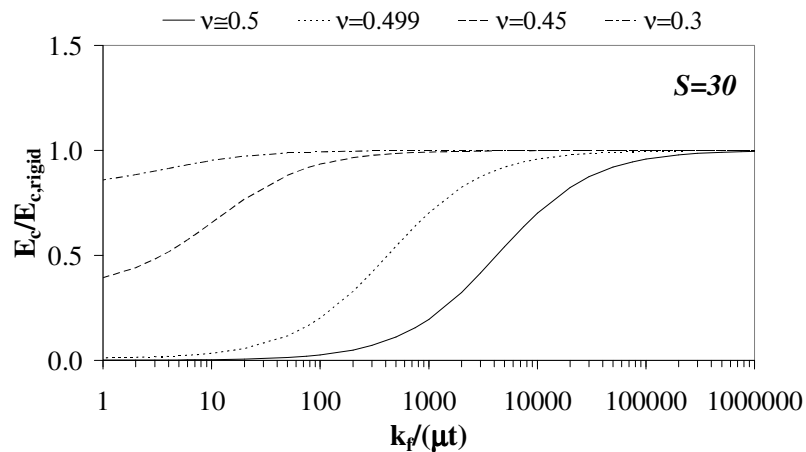
This chapter mainly aims to study the effect of the reinforcement flexibility on the compressive and bending behavior of bonded elastic layers using the analytical solutions derived from the first order theory (FOT) for infinite-strip (IS) shaped elastic layers bonded to extensible reinforcements. For easier discussions, the bending behavior of the layers is studied by considering the pure bending and pure warping cases separately. Since the effect of the reinforcement extensibility (k_f) also depends on the geometrical and material properties of the layer itself, the discussions in this chapter inherently include a study on the effects of the other two parameters, shape factor of the layer (S) and Poisson's ratio of the layer material (ν), on behavior of elastic layers bonded to flexible reinforcements.

8.1 COMPRESSIVE BEHAVIOR

The graphs in Figure 8.1 show the variation of compression modulus with the ratio of the in-plane stiffness of the reinforcement to the shear stiffness of the elastic material, $k_f^* = k_f / (\mu t)$, called “stiffness ratio”, for two different shape factors; $S=1, 30$. In the plots, E_c values are normalized by the E_c values computed for the equivalent (i.e., with the same S and ν values) rigidly-reinforced layer, denoted as $E_{c,rigid}$.



a. $S=1$



b. $S=30$

Figure 8.1 Effect of reinforcement flexibility on normalized compression modulus of bonded IS-shaped layers

As expected, E_c of an elastic layer bonded to flexible reinforcements approaches to $E_{c,rigid}$ as $k_f^* \rightarrow \infty$. While an HSF layer attains its rigid behavior at considerably large values of k_f^* , especially if the layer material is slightly/nearly incompressible, there is no need to have very large values of k_f^* for an LSF layer to behave as if it were a rigidly-bonded layer. From Figure 8.1, it can be seen that the incompressible and rigid behavior is attained in the HSF layer ($S=30$) when the stiffness ratio is about 300000. On the other hand, this limiting value is as low as 300 for the LSF layer ($S=1$).

The effects of S and ν on E_c are more apparent in the graphs presented in Figure 8.2, which are plotted for two specific values of k_f^* , 30000 and 300, corresponding, respectively, to a considerably high and a relatively low stiffness ratio. It is worth noting that the value of 30000 for k_f^* , which can be considered as a typical value for a fiber-reinforced rubber bearing, is calculated using the typical values ($E_f=210$ GPa, $\nu_f=0.3$, $t_f=0.27$ mm, $t=3$ mm, $\mu=0.7$ MPa) quoted in literature (see, e.g., Refs. [13,46]).

From Figure 8.2a, it is seen that the value of 30000 for the stiffness ratio is a sufficiently large value, even for HSF layers, to use $E_{c,rigid}$ instead of E_c for bonded elastic layers of nearly incompressible and compressible materials ($\nu \leq 0.499$). However, this is not valid, in general, for strictly incompressible materials. The curves plotted for $\nu=0.499$ deviate from the incompressible curves if S and/or k_f^* is large. This clearly shows the significance of the inclusion of the material compressibility in E_c computations of HSF layers bonded to nearly/strictly inextensible reinforcements. From Figure 8.2b, it is seen that E_c of an HSF layer drops significantly when k_f^* becomes 300 if ν is close to 0.5. For example, for $S=30$, the modulus ratio is 0.44 when $\nu=0.499$ and is as low as 0.07 when $\nu=0.5$. For the same value of the stiffness ratio ($k_f^*=300$), the effect of the reinforcement flexibility is much less in LSF layers. As an example, the layer with $S=1$ does not “sense” the flexibility of the reinforcements if $k_f^*=300$ even when $\nu=0.5$. From the figures in Figure 8.2, it can also be concluded that a bonded elastic layer attains its “incompressible” modulus at a smaller value of ν if it has a smaller S and/or k_f^* .

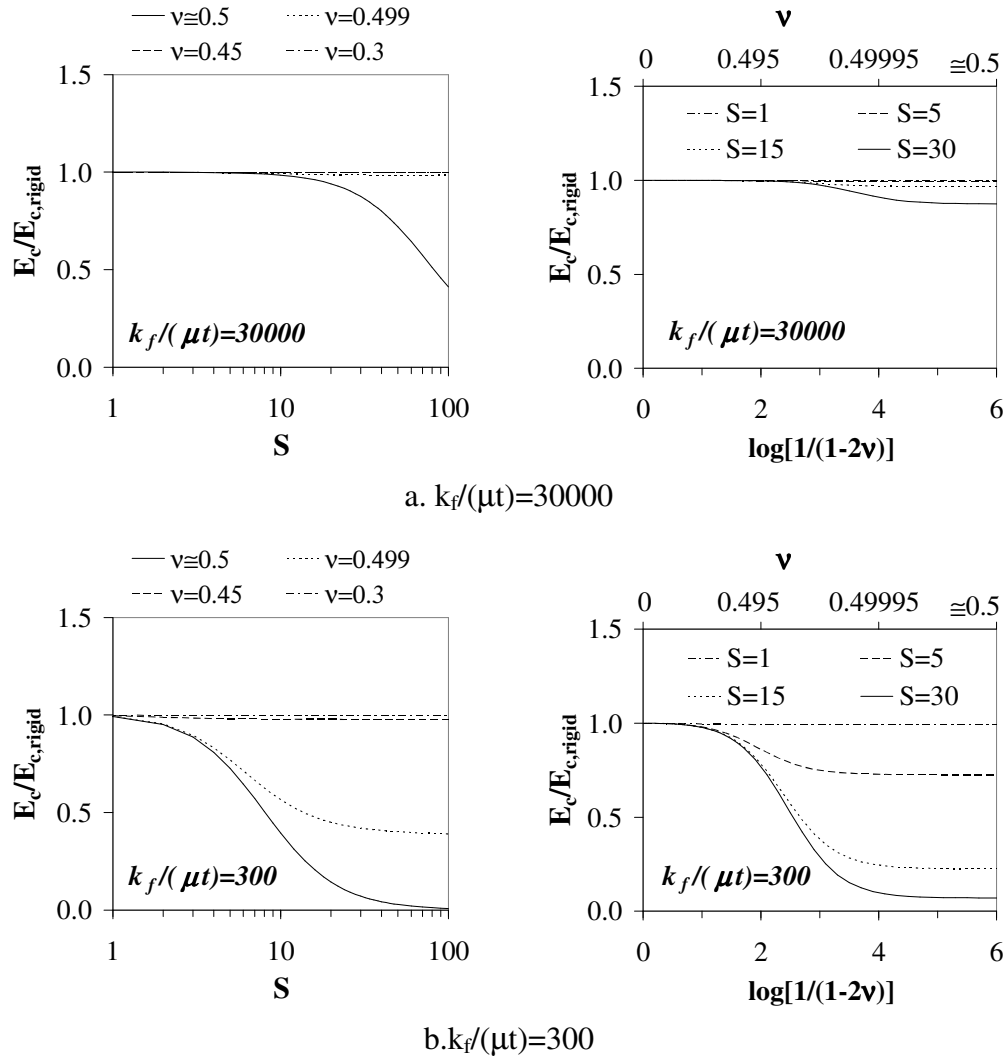


Figure 8.2 Effects of shape factor and Poisson's ratio on normalized compression modulus of an IS-shaped layer bonded to flexible reinforcements

The graphs presented in Figure 8.3 show the stress distributions in the lateral direction in an LSF layer ($S=1$) under uniform compression for various Poisson's ratios and two specific values of k_f^* , 30000 (those on the left hand side) and 30 (those on the right hand side). The smaller k_f^* value, i.e., 30, is deliberately selected to be so low since, for $S=1$, the reinforcement flexibility becomes effective only when $k_f^* < 300$ (Figure 8.1a). In the graphs, stress distributions are plotted over their most critical sections (i.e., τ_{11} and τ_{12} at $x_2 = \pm t/2$, and τ_{22} at $x_2 = 0$) and stress values are normalized with respect to the uniform pressure, i.e. $E_c \varepsilon_c$.

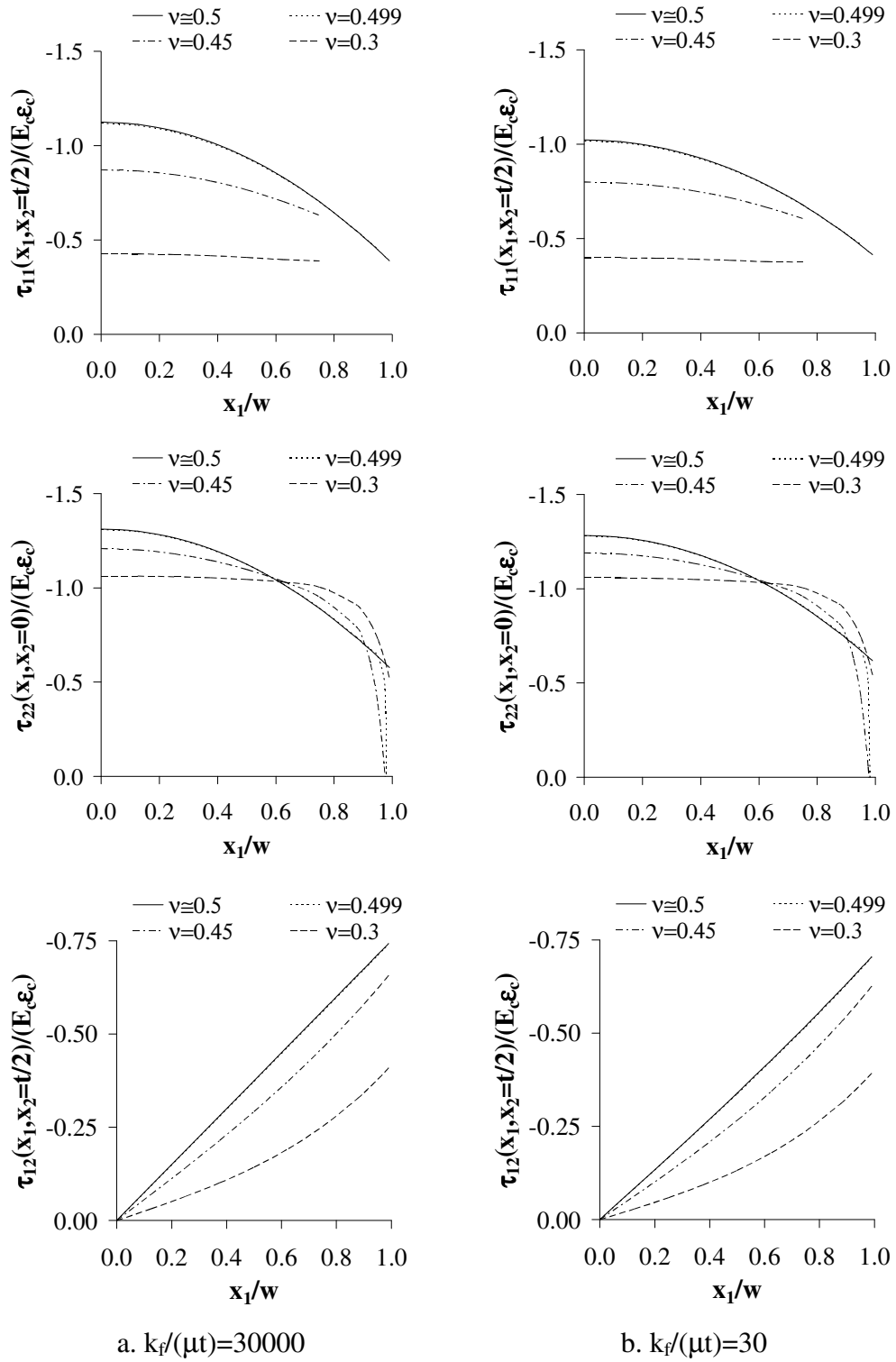


Figure 8.3 Effect of reinforcement flexibility on stress distributions in lateral direction under uniform compression for $S=1$

When the graphs in Figure 8.3a are compared with those plotted for $S=1$ in Figure 6.6 (page 146), it can be seen that they are identical. This indicates that the LSF layer behaves under uniform compression as if it were rigidly-bonded when $k_f^* = 30000$. In fact, the behavior of the LSF layer is not so different even when $k_f^* = 30$ as shown in Figure 8.3b. Stress values for $k_f^* = 30$ are slightly smaller than the rigid values.

On the other hand, the influence of k_f^* on the stress distributions in an HSF layer is remarkable especially if the layer material is nearly/strictly incompressible. This can be observed from the graphs presented in Figure 8.4 for $S=30$, which are plotted for various values of k_f^* ; 30000, 3000, 300 and 30. The comparison of the graphs in Figure 8.4a with those plotted for $S=30$ in Figure 6.6a,b (page 146) show that the HSF layer attains its rigidly-bonded compressive behavior when $k_f^* = 30000$. As k_f^* decreases, the normal stress distributions in the lateral direction becomes more uniform and the peak value at the center decreases. In fact, the same conclusion is valid also for the effect of material compressibility. Thus, it is obvious that k_f affects the behavior of bonded elastic layers in the same way that ν does.

It is interesting to see that the reinforcement flexibility also changes the effect of the material compressibility. For example, for $S=30$, while the curves plotted for strictly incompressible ($\nu \cong 0.5$) and nearly incompressible materials ($\nu = 0.499$) deviate considerably when $k_f^* = 30000$, they almost coincide when $k_f^* \leq 300$.

Figure 8.5 shows the effect of the reinforcement flexibility on the distribution of shear stress over the bonded faces of the HSF layer for $k_f^* = 30000$ and 300. As shown in the graphs, the main effect of the reinforcement flexibility is to reduce the shear stress near the center while increasing the peak value near the edge.

Since the first order theory leads to the improved expressions in the axial direction, it is also possible to investigate the effect of the reinforcement flexibility on the stress distributions through the layer thickness. The graphs presented in Figure 8.6 and Figure 8.7 for the normal stress distributions in the axial direction are plotted along the centerline ($x_1=0$), where the normal stress components take their maximum values, for two different shape factors, $S=1$ and $S=30$.

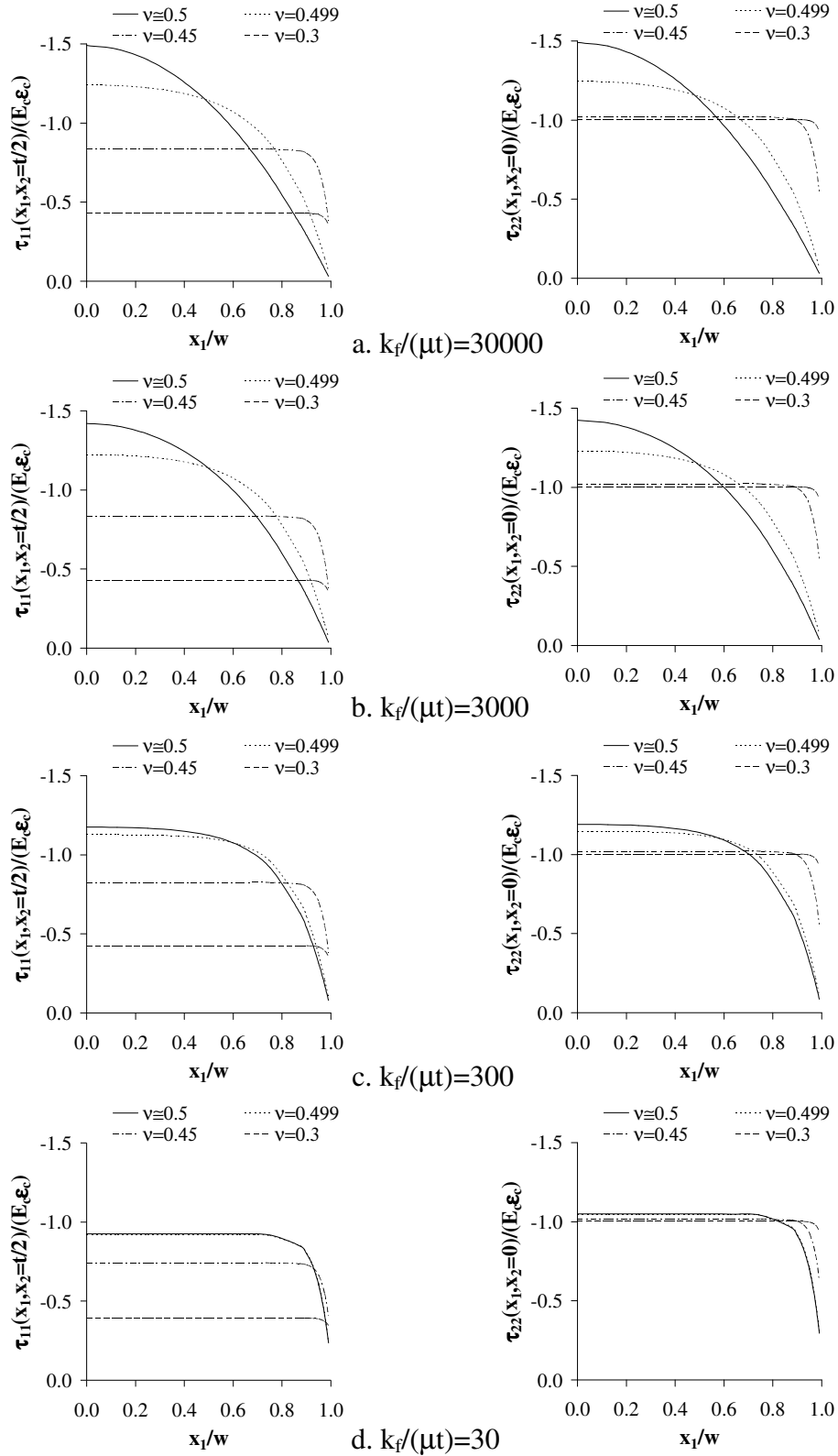
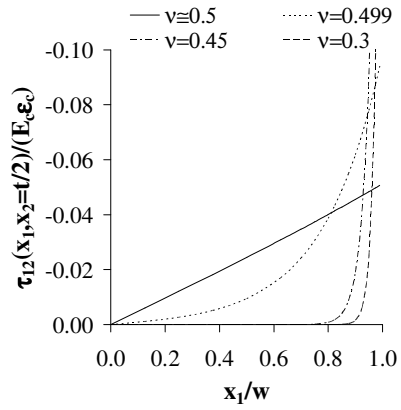
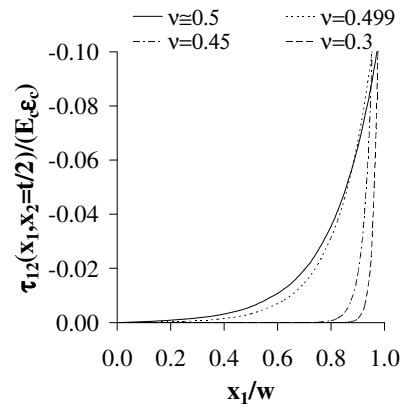


Figure 8.4 Effect of reinforcement flexibility on normal stress distributions in lateral direction under uniform compression for $S=30$

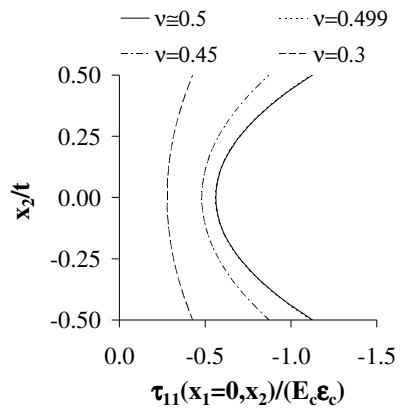


a. $k_f/(\mu t)=30000$

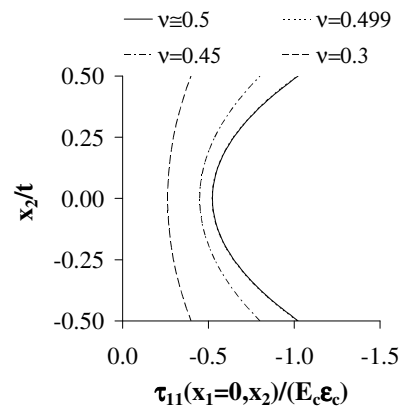


b. $k_f/(\mu t)=300$

Figure 8.5 Effect of reinforcement flexibility on shear stress distribution in lateral direction under uniform compression for $S=30$



a. $k_f/(\mu t)=30000$



b. $k_f/(\mu t)=300$

Figure 8.6 Effect of reinforcement flexibility on normal stress distributions in axial direction under uniform compression for $S=1$

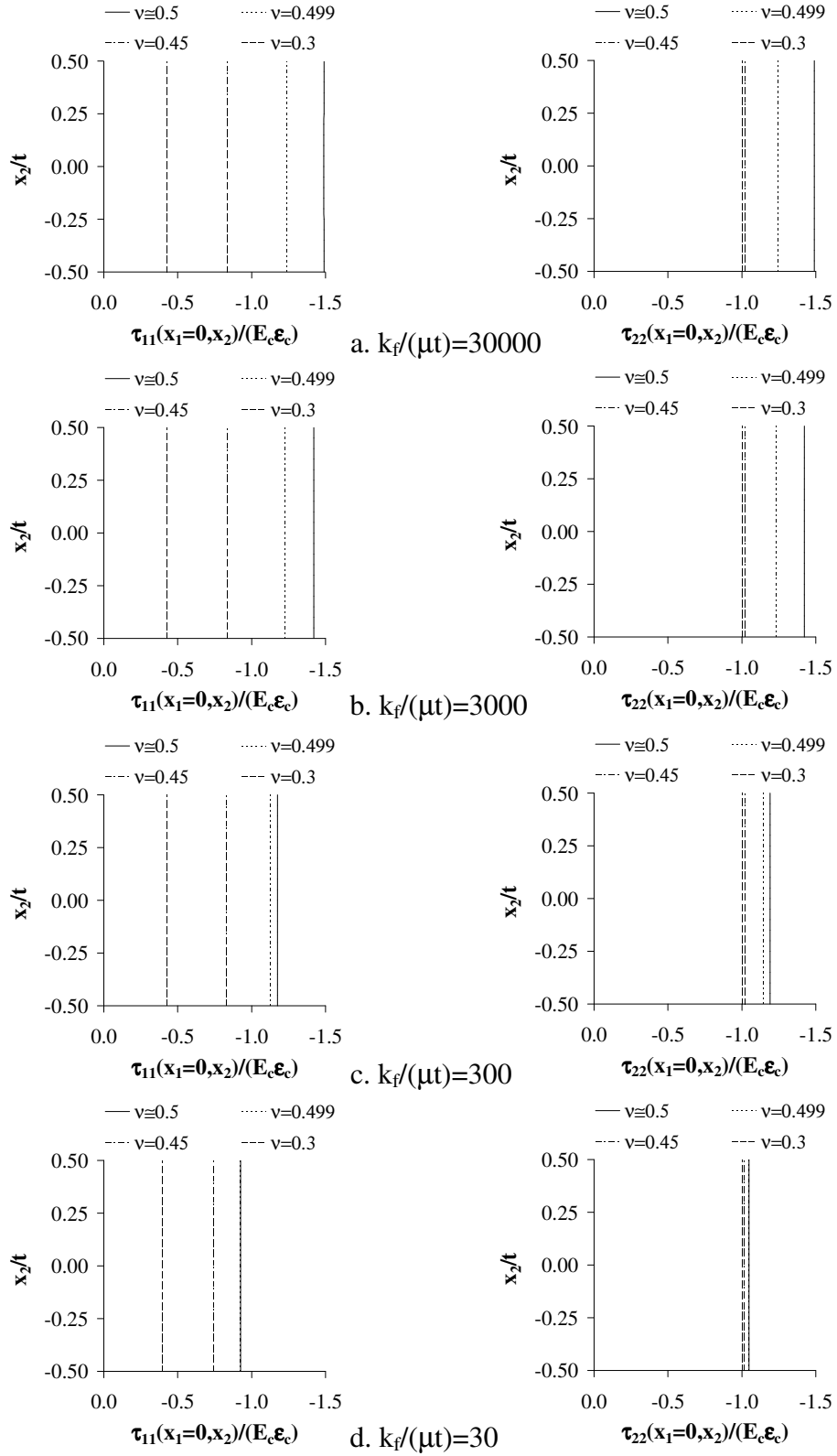


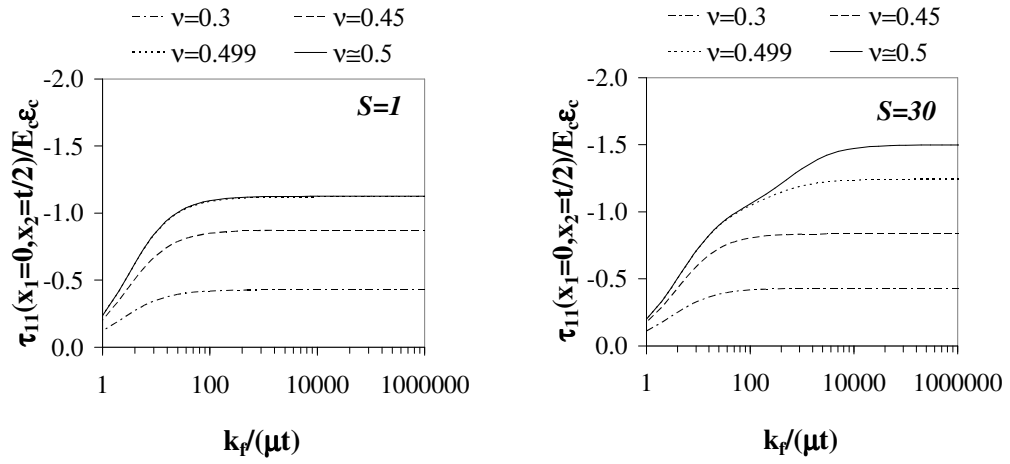
Figure 8.7 Effect of reinforcement flexibility on normal stress distributions in axial direction under uniform compression for $S=30$

When the graphs in Figure 8.6a and Figure 8.7a are compared with those in Figure 6.8a,b (page 150), it is seen that they are identical. This is compatible with the earlier conclusion that the studied layers behave, under compression, as if they were rigidly-bonded when $k_f^*=30000$. From Figure 8.6, it can be observed that the normal stress distributions in the LSF layer are not affected significantly even when k_f^* is as low as 30. Thus, the stress distributions, particularly τ_{11} distributions, are still highly nonlinear through the layer thickness especially if ν is close to 0.5. On the other hand, from Figure 8.7, it is obvious that the effect of k_f^* on the HSF layer is significant: normal stresses decrease considerably as k_f^* decreases especially if the layer material is nearly or strictly incompressible. It is to be noted that even when $k_f^*=30$, normal stresses are constant over the layer thickness in the HSF layer.

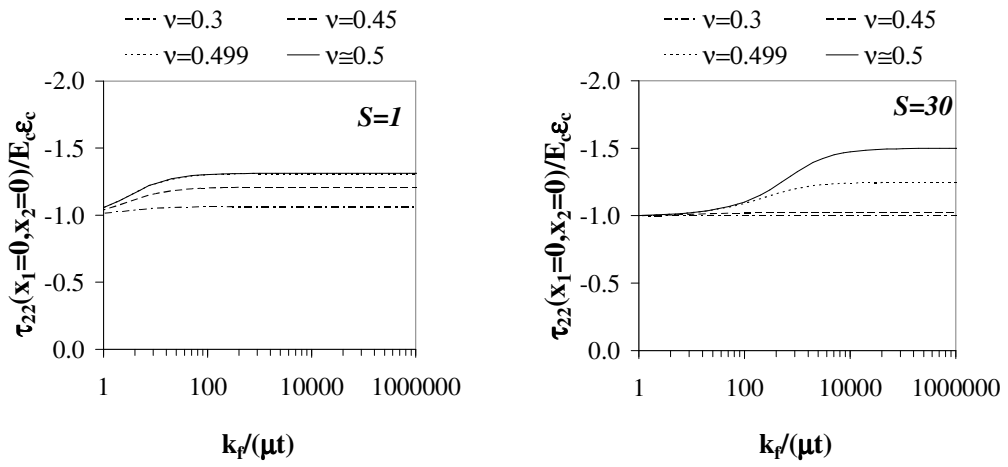
From the rigid-reinforcement case, it is known that in a bonded elastic layer subjected to uniform compression, maximum stresses are experienced at some fixed locations: $(\tau_{22})_{max}$ occurs at $(x_1=0, x_2=0)$, $(\tau_{11})_{max}$ at $(x_1=0, x_2=\pm t/2)$ and $(\tau_{12})_{max}$ at $(x_1=\pm w, x_2=\pm t/2)$. The graphs in Figure 8.3 to Figure 8.7 indicate that the reinforcement flexibility does not change the locations of the maximum stresses but can change their magnitudes considerably.

The effect of the reinforcement flexibility on the maximum stresses in a bonded IS-shaped layer under uniform compression is studied by plotting the variations of the maximum normalized stresses with k_f^* in Figure 8.8 and with S in Figure 8.9 for various values of ν .

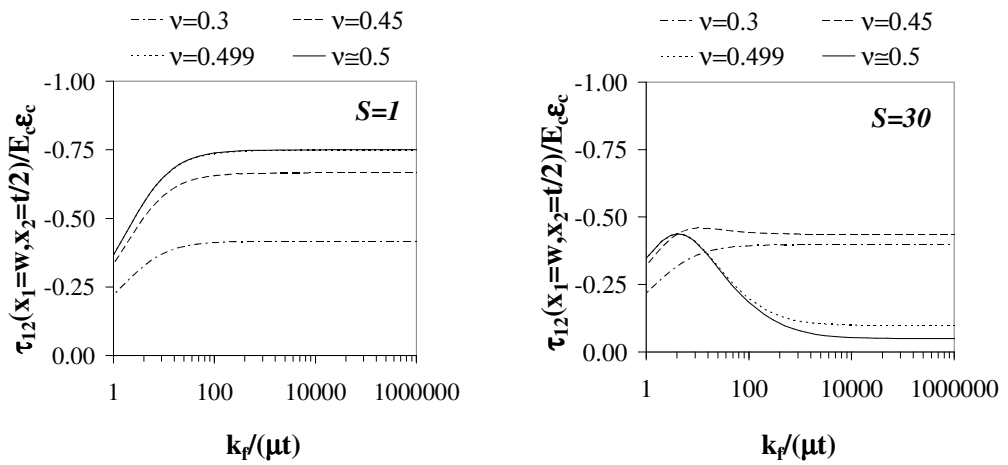
From the graphs presented in Figure 8.8, which are plotted for two different S values, 1 and 30, it can be observed that while the LSF layer ($S=1$) has already reached its incompressible behavior when $\nu=0.499$, the behavior of the HSF layer ($S=30$) when $\nu=0.499$ is considerably different than its incompressible behavior if k_f^* is sufficiently large. It is interesting to see that, for $S=30$, the deviation of the curves plotted for $\nu=0.5$ from those for $\nu=0.499$ decreases as k_f^* decreases and for approximately $k_f^*\leq 100$, they become almost identical. From Figure 8.8a,b, it can also be seen that the main effect of the reinforcement flexibility is to decrease the magnitudes of maximum normalized normal stresses.



a. maximum lateral normal stress

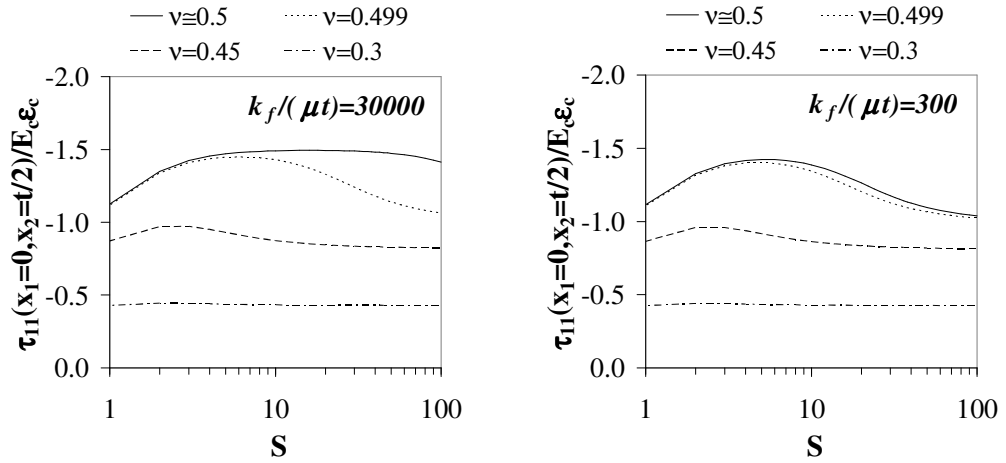


b. maximum axial stress

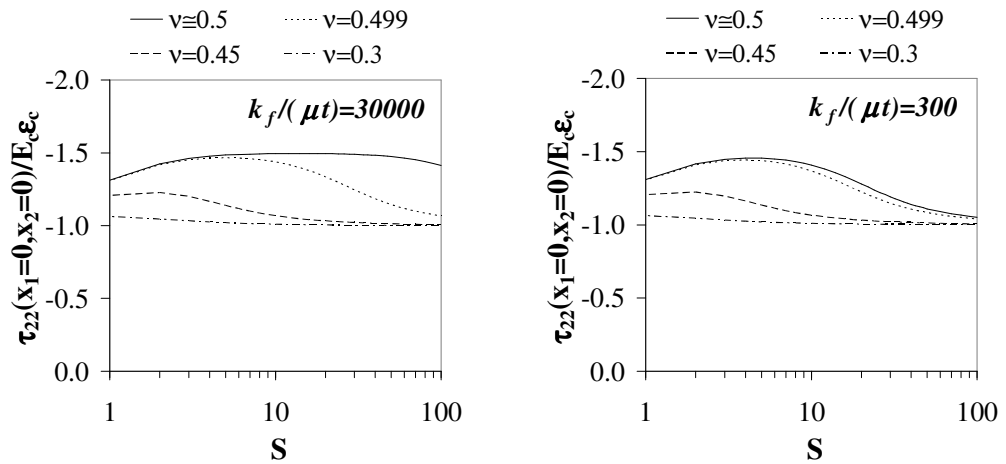


c. maximum shear stress

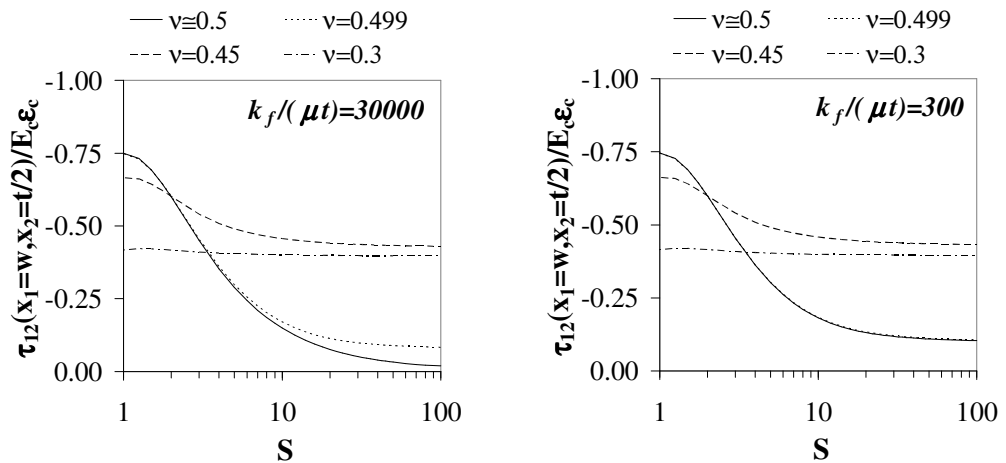
Figure 8.8 Effect of reinforcement flexibility on maximum stresses in a bonded IS-shaped layer under uniform compression



a. maximum lateral normal stress



b. maximum axial stress



c. maximum shear stress

Figure 8.9 Effect of shape factor on maximum stresses in an IS-shaped layer bonded to extensible reinforcements under uniform compression

As far as the maximum normalized shear stress is concerned (Figure 8.8c), the reinforcement flexibility affects the LSF and HSF layers differently if the layer material is nearly/strictly incompressible. As k_f^* decreases, the maximum normalized shear stress decreases in the LSF layer while it increases in the HSF layer until a peak is reached at about $k_f^*=4$. The bonded elastic layers of compressible materials start to “sense” the effect of the reinforcement flexibility when the value of k_f^* is considerably low (approximately $k_f^*\leq 100$). In this range, as k_f^* decreases, the maximum normalized shear stress decreases for both the LSF and HSF layers.

The effect of the reinforcement flexibility on the maximum stresses in bonded layers of different shape factors is more apparent in the graphs presented in Figure 8.9, which are plotted for two different k_f^* values, 30000 and 300. It can be noted that the graphs for $k_f^*=30000$ are almost identical to the graphs plotted for the rigidly-bonded layers (for the same S and ν values) presented in Figure 6.11 (page 155). The comparison of the graphs in Figure 8.9 indicates that decreasing k_f^* from 30000 to 300 mainly affects the curves for HSF layers with incompressible materials. HSF layers can no longer “sense” the slight compressibilities in the layer material when $k_f^*=300$. Thus, it can be concluded that for elastic layers bonded to extensible reinforcements, nearly incompressible and incompressible behaviors are identical even for HSF layers.

8.2 BENDING BEHAVIOR

It can be recalled from Section 4.2.1.2 that the zeroth order theory (ZOT) and first order theory (FOT) lead to two different expressions for the bending modulus E_b of IS-shaped layers bonded to flexible reinforcements (Eqs. (4.93) and (4.94)). Figure 8.10 compares the predictions of ZOT ($m=0$) and FOT ($m=1$) for E_b for two different stiffness ratios and various shape factors and Poisson’s ratios. As shown in the figure, the predictions of both theories match in the studied range of parameters. Considering the complexity of the expression predicted by FOT, it seems to be practical to use the formula by ZOT in the design calculations.

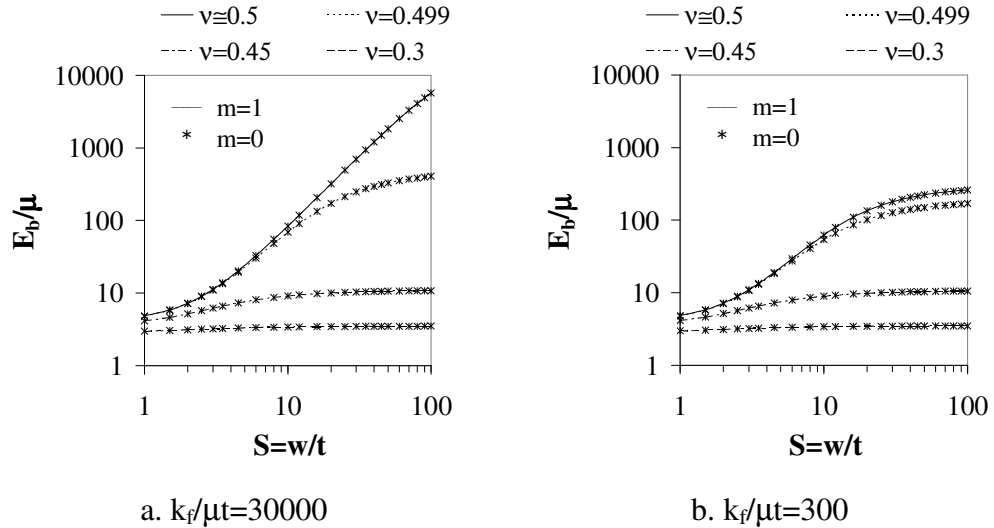


Figure 8.10 Predictions of zeroth and first order theories for bending modulus of IS-shaped layers bonded to flexible reinforcements

If the graph in Figure 8.10a is compared with that in Figure 6.12 (page 156), it is seen that they are almost identical, showing that, as far as the bending modulus is concerned, having a value of 30000 for the stiffness ratio is sufficient for a bonded IS-shaped layer to behave as if it were rigidly-bonded. The comparison of Figure 8.10a with Figure 8.10b shows that the reduction of k_f^* from 30000 to 300 mainly affects HSF layers with low compressibility. When k_f^* drops to 300, the E_b values for HSF layers of strictly incompressible materials ($\nu=0.5$) decrease considerably and approach to the E_b values computed for nearly incompressible materials ($\nu=0.499$).

As discussed in the rigid-reinforcement case, in design calculations, it is a common practice to represent E_b in terms of E_c . In Figure 8.11, the E_c/E_b ratio is plotted for various S and ν , and two specific k_f^* values. The graphs show that the value of E_c/E_b ratio can decrease considerably due to the reinforcement flexibility especially if S and ν are also large. For this reason, taking the value of this ratio as five, which is suitable only for rigidly-bonded incompressible HSF layers, can significantly underestimate the true value of the bending modulus for layers bonded to extensible reinforcements.

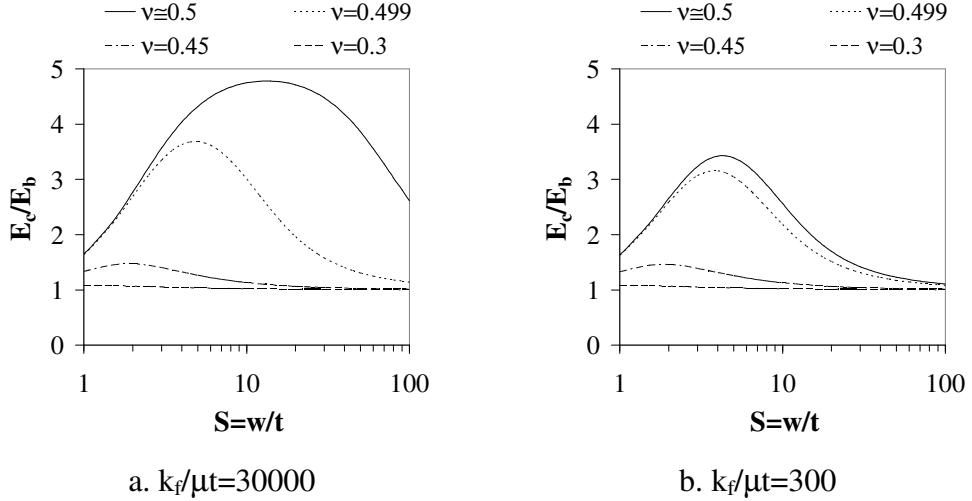


Figure 8.11 Effect of reinforcement flexibility on E_c/E_b ratio

To investigate the effect of the reinforcement flexibility on E_b in more detail, the variations of the normalized bending modulus with k_f^* , S and ν are plotted for different geometrical and material properties and presented in Figure 8.12a-c. In the plots, E_b values, which are calculated from Eq. (4.94), are normalized by the E_b values calculated for the equivalent (i.e., with the same S and ν values) rigid-reinforced layer from Eq. (4.95), denoted $E_{b,rigid}$.

When the graphs in Figure 8.12 are compared with those in Figure 8.1 and Figure 8.2b, it can be realized that the reinforcement flexibility affects the bending modulus in the same way it affects the compression modulus. However, the effect of the reinforcement flexibility on E_b seems to be less than its effect on E_c . For specific values of k_f^* , S and ν , the reduction in E_c due to the reinforcement flexibility is larger than the reduction in E_b .

The graphs presented in Figure 8.13 show the stress distributions in the lateral direction in an LSF layer ($S=2.5$) under pure bending for various Poisson's ratios and two specific values of k_f^* , 30000 (those on the left hand side) and 30 (those on the right hand side). In the graphs, stress distributions are plotted over their most critical sections (i.e., τ_{11} and τ_{12} at $x_2=\pm t/2$, and τ_{22} at $x_2=0$) and stress values are normalized by $SE_b\phi$.

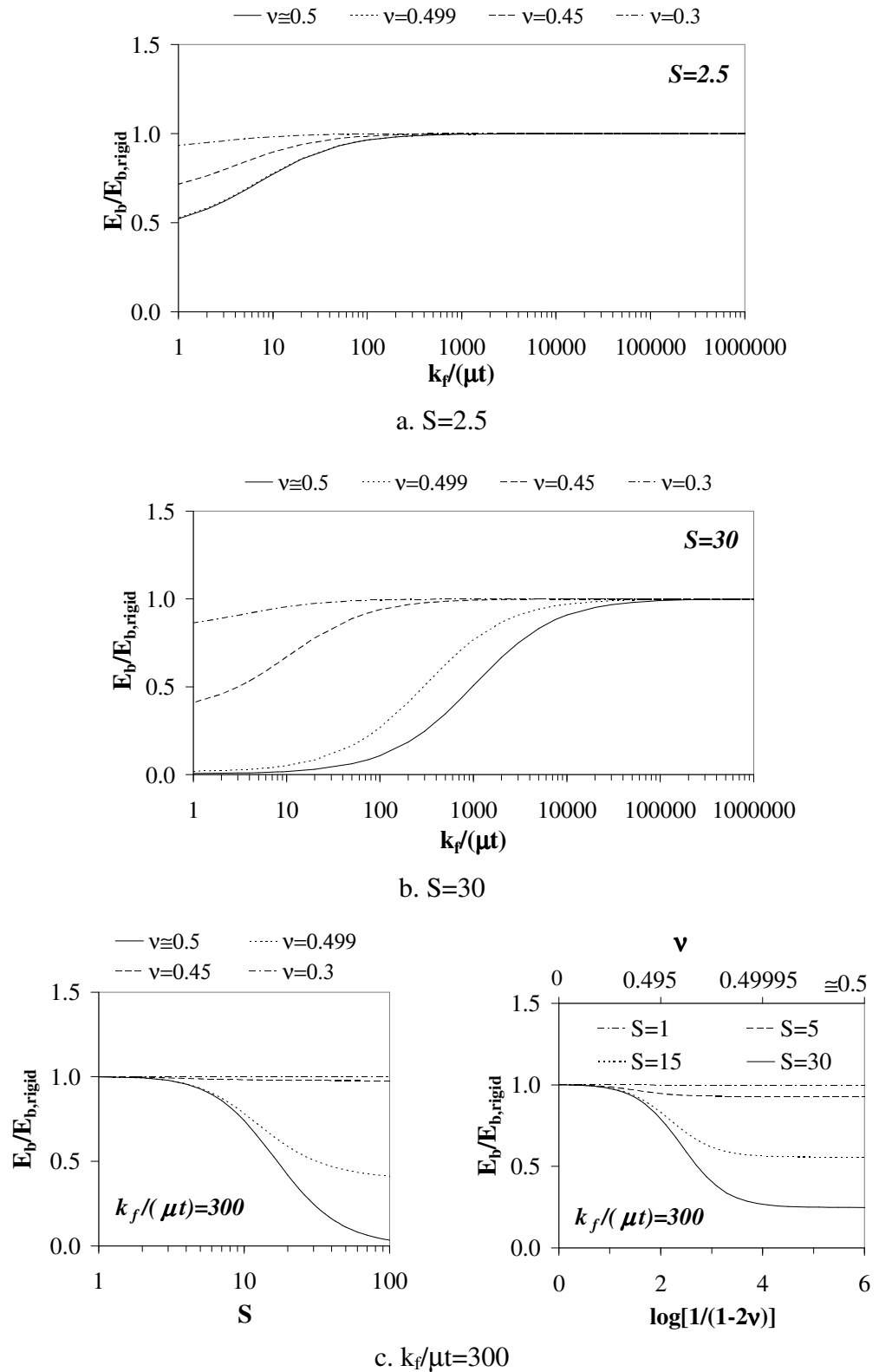


Figure 8.12 Effect of reinforcement flexibility on normalized bending modulus

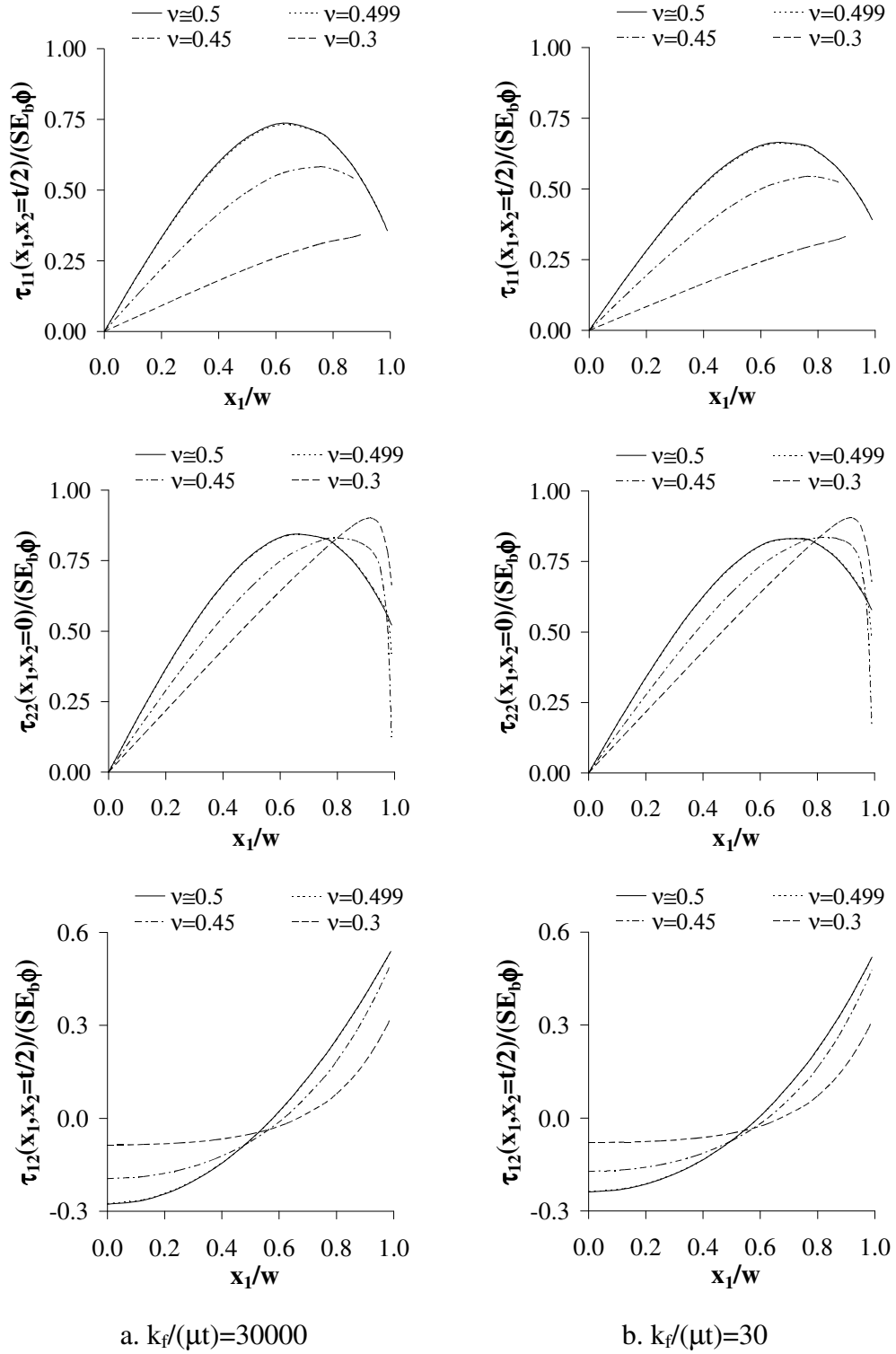


Figure 8.13 Effect of reinforcement flexibility on stress distributions in lateral direction under pure bending for $S=2.5$

As expected, the graphs in Figure 8.13a are identical to those plotted for $S=2.5$ in Figure 6.15 (page 160). Similar to the compressive behavior, the bending behavior of the LSF layer is close to its rigidly-reinforced behavior even when $k_f^*=30$. Peak values for the lateral normal and shear stresses are slightly smaller when $k_f^*=30$ than when $k_f^*=30000$ for incompressible and slightly compressible materials (Figure 8.13b).

On the other hand, the influence of k_f^* on the stress distributions in an HSF layer is significant especially if ν is close to 0.5. The graphs presented in Figure 8.14, which are plotted for $k_f^*=30000, 3000, 300, 30$, and in Figure 8.15, which are plotted for $k_f^*=30000$ and 300, show how the reinforcement flexibility affects the stress distributions in the lateral direction in an IS-shaped layer of $S=30$ under pure bending. The comparison of the graphs in Figure 8.14a and Figure 8.15a with those plotted for $S=30$ in Figure 6.15 (page 160) shows that the HSF layer attains its rigidly-reinforced bending behavior when $k_f^*=30000$.

From the graphs in Figure 8.14 and Figure 8.15, it can be observed that the effect of the reinforcement flexibility is very similar to the effect of the material compressibility. As k_f^* decreases, τ_{11} and τ_{22} distributions tend to a linear distribution and τ_{12} distributions become more uniform in the central region. Such a change in the shape of τ_{11} distributions is accompanied with a decrease in the peak value. For τ_{12} distributions, it can be noticed that stress values near the edge increase as k_f^* decreases especially if ν is close to 0.5.

From Figure 8.14 and Figure 8.15, it can also be realized that one of the earlier conclusions drawn for the compressive behavior of HSF layers, which states that the difference between the strictly incompressible and nearly incompressible behaviors is lost as k_f^* decreases, is also valid for their bending behavior.

The graphs presented in Figure 8.16 show the effect of the reinforcement flexibility on the lateral normal stress distributions in bonded IS-shaped layers with $S=2.5$ (the graphs on the left hand sides) and $S=30$ (the graphs on the right hand sides) over the vertical section at $x_1=0.6w$, which is very close to the section where τ_{11} is maximum in a rigidly-reinforced HSF layer of incompressible material.

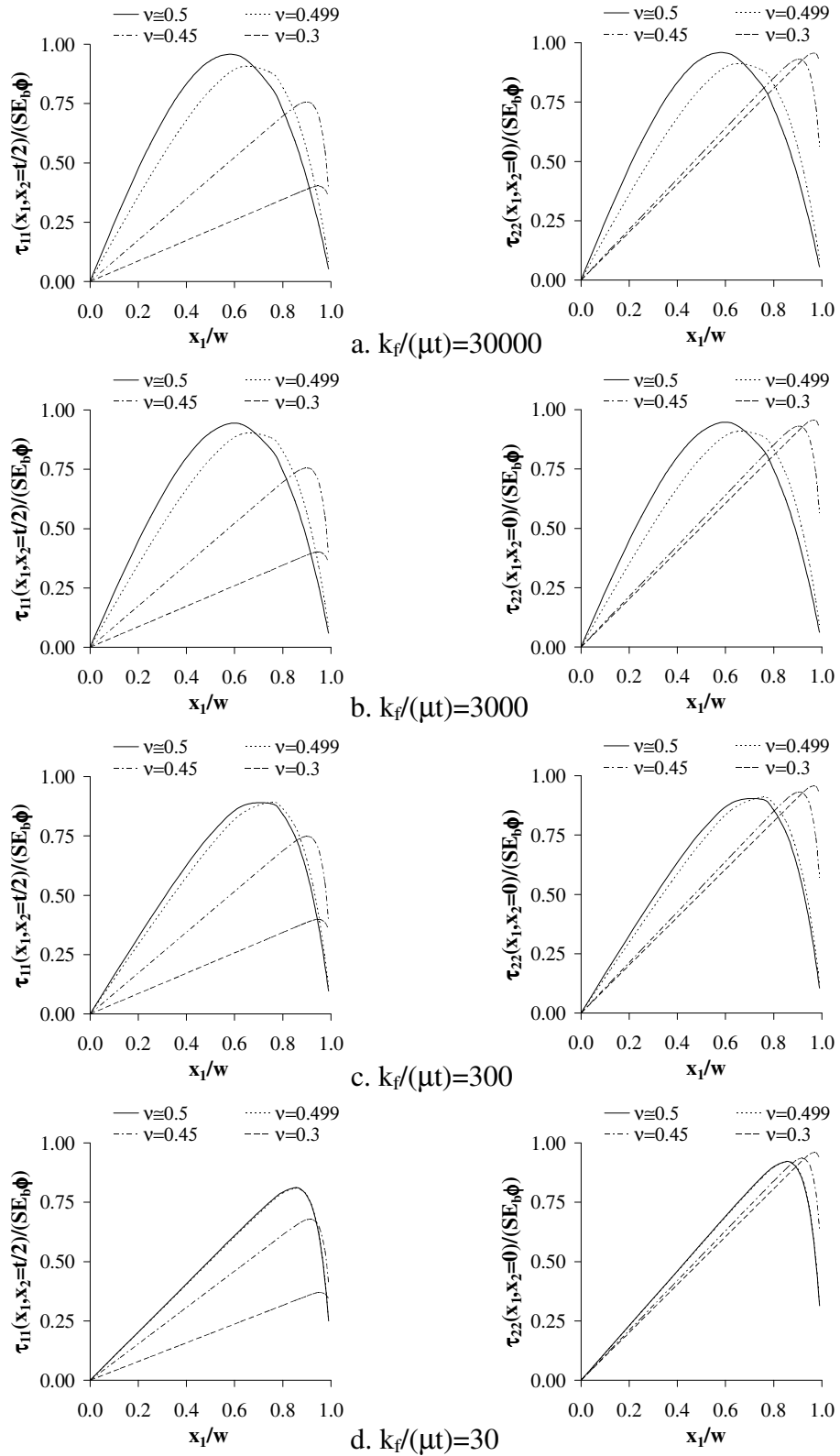


Figure 8.14 Effect of reinforcement flexibility on normal stress distributions in lateral direction under pure bending for $S=30$

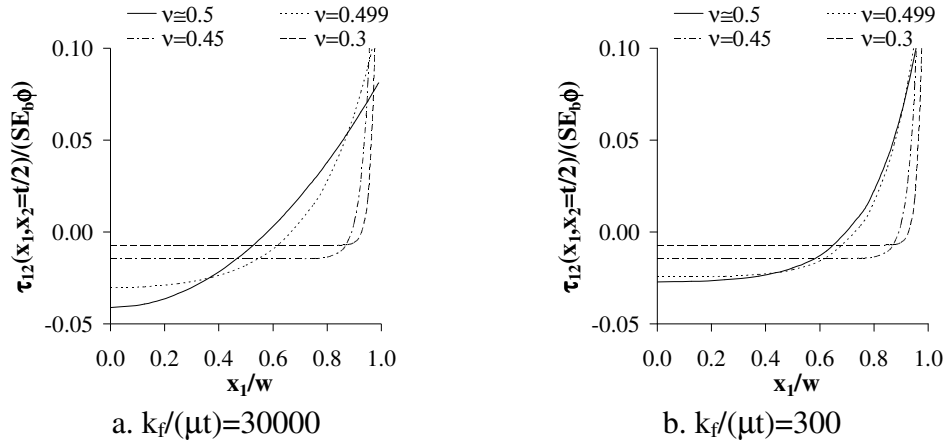


Figure 8.15 Effect of reinforcement flexibility on shear stress distribution under pure bending in lateral direction for $S=30$

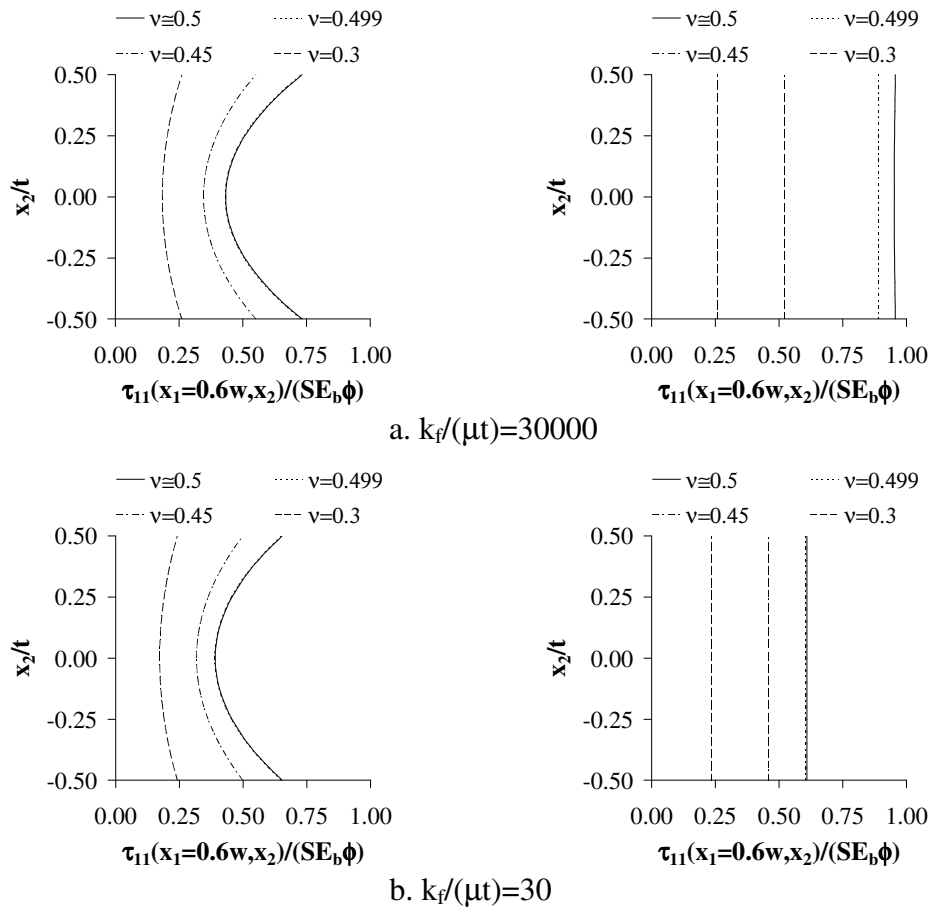
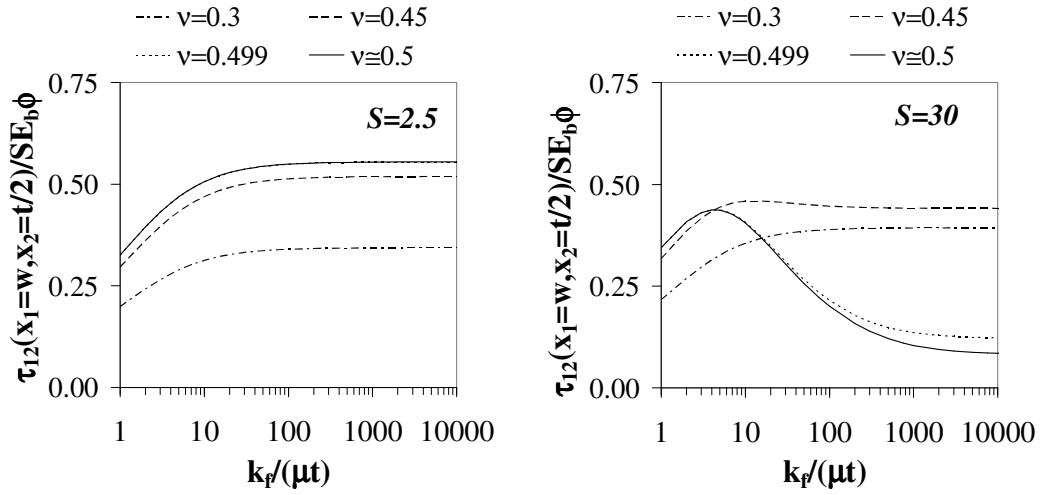


Figure 8.16 Effect of reinforcement flexibility on lateral normal stress distribution in axial direction under pure bending for $S=2.5$ (on the left hand side) and $S=30$ (on the right hand side)

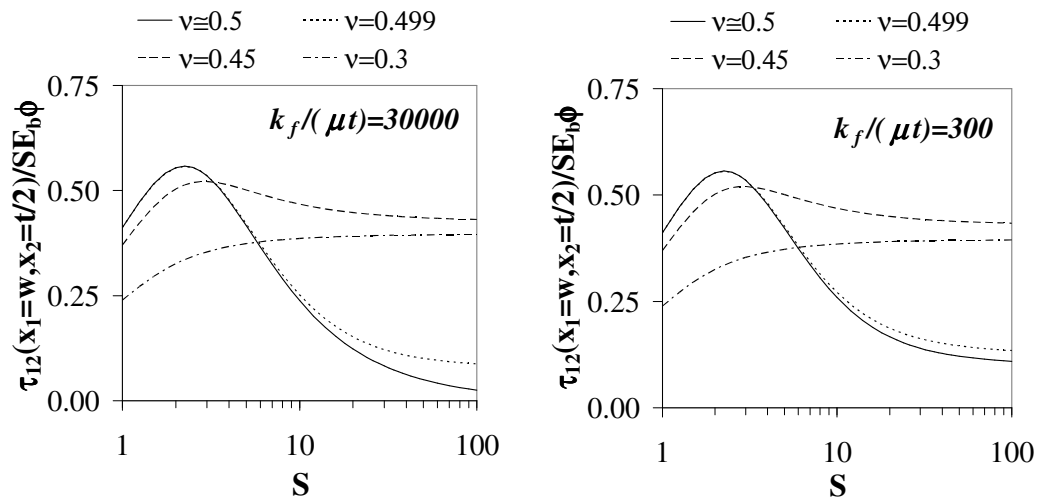
When the graphs in Figure 8.16a are compared with those in Figure 6.16a (page 162), it is seen that they are identical. This is compatible with the previous conclusion that, under pure bending, the studied layers behave as if they were rigidly-reinforced when $k_f^*=30000$. The decrease in the normalized lateral normal stress, when k_f^* becomes 30, is significant for $S=30$ especially if ν is close to 0.5. It can also be observed that even when $k_f^*=30$, the stress distributions over the layer thickness are uniform in the HSF layer and parabolically varied in the LSF layer. A similar study conducted on the axial stress distributions through the layer thickness has showed that the effect of the reinforcement flexibility on τ_{22} distribution is similar to that on τ_{11} distribution.

Since the maximum normalized shear stress developing in a bonded elastic layer under pure bending can increase considerably as the stiffness ratio decreases, it seems to be valueable to study the effect of the reinforcement flexibility on maximum shear stress. The graphs given in Figure 8.17 show the variation of the maximum normalized shear stress with k_f^* and S for various ν values. From Figure 8.17a, it is seen that for nearly/strictly incompressible materials, as k_f^* decreases, the maximum normalized shear stress decreases in the LSF layer while it increases in the HSF layer until it reaches at about $k_f^*=4$, then, it decreases. Compressible materials starts to “sense” the reinforcement flexibility when the k_f^* value is considerably low (approximately $k_f^*\leq 100$). In this range, as k_f^* decreases, the maximum normalized shear stress decreases not only for the LSF layer but also for the HSF layer. The graphs in Figure 8.17b show that decreasing k_f^* from 30000 to 300 mainly affects HSF layers, which can no longer “sense” the slight compressibilities in the layer material.

It can be recalled that similar conclusions have already been drawn for the uniform compression case. At this point, it is worth comparing the graphs in Figure 8.17 with those in Figure 8.8c and Figure 8.9c. From the comparison, it can be realized that the effect of reinforcement flexibility on the maximum normalized shear stress developing in a bonded elastic layer under pure bending is very similar to its effect on that under uniform compression.



a. variation with stiffness ratio



b. variation with shape factor

Figure 8.17 Effect of reinforcement flexibility on maximum shear stress in an IS-shaped layer bonded to extensible reinforcements under pure bending

8.3 WARPING BEHAVIOR

Since the behavior of an IS-shaped layer bonded to extensible reinforcements under pure warping is mainly controlled by the warping pattern of the reinforcements, it is wise to start the discussions in this section with a study on the warping constant “ f ”. As it has already been mentioned in Section 4.2.1.3, it is difficult and impractical to derive a closed-form expression for f when FOT is used in the formulation due to the highly nonlinear form of the stress expressions. However, it is still possible to compute f numerically and compare these numerical results with the predictions of ZOT computed from Eq. (4.113).

Figure 8.18 compares the predictions of ZOT ($m=0$) and FOT ($m=1$) for the warping constant f for two different stiffness ratios, 30000 and 300, and various shape factors and Poisson’s ratios. As shown in the graphs, the predictions of both theories almost exactly match in the studied range of parameters. While some deviation appears for very small shape factors, the differences are not significant. Thus, it can be concluded that Eq. (4.113) can be used to calculate the warping constant f .

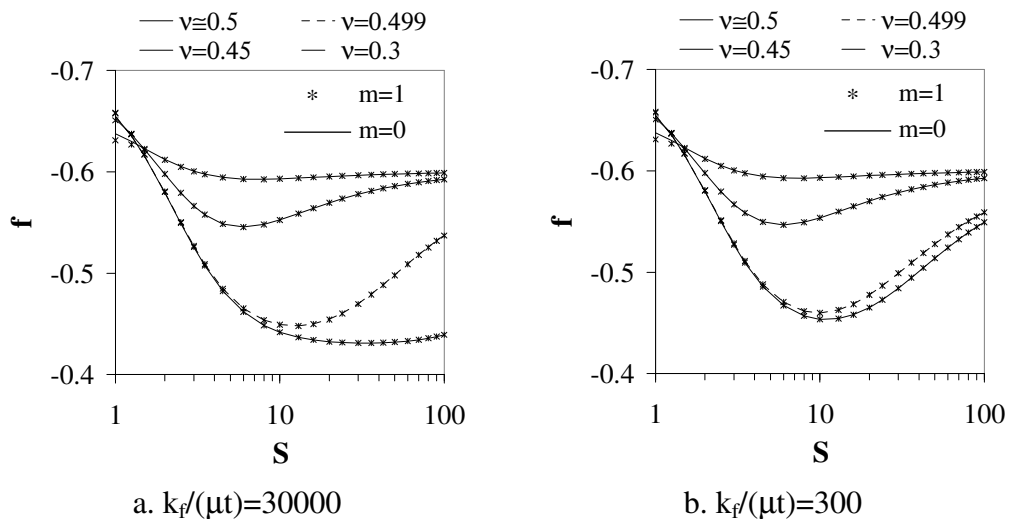


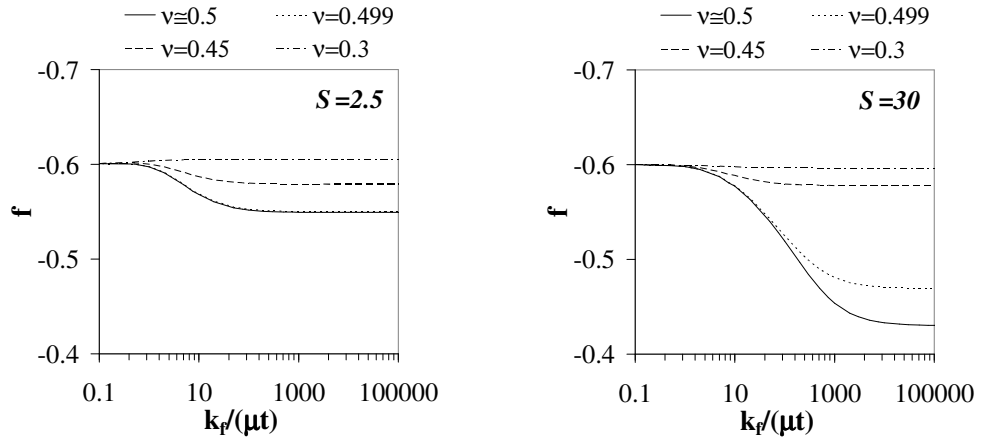
Figure 8.18 Predictions of zeroth and first order theories for warping constant “ f ”

From the review presented in Section 2.2.3, it can be inferred that there are two limiting values for the warping constant f : $f_u = -3/5$, which is the value obtained for an *unbonded* uniform short beam, and $f_b = -3/7$, which is the value predicted by the pressure method (PM) for an “incompressible” IS-shaped layer *bonded* to “inextensible” reinforcements. Figure 8.18a shows that the f values for HSF layers are equal to f_b when $\nu = 0.5$, indicating that HSF layers behave as if they were rigidly-reinforced when $k_f^* = 30000$, and to f_u when $\nu = 0.3$, indicating that HSF layers behave as if they were unbonded when $\nu = 0.3$.

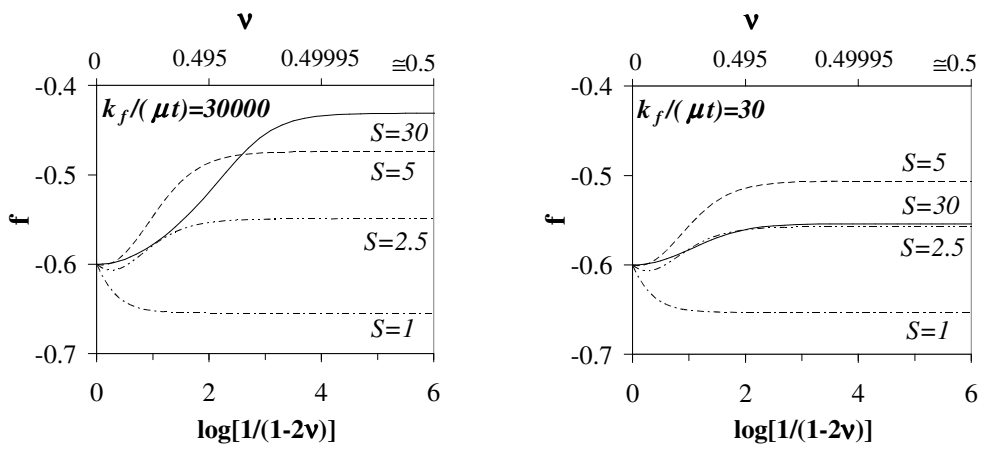
It is hard to understand the effects of k_f^* and ν on the f values computed for LSF layers from the curves given in Figure 8.18. To investigate the effects of k_f^* and ν on f thoroughly, the variations of the warping constant with these two parameters are also studied and presented in Figure 8.19. From the graphs, it is seen that f approaches f_u as $k_f^* \rightarrow 0$ and/or $\nu \rightarrow 0$. This conclusion is valid not only for HSF layers but also for LSF layers. A similar conclusion is *partially* valid for f_b ; f approaches to f_b when $k_f^* \rightarrow \infty$ and $\nu \rightarrow 0.5$ only if S is sufficiently large since PM is valid only for HSF layers. It is interesting to see that f values computed for LSF layers may even be smaller than f_u , which is observed when the layer material is highly compressible and/or the shape factor of the layer is relatively small.

As in the case of warping constant f , it is hard to obtain a closed-form expression for the warping modulus E_w using FOT. In Figure 8.20, the numerical results obtained, for E_w , from FOT are compared with the predictions of ZOT, which are computed from Eq. (4.112). Similar to f , the predictions of both theories for E_w almost exactly match in the studied range of parameters. For very small values of S , FOT predictions start to deviate from ZOT results, which are more realistic for these shape factors. Thus, as in f , one can use the expression derived for E_w from Eq. (4.112).

To investigate the effect of the reinforcement flexibility on E_w thoroughly, the variations of the normalized warping modulus with k_f^* , S and ν are plotted separately and presented in Figure 8.21a-c. In these plots, E_w values are normalized by those calculated using a considerably high value of k_f^* , denoted $E_{w,rigid}$.



a. variation with stiffness ratio



b. variation with Poisson's ratio

Figure 8.19 Effect of reinforcement flexibility on warping constant “f”

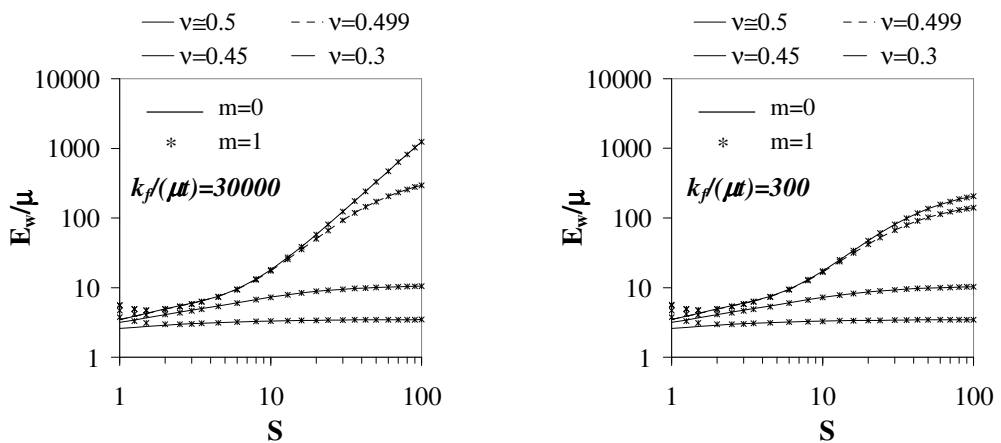
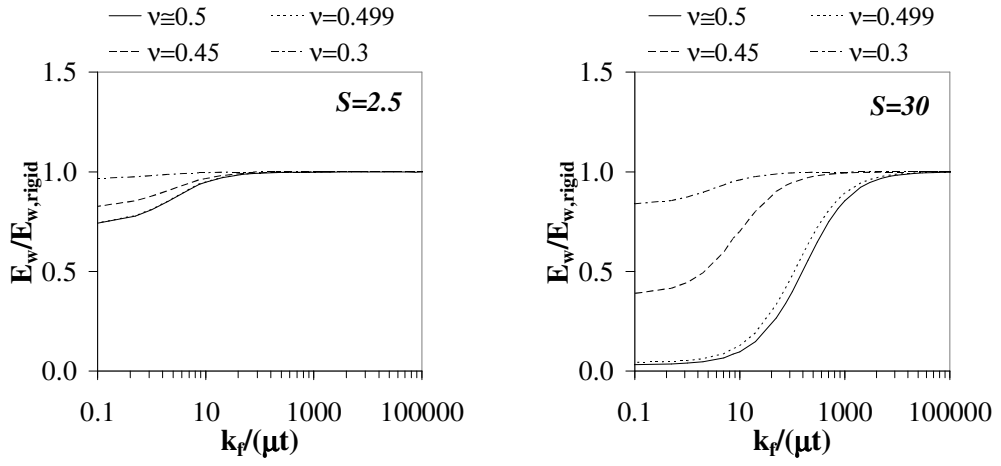
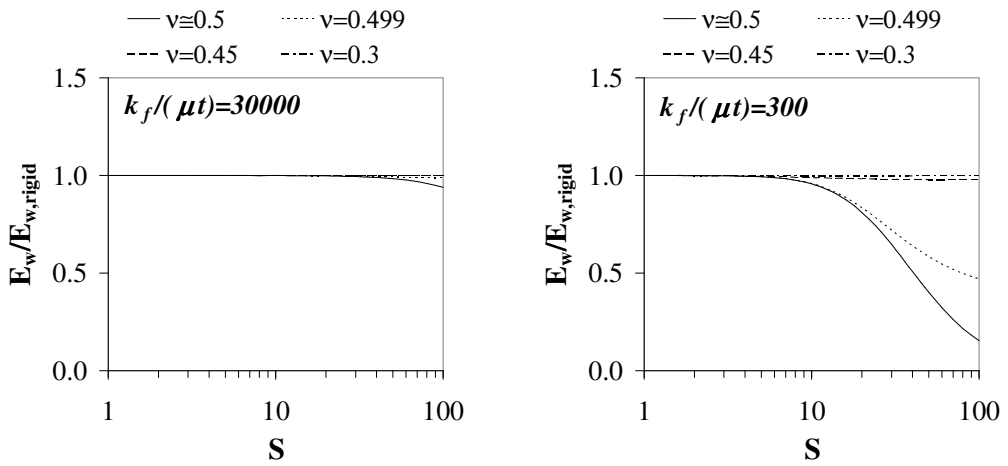


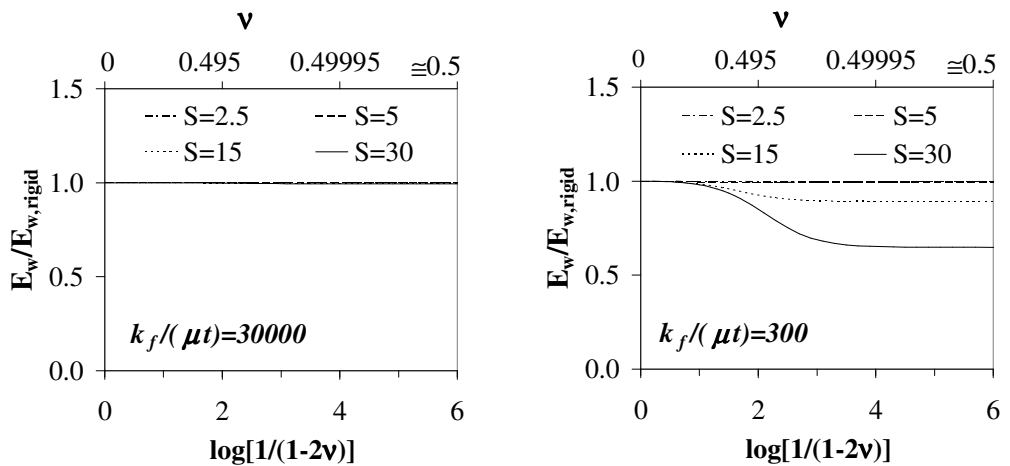
Figure 8.20 Predictions of zeroth and first order theories for warping modulus



a. variation with stiffness ratio



b. variation with shape factor



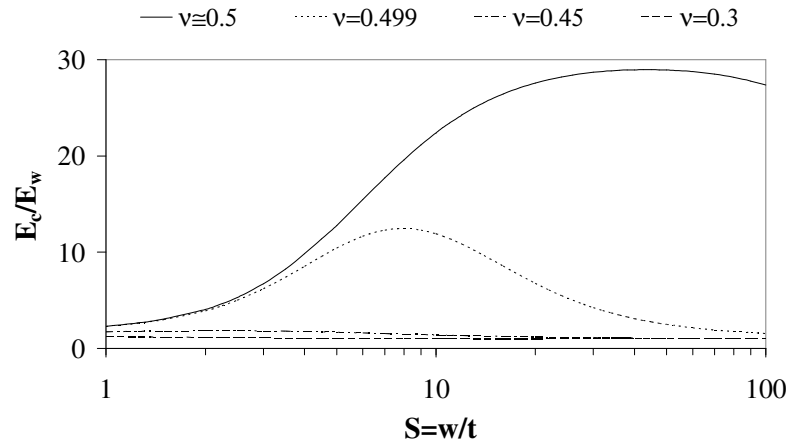
c. variation with Poisson's ratio

Figure 8.21 Effect of reinforcement flexibility on normalized warping modulus

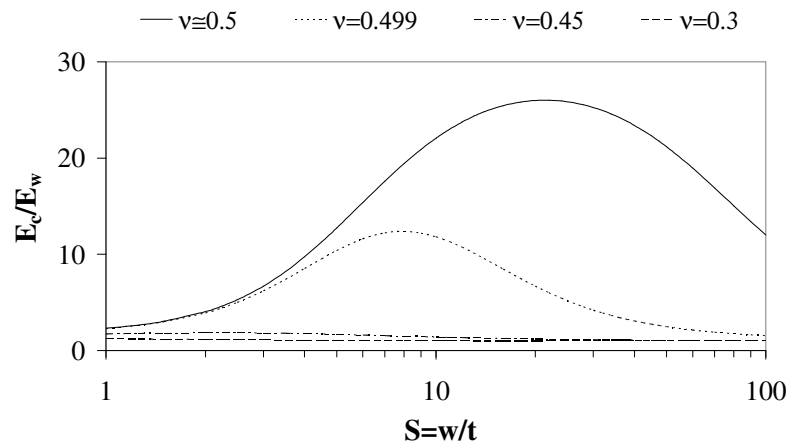
When the graphs in Figure 8.21 are compared with similar graphs in Figure 8.1, Figure 8.2 and Figure 8.12, it is realized that k_f^* affects E_w in the same way it affects E_c or E_b . However, the effect of the reinforcement flexibility on E_w is, in general, less than its effect on E_c or E_b . For specific values of k_f^* , S and ν , the reduction in E_c or E_b due to the reinforcement flexibility is larger than that in E_w .

As discussed in the compression and bending cases, it can be practical to represent E_w in terms of E_c . In Figure 8.22, the E_c/E_w ratio is plotted for various S , ν and k_f^* values. At this point, it is worth noting that PM predicts a value of 30 for the E_c/E_w ratio when the layer material is strictly incompressible (refer to Eqs. (2.94)). As shown in Figure 8.22a, when $k_f^* \rightarrow \infty$, $\nu \rightarrow 0.5$ and S is sufficiently large, FOT also leads to 30 for the E_c/E_w ratio. However, as it is seen from Figure 8.22b,c, this ratio can be much smaller than 30 especially if S , ν or k_f^* are small. Thus, taking the value of this ratio as 30 may significantly underestimate the true value of the warping modulus in IS-shaped layers bonded to extensible reinforcements.

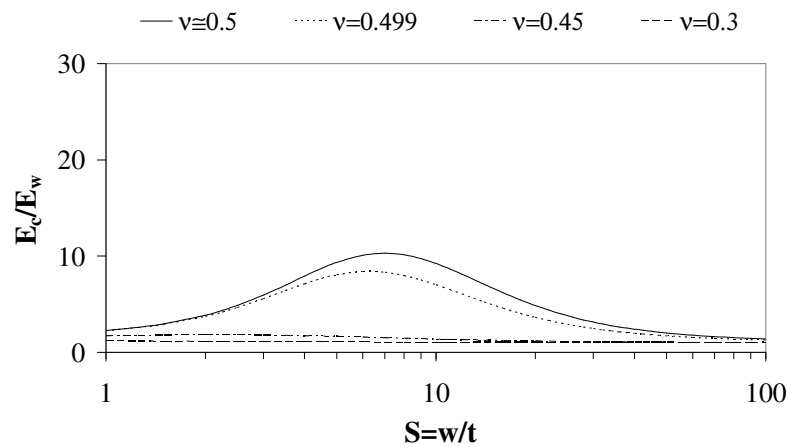
The graphs presented in Figure 8.23 to Figure 8.25 show the stress distributions in the lateral direction in a bonded IS-shaped layer under pure warping for various Poisson's ratios and two different shape factors; $S=2.5$ and $S=30$. Since the LSF layer is not influenced from the reinforcement flexibility unless k_f^* is considerably low, the graphs in Figure 8.23 are plotted only for two specific values of k_f^* , 30000 (those on the left hand side) and 30 (those on the right hand side). On the other hand, the graphs in Figure 8.24 are plotted for $k_f^*=30000, 3000, 300, 30$ to show the effect of reinforcement flexibility on the HSF layer clearly. In the graphs, the stress distributions are plotted over their most critical sections (i.e., τ_{11} and τ_{12} at $x_2=\pm t/2$, and τ_{22} at $x_2=0$) and the stress values are normalized by $E_w\Phi/t$. It is to be noted that the axial stress in a uniform short beam under pure warping, which equals to $\sigma_{zz} = E\Omega\Phi'$ (refer to Eq. (2.83)), reaches its maximum value, $(\sigma_{zz})_{\max} = 0.4E\Phi'$, at the outer edges of the layer, i.e., at $x_l=\pm w$, if the cubic function in Eq. (4.96) is selected as the warping function. Thus, normalizing the stress values by $E_w\Phi/t$ can be considered as normalizing them by the maximum axial stress developing in the corresponding unbonded layer predicted by the short beam theory.



a. $k_f/(\mu t) \rightarrow \infty$



b. $k_f/(\mu t) = 30000$



c. $k_f/(\mu t) = 300$

Figure 8.22 Effect of reinforcement flexibility on E_c/E_w ratio

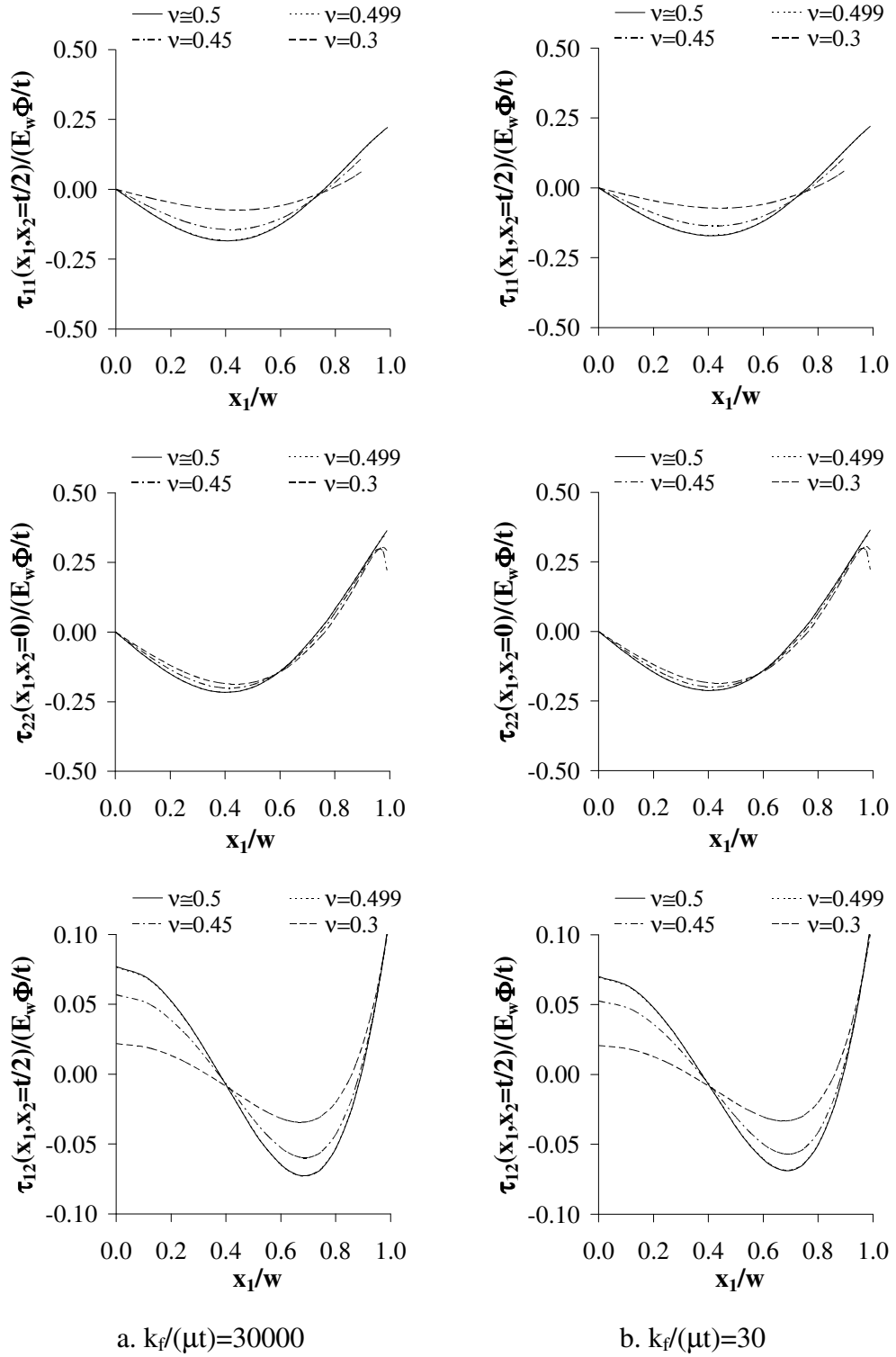


Figure 8.23 Effect of reinforcement flexibility on stress distributions in lateral direction under pure warping for $S=2.5$

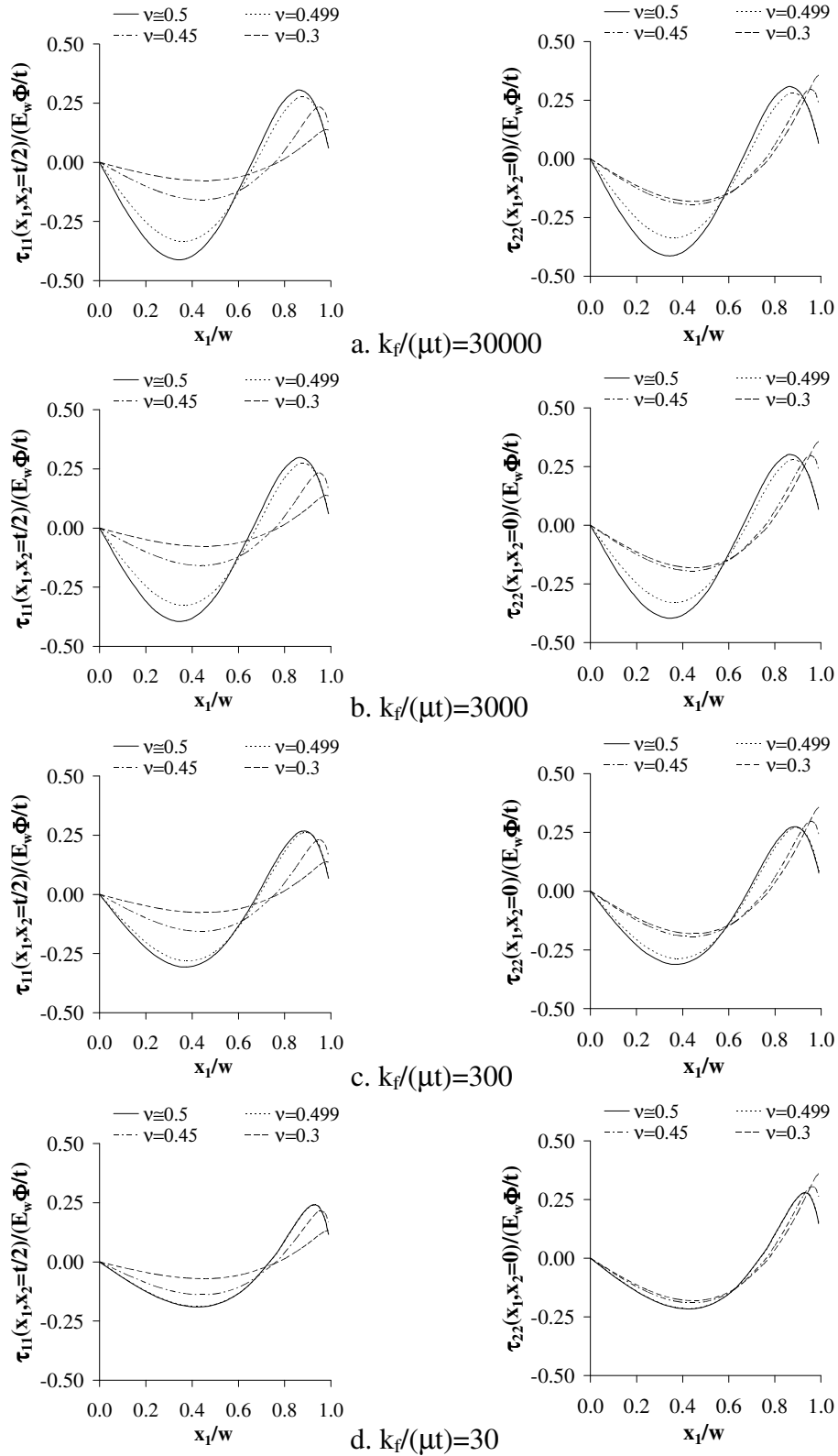


Figure 8.24 Effect of reinforcement flexibility on lateral normal stress distribution in lateral direction under pure warping for $S=30$

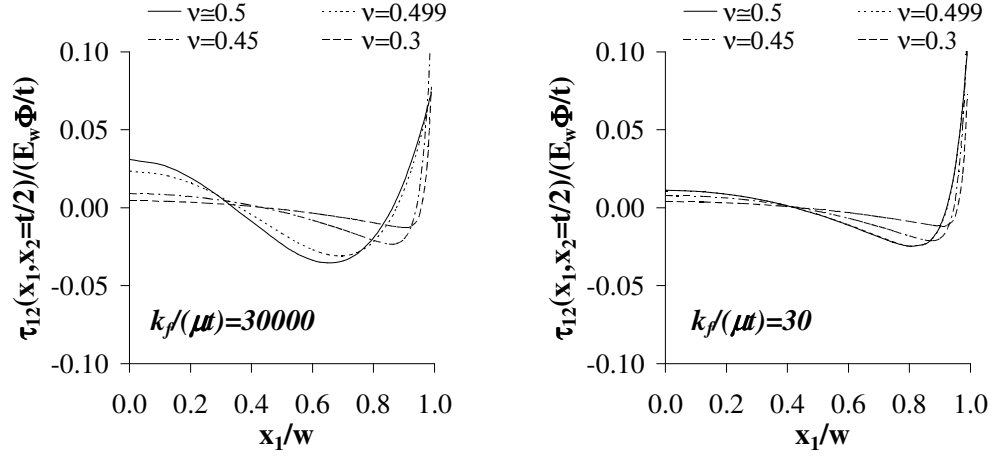


Figure 8.25 Effect of reinforcement flexibility on shear stress distribution under pure bending in lateral direction for $S=30$

From the graphs in Figure 8.23 to Figure 8.25, it is observed that the reinforcement flexibility influences the behavior of the HSF layer considerably while the LSF layer behaves as if it were rigidly-bonded even when $k_f^* = 30$. For $k_f^* = 30000$, the shapes of the stress distributions in the HSF layer highly depend on ν . For strictly incompressible materials, the distributions are as predicted by the pressure method (PM). This can be seen from Figure 8.26, where the FOT expressions for the axial and shear stress distributions in the HSF layer are compared with the PM expressions. It is to be noted that the PM predictions for the normalized axial stress distribution in Figure 8.26a are determined by dividing the stress values computed from the third term of Eq. (2.92), which is in the form of a fifth degree polynomial, by the warping modulus computed from Eq. (2.94). As far as the normalized shear stress distribution at the top face of the layer is concerned, the PM predictions can be computed from the relation $\tau_{12,PM}^+ = -(\partial_1 \tau_{22,PM})t/2$. In fact, the PM expressions for the normalized axial and shear stresses can be expressed, in the notation of the present formulation, in the following forms:

$$\frac{\tau_{22,PM}}{E_w \Phi/t} = -\frac{9}{2} \left(\frac{x_1^5}{w^5} - \frac{10}{7} \frac{x_1^3}{w^3} + \frac{3}{7} \frac{x_1}{w} \right) \quad \text{and} \quad \frac{\tau_{12,PM}}{E_w \Phi/t} = \frac{9}{4S} \left(5 \frac{x_1^4}{w^4} - \frac{30}{7} \frac{x_1^2}{w^2} + \frac{3}{7} \right) \quad (8.1)$$

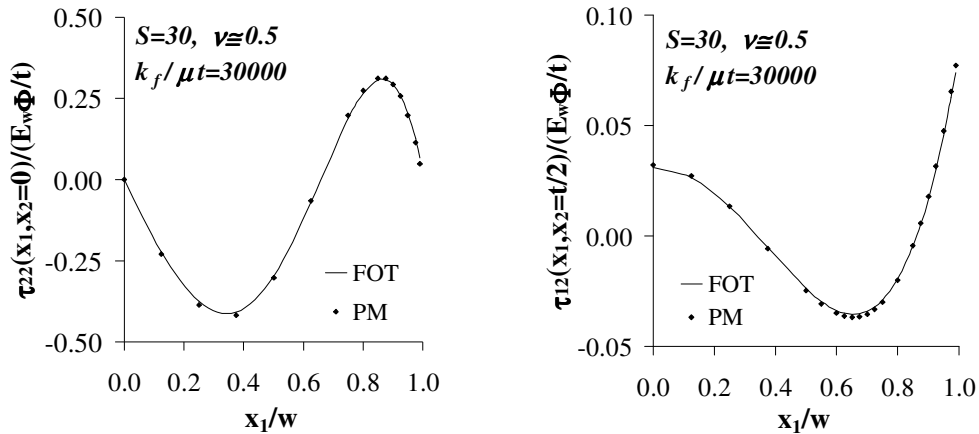


Figure 8.26 Convergence of FOT solution to PM solution for stress distributions in an HSF layer ($S=30, k_f/\mu t=30000$) of incompressible materials

On the other hand, for compressible materials, the axial stress distribution in the HSF layer is much closer to the prediction of the short beam theory. In fact, for $\nu=0.3$, the predictions of the both theories are almost the same even for the LSF layer, as shown in Figure 8.27. It is to be noted that the prediction of the short beam theory for the normalized axial stress simply equals to the warping shape. It is interesting to see from Figure 8.27 that the HSF layer of highly compressible material ($\nu=0.3$) behaves as if it were an unbonded layer even when $k_f^*=30000$.

When the graphs in Figure 8.24 are further examined to investigate the effect of the reinforcement flexibility on the normal stress distributions in the HSF layer, it is seen that k_f^* affects the stress distributions in the same way that ν does. The shape of the normalized axial stress distribution changes from a fifth degree polynomial to a third degree polynomial as k_f^* decreases. Similar to the uniform compression and pure bending cases, the difference in warping behavior of HSF layers of strictly and nearly incompressible materials disappears as k_f^* decreases. It should be noted that when $k_f^*=30$, the normalized axial stress distribution in the HSF layer becomes almost independent of the material compressibility. On the other hand, the normalized stress distributions for the lateral normal component are affected from ν considerably even when $k_f^*=30$: the stress values decrease as the material compressibility increases, which is also valid for the LSF layer.

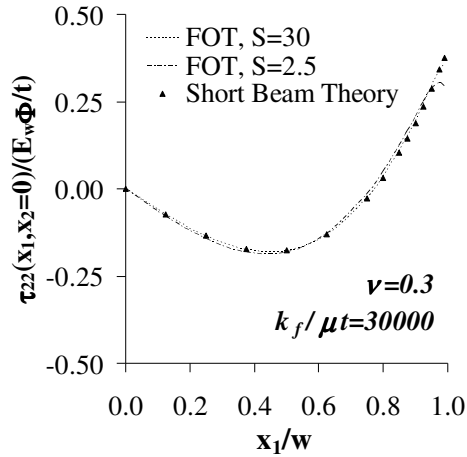


Figure 8.27 Convergence of FOT solution to the “short beam” solution for axial stress distribution in an LSF (S=2.5) and HSF (S=30) layer of compressible ($\nu=0.3$) materials bonded to flexible reinforcements ($k_f/\mu t=30000$)

From the graphs plotted for the shear stress distributions in Figure 8.23 and Figure 8.25, it is seen that, for the same values of k_f^* and ν , the normalized shear stress in the LSF layer is, in general, larger than that in the HSF layer. It is also observed that the normalized shear stress in the LSF layer decreases when the material compressibility increases. Similarly, the main effect of decreasing k_f^* or ν on the normalized shear stress distribution in the HSF layer is to decrease the stress values in the layer except for the edges.

From the plots in Figure 8.23 and Figure 8.24, one can also notice that normal stress distributions have two extremum points in the range $0 \leq x_1/w \leq 1$. Eq. (8.1) indicates that for the axial stress distribution in HSF layers of incompressible materials and inextensible reinforcements, these extremum points occur at $x_1 \cong 0.34w$ and $x_1 \cong 0.86w$. At these extremum points, the normalized axial stress reaches its peak values, which are approximately equal to -0.42 at $x_1 \cong 0.34w$ and 0.31 at $x_1 \cong 0.86w$. It should be noticed that the peak values do *not* depend on the shape factor of the layer. Since the behavior of a bonded elastic layer tend to the short beam behavior as the reinforcement extensibility or material compressibility increases, these extremum points move toward $x_1 \cong 0.45w$ and $x_1 = w$, which are the

two extremums for the cubic warping shape when $f=-3/5$. The peak values also change approximately to -0.18 at $x_1=0.45w$ and to 0.4 at $x_1=w$.

Similarly, from the graphs in Figure 8.23 and Figure 8.25, it can be seen that there are three critical points in the range $0 \leq x_1/w \leq 1$ for the shear stress distributions. Two of them have fixed locations: at the center ($x_1=0$) and at the edges ($x_1=w$). PM predicts the location of the third critical point as $x_1=\sqrt{3/7} w$ for HSF layers of incompressible materials and inextensible reinforcements and the peak values for the normalized shear stress at these extremum points as approximately $\{0.96/S, -1.10/S, 2.57/S\}$ at respectively $x_1=\{0, \sqrt{3/7} w, w\}$. When k_f^* or ν decreases, the location of the critical point near the center of the half-width moves towards the edge and the normalized shear stress over the cross section reduces, except for the edges. At the limit, when a bonded elastic layer starts to behave as if it were a short uniform beam, shear stress is concentrated only on the edges where it can reach significant values.

Using the stress expressions derived from FOT, it is also possible to study the effect of the reinforcement flexibility on the stress distributions in axial direction. In the graphs given in Figure 8.28 and Figure 8.29, the normal stress distributions are plotted at the vertical section $x_1=0.35w$ and the shear stress distributions are plotted at $x_1=0.65w$, which are very close to the extremum points discussed above for HSF layers of incompressible materials and inextensible reinforcements, for two different shape factors; $S=2.5$ and $S=30$. The effect of reinforcement flexibility on stress distributions is examined by plotting the graphs for two specific values of k_f^* ; 30000 (those on the left hand side) and 30 (those on the right hand side).

The graphs in Figure 8.29 show that the normal stresses are uniformly and shear stress is linearly distributed through the layer thickness for HSF layers, which is not valid, in general, for LSF layers, as shown in Figure 8.28. From the graphs, it can also be concluded that the pressure assumption is valid only for the HSF layer of nearly incompressible materials provided that the reinforcements are not too flexible. From the graphs plotted for $S=30$ and $k_f^*=30$, one can observe that the axial stress is no longer equal to the lateral normal stress at the studied section.

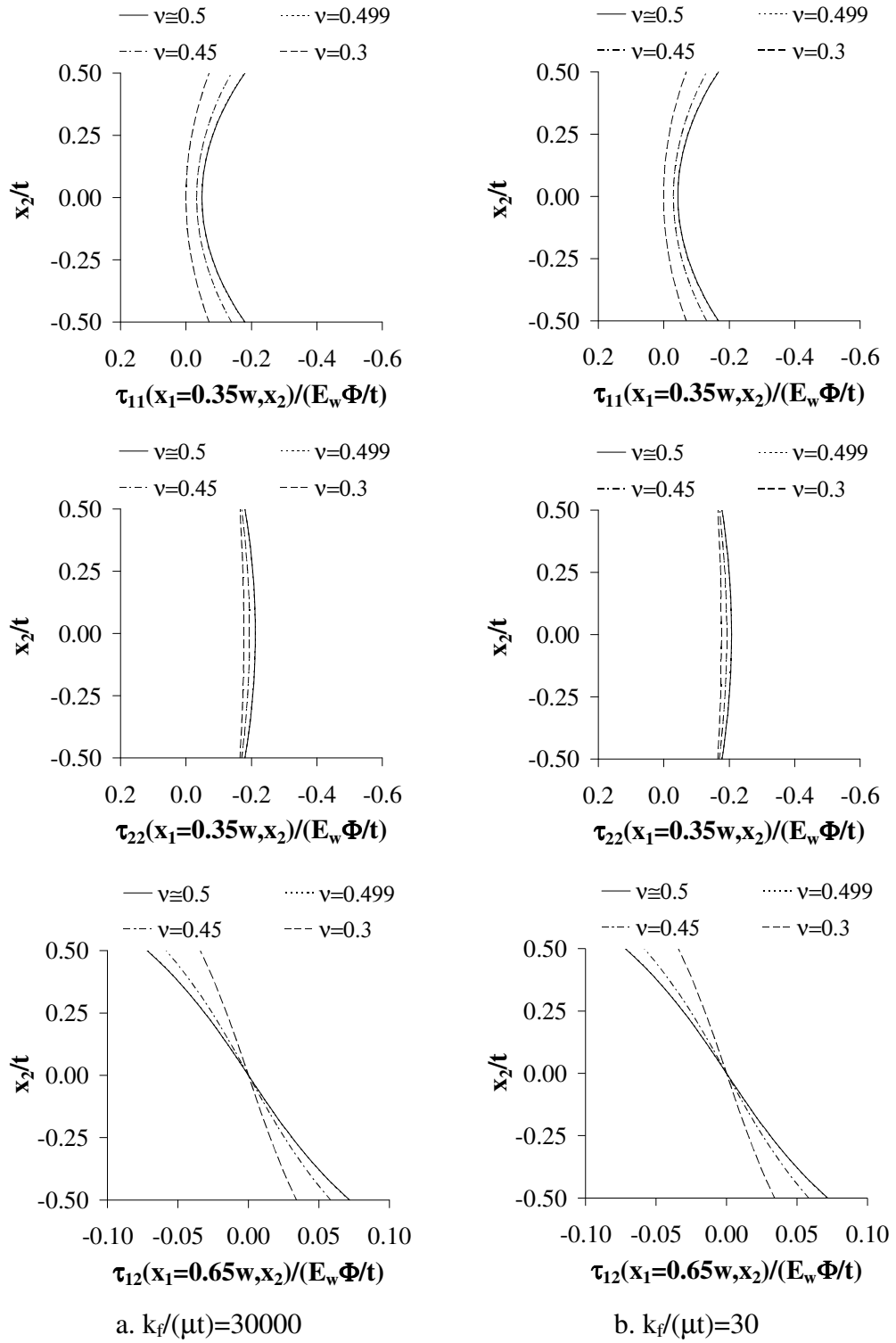


Figure 8.28 Effect of reinforcement flexibility on stress distributions in axial direction under pure warping for $S=2.5$

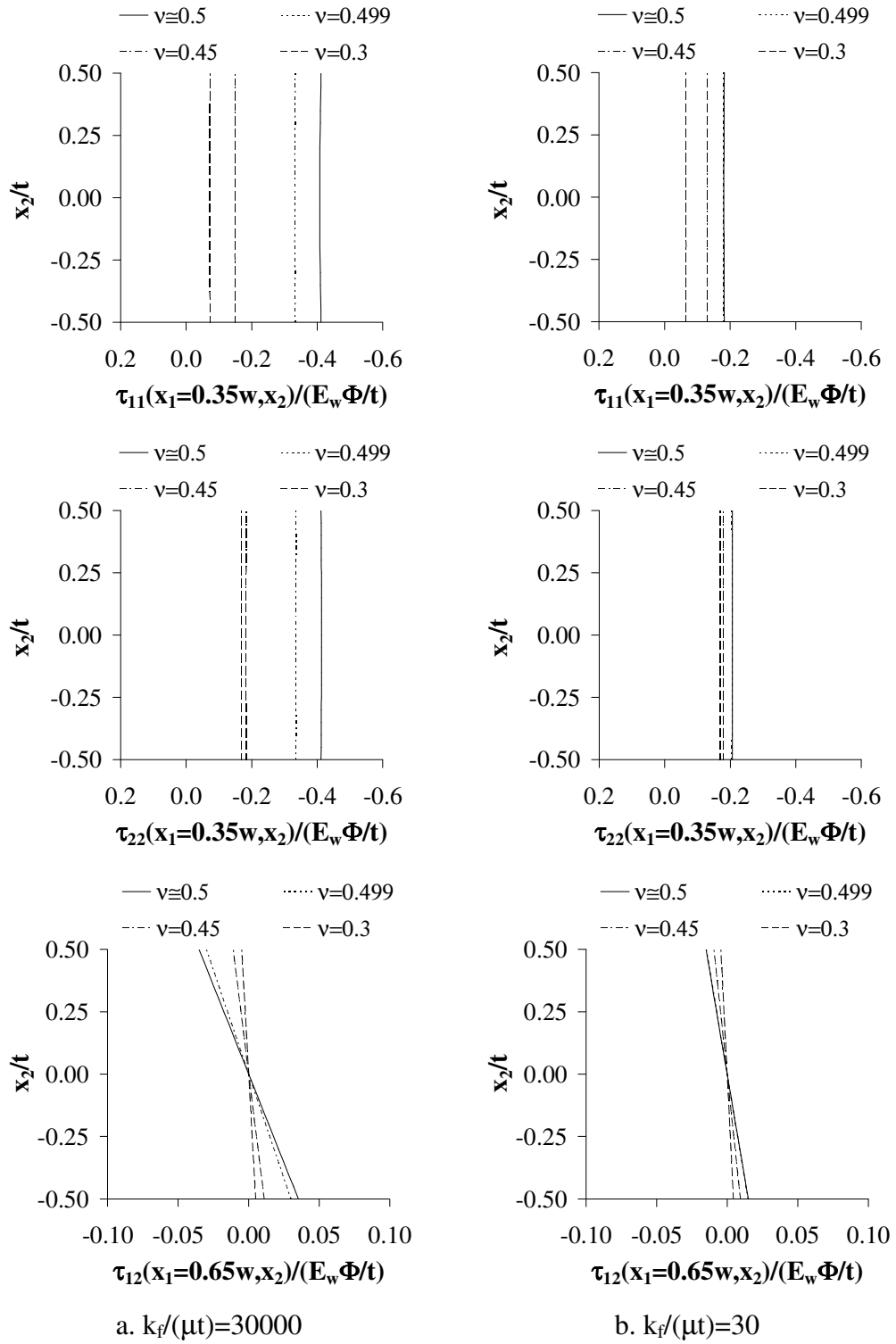


Figure 8.29 Effect of reinforcement flexibility on stress distributions in axial direction under pure warping for $S=30$

CHAPTER 9

CONCLUSIONS

In this dissertation, a new formulation is proposed for linear analysis of bonded elastic layers under some basic deformation modes. Developed using an approximate theory due to Mengi [19], this new formulation has some distinct advantages over the others in literature. Since the displacement boundary conditions are included in the formulation itself, there is no need to start the formulation with some assumptions on stress and/or displacement distributions in the elastic layer or in the reinforcing plates, or with some limitations on the geometrical and material properties. For this reason, the solutions are valid not only for HSF layers of incompressible or nearly incompressible materials but also for HSF layers of highly compressible materials and for LSF layers. Since, in the formulation, the most general forms of governing equations are derived by keeping the order of the theory and the shape of the layer arbitrary, one can easily apply the formulation to any shape of a bonded elastic layer and obtain solutions much closer to exact by increasing the order of the theory.

The analyses conducted in this dissertation indicate that the selection of Legendre polynomials as distribution functions in the proposed formulation, when used with the zeroth order theory (ZOT), leads to the same solutions obtained in literature by the formulations which “average” the variables and the equations through the layer thickness (see, e.g., Refs. [30,40,48]). Free from the widely used “pressure assumption”, these solutions are based on two kinematics assumptions: (i) the plane sections remain plane during the deformation and (ii) parabolic bulging.

The increase of the order of the theory to one eliminates the first kinematic assumption, retaining solely the parabolic bulging assumption. The results show that the main contribution of the use of first order theory (FOT) in the formulation is to improve the expressions for the axial displacement, in turn, for the stress distributions. Governing equations clearly reveal that the second order theory also removes the parabolic bulging assumption. However, it may not always be possible to derive closed-form solutions in the case of higher order theories due to the complex and coupled forms of the governing equations. At this point, it is worth noting that the validity of these two kinematic assumptions are investigated in Section 5.3.3 for an infinite-strip (IS) shaped layer of $S=5$ with various compressibility characteristics by using boundary element method (BEM). BEM results (presented in Figure 5.20) clearly indicate that while the parabolic bulging assumption is fairly realistic for all studied levels of compressibility, the assumption “plane sections remain plane” is not valid for $\nu \geq 0.45$ for $S=5$, showing the significance of the elimination of this assumption in the analysis of LSF layers.

In general, as far as the layer moduli are concerned, FOT predictions do not introduce any improvement if a closed-form expression for the layer modulus has already been derived using a formulation which averages the layer behavior. To the author’s knowledge, there are no such solutions for the compression modulus of rigidly-bonded annular discs and for the bending and warping moduli of infinite-strip-shaped layers bonded to flexible reinforcements. Thus, it can be said that the new formulation proposed in this dissertation leads to advanced solutions even for the layer modulus in these cases.

Furthermore, the formulation of the apparent shear problem in the same way the compression, bending and warping problems are handled, is the first trial, to the author’s knowledge, in literature for the study of the apparent shear behavior of bonded elastic layers. In addition, if the studies of Kelly [44] and Tsai and Kelly [46], where only an expression for the warping modulus is derived without any discussion on the warping behavior of bonded elastic layers, are excluded, the detailed study conducted in the dissertation on the warping behavior of infinite-strip-shaped layers may be considered as the first study on the subject.

It is worth noting that the proposed formulation is assessed by comparing the solutions derived using FOT with the numerical results obtained from BEM for various shapes, shape factors and Poisson's ratios. Good matches between the analytical and numerical predictions for all studied deformation modes, geometrical and material properties justify the reliability of the use of the new formulation in the analysis of bonded elastic layers.

In the dissertation, the behavior of bonded elastic layers under their fundamental deformation modes is studied by using the advanced solutions obtained from FOT. In the analyses, the effects of the three key parameters; (i) shape factor of the layer (S), (ii) Poisson's ratio of the layer material (ν) and (iii) stiffness of the reinforcing plates (k_f) on effective layer moduli, displacement and stress distributions over the entire layer, and location and magnitude of maximum stresses developing in the layer are investigated. Additionally, how the compressive behavior of a bonded circular disc is affected from the existence of a central hole is also examined in detail. Some of the findings obtained from this investigation are stated below:

- S , ν and k_f are the three key parameters that control the behavior of a bonded elastic layer under its fundamental deformation modes. They have significant effects not only on the layer stiffnesses but also on the displacement/stress distributions and the magnitude and/or location of the maximum stresses in the layer.
- The behavior of an LSF layer may be considerably different from that of an HSF layer. The widely used pressure method seems to be valid, in general, only for HSF layers of incompressible or nearly incompressible materials bonded to inextensible or nearly inextensible reinforcements. On the other hand, the stress assumptions of the pressure method, which involve assuming uniform distribution for normal stresses and linear distribution for shear stress over the thickness of the layer, are inconsistent with the results obtained for LSF layers. Results indicate that, in an LSF layer subjected to uniform compression, pure bending or pure warping, stresses are distributed

over the layer thickness in such a way that the maximum lateral (or radial) normal and shear stresses occur at the bonded faces of the layer while the maximum axial stress occurs at the central plane. Since the normal stress distributions may be highly nonuniform over the layer thickness in an LSF layer, the formulations that “average” the behavior of the layer through the layer thickness can not give accurate solutions for LSF layers while the expressions derived using FOT can predict the behavior accurately.

- The behavior of a bonded elastic layer approaches asymptotically to its incompressible behavior as Poisson’s ratio approaches 0.5. LSF layers reach their incompressible limits at much smaller values of ν . For this reason, the behavior of an LSF layer is not influenced significantly from the existence of slight compressibility ($\nu=0.499$). On the other hand, the behavior of a slightly compressible HSF layer can be considerably different from its incompressible behavior.
- The behavior of a bonded elastic layer approaches asymptotically to its rigidly-bonded behavior as the reinforcement stiffness tends to infinity. While an HSF layer attains its rigidly-bonded behavior at considerably large values of k_f especially if the layer material is strictly/nearly incompressible, there is no need to have very large values of k_f for an LSF layer to behave as if it were rigidly-bonded.
- In general, the reinforcement flexibility affects the behavior of a bonded elastic layer in the same way the material compressibility does. The behavior of a bonded elastic layer approaches its unbonded behavior as the reinforcement flexibility and/or material compressibility increases. It is important to note that the reinforcement flexibility also changes the effect of the material compressibility: a bonded elastic layer with a smaller k_f reaches its incompressible behavior at a smaller value of ν than a layer with the same shape factor, but, with a larger k_f . Similarly, a bonded elastic layer with a smaller ν reaches its rigidly-bonded behavior at a smaller k_f value than a layer with the same shape factor, but, with a larger ν .

- In design calculations, it is a common practice to represent the bending or warping modulus of a bonded elastic layer in terms of its compression modulus. The commonly used values, 5 for the E_c/E_b ratio and 30 for the E_c/E_w ratio, are valid only for layers of incompressible materials, high shape factors and rigid reinforcements. It is shown that the use of the mentioned values for LSF layers and/or for compressible materials and/or for flexible reinforcements may significantly underestimate the true value of the bending and warping stiffnesses of the layers.
- Determination of the magnitude and location of maximum hydrostatic tension developing in a bonded elastic layer subject to bending is essential for investigating its internal rupture behavior. It is shown that the prediction of Gent and Meinecke [20] is valid only for incompressible HSF layers. For lower shape factors or compressible materials, the site of failure shifts towards the edge of the layer and the value of maximum hydrostatic tension gets smaller.
- Studies on compressive behavior of rigidly-bonded circular discs have shown that a bonded disc starts to “sense” the existence of a central hole when the size of the hole reaches a critical value. This critical hole size is larger for an LSF layer than for an HSF layer. The main effect of the existence of a central hole in a bonded elastic layer is to decrease the compression modulus of the layer and to increase the maximum shear strain developing in the layer. Maximum shear strain in an HSF layer can be magnified significantly due to the existence of a very small hole especially if the layer material is also incompressible. For example, for a layer with an “initial shape factor” (shape factor of the corresponding solid disc with the same external radius and thickness) of $S_o=30$, it is possible to have a maximum shear strain ratio of as large as 15 when $\nu \cong 0.5$. It is to be noted that the presence of even slight compressibility in the layer material alleviates most of the severe effects of the hole on compressive behavior of HSF layers.

- A bonded annular layer starts to behave as if it were an infinite-strip shaped bonded layer when the size of the central hole is *sufficiently* “large”. Then, it is possible to approximate the behavior of the disc with the behavior of the “equivalent” strip-shaped layer. In literature, it has also been proposed to approximate the behavior of a bonded annular layer with the behavior of “equivalent” bonded solid circular layer, if the size of the hole is *sufficiently* “small”. It is shown in the dissertation that it is rather difficult to define the terminology “small” and “large” used for the limiting sizes of the hole since such definitions also highly depend on S_o and ν .

In the light of the studies conducted in this dissertation, the following recommendations can be made towards future research on the subject.

- The application of the formulation to the shapes which are not handled in this dissertation can be considered. Such a study can easily be done for any shape of rigidly-bonded elastic layers since the governing equations are derived both in rectangular and cylindrical coordinates. On the other hand, for layers bonded to flexible reinforcements, it may also be necessary to derive the governing equations in cylindrical coordinates for this case.
- Although it does not seem to be possible to derive closed-form solutions in the case of higher order theories due to the complex and coupled forms of the governing equations, the governing equations can be attempted to solve numerically for the second order theory and, if possible, for even higher order theories.
- Since the bulging shape starts to deviate from the parabolic shape as the shape factor of the layer decreases, it can be valuable to restudy each problem by using a new set of distribution functions, possibly the hyperbolic functions. For this purpose, the general form of the equations presented in this dissertation can be used since these equations are derived for an arbitrary set of distribution functions.
- One of the assumptions made in the dissertation during the analysis of elastic layers bonded to flexible reinforcements is the assumption that the

reinforcing plates have no flexural rigidity. It can be valuable to remove this assumption.

- Finally, in this dissertation, two of the three fundamental deformation modes are studied for elastic layers bonded to flexible reinforcements; uniform compression and bending. The third mode, the shear mode, can be attempted to formulate in a future study.

REFERENCES

1. Hall M.M., 1971. "Pressure distribution over the flat end surfaces of compressed solid-rubber cylinders". *Journal of Strain Analysis* 6 (1), 38-44.
2. Gent A.N., Lindley P.B., 1959. "The compression of bonded rubber blocks". *Proceedings of the Institution of Mechanical Engineers* 173 (3), 111-122.
3. Koh C.G., Kelly J.M., 1989. "Compression stiffness of bonded square layers of nearly incompressible material". *Engineering Structures* 11, 9-15.
4. Lindley P.B., 1968. "Effect of Poisson's ratio on compression modulus". *Journal of Strain Analysis* 3, 142-145.
5. Clark P.W., Aiken I.D., Kelly J.M., 1997. "Experimental studies of the ultimate behavior of seismically-isolated structures". *Report UCB/EERC – 97/18*, Earthquake Engineering Research Center, University of California, Berkeley, California, USA.
6. Naeim F., Kelly J.M., 1999. "Design of seismic isolated structures". John Wiley & Sons, Inc.
7. Kelly J.M., 1997. "Earthquake resistant design with rubber". Springer-Verlag, London.
8. Columbia University in the city of New York, (February 23) 2007, "Tuned mass dampers", <http://www.columbia.edu/cu/gsap/BT/BSI/TMD/rubber-4.jpg>, the last date accessed: February 23, 2007.

9. Imbimbo M., De Luca A., 1998. "F.E. stress analysis of rubber bearings under axial loads". *Computers and Structures* 68 (1), 31-39.
10. Kelly J.M., 1999. "Analysis of fiber-reinforced elastomeric isolators". *Journal of Seismology and Earthquake Engineering* 2 (1), 19-34.
11. Tsai H.-C., Kelly J.M., 2002. "Bending stiffness of fiber-reinforced circular seismic isolators". *Journal of Engineering Mechanics ASCE* 128 (11), 462-470.
12. Moon B.-Y., Kong G.-J., Kong B.-S., Kelly J.M., 2002. "Design and manufacturing of fiber reinforced elastomeric isolator for seismic isolation". *Journal of Materials Processing Technology* 130-131, 145-150.
13. Kelly J.M., 2002. "Seismic isolation systems for developing countries". *Earthquake Spectra* 18 (3), 385-406.
14. Kelly J.M., Takhirov S.M., 2001. "Analytical and experimental study of fiber-reinforced elastomeric isolators". *PEER Report 2001/11*, Pacific Earthquake Engineering Research Center, University of California, Berkeley, California, USA.
15. Kelly J.M., Takhirov S.M., 2002. "Analytical and experimental study of fiber-reinforced strip isolators". *PEER Report 2002/11*, Pacific Earthquake Engineering Research Center, University of California, Berkeley, California, USA.
16. Constantinou M.S., Kartoum A., Kelly J.M., 1992. "Analysis of compression of hollow circular elastomeric bearings". *Engineering Structures* 14 (2), 103-111.
17. Gent A.N., Henry R.L., Roxbury M.L., 1974. "Interfacial stresses for bonded rubber blocks in compression and shear". *Journal of Applied Mechanics* 41, 855-859.
18. Roder C.W., Stanton J.F., 1983. "Elastomeric bearings: state-of-the-art". *Journal of Structural Engineering ASCE* 109 (12), 2853-2871.

19. Mengi Y., 1980. "A new approach for developing dynamic theories for structural elements Part 1: Application to thermoelastic plates". *International Journal of Solids and Structures* 16, 1155-1168.
20. Gent A.N., Meinecke E.A., 1970. "Compression, bending and shear of bonded rubber blocks". *Polymer Engineering and Science* 10 (2), 48-53.
21. Gent A.N., 1992. "Engineering with rubber: How to design rubber components". Oxford University Press, New York.
22. Tsai H.-C., 2005. "Compression analysis of rectangular elastic layers bonded between rigid plates". *International Journal of Solids and Structures* 42 (11-12), 3395-3410.
23. Haddow J.B., Ogden R.W., 1988. "Compression of bonded elastic bodies". *Journal of the Mechanics and Physics of the Solids* 36 (5), 551-579.
24. Gent A.N., 1994. "Compression of rubber blocks". *Rubber Chemistry and Technology* 67 (3), 549-558.
25. Koh C.G., Lim H.L., 2001. "Analytical solution for compression stiffness of bonded rectangular layers". *International Journal of Solids and Structures* 38 (3), 445-455.
26. Lindley P.B., 1979. "Compression module for blocks of soft elastic material bonded to rigid end plates". *Journal of Strain Analysis* 14, 11-16.
27. Chalhoub M.S., Kelly J.M., 1990. "Effect of bulk compressibility on the stiffness of cylindrical base isolation bearings". *International Journal of Solids and Structures* 26 (7), 743-760.
28. Chalhoub M.S., Kelly J.M., 1991. "Analysis of infinite-strip-shaped base isolator with elastomer bulk compression". *Journal of Engineering Mechanics ASCE* 117 (8), 1791-1805.
29. Yeoh O.H., Pinter G.A., Banks H.T., 2002. "Compression of bonded rubber blocks". *Rubber Chemistry and Technology* 75 (3), 549-561.

30. Tsai H.-C., Lee C.C., 1998. "Compressive stiffness of elastic layers bonded between rigid plates". *International Journal of Solids and Structures* 35 (23), 3053-3069.
31. Horton J.M., Tupholme G.E., Gover M.J.C., 2002. "Axial loading of bonded rubber blocks". *Journal of Applied Mechanics ASME* 69 (6), 836-843.
32. Horton J.M., Tupholme G.E., Gover M.J.C., 2003. "Axial loading of annular bonded rubber blocks". *Rubber Chemistry and Technology* 76 (5), 1194-1211.
33. Mott P.H., Roland C.M., 1995. "Uniaxial deformation of rubber cylinders". *Rubber Chemistry and Technology* 68, 739-745.
34. Moghe S.R., Neff H.F., 1971. "Elastic deformations of constrained cylinders". *Journal of Applied Mechanics ASME* 38, 393-399.
35. Papoulia K.D., Kelly J.M., 1996. "Compression of bonded soft elastic material: Variational solution". *Journal of Engineering Mechanics ASCE* 122 (2), 1791-1805.
36. Ling Y., 1996. "An approximate solution for the compression of a bonded thin annular disk". *Journal of Applied Mechanics ASME* 63 (3), 780-787.
37. Holownia B.P., 1972. "Effect of Poisson's ratio on bonded rubber blocks". *Journal of Strain Analysis* 7, 236-242.
38. Fenner R.T., Remzi E.M., 1983. "Boundary integral equation evaluation of compression moduli of bonded rubber blocks". *Journal of Strain Analysis* 18 (4), 217-223.
39. Lindley P.B., 1979. "Plane strain rotation module for of soft elastic blocks". *Journal of Strain Analysis* 14, 17-21.
40. Tsai H.-C., Lee C.C., 1999. "Tilting stiffness of elastic layers bonded between rigid plates". *International Journal of Solids and Structures* 36 (17), 2485-2505.

41. Tsai H.-C., 2003. "Flexure analysis of circular elastic layers bonded between rigid plates". *International Journal of Solids and Structures* 40 (12), 2975-2987.
42. Horton J.M., Tupholme G.E., Gover M.J.C., 2002. "Bending of circular-section bonded rubber blocks". *International Journal of Solids and Structures* 39 (24), 5879-5893.
43. Rivlin R.S., Saunders D.W., 1949. "Cylindrical shear mountings". *IRI Transactions* 24, 249-306.
44. Kelly J.M., 1994. "The influence of plate flexibility on the buckling load of elastomeric isolators". *Report UCB/EERC-94/03*, Earthquake Engineering Research Center, University of California, Berkeley, California, USA.
45. Tsai H.-C., Kelly J.M., 2005. "Buckling of short beams with warping effect included", *International Journal of Solids and Structures* 42 (1), 239-253.
46. Tsai H.-C., Kelly J.M., 2005. "Buckling load of seismic isolators affected by flexibility of reinforcement", *International Journal of Solids and Structures* 42 (1), 255-269.
47. Tsai H.-C., Kelly J.M., 2001. "Stiffness analysis of fiber-reinforced elastomeric isolators". *PEER Report 2001/05*, Pacific Earthquake Engineering Research Center, University of California, Berkeley, California, USA.
48. Tsai H.-C., 2004. "Compression stiffness of infinite-strip bearings of laminated elastic material interleaving with flexible reinforcements". *International Journal of Solids and Structures* 41 (24-25), 6647-6660.
49. Pinarbasi S., Akyuz U., 2005. "Evaluation of the "pressure method" for the linear analysis of elastomeric bearings". *9th World Seminar on Seismic Isolation, Energy Dissipation and Active Vibration Control of Structures*, Kobe, Japan.
50. Ozkan G., 1995. "A boundary element method for axisymmetric elastodynamic analysis". Ph.D. Dissertation, Middle East Technical University, Ankara.

51. Mengi Y., Tanrikulu A.H., Tanrikulu A.K., 1994. "Boundary element method for elastic media: An introduction". Middle East Technical University, Ankara.
52. Ling Y.L., Engel P.A., Brodsky L., 1995. "Compression of bonded annular rubber blocks". *Journal of Engineering Mechanics*, 121 (6), 661-666.

CURRICULUM VITAE

PERSONAL INFORMATION

Surname, Name: Pınarbaşı, Seval
Nationality: Turkish (TC)
Date and Place of Birth: 21 November 1976, Afşin
Email: sevalp@metu.edu.tr

EDUCATION

Degree	Institution	Year of Graduation
PhD	METU, Department of Civil Engineering	2007
MS	METU, Department of Civil Engineering	2000
BS	METU, Department of Civil Engineering	1998
High School	Atatürk High School, Ankara	1993

ACADEMIC EXPERIENCE

Year	Place	Rank
1998-2007	METU, Department of Civil Engineering	Research Assistant
Sept. 2005 - July 2006	University of California at Berkeley, Earthquake Engineering Research Center	Visiting Scholar

PUBLICATIONS

1. Pınarbaşı S., Akyuz U., Mengi Y., 2006. "A new formulation for the analysis of elastic layers bonded to rigid surfaces". *International Journal of Solids and Structures* 43, 4271-4296.
2. Pınarbaşı S., Konstantinidis D., Kelly J.M., "Seismic isolation for soft-story buildings". *10th World Conference on Seismic Isolation, Energy Dissipation and Active Vibration Control of Structures*, Istanbul, Turkey, May 2007 (abstract accepted).
3. Pınarbaşı S., Akyuz U., Özdemir G., "An experimental study on low temperature behavior of elastomeric bridge bearings". *10th World*

Conference on Seismic Isolation, Energy Dissipation and Active Vibration Control of Structures, Istanbul, Turkey, May 2007 (abstract accepted).

4. Pinarbasi S., Akyuz U., Mengi Y., 2006. "Uniform compression of bonded elastic layers". *4th International Conference on Earthquake Engineering*, Taipei, Taiwan.
5. Pinarbasi S., Akyuz U., 2005. "Bending behavior of infinite-strip-shaped bonded elastic layers". *International Conference on Earthquake Engineering*, Skopje-Ohrid, Macedonia.
6. Pinarbasi S., Ozdemir G., Akyuz U., 2005. "An experimental study on behavior of low shape factor rubber bearings under large compressions". *International Conference Earthquake Engineering*, Skopje-Ohrid, Macedonia.
7. Pinarbasi S., Akyuz U., 2005. "Evaluation of the "Pressure Method" for the linear analysis of elastomeric bearings". *9th World Seminar on Seismic Isolation, Energy Dissipation and Active Vibration Control of Structures*, Kobe, Japan.
8. Pınarbaşı S., Akyüz U., 2005. "Sismik izolasyon ve elastomerik yastık deneyleri". *TMMOB İnşaat Mühendisleri Odası Teknik Dergi*, 16, 3581-3598.
9. Pinarbasi S., Akyuz U., 2004. "Investigation of compressive stiffness of elastomeric Bearings", *Sixth International Conference on Advances in Civil Engineering*, Istanbul, Turkey.
10. Pınarbaşı S., Akyüz U., 2004. "Çelik plakalı elastomerik köprü yastıklarının düşük sıcaklık kayma deneyleri". *Türkiye İnşaat Mühendisliği 17. Teknik Kongre ve Sergisi*, İstanbul.
11. Pinarbasi S., Akyuz U., 2003. "Seismic base isolation: philosophy, development and applications". *International Conference on Earthquake Engineering 40 SWEE*, Skopje-Ohrid, Macedonia.
12. Pınarbaşı S., Akyüz U., 2003. "Elastomerik yastıkların mekanik özelliklerinin belirlenmesi". *TÜBİTAK-Yapı Mekaniği Laboratuvarları Toplantısı II*, 141-144, Konya.
13. Pınarbaşı S., 2003. "Sismik temel izolasyonu yaklaşımı". *İMO Kocaeli Bülten* 1(2), 11-16.
14. Tankut T., Ersoy U., Pinarbasi S., Arıoğlu E., Ozdil E., Yorulmaz M., 2002. "Tests on a post tensioned moment resisting connection for precast concrete structures". *17th International Congress of the Precast Concrete Industry*, Istanbul, Turkey.